White dwarf and hot subdwarf binaries as possible progenitors of type I a Supernovae

Christian Karl

July 2004

White dwarf and hot subdwarf binaries as possible progenitors of type I a Supernovae

Den Naturwissenschaftlichen Fakultäten
der Friedrich-Alexander-Universität Erlangen-Nürnberg
zur
Erlangung des Doktorgrades

vorgelegt von
Christian Karl
aus Bamberg

Als Dissertation genehmigt von den Naturwissenschaftlichen Fakultäten
der Universität Erlangen-Nürnberg

Tag der mündlichen Prüfung:	09 Aug 2004
Vositzender der Promotionskommission:	Prof. Dr. L. Dahlenburg
Erstberichterstatter:	Prof. Dr. U. Heber
Zweitberichterstatter:	Prof. Dr. K. Werner

Contents

1 The SPY project **7**

2 Selection of DB white dwarfs **14**
2.1 Color criteria 14
2.2 Absorption line criteria 16
2.3 Summary of the DB selection 18

3 The UV Visual Echelle Spectrograph **19**
3.1 Instrumental setup 20
3.2 UVES data reduction 20
3.3 ESO pipeline vs. semi-automated pipeline 26

4 Derivation of system parameters **27**
4.1 Definition of samples 27
4.2 Radial velocity curves 28
4.2.1 Follow-up observations 28
4.2.2 Radial velocity measurements 28
4.2.3 Power spectra and RV curves 29
4.3 Gravitational redshift 31
4.4 Quantitative spectroscopic analysis 33
4.4.1 Stellar parameters of single-lined systems 34
4.4.2 Stellar parameters of double-lined systems 34
4.4.3 Projected rotational velocities 35
4.4.4 Metal abundances of sdB stars 35

5 Double-lined white dwarfs **36**
5.1 Systems analyzed from their radial velocity curves alone 37
5.1.1 WD 0028−474 39
5.1.2 HE 0315−0118 42
5.1.3 WD 1349+144 45
5.2 Systems that cannot be solved from their RV curves alone 48
5.2.1 HE 2209−1444, a system solved through an additional spectral analysis . 48
5.2.2 WD 0453−295, a system in need of an additional spectral analysis 53

6 White dwarfs with M dwarf companions **56**
6.1.1 WD 0419−487 alias RR Caeli . . . 58
6.1.2 WD 1013−050 . . . 61
6.1.3 HS 1606+0153 . . . 64
6.1.4 HE 2147−1405 . . . 67

7 Single-lined systems **69**
7.1 White dwarf primaries . . . 69
7.1.1 WD 0326−273 . . . 71
7.1.2 WD 1210+140 . . . 73
7.1.3 HS 1334+0701 . . . 75
7.1.4 WD 1824+040 . . . 77
7.2 Subdwarf B primary . . . 79
7.2.1 WD 0048−202 . . . 83
7.2.2 HE 0532−4503 . . . 86
7.2.3 HE 0929−0424 . . . 90
7.2.4 HE 1421−1206 . . . 94
7.2.5 HE 1448−0510 . . . 96
7.2.6 HE 2135−3749 . . . 99
7.2.7 HE 2150−0238 . . . 103
7.3 Subdwarf O primary . . . 107
7.3.1 HE 1059−2735 . . . 108
7.3.2 HE 1115−0631 . . . 110
7.3.3 HE 1318−2111 . . . 112

8 Peculiar objects **114**
8.1.1 PN G 2119+226 alias EGB 5, a central star of a planetary nebula . . . 114
8.1.2 WD 1914+094, a white dwarf with a peculiar Hα profile? . . . 117

9 Stars with small RV amplitudes **120**
9.1.1 HE 2208+0126 . . . 121
9.1.2 WD 0710+216 . . . 124
9.1.3 WD 1058−129 . . . 125
9.1.4 WD 1229−012 . . . 126
9.1.5 WD 1449+168 . . . 127
9.1.6 WD 1736+052 . . . 128
9.1.7 HS 2108+1734 . . . 129

10 Conclusion and outlook **131**
10.1 Conclusion . . . 131
10.2 Outlook . . . 134

A Selected DB candidates from the Hamburg ESO Survey **135**

B Follow-up campaigns **137**
B.1 Campaigns at the DSAZ 3.5m telescope 137
B.2 Campaigns at the ESO NTT 137
B.3 Campaigns at the ESO VLT 138
B.4 Campaigns at the WHT and INT 138

C Radial velocity measurements **139**

D Equivalent widths measurements **161**

E List of abbreviations **171**

List of Figures

1.1 Spectrum of a type Ia Supernova 8
1.2 Lightcurve of a type Ia Supernova 9
1.3 Progenitors of type Ia Supernova 11
1.4 Sample UVES spectrum of a hydrogen-rich DA white dwarf 12
1.5 White dwarf distribution 13
1.6 SPY detection probability as a function of orbital period 13

2.1 DB selection: Color criteria 15
2.2 DB selection: Significance threshold 17
2.3 DB selection: Cutoff criteria 17

3.1 The UV Visual Echelle Spectrograph 19
3.2 Sample UVES CCD exposure 20
3.3 UVES reduction pattern 21
3.4 Order definition for UVES spectra 23
3.5 Overlapping, unblazed echelle orders 24
3.6 The ripple problem 25
3.7 Reduced UVES spectrum: ESO pipeline vs. our own semi-automated pipeline . . 26

4.1 RV determination by means of MIDAS fits 30
4.2 RV curves of a single and a double lined system 31
4.3 Mass-radius relation for white dwarfs 32
4.4 Evolutionary tracks for DA white dwarfs 33
4.5 Evolutionary tracks for sdB stars 34

5.1 Sample model fits of double-lined systems 36
5.2 Analysis of a double-lined system 38
5.3 WD 0028−474: Observed line profile 39
5.4 WD 0028−474: Best fit RV curve and power spectrum 40
5.5 HE 0315−0118: Best fit RV curve and power spectrum 43
5.6 WD 1349−144: Best fit RV curve and power spectrum 46
5.7 HE 2209−1444: Line shift within one night 49
5.8 HE 2209−1444: Best fit RV curve and power spectrum 50
5.9 HE 2209−1444: Sample model atmosphere fits 52
5.10 WD 0453−295: Observed line profiles 53
5.11 WD 0453−295: Best fit RV curve and power spectrum 54

6.1 Sample UVES spectrum of a white dwarf with an M dwarf companion 57
6.2 WD 0419−487: Best fit RV curve and power spectrum 59
6.3 WD 1013−050: Emission lines 61
6.4 WD 1013−050: Splitted Balmer lines 62
6.5 WD 1013−050: Best fit RV curve and power spectrum 62
6.6 HS 1606+0153: Best fit RV curve and power spectrum 65
6.7 HS 1606+0153: Observed line profiles 65
6.8 HE 2147−1405: Best fit RV curve and power spectrum 68

7.1 Analysis of single-lined systems 70
7.2 WD 0326−273: Best fit RV curve and power spectrum 71
7.3 WD 1210+140: Best fit RV curve and power spectrum 74
7.4 HS 1334+0701: Best fit RV curve and power spectrum 76
7.5 WD 1824+040: Best fit RV curve and power spectrum 78
7.6 Sample UVES spectrum of an sdB star 80
7.7 Sample model fit of an sdB star 81
7.8 Determination of the microturbulence ξ 82
7.9 Projected rotational velocity $v_{\rm rot}$ sin i 82
7.10 WD 0048−202: Best fit RV curve and power spectrum 84
7.11 WD 0048−202: Metal abundance pattern 85
7.12 HE 0532−4503: Best fit RV curve and power spectrum 87
7.13 HE 0532−4503: Metal abundance pattern 88
7.14 HE 0532−4503: Post RGB evolutionary scenario 89
7.15 HE 0929−0424: Best fit RV curve and power spectrum 91
7.16 HE 0929−0424: Metal abundance pattern 92
7.17 HE 1421−1206: Best fit RV curve and power spectrum 95
7.18 HE 1448−0510: Best fit RV curve and power spectrum 97
7.19 HE 1448−0510: Metal abundance pattern 98
7.20 HE 2135−3749: Best fit RV curve and power spectrum 100
7.21 HE 2135−3749: Metal abundance pattern 101
7.22 HE 2150−0238: Best fit RV curve and power spectrum 104
7.23 HE 2150−0238: Metal abundance pattern 105
7.24 Sample UVES spectrum of an sdO star 107
7.25 HE 1059−2735: Best fit RV curve and power spectrum 109
7.26 HE 1115−0631: Best fit RV curve and power spectrum 111
7.27 HE 1115−0631: Best fit RV curve and power spectrum 113

8.1 PN G 2119+226 or EGB 5: $T_{\rm eff}$ - log g - diagram 115
8.2 PN G 2119+226 or EGB 5: Best fit RV curve and power spectrum 116
8.3 WD 1914+094: Observed Hα line profiles 117
8.4 WD 1914+094: Best fit RV curve and power spectrum 118

9.1 HE 2208+0126: Best fit RV curve and power spectrum 122
9.2 Best fit RV curves 130

10.1 *P-M* Diagram for $i = 52^{\rm o}$ 132
10.2 *P-M* Diagram for $i = 90^{\rm o}$ 133

List of Tables

4.1 Follow-up observations 29

5.1 WD 0028−474: System composition 41
5.2 HE 0315−0118: System composition 43
5.3 WD 1349+144: System composition 47
5.4 HE 2209−1444: Results of the model atmosphere analysis with FITSB2 51
5.5 WD 0453−295: System parameters and derived results 55

6.1 WD 0419−487: System composition 59
6.2 HS 1606+0153: Scenarios 66
6.3 HE 2147−1405: Scenarios 68

7.1 WD 0326−237: Scenarios 72
7.2 WD 1210+140: Scenarios 74
7.3 HS 1334+0701: Scenarios 76
7.4 WD 1824+040: Scenarios 78
7.5 WD 0048−202: Metal abundances 84
7.6 WD 0048−202: Scenarios 85
7.7 HE 0532−4503: Metal abundances 87
7.8 HE 0532−4503: Scenarios 89
7.9 HE 0929−0424: Metal abundances 91
7.10 HE 0929−0424: Scenarios 92
7.11 HE 1421−1206: Scenarios 95
7.12 HE 1448−0510: Metal abundances 97
7.13 HE 1448−0510: Scenarios 98
7.14 HE 2135−3749: Metal abundances 100
7.15 HE 2135−3749: Scenarios 101
7.16 HE 2150−0238: Metal abundances 104
7.17 HE 2150−0238: Scenarios 105
7.18 HE 1059−2735: Scenarios 109
7.19 HE 1115−0631: Scenarios 111
7.20 HE 1318−2111: Scenarios 113

8.1 PN G 2119+226 or EGB 5: Scenarios 116
8.2 WD 1914+094: Scenarios 119

9.1 HE 2208+0126: Scenarios 122

9.2 WD 0710+216: Scenarios 124
9.3 WD 1058−129: Scenarios 125
9.4 WD 1229−012: Scenarios 126
9.5 WD 1449+168: Scenarios 127
9.6 WD 1736+052: Scenarios 128
9.7 HS 2108+1734: Scenarios 129

A.1 Selected DB candidates from the HES 135

C.1 Radial velocity measurements 139

D.1 Equivalent width measurements 161

E.1 Abbreviations 171

Zusammenfassung

Die vorliegende Arbeit beschäftigt sich hauptsächlich mit der Analyse Weißer Zwerge und unterleuchtkräftiger B und O Sterne in Doppelsternsystemen. Dabei soll anhand der Beobachtungsdaten vor allem geklärt werden, ob die untersuchten Systeme mögliche Vorläufer von Supernovae des Typs Ia darstellen.

Supernovae des Typs Ia (SNe Ia) spielen eine Schlüsselrolle in vielen Bereichen der modernen Astronomie. Sie sind die wichtigsten Produzenten von Eisen im Universum und dienen als "Standardkerzen" außerdem zur Bestimmung extragalaktischer Entfernungen. In letzterem Falle wird davon ausgegangen, daß alle SN Ia Explosionen ähnliche Lichtkurven, insbesondere gleiche absolute Maximalhelligkeiten aufweisen. Aus der tatsächlich auf der Erde gemessenen, scheinbaren Helligkeit kann so auf die Entfernung geschlossen werden, in der die beobachtete Explosion stattfand. Derartige Messungen ermöglichten es den Astronomen in den letzten Jahren, den Wert der Hubblekonstanten mit bisher nie erreichter Präzision zu bestimmen. Darüber hinaus ergaben sich die ersten Hinweise auf ein beschleunigt expandierendes Universum.

Trotz ihrer herausragenden Bedeutung ist noch immer nicht zweifelsfrei geklärt, wie Supernovae vom Typ Ia entstehen. Als sicher gilt, daß es sich bei einem SN Ia Ereignis um die Explosion eines Weißen Zwerges handelt, der eine kritische Masse überschreitet. Diese ist wahrscheinlich die sogenannte Chandrasekharmasse M_{Chandra}, welche die Maximalmasse eines Weißen Zwerges und den Übergang zum Neutronenstern charakterisiert. Allerdings kann sich ein Weißer Zwerg dieser Grenzmasse nur annähern, wenn er als Komponente eines Doppelsternsystems Masse von einem Begleiter erhält. Die genaue Art dieses Doppelsternsystems – v.a. die Natur des Begleiters – ist allerdings noch nicht eindeutig geklärt und Gegenstand aktueller Forschung. Bisher werden zwei Szenarien favorisiert:

- Im sogenannten "Single Degenerate" Szenario besteht das Doppelsternsystem aus einem Weißen Zwerg und einem Hauptreihen- oder Riesenstern. Von Letzterem findet ein kontinuierlicher Massenüberstrom auf den Weißen Zwerg statt, bis dieser seine kritische Masse erreicht und in einer Supernovaexplosion vergeht. Dieses Szenario ist konform mit der Annahme, daß jede SNe Ia Explosion eine genau definierte absolute Maximalhelligkeit besitzt.

- Im sogenannten "Double Degenerate" Szenario ist der SN Ia Vorläufer Teil eines aus zwei Weißen Zwergen bestehenden, engen Doppelsternsystems. Dieses kann durch Gravitationsstrahlung Drehimpuls abgeben, was schließlich zu einem Verschmelzen beider Sterne führt. Ein derartiges System gilt als Supernovavorläufer, falls beide Komponenten innerhalb einer Hubblezeit T_{H} fusionieren und deren Gesmatmasse die Chandrasekharmasse überschreitet. Nach diesem Szenario sind auch sehr viel massereichere Supernovae denkbar, die leuchtkräftiger wären als bisher angenommen.

Noch ist nicht geklärt, welches der beiden Szenarien der Realität am ehesten entspricht.

Denkbar ist auch, daß beide relevant sind. Um aber Typ Ia Supernovae auch im jungen Universum als "Standardkerzen" nutzen zu können, müssen Entwicklungseffekte berücksichtigt werden. Daher ist es unbedingt notwendig zu ermitteln, wie wichtig der Beitrag des "Double Degenerate" Szenarios für die Bildung von Supernovae des Typs Ia tatsächlich ist.

Um diese Problematik näher zu analysieren wurde 2000 das **S**upernova Ia **P**rogenitor Surve**Y** (SPY) Projekt ins Leben gerufen (siehe Napiwotzki et al. 2003a), mit dem Ziel, das "Double Degenerate" Szenario durch Beobachtungen zu überprüfen. Eine große Anzahl möglicher SN Ia Kandidaten – manche eigens für SPY aus dem **H**amburg/**E**SO **S**urvey (HES) selektiert – wurde am **V**ery **L**arge **T**elescope (VLT) der Europäischen Südsternwarte (**E**uropean **S**outhern **O**bservatory, ESO) beobachtet. Der **U**V **V**isual **E**chelle **S**pectrograph (UVES) und eine selbstentwickelte, halbautomatische Reduktionsroutine lieferten hochaufgelöste Spektren, anhand derer nach Weißen Zwergen mit variablen Radialgeschwindigkeiten gesucht wurde. Bei 137 der untersuchten Weißen Zwerge wurden Geschwindigkeitsvariationen gefunden, die auf einen unsichtbaren Begleiter hindeuten, der mit dem im Spektrum sichtbaren Hauptstern den gemeinsamen Schwerpunkt umläuft. 16 der untersuchten Objekte waren sogar "doppellinige" Systeme, deren Spektren direkte Anzeichen eines Begleiter aufweisen. Bis dato waren nur sechs solcher Systeme bekannt. Insgesamt konnte mit den neuentdeckten Systemen die Zahl der bekannten Weißen Zwerge in Doppelsternen mehr als versiebenfacht werden.

Parallel zum Survey wurde begonnen, die gefundenen Systeme am 3.5 m Teleskop des **D**eutsch **S**panisches **A**stronomisches **Z**entrum (DSAZ), am ESO - VLT, am **N**ew **T**echnology **T**elecscope (NTT) der ESO und am **W**illiam **H**erschel **T**elescope (WHT) nachzubeobachten und auf ihre Eignung als mögliche Vorläufer einer Typ Ia Supernova hin zu untersuchen.

Im Rahmen der vorliegenden Arbeit wurden sowohl mögliche SN Ia Kandidaten aus dem HES selektiert (Kapitel 2) als auch eine neue und verbesserte Reduktionsroutine für UVES Daten entwickelt (Kapitel 3). Hauptziel war es aber, Nachbeobachtungen am DSAZ und NTT durchzuführen und zu analysieren (Kapitel 5 bis 9).

Besonders sechs doppellinige Systeme sind hervorzuheben, deren Spektren bereits Rückschlüsse auf die Bewegung beider Komponenten des Doppelsterns zulassen. Daher konnte durch eine Analyse der Radialgeschwindigkeitskurven das Massenverhältnis $M_{\rm prim}/M_{\rm sec}$ beider Komponenten bestimmt werden. Für vier der Systeme konnten zusätzlich Unterschiede in den Gravitationsrotverschiebungen der Einzelsterne dazu genutzt werden, deren absolute Massen und die Zeit $t_{\rm m}$ bis zu deren Verschmelzung zu bestimmen. Diese Methode funktionierte allerdings nicht für die verbliebenen doppellinigen Systeme, da sich deren Rotverschiebungsdifferenzen als nicht aussagekräftig erwiesen. Um die Zahl der freien Systemparameter weiter einzuschränken, wurde deshalb eine quantitative Spektralanalyse versucht – eine Untersuchungsmethode, die bislang nur auf Einzelsterne angewandt wurde. Da es sich bei Spektren doppelliniger Systeme um eine Überlagerung zweier Einzelsternspektren handelt, erforderte diese Analyse die Entwicklung eines neuartigen Programms. Für HE 2209−1444 gelang mit dessen Hilfe schließlich eine Spektralanalyse, allerdings nur, da aufgrund der Ähnlichkeit beider Komponenten weitere freie Parameter eliminiert werden konnten. Das letzte doppellinige System WD 0453−295 bleibt dagegen noch ungelöst.

Vor allem WD 0028−202 erwies sich als ausgezeichneter SN Ia Vorläuferkandidat. Beide Komponenten des aus zwei Weißen Zwerge bestehenden Doppelsternsystems werden innerhalb einer halben Hubblezeit zu einem Objekt verschmelzen, das die Chandrasekharmasse überschreitet. Damit erfüllt WD 0028−202 als eines von nur drei Systemen alle Kriterien, die vom "Double Degenerate" Szenario an einen möglichen SN Ia Voräufer gestellt werden. Im Rah-

men des SPY Projektes wurden darüber hinaus noch zwei weitere Systeme gefunden, welche die Qualifikationskriterien nur knapp verfehlen. Den Anteil der im "Double Degenerate" Szenario erzeugten SNe Ia können zwar erst Modellrechnungen exakt bestimmen, aber bereits jetzt dürfte aufgrund der gefundenen Beobachtungsergebnisse klar sein, daß dieses Szenario als möglicher, wenn nicht gar entscheidender Weg zur Bildung von Typ Ia Supernovae angesehen werden muß.

Zu den bereits beschriebenen doppellinigen Systemen wurden noch 26 weitere, einlinige Systeme untersucht, deren Spektren keine zweifelsfreie Analyse der Bewegung der zweiten Komponente zulassen. Dennoch ergaben Radialgeschwindigkeitsanalysen für 17 dieser Systeme eindeutige Ergebnisse für die Bahnparameter, während für die verbleibenden neun Systeme aufgrund des vorliegenden Datenmaterials keine eindeutigen Lösungen gefunden werden konnte. Für Letztere sind deshalb noch zusätzliche Beobachtungen nötig, um eine Aussage über ihre Systembeschaffenheit treffen zu können.

Unter den 17 eindeutig gelösten Systemen stellten sich drei als Weiße Zwerge mit M Hauptreihensternen als Begleiter heraus, die somit nach dem "Double Degenerate" Szenario nicht als Typ Ia Supernovavorläufer in Frage kommen. Die übrigen 14 Systeme konnten nur über ihre Massenfunktion weitergehend untersucht werden. Diese Funktion verknüpft die Massen $M_{\rm vis}$ und $M_{\rm invis}$ beider Komponenten eines Doppelsternsystems mit dem Inklinationswinkel i. Während sich die Massen $M_{\rm vis}$ der sichtbaren Komponente entweder durch eine quantitative Spektralanalyse bestimmen oder aus Evolutionsrechnungen ableiten lassen, bleibt die Inklination i unbestimmt, da ihre Festlegung außer für Bedeckungsveränderliche kaum möglich ist. Die einzig weitere Möglichkeit der Inklinationsmessung bieten besonders enge Systeme, bei denen die Sternrotation durch Gezeitenkräfte wie beim Erde-Mond System mit der orbitalen Bahnbewegung synchronisiert ist. Mit Hilfe des Dopplereffekts kann aus den Spektren die projizierte Rotationsgeschwindigkeit bestimmt und durch Vergleich mit der Bahnbewegung schließlich auf den Inklinationswinkel geschlossen werden. Diese Methode wurde auf sechs unterleuchtkräftige B Sterne des Samples angewandt, deren schmale Metallinien sich besonders gut für eine derartige Analyse eignen. Die Auswertung ergab allerdings nur für HE 2135−3749 sinnvolle Werte. Bei den übrigen Objekten stellte sich entweder die Annahme gebundener Rotation als falsch heraus, oder es zeigte sich, daß die Messungen der Rotationsgeschwindigkeiten aufgrund der nicht genau bekannten spektralen Auflösung der Beobachtungsdaten nicht zuverlässig genug waren.

Wegen der Unbestimmtheit der Inklination wurden die Doppelsternsysteme zunächst unter der Annahme maximaler Inklination ($i = 90^{\rm o}$) untersucht. Da diese Annahme in den Minimalmassen der unsichtbaren Komponenten resultiert, werden die wirklichen Massen stets unterschätzt. In diesem Sinne ergibt diese Annahme das strikteste Auswahlkriterium für eventuelle SN Ia Kandidaten: Zwar werden potentielle SN Ia Kandidaten möglicherweise nicht erkannt, aber auch keine ungeeigneten Systeme als solche fehlklassifiziert.

Des Weiteren wurden die Systeme unter der Annahme eines Inklinationswinkels von $i = 52^{\rm o}$ untersucht. Dieser Winkel ist der statistisch wahrscheinlichste Wert der Inklination und liefert somit auch die wahrscheinlichste Begleitermasse.

Wie sich zeigte, konnte bei den einlinigen Systemen weder unter der Annahme $i = 90^{\rm o}$ noch $i = 52^{\rm o}$ ein System gefunden werden, das sich als SN Ia Kandidat eignet. Vier der untersuchten Doppelsternsysteme könnten allerdings für Winkel kleiner als $52^{\rm o}$ die Voraussetzungen erfüllen und als SN Ia Vorläufer gelten. Die Perioden der übrigen zehn Systeme sind jedoch zu groß, als daß selbst der massereichste Weiße Zwerg ($M_{\rm invis} = M_{\rm Chandra}$) noch innerhalb einer Hubblezeit mit der sichtbaren Komponente verschmelzen könnten.

Als Nebenprodukt der Radialgeschwindigkeitsanalysen wurden chemische Häufigkeitsmuster

der untersuchten Sterne bestimmt. Für fünf der untersuchten Objekte decken sich die gefundenen Häufigkeiten mit denen normaler, unterleuchtkräftiger B Sterne. Nur HE 2135−3749 fiel durch seine ungewöhnliche Titananreicherung auf. Solche "pekuliären" Häufigkeitsmuster wurden nur bei drei anderen Objekten beobachtet, verstanden sind sie allerdings noch nicht.

Bislang sind erst etwa 30 % aller 137 von SPY gefundenen Doppelsterne nachbeobachtet und analysiert. Allerdings zeigen bereits die in dieser Arbeit erzielten Ergebnisse deutlich, daß das "Double Degenerate" Szenario für die Entstehung von Typ Ia Supernovae eine wichtige, wenn nicht sogar entscheidende Rolle spielt. Darüberhinaus wird SPY nach Abschluss aller Nachbeobachtungen ein statistisch vollständiges, flußlimitiertes Beobachtungssample liefern, anhand dessen wichtige Entwicklungsparameter der Doppelsternentwicklung kalibriert werden können. In diesem Sinne tragen alle gefundenen und analysierten Systeme, gleich ob SN Ia Vorläufer oder nicht, zum besseren Verständnis enger Doppelsterne bei.

Das SPY Projekt wird in Kapitel 1 detailliert erläutert. Kapitel 2 beschäftigt sich mit der Selektion Weißer Zwerge aus dem Hamburg/ESO Survey, die im Rahmen von SPY beobachtet werden sollten. Kapitel 3 stellt den für den Survey verwendeten Spektrographen (UVES) und die dafür neu entwickelte Reduktionsroutine vor. Die Methoden zur Analyse der gewonnenen Spektren werden in Kapitel 4 näher erläutert, während die Ergebnisse in den Kapiteln 5 bis 9 diskutiert werden. Schlußbemerkungen und ein weiterführender Ausblick finden sich im letzten Kapitel.

Abstract

Supernovae of type Ia (SNe Ia) play a prominent role in many astrophysical environments, and their use as cosmological tools is being pushed to redshift 1 and beyond. The nature of their progenitors, however, remains a mystery which represents a major limitation both for understanding the astrophysical phenomena in which SNe Ia are involved and for their use as cosmological probes. In one of the two possible scenarios, the SN Ia results from the merging of a binary composed of two white dwarfs exceeding a critical mass (most likely the Chandrasekhar mass $M_{\rm Chandra}$). However, previous searches for binary white dwarfs (double degenerates) have failed to produce a statistically significant sample to test this scenario. Therefore, the **S**upernova Ia **P**rogenitor Surve**Y** (SPY) was proposed at the **V**ery **L**arge **T**elescope (VLT) of the **E**uropean **S**outhern **O**bservatory (ESO). This project was a large spectroscopic survey of white dwarfs with the **U**V **V**isual **E**chelle **S**pectrograph (UVES). The purpose was to observe more than 1000 white dwarfs, which would provide a definite test of the double degenerate (or merger) scenario. The target-list was composed of already known objects selected from various catalogs, as well as newly identified white dwarfs, e.g. 50 helium-rich DB white dwarfs from the Hamburg/ESO survey. A self-developed, semi-automated reduction pipeline provided us with high quality spectra to search for radial velocity variations – an unambiguous hint for binarity.

Follow-up observations were started parallel to the survey in order to obtain radial velocity curves for the most promising merger candidates found by SPY. These follow-ups were done with the 3.5 m telescope of the **D**eutsch **S**panisches **A**stronomisches **Z**entrum (DSAZ), the ESO **N**ew **T**echnology **T**elecscope (NTT), the ESO-VLT and the **W**illiam **H**erschel **T**elescope (WHT).

This thesis addresses the target selection from the HES (chapter 2) and the reduction-pipeline for UVES data (chapter 3). The main part, however, deals with the results of the follow-up campaigns done at the DSAZ and the NTT (chapters 5 to 9). In the course of these observations, a total of 32 binary systems have been observed and analyzed in order to test whether they qualify as SN Ia progenitors, i.e. whether the total mass is larger than $M_{\rm Chandra}$ and they merge in less than the Hubble time $T_{\rm H}$ due to gravitational wave radiation.

Six of these systems are double-lined, already revealing evidence for a companion in their spectra. Thus, the radial velocity analyses provide information not only about the motion of the primary, but also of the secondary. This offers the possibility to derive all orbital parameters as well as the masses of both components. The highlight is the detection of the double-lined system WD 0028−474. This white dwarf binary has a total mass above $M_{\rm Chandra}$ and will merge in less than a Hubble time. Therefore, WD 0028−474 fulfills all criteria defined by the merger scenario to qualify as a SN Ia progenitor. Along with another SPY object (see Napiwotzki et al. 2003a) and the subdwarf B (sdB) plus white dwarf binary KPD 1930+2752 (Maxted et al. 2000c), WD 0028−474 is the third system supposed to produce a SN Ia event. In addition, the SPY objects HE 2209−1444 (this thesis and Karl et al. 2003) and HE 1414−0848 (Napiwotzki

et al. 2002) are only 10 - 20 % below the limit. The relevance of the merger scenario is therefore strongly enforced, all the more if one considers that only about 30 % of the radial velocity variable objects found by SPY have been analyzed so far.

In addition to the double-lined objects, 26 single-lined systems are analyzed as well. For 17 we derive very accurate orbital solutions, whereas for the remaining systems the solutions are still ambiguous and more observations are needed to solve them definitely. Moreover, three systems show evidence for a main sequence companion and are therefore not suited for a SN Ia precursor according to the double degenerate scenario.

For the remaining 14 objects we determined the masses of the visible components via quantitive spectral analyses and evolutionary calculations (e.g. the mass-radius relation), respectively, whereas the masses of the unseen components are estimated from the mass functions $f_{\rm m}$. To solve this equation definitely, however, the determination of the the inclination i is crucial. The inclination angle can be determined most easily in the case of eclipsing binaries. However, our systems are not known to be eclipsing. Nevertheless, assuming tidally locked rotation, we compared the orbital motions of six sdB stars with their spectroscopically derived projected rotational velocities $v_{\rm rot} sini$ in order to estimate upper limits for i at least. Unfortunately, this method yields plausible results for HE 2135−3749 only. We conclude, that either the remaining objects do not rotate tidally locked or the determination of $v_{\rm rot} sini$ was not accurate due to insufficient information about the instrumental profile.

Since the inclination i is still indetermined, we estimate the most likely system compositions from their mass functions and the statistically most probable inclination $i = 52^{\rm o}$, whereas the companions' minimum masses are derived for $i = 90^{\rm o}$. The latter inclination results in the systems' minimum masses and is therefore the most conservative criterium to select probable SN Ia candidates. Although the analysis yields neither for $i = 90^{\rm o}$ nor for $i = 52^{\rm o}$ a probable SN Ia candidate, four systems could pass the criteria if their inclination angles are below $52^{\rm o}$. For the remaining ten binaries, however, the merging time $t_{\rm m}$ exceeds the Hubble time even for the most favorable scenario. Thus, these systems certainly do not qualify as SNe Ia precursors.

Besides the search for SN Ia candidates, the sample of white dwarf binaries discussed in this thesis will improve our understanding of close binary evolution. Simulations of stellar populations forming double degenerates need several input parameters which describe the formation of stars, stellar evolution and the outcome of close binary interactions (in particular common envelope ejection). Some of the crucial parameters are only weakly constrained by present theoretical calculations, and thus it is essential to calibrate them empirically. Once the analysis of all double degenerates found by SPY is completed, our binary sample will provide a flux-limited, nearly complete sample as an ideal laboratory for this task.

As a spin off, we determined metal abundance patterns of six radial velocity variable sdB stars. The derived abundances for five of the objects are considered to be "normal", whereas for one, the subdwarf HE 2135−3749, an overabundance of titanium was measured. HE 2135−3749 is only the fourth sdB star with a "peculiar" abundance pattern that has been discovered. The existence of these super-metal-rich sdBs are without an explanation by theory so far.

Chapter 1

The SPY project

SPY is the **S**upernova Ia **P**rogenitor Surve**Y**, an ESO large program carried out at the VLT to test the double degenerate (DD) evolutionary channel for the formation of Supernovae (SNe) of type Ia.

Supernovae ...

Supernovae mark the violent termination of a star's life in a thermonuclear explosion. According to the shape of their lightcurves and their spectral appearance they can be divided in two main classes and a large number of subclasses.

- Supernovae of type II
  - show evidence for hydrogen within their spectra
  - have highly diverse lightcurves
- Supernovae of type I
  - show no evidence for hydrogen within their spectra (cf. figure 1.1)
  - have almost uniform lightcurves (cf. figure 1.2)

However, due to their spectral appearance, type I SNe are subdivided into Ia, Ib and Ic, and even these subtypes show peculiarities in their abundance patterns and lightcurve characteristics (e.g. SN 1986G, SN1991bg or SN 1991T, see Li et al. 2001 and Branch et al. 1993).

... Ia ...

SNe Ia are believed to be the prime producers of iron in the universe. Furthermore, the absolute magnitude of SNe Ia is well defined at $M_B = -19.6 \pm 0.2$ (Figure 1.2 and Branch et al. 1992). They are therefore used as an important tool for cosmological distance determination. The role of SNe Ia as cosmological standard candles are fortified even more by Phillips (1993) when he found an empirical relation between the decline rate of their lightcurves and their absolute magnitudes.

Distance measurements from SNe Ia allowed the Hubble constant H_0 to be determined with high accuracy. SN Ia studies have also provided the first evidence for an accelerating expansion

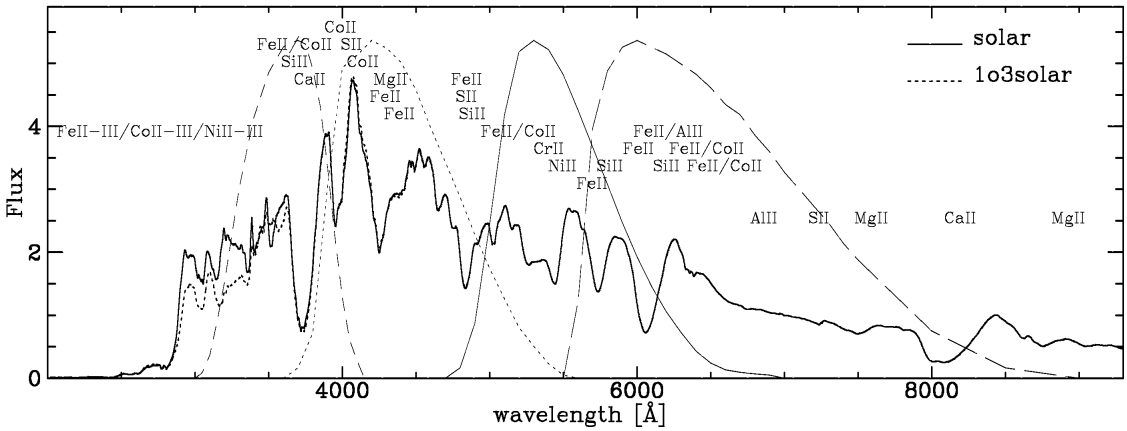

Figure 1.1: Type Ia SN model spectral energy distribution for solar and 1/3 solar metalicities. Superposed are transmission functions for standard passbands; from left to right is U, B, V, and R. The figure is taken from Höflich et al. (1998).

of the universe, i.e. $\Lambda > 0$ (Riess 2000). This astonishing result was recently confirmed by WMAP investigations of the cosmic microwave background (Wright 2003). Moreover, Riess et al. (1998) and Leibundgut (2001) set better constraints to the density parameter Ω and the cosmological constant Λ by the means of SN Ia observations. Yet, the kind of stars that produce SN Ia events remain a mystery (e.g. Livio 2000).

... Progenitor ...

Host galaxies for SNe of type II, Ib or Ic are spirals and irregulars containing young stellar population, whereas SN Ia can be observed in all types of galaxies, even in ellipticals with old stellar population only.

The rapid evolution of SN Ia lightcurves (see figure 1.2) gives a hint on the nature of SNe Ia precursors since they are dominated by the decay of the radioactive material synthesized in the explosion. This is mainly ^{56}Ni (half-life 6.1$^{\mathrm{d}}$) sitting on the top of a decay chain leading to ^{56}Co (half-life 77$^{\mathrm{d}}$) and finally to stable ^{56}Fe. Due to the fact that massive progenitors would be able to hold back the γ-rays produced by the radioactive decay, the precursors of SNe Ia must be low-mass, compact objects. The only candidates fulfilling the criteria, therefore, are white dwarfs. To explode, however, a white dwarf has to be forced into a density and temperature regime where carbon and oxygen burn explosively and disrupt the star. This happens at masses near or above the Chandrasekhar limit of $\approx$1.4 $M_\odot$, where the electron degeneracy no longer stabilizes the star against the gravity. At this point the white dwarf has either to collapse into a neutron star or explode as a SN.

Since no physical process is known leading to such conditions in a single white dwarf, the SN Ia precursor must be part of a multiple system with matter being transferred from a companion to the white dwarf until the Chandrasekhar mass limit is reached. Although there is little doubt with regard to the white dwarf, the definite nature of the progenitor system remains unclear. Two main scenarios exist that differ by the type of the donor star:

In the so-called single degenerate (SD) scenario the white dwarf is accompanied by a regular star as mass donor, either a main sequence star, a (super)giant or a helium star (Whelan & Iben 1973). The system possibly appears as a symbiotic binary (Munari & Renzini 1992), a supersoft

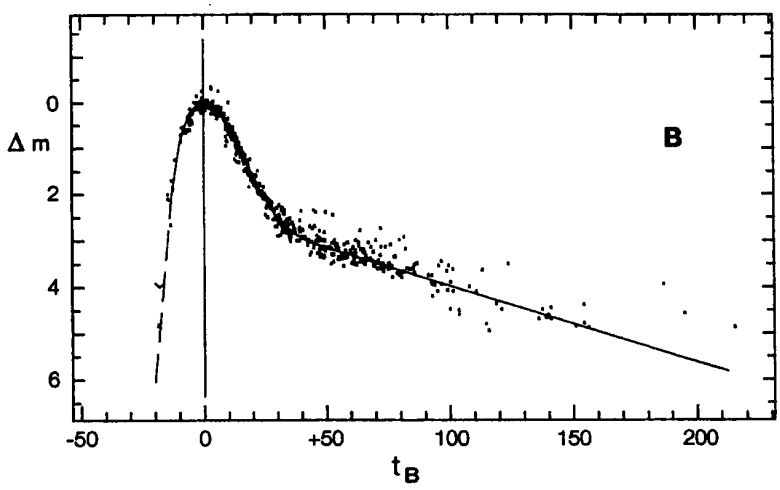

Figure 1.2: Lightcurve of a typical SN Ia (Branch et al. 1992). The horizontal axis shows the time given in days before and after maximum brightness.

X-ray source (van den Heuvel et all 1992) or a recurrent nova (Hachisu & Kato 2001). Although we know that white dwarfs accreting from a non-degenerate companion do exist, we don't know whether such systems exist in sufficient numbers to account for the observed SN Ia frequency, nor whether the white dwarf grows enough to reach the critical mass for ignition.

Contrary to the SD scenario, the white dwarf's companion is another white dwarf in the so-called double degenerate (DD) scenario (Iben and Tutukov 1984). Close double degenerates radiate gravitational waves that cause the orbit to shrink due to the loss of energy and angular momentum until the system eventually merges. To qualify as a SN Ia progenitor, however, the initial separation of the system has to be close enough that the two white dwarfs will merge within a Hubble time and the combined mass has to exceeds the critical mass. Because we know that most stars end up as white dwarf remnants and that a major fraction of stars are in binary systems, double degenerates must be common among white dwarfs. Nevertheless, we do not know if there exist enough double degenerates able to merge in less than a Hubble time and produce a SN Ia event.

Figure 1.3 illustrates both evolutionary channels for SN Ia formation.

The solution of the SD vs. DD dilemma is of great importance for assessing the role of SNe Ia in a variety of astrophysical situations, and – perhaps even more importantly – their effectiveness as accurate cosmological probes.

... SurveY

Several systematic radial velocity (RV) searches for double degenerates have been undertaken starting in the mid 1980's. Among 200 investigated white dwarfs, however, only 18 double degenerates were indeed discovered and their periods determined (Marsh 2000), but none of them qualify as a SN Ia precursor. The absence of a SN Ia precursor in the sample of 18 double degenerates is not surprising, considering the fact that theoretical predictions assume only a few percent of all double degenerates to be SN Ia progenitors (Iben et al. 1997, Nelemans et al. 2001). In order to provide a definite test of the DD scenario we therefore have to overcome

the lack of a statistically significant sample of white dwarfs being checked for radial velocity variations.

The purpose of SPY was to check more than 1000 white dwarfs for radial velocity variability by the means of high-resolution spectra. Therefore, we proposed to use the ESO VLT UT2 telescope (Kueyen), equipped with the Ultraviolet Visual Echelle Spectrograph (UVES, cf. section 3) to do this. Our program takes advantage of those observing conditions which are not usable by most other programs like bright moon, bad seeing and clouds and therefore was conducted in service mode by ESO staff astronomers. SPY kept the VLT busy even when other programs could not be carried out. During the four years that SPY was running we used as much as 4 % of the time at the UT2 every year.

Figure 1.4 shows a typical example of a hydrogen-rich DA white dwarf's spectrum, taken with UVES. A characteristic feature of DA white dwarfs are the broad spectral lines caused by the high densities in their atmospheres. Obviously, these broad lines are very ill-suited for radial velocity measurements. However, deviations from the local thermal equilibrium (LTE) produce sharp non-LTE cores of the Balmer lines – especially of Hα – which allow very accurate radial velocity determinations. This feature is not present in white dwarfs of spectral types DB and DO without hydrogen, but helium in their atmospheres. The use of several helium lines, however, enables us to reach similar accuracy as for DA white dwarfs.

To obtain a sufficiently high signal-to-noise ratio, we restricted our input sample to objects brighter than $B \leq 16.5\,\mathrm{mag}$. Moreover, only objects at $\delta \leq +25^{\circ}$ qualified for SPY due to the location of the VLT on the southern hemisphere. Suitable DA candidates have been drawn by Ralf Napiwotzki from an up to date version of the McCook & Sion Catalogue (1999), the Hamburg-ESO survey (Wisotzki et al. 1996, Reimers & Wisotzki 1997, Christlieb et al. 2001), the Hamburg-Quasar survey (Hagen et al. 1995), the Montreal-Cambridge-Tololo survey (Lamontagne et al. 2000) and the Edinburgh-Cape survey (Stobie et al. 1997, Kilkenny et al. 1997). In addition, Norbert Christlieb and I selected helium rich DB white dwarfs from the Hamburg-ESO survey (cf. chapter 2.1). A map of all known white dwarfs (observed and unobserved by SPY) fulfilling the SPY criteria is shown in figure 1.5.

In order to detect radial velocity variations among the input sample, we took at least two exposures of each object at random epochs separated by at least one night. Radial velocity shifts of these survey spectra were evaluated by the means of a "cross-correlation" based on a χ^2 test (see Napiwotzki et al 2001a). The great advantage of the procedure is its flexibility, which makes it an easy task to apply it to measure radial velocity shifts in stars of different spectral types (Balmer lines for DA white dwarfs, He I lines for DBs, He II and metal lines for DOs, and so on). The accuracy of this procedure is about $2\,\mathrm{km\,s^{-1}}$. Since merger precursors typically have orbital velocities of $150\,\mathrm{km\,s^{-1}}$ or higher, we are running only a small risk of missing a SN Ia progenitor. Figure 1.6 displays the detection probability on this basis as a function of orbital period.

Promising candidates are observed within our follow-up campaigns in order to derive the system parameters definitely (chapter 4).

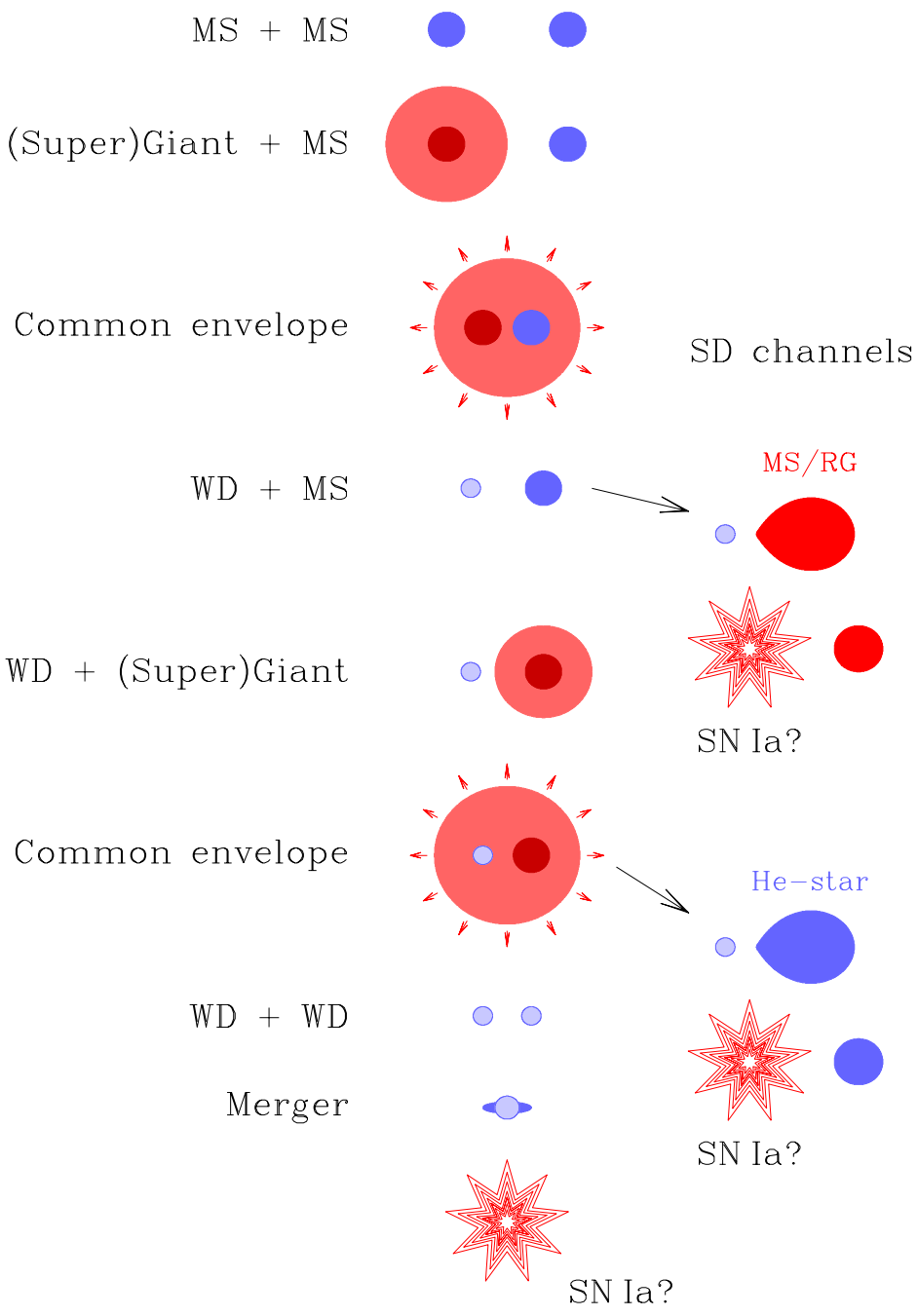

Figure 1.3: Possible evolutionary channels for SN Ia formation via the double degenerate (DD) and the single degenerate (SD) scenarios. (Napiwotzki et al. 2003). The evolution starts with two main sequence (MS) stars. The more massive star becomes a red giant and its envelope is ejected in a common envelope event. In the double degenerate scenario, the second MS star also evolves to a red giant with a second common envelope event. The result is the formation of a close binary of two white dwarfs. If this double degenerate system is close and massive enough, it will merge within a Hubble time due to gravitational wave radiation and will produce a SN Ia event. In the two variants of the SD scenario the secondary fills its Roche lobe while i) close to the main sequence or as a red giant (RG) or ii) as a He-star after another common envelope phase. Mass is being transferred to the white dwarf and increases its mass until the critical mass limit is reaches. At this point, the white dwarf will explode as a SN Ia. The picture is taken from Napiwotzki et al. (2003).

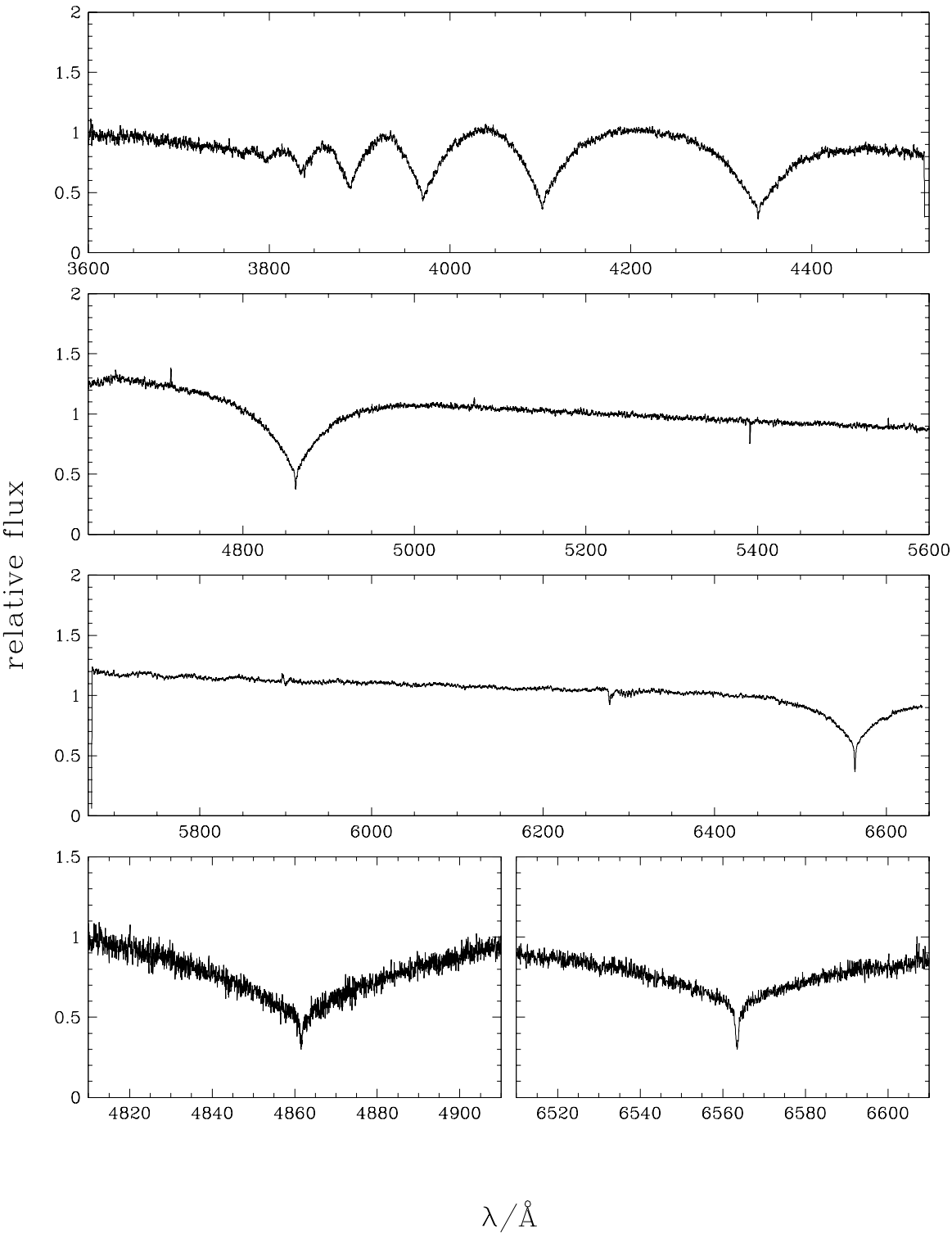

Figure 1.4: Sample UVES spectrum of a hydrogen-rich DA white dwarf. The upper three panels correspond to the blue channel and to both parts of the red channel covered by different CCDs. The lower panels show the Hα and Hβ line cores. For more details on the UVES instrument and the data reduction we refer to section 3 and the references therein.

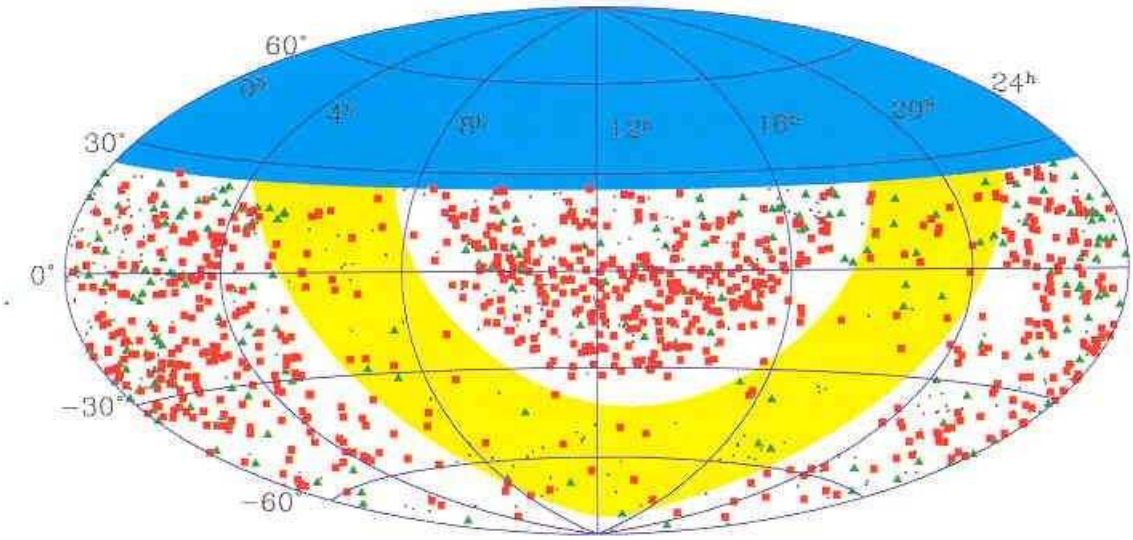

Figure 1.5: Distribution of all known white dwarfs south of $\delta = 25^{o}$ and brighter than $V = 16.5$. Squares and triangles indicates SPY observations, while dots are unobserved objects. The yellow band indicates the position of the galactic disk. The figure was taken from Napiwotzki et al. (2003).

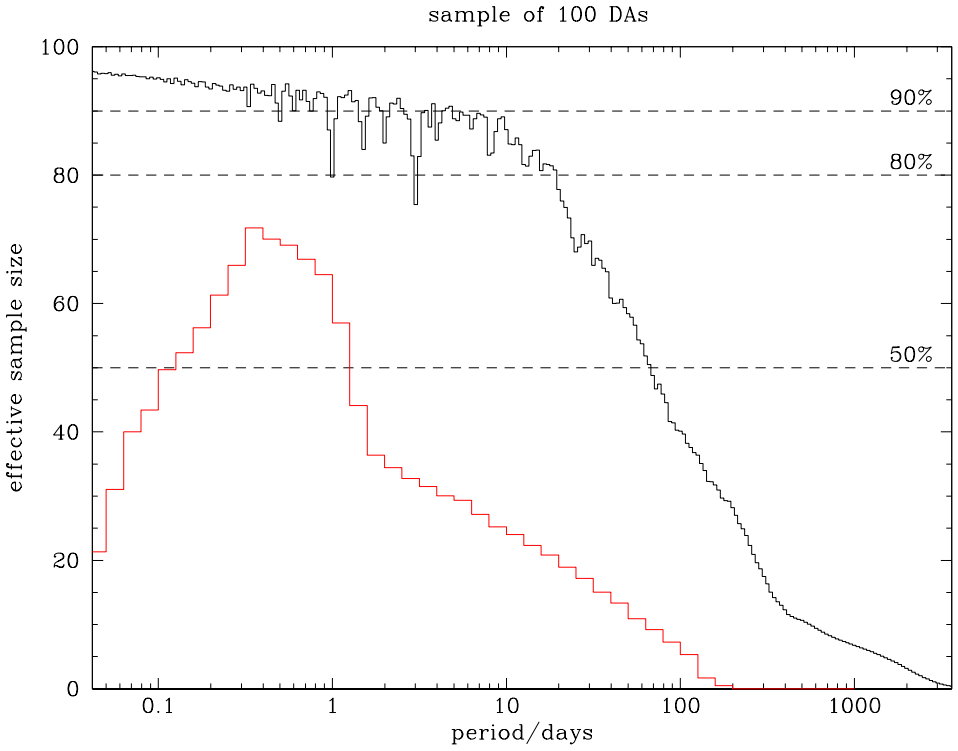

Figure 1.6: Detection probability as a function of period for SPY objects (black line). A Monte Carlo simulation of the detection probability as a function of orbital period was performed for a sample of 100 objects (gray line). The simulation takes into account epoch differences between exposures and measurement errors on a star-by-star basis. The results for the sample are coadded. Dips of the efficiency curve at e.g. $P = 1^{d}$ correspond to typical time intervals between exposures (figure by R. Napiwotzki, priv. com.).

Chapter 2

Selection of DB white dwarfs

Apart from the hydrogen rich DA white dwarfs, our survey intends to observe white dwarfs of all spectral types. However, up to July 2001 only DAs were selected from the Hamburg/ESO survey (HES, Christlieb et al. 2001). Thus, Norbert Christlieb and I performed a DB selection in August 2001 by means of mining the HES data base of objective prism spectra.

DB white dwarfs display strong He I absorption lines over a wide effective temperature range, which are readily detectable in the HES objective-prism spectra. The strongest line is He I 4471 Å, which is located in a spectral region where confusion with absorption lines of normal stars is avoided. We therefore implemented algorithms for detecting that line in HES spectra (section 2.2). The sum of the equivalent widths of Hβ–δ was successfully used by Christlieb et al. 2001 for the selection of DAs, and it can therefore also be used to reject them from the sample of DB candidates (section 2.2). However, the first step in the selection of DBs is a separation from non-degenerate stars by means of color criteria (section 2.1).

2.1 Color criteria

$U-B$ and $B-V$ colors, as well as the Strömgren medium-band color index c_1, can be determined directly from HES spectra, as has been described in Christlieb et al.(2001). The average measurement accuracies of these colors in the HES are $\sigma_{U-B} = 0.09$ mag, $\sigma_{B-V} = 0.10$ mag, and $\sigma_{c_1} = 0.15$ mag, for a large variety of object types covering the total HES magnitude range. DBs can therefore be roughly separated from non-degenerate stars, like field horizontal-branch A-type (FHB/A) stars, or main-sequence turnoff stars, by means of color criteria. We explored the behavior of these stars in color-color diagrams, using a sample of 521 objects of known type described in Christlieb et al. (2001), and 29 known DBs from McCook & Sion (1999) and Friedrich et al. (2000) present in the data set presently used for the exploitation of the stellar content of the HES, that is, a set of 3 437 630 overlap-free HES spectra with $S/N > 5$ from 329 HES plates. Hereafter we refer to this data set as "the stellar HES".

We have chosen conservative color cutoff criteria such that almost all DBs of our test sample are included (see figure 2.1), that is,

$$U - B < -0.2 \quad (2.1)$$

$$B - V < 0.4 \quad (2.2)$$

$$c_1 < 0.3. \quad (2.3)$$

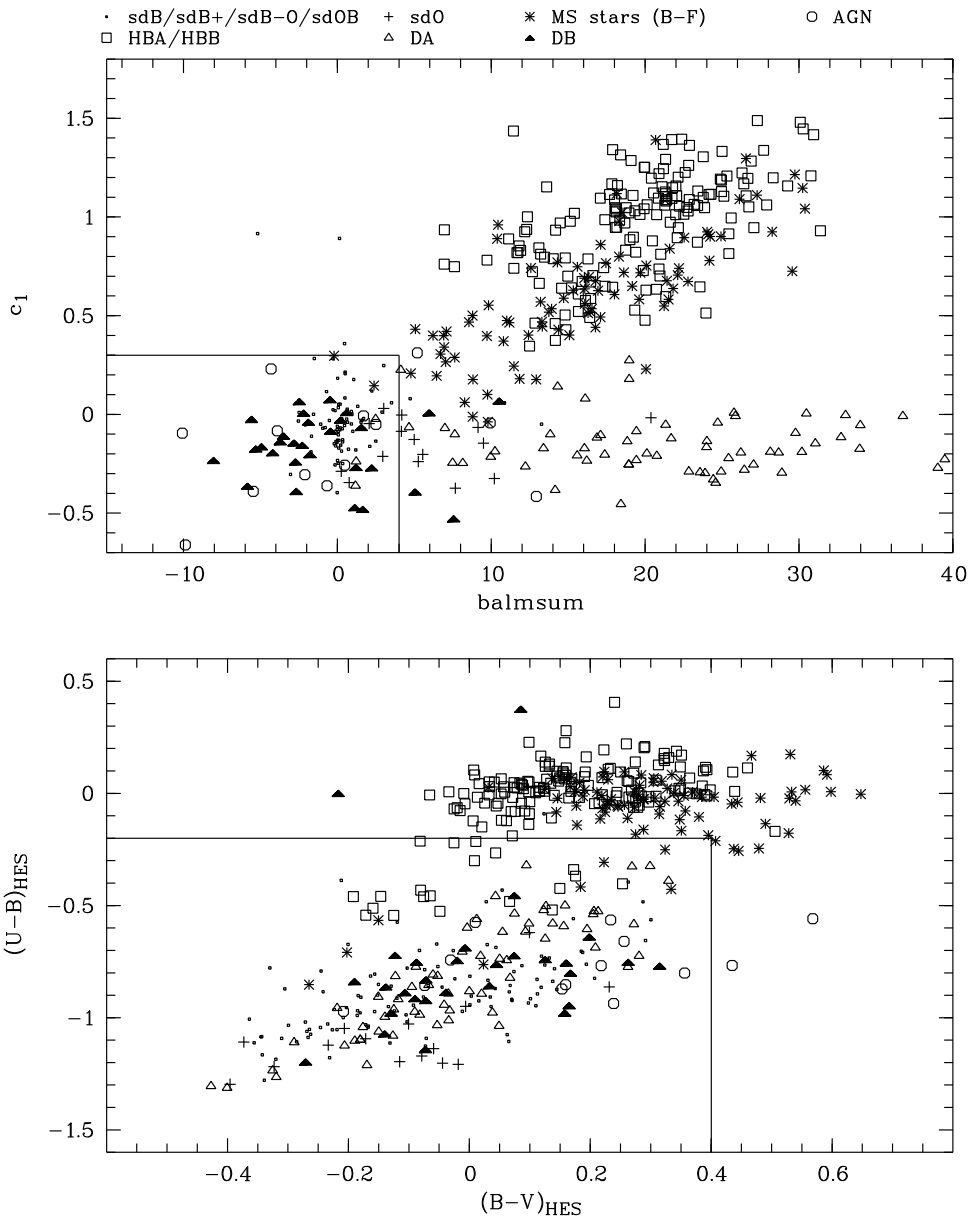

Figure 2.1: DB pre-selection in color-color space and c_1 versus Balmer line sum feature space. Solid lines: adopted selection box.

We verified with $U-B$, $B-V$ colors and c_1 indices derived from a grid of synthetic DB spectra (Koester, priv.com.) that no DB in the effective temperature range $T_{\rm eff} = 10,000$–$40,000\,{\rm K}$ is rejected by our criteria. The lowest values measured on that grid are $U-B = -0.64$, $B-V = 0.14$, and $c_1 = 0.69$. That is, a DB in the above mentioned temperature range will not be rejected by our color criteria unless one of its $U-B$, $B-V$ colors or its c_1 color index, as measured in the HES spectrum, are in error by more than $4.9\,\sigma$, $2.7\,\sigma$, and $2.6\,\sigma$, respectively.

2.2 Absorption line criteria

As can be seen from figure 2.1, it is possible to separate DBs from the main sequence and Horizontal Branch (HB) stars and form AGNs, but not from DAs and sdBs by broad- and medium-band colors alone. Therefore, additional spectral properties have to be used; that is, absorption lines.

Detection of He I 4471 Å

We used three variants of the line detection algorithm described by Christlieb et al. (2001), and a line index for detecting He I 4471 Å in HES spectra. However, the helium lines of DB white dwarfs are weaker than the Balmer lines of the DAs, which makes feature detection and consequently candidate selection more complicated for DBs.

We fit the He I 4471 Å line by a Gaussian, simultaneously with the continuum, which is approximated by a straight line, in a ~ 300 Å wide region centered on the line. It was found that the stability of the fit critically depends on how close the start value for the position of the line is to the real position. The wavelength calibration zero point of the HES spectra, derived from an astrometric transformation between DSS I direct plates and HES plates, is accurate to $\sigma = 7.5$ Å at 4471 Å, allowing to predict the position of the He I line with this accuracy. We used two different methods to further improve the start value: (a) the x position of the global flux minimum in the ~ 300 Å wide fit region is used; and (b) the x position of the global flux minimum in a small region around the predicted line position is used.

It is important for the candidate selection to distinguish real detections from fake detections due to noise. We apply two criteria to do this. First, the detected line is required to have a full-width at half maximum (FWHM) broader than the minimum FWHM of the cross-dispersion profile (h_0), as measured during the extraction of the HES spectra. Second, the position of the line, as determined in the fit, must not deviate more than 3σ from the predicted line position, where σ is the uncertainty in x direction caused by the astrometric transformation between DSS I direct plates and HES plates.

In a third variant of the fit method, we fit the He II 4388 Å line simultaneously with He I 4471 Å, which improves the stability of the fit for hotter DBs. The same rejection criteria as above are applied.

Finally, we compute a line index by comparing the integrated flux in two continuum bands neighboring He I 4471 Å (4205–4303 Å and 4569–4651 Å) with the integrated flux in a band centered on the line (4422–4511 Å). False detection are rejected by means of "significance threshold" as a function of a HES internal magnitude (cf. figure 2.2), with the help of a brake finding algorithm. Wisotzki et al. (2000) used this algorithm for the selection of UV-excess objects.

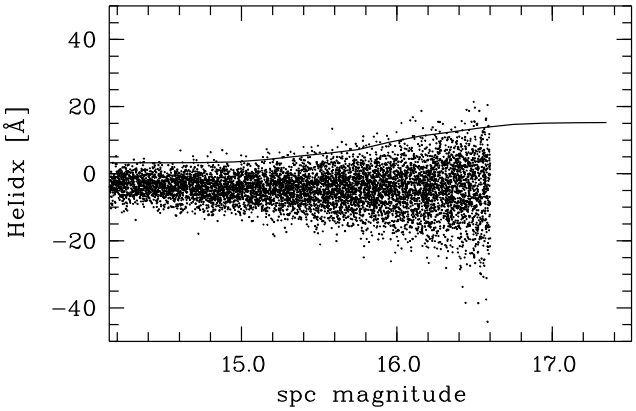

Figure 2.2: "Significance threshold" for the He I 4471 Å line index as a function of a HES internal magnitude, on one HES plate. The threshold is determined with a brake finding algorithm.

Balmer lines

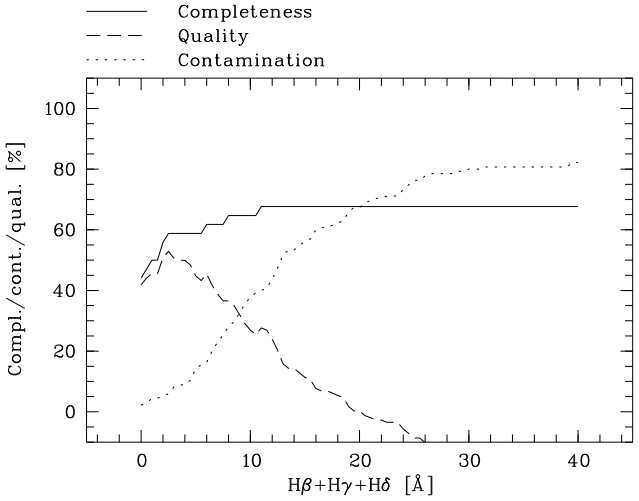

Figure 2.3: Adjustment of the cutoff criterion for the Balmer line equivalent sum.

The algorithm for measuring the equivalent widths of stellar absorption lines is described in Christlieb et al. (2001). The authors used `balmsum`, the sum of equivalent widths of Hβ–Hδ successfully for selecting DA white dwarfs in the HES. Here we use this feature for rejecting non-DBs from our sample. As can be seen in figure 2.1, there is a `balmsum` region in which DBs as well as DAs is present, and it is therefore a priori unclear which cutoff value of `balmsum` one should choose. However, a quantitative evaluation of the expected completeness and contamination of the sample in dependence of `balmsum`, can guide the choice.

We define the *quality* Q of a selection as completeness rate minus contamination rate. This yields $Q = 100\,\%$ for a selection with $100\,\%$ completeness (all DBs of the test sample selected) and $0\,\%$ contamination. One can regard the selection with the highest Q as the optimum, and

we have indeed adopted the corresponding `balmsum` cutoff value of 4 Å (see figure 2.3). This choice yields

$$\begin{aligned} \text{completeness} &= 59\,\% \\ \text{contamination} &= 9\,\%. \end{aligned}$$

The `balmsum` cutoff was applied applying the three color criteria (2.1)–(2.3), and the He I 4471 Å line detection criteria. Note that the above estimates for completeness and contamination are only valid if the relative fractions of DBs and non-DBs in this subsample of the test sample are representative.

2.3 Summary of the DB selection

A star enters the raw candidate sample if its HES spectrum fulfill all of the three color criteria (2.1)–(2.3), if the sum of equivalent widths of Hβ–Hδ is less than 4 Å, and if the He I 4471 Å line is detected by at least one of the four detection methods described in section 2.2. Detected means in case of the three variants of the fit algorithm that the line fit has not been rejected because of too small FWHM or deviating line position, and in case of the line index it means that the line index value must be larger than the significance threshold applicable for the spectrum.

These methods worked very well for our test sample presented in section 2.1, for which 23 out of the 29 DBs were re-discovered. Applying the procedure to the complete HES, a set of 1301 raw candidates were selected. By means of visual inspection of the proper objective-prism spectra, 290 objects were finally not rejected as false candidates – and by means of an even stricter "by eye" classification criterium, 50 out of the 290 candidates were classified as very likely DB white dwarfs. These objects are displayed in table A.1 in the appendix.

In the course of our SPY project, we observed 21 of the selected objects totally. However, it had turned out that our criteria are also sensitive to subdwarfs of the spectral types O and B. Thus, from the high-resolution UVES spectra (cf. section 3) it became obvious that 11 of the 21 observed objects were in fact sdO and sdB stars showing weak Balmer lines only. Lisker (2003) classified these helium-dominated object as He-sdBs and He-sdOs.

Chapter 3

The UV Visual Echelle Spectrograph

For our SPY project, more than 2000 high resolution spectra were taken over the course of four years, using the Ultraviolet Visual Echelle Spectrograph (UVES) at the VLT. Figure 3.1 shows a picture of the UVES instrument mounted at the Nasmyth B focus of the UT2 (Kueyen) telescope of the VLT at Paranal Observatory, Chile.

Figure 3.1: The Ultraviolet Visual Echelle Spectrograph (UVES) at the Nasmyth B focus of the UT2 telescope (Kueyen) of the VLT (picture taken from the UVES web-page *http://www.eso.org/instruments/uves*).

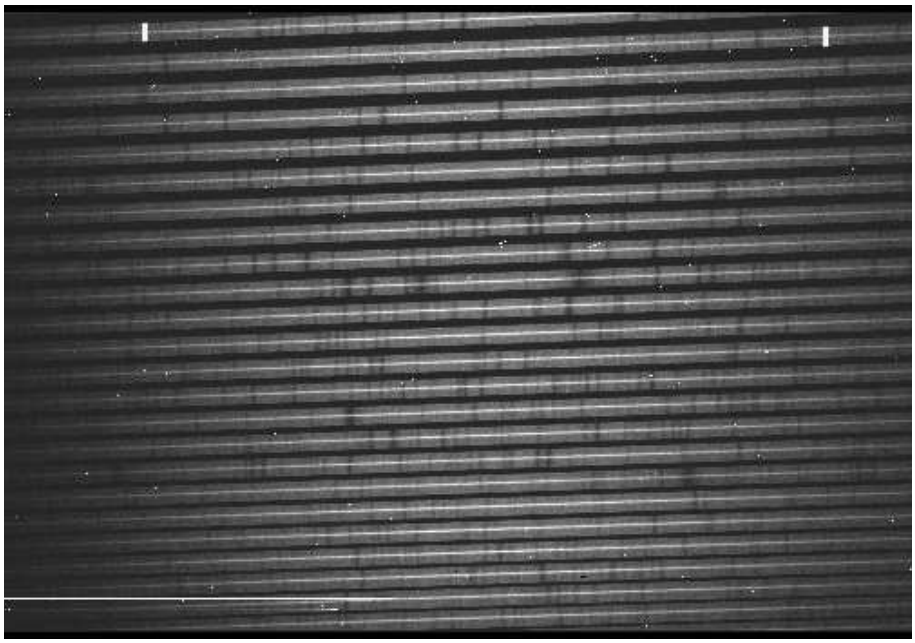

Figure 3.2: Sample raw CCD image of a typical UVES observation. Displayed here is the lower part of the red arm. Within the individual echelle orders, the bright sky-background and its typical absorption lines can be seen beneath the more intense star spectrum. In the lower left corner there are some bad rows on the CCD.

3.1 Instrumental setup

The setup used for our SPY project operated the instrument in dichroic mode, using Dichroic No. 1 at central wavelengths of 3900 Å in the blue and 5640 Å in the red. Nearly complete wavelength coverage from 3200 Å to 6650 Å with only two small 80 Å wide gaps at 4580 Å and 5640 Å is achieved. A 2x2 binning was used to reduce read out noise and a wide 2.1" slit to minimize slit losses. The wide slit reduces the resolution to $R = 18\,500$ (0.36 Å at Hα), or better if the seeing discs were smaller than the slit width. Exposure times were 5 to 10 minutes, depending on the brightness of the targets. The S/N per binned pixel (0.03 Å) of the extracted spectrum is usually 15 or better. Figure 3.2 shows an example for a raw CCD frame. For more details on the UVES instrument, see D'Odorico (2000) and the UVES manual (D'Odorico et al. 2000).

3.2 UVES data reduction

For most of the nights, a complete set of *calibration frames* were taken for each arm in addition to the *science frames*. These calibrations include multiple *bias* and *flat field* exposures as well as an *order definition flatfield* (a flatfield exposure taken with a very small slit) and a *ThAr calibration frame*.

ESO provides a special UVES-pipeline based on MIDAS procedures to carry out the data reduction. Although the outcome of this pipeline was of good quality in most cases, some spectra show artifacts of varying strength, e.g. a quasiperiodic pattern, in appearance similar to

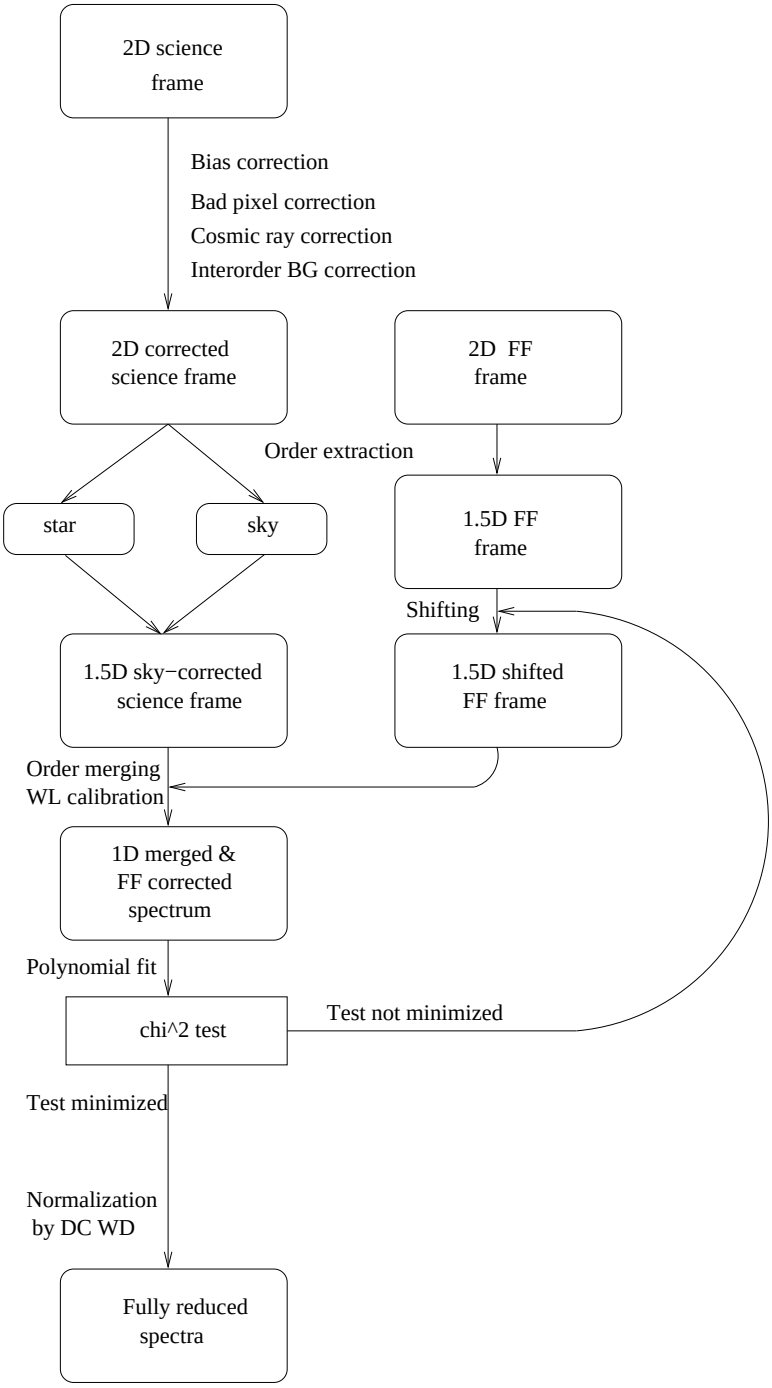

Figure 3.3: Schematic diagram of the reduction process according to our self-developed, semi-automated pipeline. An explanation of the individual reduction steps in more detail is given in the text.

a fringing pattern (see figure 3.7 for example). Nevertheless, the pipeline reduction was extremely useful for a fast selection of radial velocity variable objects for follow-up observations (see below). For a more accurate data reduction, however, we developed our own set of procedures. This enabled us, for example, to determine stellar parameters by the means of spectroscopic analysis

(Koester et al. 2001) with high accuracy.

Our self-developed, semi-automated program is based on MIDAS routines already used in the ESO pipeline. However, our procedure differs from the pipeline sequence, and it enables me to intervene the reduction at crucial points to handle problems. Figure 3.3 gives a schematic overview about the reduction process in our self-developed pipeline. In more detail, the individual steps displayed in this diagram are:

Bias correction

To correct the offset caused by dark current, we computed a two dimensional *master bias* from the *bias* frames taken in each night. Subsequently, this *master bias* was subtracted from each *science* frame.

Cosmic ray correction

To purge the two dimensional *science frames* from cosmics rays, we compared each frame with a smoothed frame of itself. Therefore, each row was filtered by the means of a three pixel wide median to create the smoothed template. After that, we compared this template to the raw *science frames*. Pixels that differ by more than $+3\,\sigma$ (defined by read out noise and gain of the CCD) from the smoothed frame are substituted by the median value. Since the echelle orders on the CCD are nearly horizontal, the filter used for the template works in the same direction as the dispersion. The spectrum itself is therefore unaffected by the procedure.

Bad pixel correction

As can be seen from figure 3.2 are the CCDs used in the UVES instrument not perfect but show several defect columns and rows. To correct these "bad pixel" we therefore substituted their values by values of neighboring pixels.

Order definition

To get an idea about the position of the echelle orders on the CCD, a Hough-transform was performed for a special *order definition* flatfield taken in the same night as (or close to) the *science* frames. This order definition was essential for the determination of the interorder background from the *science* frames later on, and for obtaining the dispersion relation from the *ThAr calibration* frame.

Interorder background correction

The interorder background was computed from the echelle raw spectrum in the sampling space pixel to pixel. Background values were estimated at reference positions between the orders and interpolated by a bivariate polynomial. Afterwards, the correction was carried out by subtraction of interorder background from the *science* frame.

Wavelength calibration

The echelle orders of a *ThAr calibration* frame were extracted at the CCD positions specified by the order definition routine. An automatic line identification was done and the dispersion

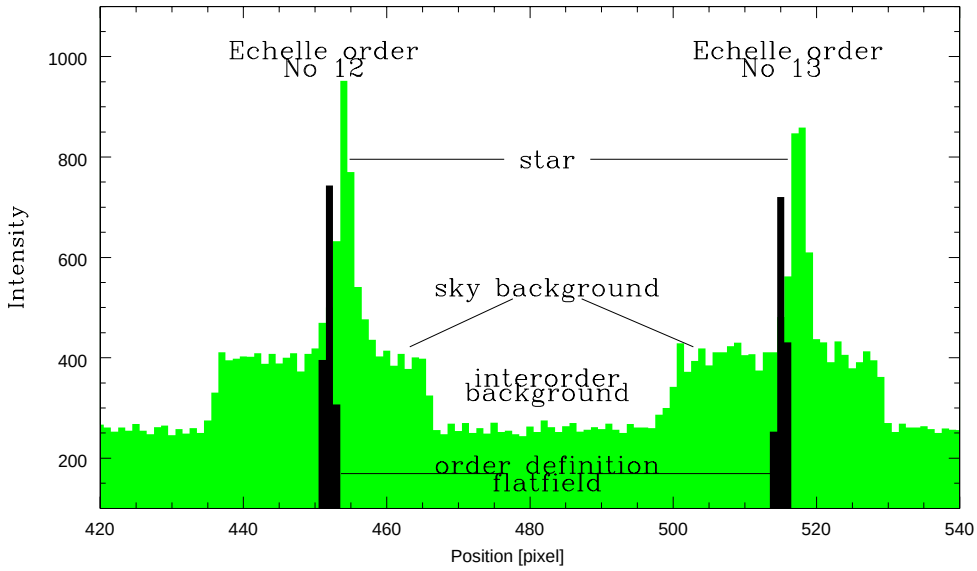

Figure 3.4: Vertical cut through a two dimensional UVES spectrum. The *order definition* flatfield is overlayed to the normal *science* frame. Using plots like this we estimated the offset relative to the order definition frame and the window-size for the extraction of the star and the sky-background.

relation was determined for each order. Line tables for two sky windows and for the object window of the detected orders result. Each window has a width of 15 pixels or 3".

Spectrum extraction

Since we were interested in an optimized data reduction, we extracted the spectral orders not at the full slit window but at a smaller one to increase the S/N ratio. Window-size and offset relative to the *order definition* frame (caused by refraction) were determined for each observation individually by the means of a vertical cut through the two dimensional CCD frame (cf. figure 3.4). Since the offset is less than 15 pixels, the wavelength calibration done previously is still sufficiently accurate and can be assigned to the extracted echelle orders later on.

The extracted orders are stacked into a single data file which we call the $1\frac{1}{2}$ *dimensional* data set.

Sky background correction

The sky background was extracted at a CCD position "above" and 'below" the star's spectrum. As for the extraction of the spectrum, offset and window-size had to be determined individually for each observation from vertical cuts similar to the one displayed in figure 3.4. The extracted sky-backgrounds were merged and subsequently weighted relative to the proper spectrum by the means of the window-sizes. Finally, the weighted sky-background is subtracted from the extracted star's spectrum.

Flatfield correction and the ripple problem

The general purpose of the flatfield correction is to correct for pixel to pixel variations. However, it was also used in order to correct the wavelength dependent sensitivity of the instrument as

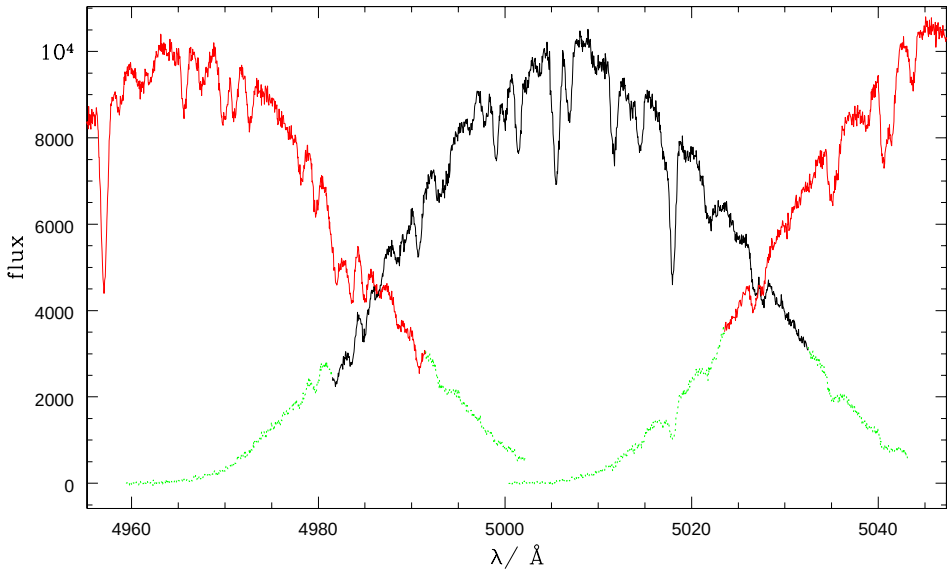

Figure 3.5: Three overlapping echelle orders extracted from the lower part of the red arm. Since they are not flatfield-corrected yet, they still show a blaze efficiency distribution. In order to avoid edge effects and to increase the S/N ratio, the dashed parts are cut of before we merged the orders.

well. Dominated by the grating efficiency, the instrument's sensitivity function is mainly a blaze distribution which can be described by a *sinc* function. The shape of the blaze distribution can be seen from figure 3.5, where three overlapping echelle orders are displayed before the flatfield correction was done.

To do the blaze correction, we merged all *flatfield* frames to create a single *master flatfield*, which was afterwards corrected for the *master bias*. Out of this 2 dimensional *master flatfield* we extracted echelle orders at the same position and with the same offset as we did for the *science* frame. Subsequently, the echelle orders of the star's spectrum were divided by its proper flatfield order.

Even though this ought to correct for the instrument's sensitivity, sometimes ripple features remained in the wavelength calibrated and merged spectra. This problem is very similar to the ripples produced by the ESO pipeline.

A close inspection of these features shows that each ripple corresponds to a individual echelle order. The described flatfield correction will not rectify the blaze function very accurately. The reason for the remaining spectral trend even in the corrected orders seems to be a difference in the gradient of the flatfield and the spectrum (cf. upper panel of figure 3.6). To get rid of the ripple problem we therefore tried to match both gradients by shifting the extracted flatfield relative to the extracted star's spectrum (cf. lower panel of figure 3.6).

Even a small shift of about a few pixel will heavily reduce the ripples. By iteration we determined the optimum shift, as can be seen from figure 3.3. The flatfield was shifted within a range of +30 to −30 pixels in steps of 1 pixel. The resulting spectra were subsequently checked by fitting a second-order polynomial function to a wavelength region where no spectral lines are expected in DA white dwarfs. Since this fit was done by means of a χ^2 test, the χ^2 gives an idea about the fit's quality. Scanning the χ^2 values for the full shift range of +30 to −30 pixels we determined the best shift.

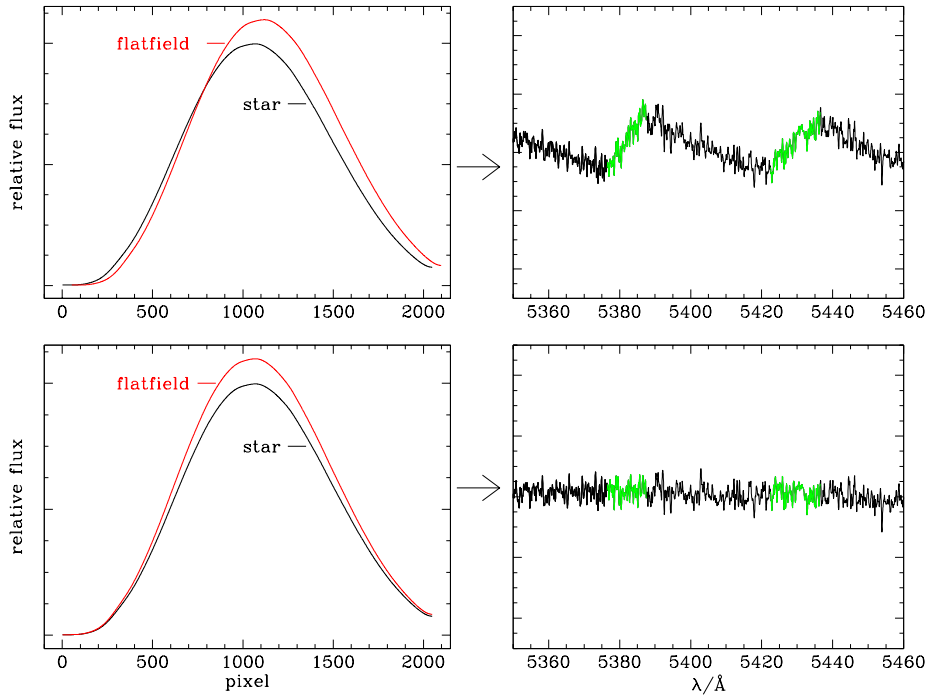

Figure 3.6: The cause of the ripple problem. The offset between the extracted flatfield and the star is displayed schematically on the left hand side, while the right hand side shows three fully reduced and merged echelle orders as an example for the result of the flatfield correction, done for the proper gradients on the left. Gray shaded wavelength regions mark the overlap between two neighboring orders. The upper panels displays a large shift of several pixels that results in a ripple problem like the one apparent in some of the ESO pipeline spectra. The lower panel displays a flatfield that is shifted, but now matched the star's spectrum. In this case, the ripple problem is small.

Calibrating the object spectrum

After the best flatfield shift was found and the corrected for a wavelength calibration of the $1\frac{1}{2}$ dimensional *science* frame was performed. This was carried out by the means of the dispersion relation found previously.

Order merging

The merging process was done by an algorithm that computes a weighted average in the overlapping region of adjacent orders. The normalized weight was a linear ramp between 0 and 1 in the overlapping region.

To avoid low S/N and artifacts caused by the echelle blaze function at the CCDs edges, however, the boundary regions of the echelle orders were cut off before merging the orders (cf. figure 3.5). Since the overlap of the orders is large enough, the loss of information was a small price payed for an increased quality of the merged data set.

Normalization

Finally, we normalized the resulting star's spectrum by means of a spectrum of a white dwarf of spectral type DC. Since this kind of star shows no lines at all in the optical wavelength range, the DC's spectrum was smoothed until no feature (noise peaks, cosmics, artifacts, and so on) but the continuum remains. The resulting smoothed spectrum was used as the flux distribution by which the science spectrum was divided to become normalized.

3.3 ESO pipeline vs. semi-automated pipeline

Although the ESO pipeline provides a reduction quality sufficient for a fast detection of radial velocity variability among the survey objects, the ripples that become obvious for some spectra are a handicap for a quantitative spectral analysis as performed by Koester et al. (2001).

Our self-developed pipeline, on the other hand, handle the ripple problem very well by shifting the *flatfield* relative to the *science* frame. To do this, the best shift is determined by iterative means. A disadvantage compared to the ESO pipeline, however, is the semi-automated nature of our pipeline. Therefore, in preparation for the extraction process the window-size and the offset relative to the *order definition flatfield* has to be determined "by eye" (cf. figure 3.4). This has to be done for the star's spectrum as well as for the sky-background. However, this disadvantage is counterbalanced by the great advancement in reduction quality, as can be seen from figure 3.7.

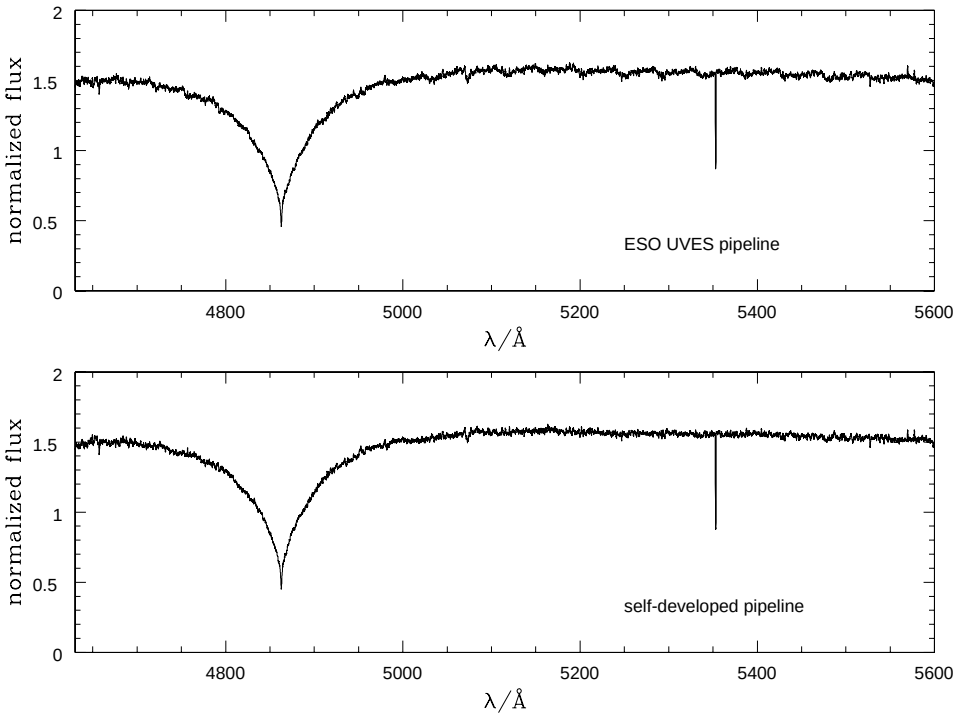

Figure 3.7: A comparison of the two reduction pipelines for UVES data. The upper panel of the figure displays the result of the UVES pipeline provided by ESO. Ripples produced by this pipeline are obvious. The result of our self-developed, semi-automated pipeline is displayed in the lower panel. The improvement concerning the ripple problem is great although the flatfield was shifted by only two pixels relative to the object.

Chapter 4

Derivation of system parameters

Only double degenerate mergers with a total mass above the Candrasekhar mass limit and within a merging time less than the Hubble time qualify as SN Ia progenitors. While the system's total mass results straight from the masses of the individual components, the merging time deduced form gravitational wave radiation is a function of the individual masses and the system's period (Landau & Lifshitz, 1951):

$$t_{\mathrm{M}} = 10^7 \frac{(M_1 + M_2)^{1/3}}{M_1 M_2} P^{8/3}. \tag{4.1}$$

In this equation, the merging time is given in years, whereas the masses are in solar units and the orbital period in hours.

To answer the question whether or not a double degenerate qualifys as a SN Ia precursor, we have determine the system parameters and in particular the orbital period and masses of its components. Therefore, we used a variety of astronomical techniques that are presented within the next sections in more detail.

4.1 Definition of samples

From the full set of candidate systems discovered by the SPY project we defined two subsamples. Sample one was constructed to search for SN Ia progenitors and sample two for obtaining a statistical complete, flux-limited sample in order to test binary evolution theory.

1. The most probable SN Ia precursors are systems with short periods and large radial velocity (RV) amplitudes and unambiguous binaries. Therefore, we checked our survey for the most promising merger candidates: double-lined systems (both white dwarfs visible) and double degenerates with radial velocity variations of $80\,\mathrm{km\,s^{-1}}$ and more (up to $200\,\mathrm{km\,s^{-1}}$). This sample contains 44 objects.

2. An additional sample was a magnitude limited one, composed of double degenerates with $V \leq 15.5$. In order to test binary evolution theory it is important to avoid observational biases – i.e. by selecting against long period and low-amplitude systems (as is done in in the first sample). Thus, the second sample will improve our understanding of double degenerate population dramatically. Sample two contains 63 stars totally.

Objects of both samples were subsequently re-observed in the course of follow-up campaigns in order to derive their periods and RV curves definitely. For a single-lined system, this finally yields the mass functions $f_{\rm m}$. If the system is double-lined the mass ratio of the components can be determined.

4.2 Radial velocity curves

4.2.1 Follow-up observations

The follow-up campaigns were performed at the *European Southern Observatory*, Chile (ESO), either at Paranal using UVES at the VLT UT2 or at La Silla using the *New Technology Telescope* (NTT) equipped with the *ESO Multi Mode Instrument* (EMMI). Additional observations were done at the 3.5 m telescope of the *Deutsch Spanisches Astronomisches Zentrum* (DSAZ) at Calar Alto, Spain, equipped with the medium-resolution TWIN Spectrograph (TWIN) at the Cassegrain focus. Our data set was complemented by spectra taken with the IDS or ISIS instrumentation mounted at the *William Herschel Telescope* (WHT), operated by the *Isaac Newton Group of Telescopes* (ING), Spain. Table 4.1 gives an overview of all follow-up runs. For more details on individual observational sites, the proper instrumentation and the reduction techniques we refer to section B in the appendix.

4.2.2 Radial velocity measurements

Radial velocities of the individual observations are determined by calculating the shifts of the measured wavelengths to laboratory measurements. Therefore, we performed a simultaneous fit of a set of mathematical functions to the observed line profiles using the ESO MIDAS package. Unless otherwise noted, we concentrated on the Hα line for the fit process because of its sharp and well defined non-LTE line core. A linear function was used to reproduce the overall spectral trend, a Lorentzian to model the line wings and a Gaussian for the innermost line core. The central wavelengths of the Lorentzian were fixed to that of the Gaussian for physical reasons.

Although we were mainly interested in double degenerates, some objects observed within the follow-up campaigns were subdwarfs of the sdO and sdB subtype or white dwarfs with a M dwarf companion. These objects show not only hydrogen absorption lines but have a more diverse spectral appearance than DA white dwarfs. Thus, we usually used the He-lines (namely at 4471 Å and at 4686 Å) for radial velocity determination as well as Hα whenever analyzing He-rich objects. Due to the fact that He-lines are much shallower and more narrow than the lines from the Balmer series, only a linear function and a single Gaussian were required for the fitting process.

In the case of a white dwarf system with an M dwarf companion, the Balmer series of the white dwarf is overlayed by strong emission features produced by the dM. The innermost core of the white dwarf's absorption line is hardly visible, making a fit difficult or even impossible. Thus, we usually can not determine the white dwarfs motion. However, both components are clearly visible in some outstanding cases (like WD 0419−487, cf. section 6.1.1). The same set of functions used for single lined white dwarfs can easily reproduce the dM's emission feature as well, as far as the Gaussian is fitted in emission and de-coupled from the Lorentzian. This procedure finally yields very accurate radial velocity measurements for the M dwarf companion. Some examples for fits to the observed line profiles of different kind of systems can be seen from figure 4.1.

Table 4.1: Follow-up observations done of candidates identified by the SPY project. The first column lists the date of observation, while in the second the used telescope and instrumentation is shown. The last column displays the participating observers.

	Date		Telescope & Instrument		Observer
2001	March	10 – 13	DSAZ 3.5m	TWIN	R. Napiwotzki, E.-M. Pauli
	July	06 – 15	DSAZ 3.5m	TWIN	R. Napiwotzki, C. Karl
	October	11 – 12	ESO VLT	UVES	R. Napiwotzki
	October	26 – 01	ING INT	IDS	G. Nelemans, T. Reerink
2002	February	22 – 26	DSAZ 3.5m	TWIN	C. Karl, T. Lisker
	June	04 – 05	ESO VLT	UVES	R. Napiwotzki
	August	11 – 16	DSAZ 3.5m	TWIN	C. Karl (S)
	September	23 – 26	ESO NTT	EMMI	C. Karl
	October	15 – 16	DSAZ 3.5m	TWIN	C. Karl (S)
	November	10 – 13	ESO VLT	UVES	R. Napiwotzki
2003	January	22 – 25	ING WHT	ISIS	G. Nelemans, P. Groot
	February	17 – 21	ESO NTT	EMMI	C. Karl
	March	17 — 20	ESO VLT	UVES	R. Napiwotzki
	March	20 – 23	ING WHT	ISIS	G. Nelemans, R. Izzard
	April	14 – 20	DSAZ 3.5m	TWIN	C. Karl (S)
	May	13 – 18	DSAZ 3.5m	TWIN	C. Karl (S)
	July	01 – 17	DSAZ 3.5m	TWIN	C. Karl (S)
	August	06 – 09	ING WHT	ISIS	G. Nelemans, M. Montgomery
2004	January	01 – 04	ESO NTT	EMMI	C. Karl

(S): Service-mode carried out by a staff astronomer at Calar Alto and the author via internet

Gijs Nelemans from the University of Cambridge provided additional radial velocity measurements derived from IDS and ISIS spectra. These measurements were done by means of the MOLLY routine (Marsh et al. 1995).

4.2.3 Power spectra and RV curves

In preparation for further analysis, all measured radial velocities as well as the times of observation have been barycentrically corrected. As reference, the time of the middle of exposure is used.

The period search was carried out by means of a periodogram based on the *Singular Value Decomposition* (SVD) method. A sine-shaped RV curve was fitted to the observations for a multitude of phases, which were calculated as a function of period (see Napiwotzki et al. 2001b). The difference between the observed radial velocities and the best fitting theoretical RV curve for each phase set was evaluated in terms of the logarithm of the sum of the squared residuals (χ^2) as a function of period. This method finally results in the data-set's power spectrum which allows to determine the most probable period of variability (see Lorenz et al. 1995).

From the best fit RV curve corresponding to the most probable period, the ephemeris, the system's velocity and the semi-amplitude were derived. Figure 4.2 shows two examples for RV

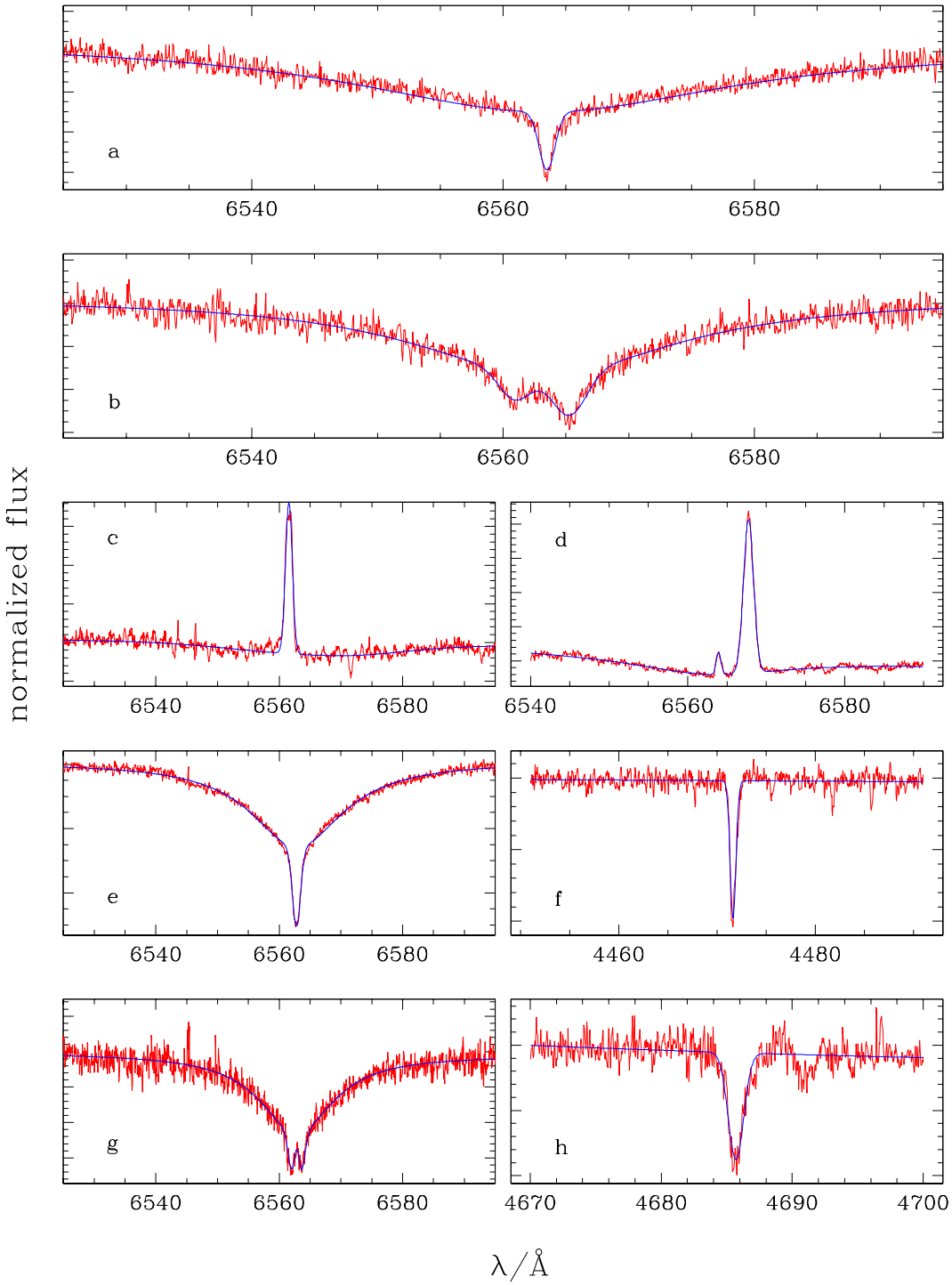

Figure 4.1: RV determination by means of MIDAS fits: a) Results for a single lined DA white dwarf (WD 1824+040); b) Double-lined white dwarf (HE 2209−1444); c) The M dwarf plus white dwarf system HE 2147−1405. The white dwarf can not be fitted for this object, but it can for WD 0419−487 (d). Panels e) and f) display the fits of the Hα and HeI (4471 Å) for the sdB star HE 2135−3749. Results for the sdO HE 1318−2111 can be seen from g) and h). Note that the central emission in panel g is caused by a non-LTE effect in the photosphere of the sdO star.

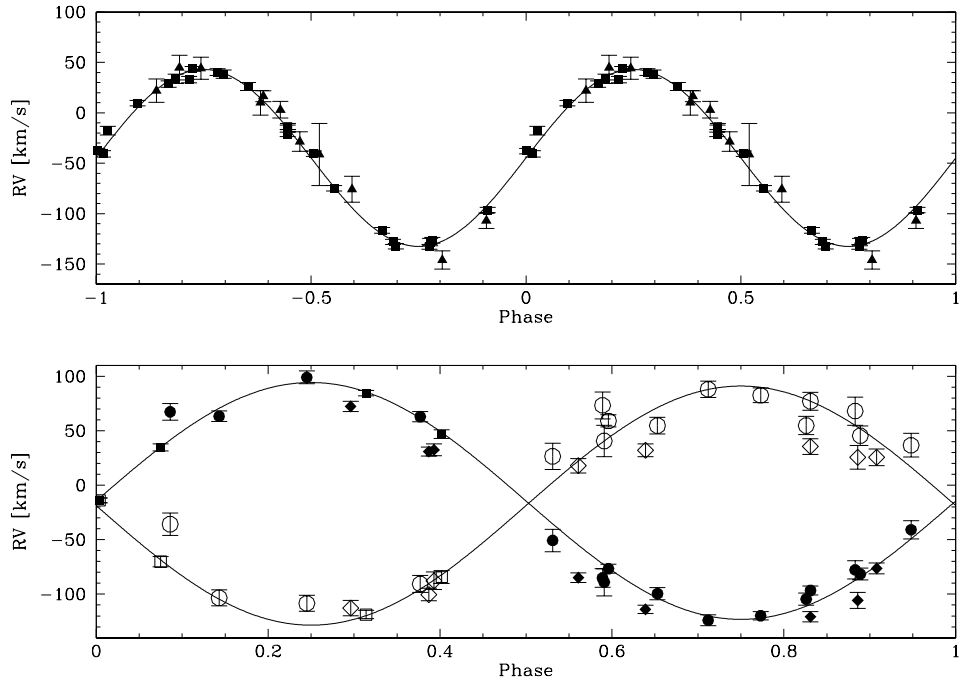

Figure 4.2: Best fit RV curves. In the upper panel, the RV curve of the single lined system HE 1059−2735 is displayed whereas the double lined system HE 2209−1444 can be seen in the lower panel.

curves. The upper panel displays the best fit RV curve of a single lined system, from which the mass function $f_{\rm m}$ can be derived:

$$f_{\rm m} = \frac{M_{\rm invis} \sin^3 i}{(M_{\rm invis} + M_{\rm vis})^2} = \frac{PK^3}{2\pi G}. \tag{4.2}$$

The lower panel, however, displays the RV curve of a double lined system. The mass ratio of both components can be computed from the ratio of the radial velocity semi-amplitudes:

$$\frac{M_{\rm prim}}{M_{\rm sec}} = \frac{K_{\rm sec}}{K_{\rm prim}} \tag{4.3}$$

4.3 Gravitational redshift

In the gravitational field of a star with mass M and radius R a photon suffers an energy loss which results in a redshift:

$$z = \frac{v_{\rm grav}}{c} = \frac{\Delta\lambda}{\lambda} \approx -\frac{\Delta\nu}{\nu} = -\frac{GM}{Rc^2} = \frac{\sqrt{GMg}}{c} \tag{4.4}$$

Thus, the measured radial velocities of white dwarfs are always a combination of the intrinsic star's velocity and the gravitational redshift z due to the high surface gravities of white dwarfs. To correct for this effect we have to obtain the star's mass and radius from other methods.

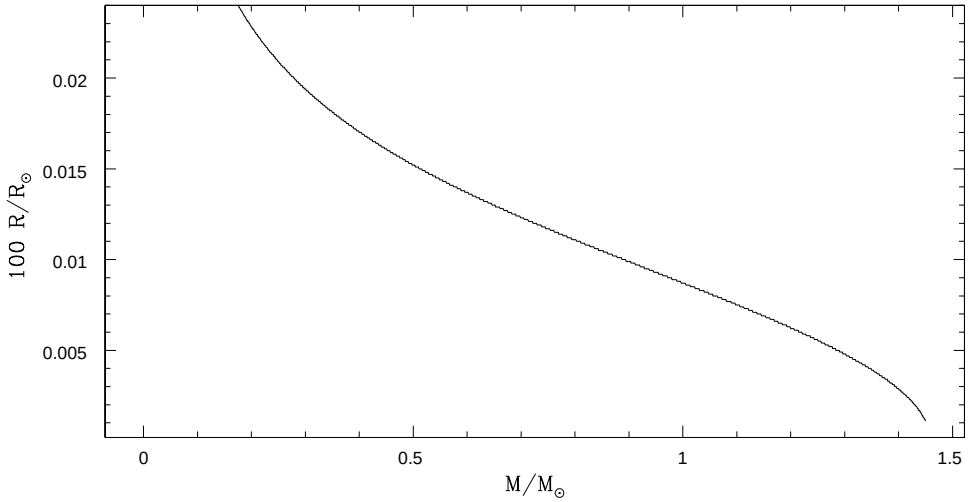

Figure 4.3: Mass-radius relation of white dwarfs according to Eggelton (published in Truran & Livio 1986).

For double-line systems, however, the gravitational redshift offers the possibility to derive the masses for both components. For some of these systems, it become obvious that the system velocities of the individual components do not match. In other words, $\gamma_{\rm prim} \neq \gamma_{\rm sec}$ due to different gravitational redshifts:

$$\Delta z = \frac{\Delta\gamma}{c} = \frac{G}{c^2}\left(\frac{M_{\rm prim}}{R_{\rm prim}} - \frac{M_{\rm sec}}{R_{\rm sec}}\right) \tag{4.5}$$

This equation enables us to estimate the redshift as a function of white dwarf mass. Due to the fact that the mass ratio is also given by the RV curve (equation 4.3), only one combination of masses can fulfill both constraints for a given mass-radius relation. However, if the surface gravity is low (e.g. for sdB and sdO stars) or if the masses of the components are equal Δz will not be measurable.

The mass - radius relation of white dwarfs

It has been shown by Chandrasekhar (1939) that for white dwarfs a mass-radius relation holds. Modern evolutionary calculations for white dwarfs result in accurate mass-radius relations (Blöcker et al. 1997, Wood 1995) for different hydrogen-envelope masses. However, to utilize these tables the effective temperatures and the surface gravities of both components have to be known. Whereas it is straight forward to determine $T_{\rm eff}$ and $\log g$ for single-lined systems via spectral analysis (see e.g. Koester et al. 2001), double-lined systems are more difficult (cf. section 4.4). Therefore, we had to use a general mass-radius relation derived by Eggelton (first published in Truran & Livio 1986) for double-lined systems. The advantage of this relation is, that it does not depend on stellar parameters. This relation is displayed in figure 4.3.

In order to compare Eggelton's mass-radius relations with relations derived by Blöcker et al. (1997) and Wood (1995), we compared the masses determined by means of different distributions with each other. We found that the masses derived from the different relations agree to

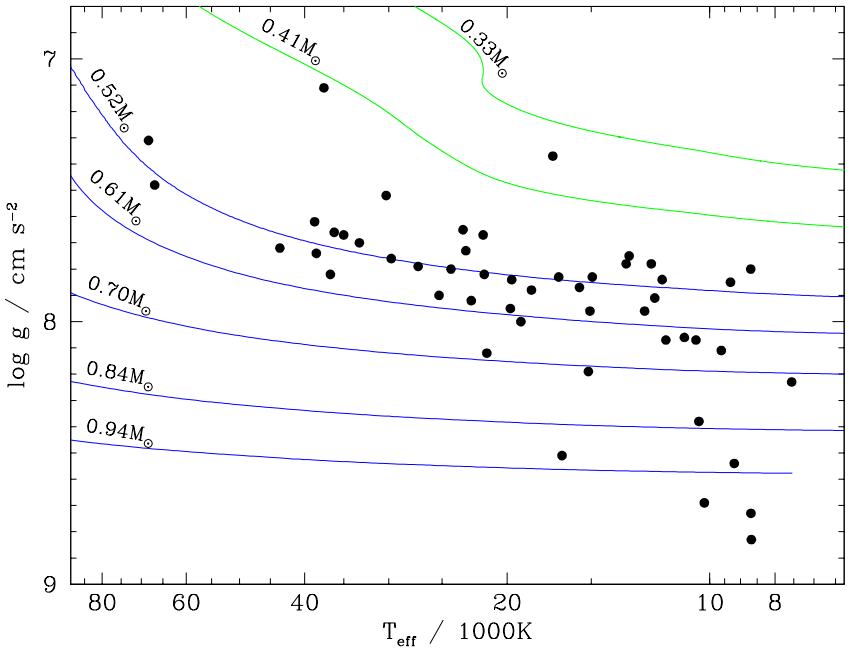

Figure 4.4: Mass determination of (single and binary) DA white dwarfs. Temperature and gravity, determined from model atmosphere analysis of the UVES spectra (Koester et al. 2001 and priv.com.) are compared to cooling sequences of white dwarfs (Blöcker et al. 1997) for a range of masses. The figure was taken from Napiwotzki et al. (2003a).

each other within the error margins, and thus we conclude that the discrepancies between them are insignificant, which justifies our use of Eggelton's relation.

4.4 Quantitative spectroscopic analysis

A direct approach to estimate the mass over radius ratio (M/R) of the objects is by determining their stellar parameters $T_{\rm eff}$, log g and $n_{\rm He}$ by means of a quantitative spectral analysis. Subsequently, the stellar masses can be estimated by comparison of the spectroscopically derived temperature and gravity to evolutionary calculations, like the tracks computed by Blöcker et al. (1997) for white dwarfs (figure 4.4).

For subdwarf B stars, appropriate computations were done by Dorman et al. (1993, cf. figure 4.5). Their evolutionary tracks were evaluated for single star evolution. However, sdB stars can also form in the course of evolution of close binary systems by mass transfer. Han et al. (2003) calculated evolutionary sequences for subdwarfs in binary systems for twelve parameter sets. The masses range from $\approx 0.3 M_\odot$ to $\approx 0.7 M_\odot$, but all distributions peak near $\approx 0.47 M_\odot$, which corresponds to the canonical mass of sdB stars. Therefore we adopt $M_{\rm sd} = 0.47\,M_\odot$ throughout this study. Nevertheless, accurate stellar parameters were determined in order to determine the projected rotational velocities and subsequently the systems' inclinations angles (cf. section 4.4.3).

4.4.1 Stellar parameters of single-lined systems

By means of spectral analyses, Detlev Koester from the Christian - Albrechts Universität in Kiel evaluated $T_{\rm eff}$ and $\log g$ for a large sample of single-lined DA white dwarfs from SPY (Koester et al. 2001, and priv. com.). Recently, Ralf Napiwotzki (priv. com.) completed this sample for DA white dwarfs brighter than 15.5 mag. The subdwarf B stars were analyzed by Thorsten Lisker (Lisker et al. 2004) and the sdOs by Alexander Ströer (2004).

4.4.2 Stellar parameters of double-lined systems

The spectral analysis of a double-lined system is more complex than for a single-lined system because the spectrum of the former is always a superposition of two individual spectra. This problem is sometimes circumvented by assuming that the results of a simple single-lined model fit is representative for the average parameters. One possibility would be to estimate the mean gravity and individual temperatures of the components of the analysis of individual spectra taken close to conjunction and quadrature phases (e.g. HE 1414−0848 in Napiwotzki et al. 2002). However, this approach can only be applied if both components have quite similar parameters.

A direct approach would be to disentangle the observed spectrum by means of deconvolution techniques into the spectra of the components. Subsequently, these spectra could be analyzed by fitting synthetic spectra developed for single-lined white dwarfs to the individual line profiles. Such a disentangling procedure has been developed by Simon and Sturm (1994) and was successfully applied to main sequence double-lined binaries. However, it has not been tested

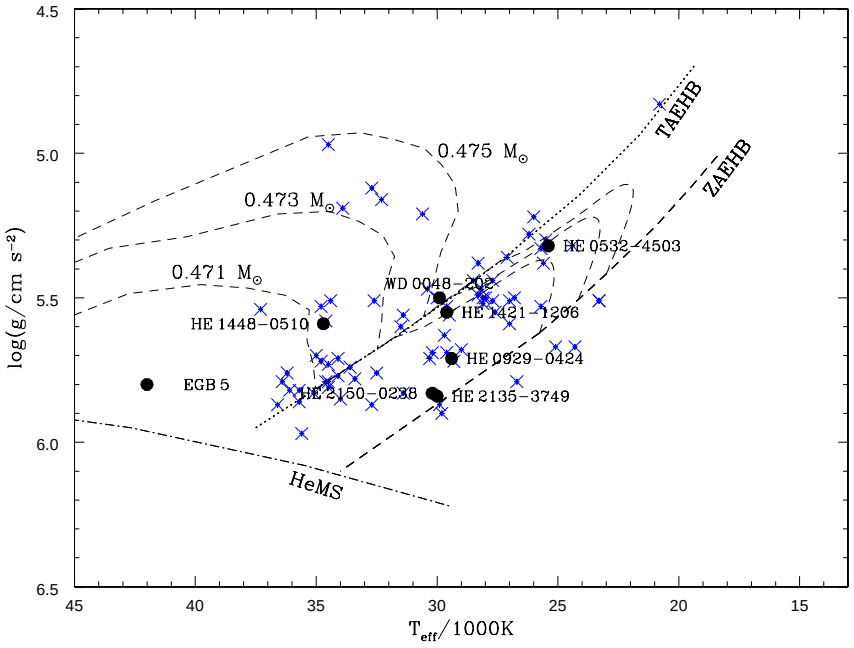

Figure 4.5: Mass determination of single sdB stars. Temperature and gravity, determined from model atmosphere analysis of the UVES spectra compared to evolutionary tracks (Dorman et al. 1993) for a range of masses. Our own determinations are marked as black dots whereas parameters derived by Likser et al. (2004) are indicated as gray crosses

for white dwarfs, for which the wavelength shifts caused by orbital motions are much smaller than the line widths of the broad Balmer lines. Therefore we chose a different approach for our analyses. Ralf Napiwotzki developed the program FITSB2 (Napiwotzki et al. 2003b), which performs a spectral analysis of both components of a double-lined system. FITSB2 is based on a χ^2 minimization technique using a simplex algorithm. The fit is performed on all available spectra covering different spectral phases simultaneously. Thus, all available spectral information is combined into the parameter determination procedure. An application of the program FITSB2 to the known system HE 1414−0848 (Napiwotzki et al. 2002) yielded encouraging results (Napiwotzki et al. 2003b). In the following study, FITSB2 was also applied to HE 2209−1444 (section 5.2.1). A detailed description of the program and an evaluation of its performance will be given by Napiwotzki (in prep.).

4.4.3 Projected rotational velocities

The rotation of a star causes a broadening of the spectral lines due to the Doppler effect. However, the rotational axis is usually not perpendicular to the line of sight and thus we can only determine the projected rotational velocity $v_{\rm rot}$ sin i by means of a spectral analysis. In combination with the period P and the stellar radius R, however, we can therefore estimate the unknown inclination i if we assume bound rotation caused by tidal locking:

$$sini = \frac{v_{\rm rot} P}{2\pi R_\star} \tag{4.6}$$

Whereas the period is usually well defined by the power spectrum, the radius has to be estimated from a mass-radius relation by means of the stellar atmospheric parameters $T_{\rm eff}$ and log g. This $M - R$ relation is based on evolutionary calculations like the Blöcker tracks for white dwarfs (Blöcker at el. 1997). For sdB stars the canonical mass is adopted and the radius follows from:

$$\frac{M_\star G}{R^2} = g \Rightarrow R = \sqrt{\frac{0.47 M_\odot G}{g}} \tag{4.7}$$

White dwarfs can be analyzed for $v_{\rm rot}\, sin\, i$ from the NLTE core from the Hα line as has been shown by various studies (e.g. Koester et al. 1998, Heber et al. 1997, Karl et al. 2004). DA white dwarfs display no other spectral lines beside the Balmer lines. Subdwarf B stars, however, show helium and metal lines in addition to the Balmer series.

4.4.4 Metal abundances of sdB stars

The best-suited lines are narrow metal lines, e.g. the Mg II doublet at 4481.13 Å and 4481.33 Å or the N II lines between 5000 Å and 5010 Å. Thus, the metal rich sdB stars are the best candidates for a study on rotational velocities.

In order to derive $v_{\rm rot}\, sin\, i$ we therefore determined metal abundance patterns for six sdB stars and calculated synthetical line profiles for these objects. Finally, the projected rotational velocity was estimated by comparison of the synthetic and the observed line profiles. The inclination of the sdB systems or lower limits were computed thereof (see section 7.2).

Chapter 5

Double-lined white dwarfs

The spectra of the so-called double-lined systems reveal spectral features arising from a companion. This may either be a displaced Balmer absorption line in the case of a DA+DA system or an emission line of a M dwarf companion in the case of a DA+dM system. In any case, fitting these features provides additional information about the system. Figure 5.1 shows typical examples for double-lined systems. In the upper panel the DA+DA white dwarf system HE 2209−1444 is displayed, whereas the DA+dM binary WD 0419−487 can be seen in the lower panel. In the following chapter we concentrate on white dwarf systems (DA+DA), while white dwarfs with M dwarf companions will be discussed in the next chapter 6.

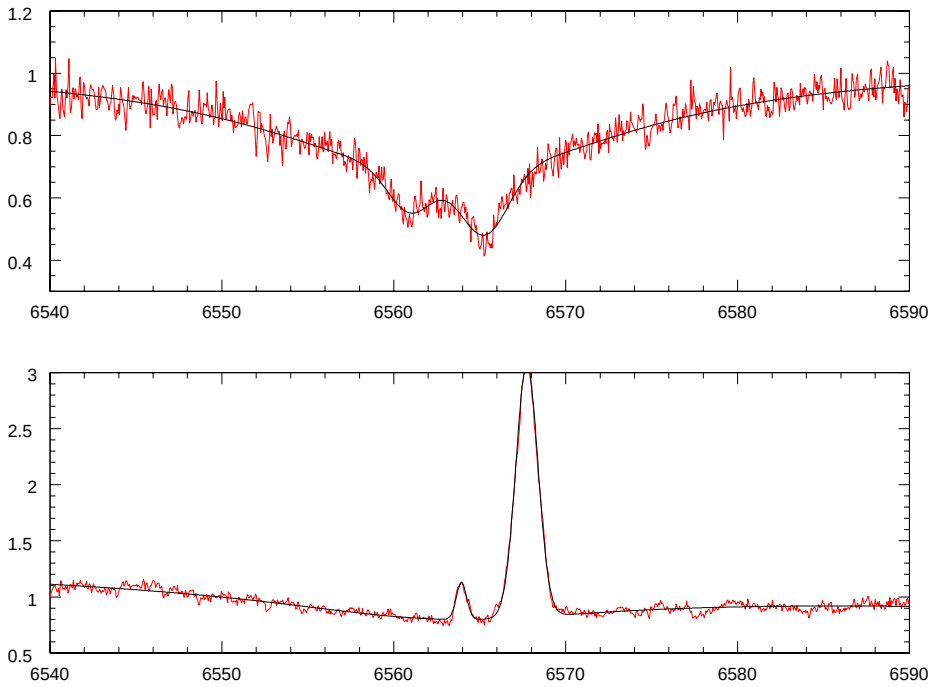

Figure 5.1: Double-lined systems. The upper panel displays the DA+DA white dwarf binary HE 2209−1444 and the lower panel WD 0419−487, a DA+dM system. Note that the last system displays two emission lines: one from the M dwarf and the second one most probably from a hot DA white dwarf.

Obviously, the period has to be the same for both components of a binary system. Therefore, once the period is determined by any means, we can compute RV curves, getting the ephemeris, the system velocity and semi-amplitude for the *primary* as well as for the *secondary*.

In order to form a binary system, the origin of the ephemeris for the two components have to differ in phase by $\Delta\,\Phi = 0.5$. In some cases, the system velocities derived from the RV curves are influenced by mass dependent gravitational redshift. For a given mass-radius relation, the redshift can be computed as a function of white dwarf mass (cf. section 4.3), and since the mass ratio is also given from the RV curve only one combination of masses can fulfill both constraints.

With information about the absolute masses of the components, we can compute their separation from the third Kepler-law. The total separation becomes

$$A_{\rm tot} = \sqrt[3]{\frac{GP^2(M_{\rm prim} + M_{\rm sec})}{4\pi^2}}. \tag{5.1}$$

According to the individual masses, the distances of the components from the barycenter can be computed to be

$$A_{\rm prim} = A_{\rm tot}\frac{M_{\rm sec}}{M_{\rm sec} + M_{\rm prim}} \tag{5.2}$$

and similarly for the *secondary*. The orbital velocities result from the system's period and the distances from the barycenter according to

$$v_{\rm prim} = \frac{2\pi A_{\rm prim}}{P}. \tag{5.3}$$

Finally, the inclination angle can be computed from a comparison of the measured semi-amplitudes derived from the RV curve and the orbital velocities calculated from equation 6.1.4 to be

$$\sin i = \frac{K_{\rm prim,sec}}{v_{\rm prim,sec}} \tag{5.4}$$

Usually, no spectral analysis was performed for double-lined systems due to the difficulties mentioned in section 4.4.2. The components of HE 2209−1444, however, were found to be quite similar with no measurable gravitational redshift difference ($\Delta\,\gamma \approx 0$). This object could be analyzed by means of the `fitsb2` program package (cf. sections 4.4 and 5.2.1).

5.1 Systems analyzed from their radial velocity curves alone

The following systems are analyzed without having use of a quantitative spectroscopical analysis. Figure 5.2 displays the approach for analyzing these systems in a schematic way.

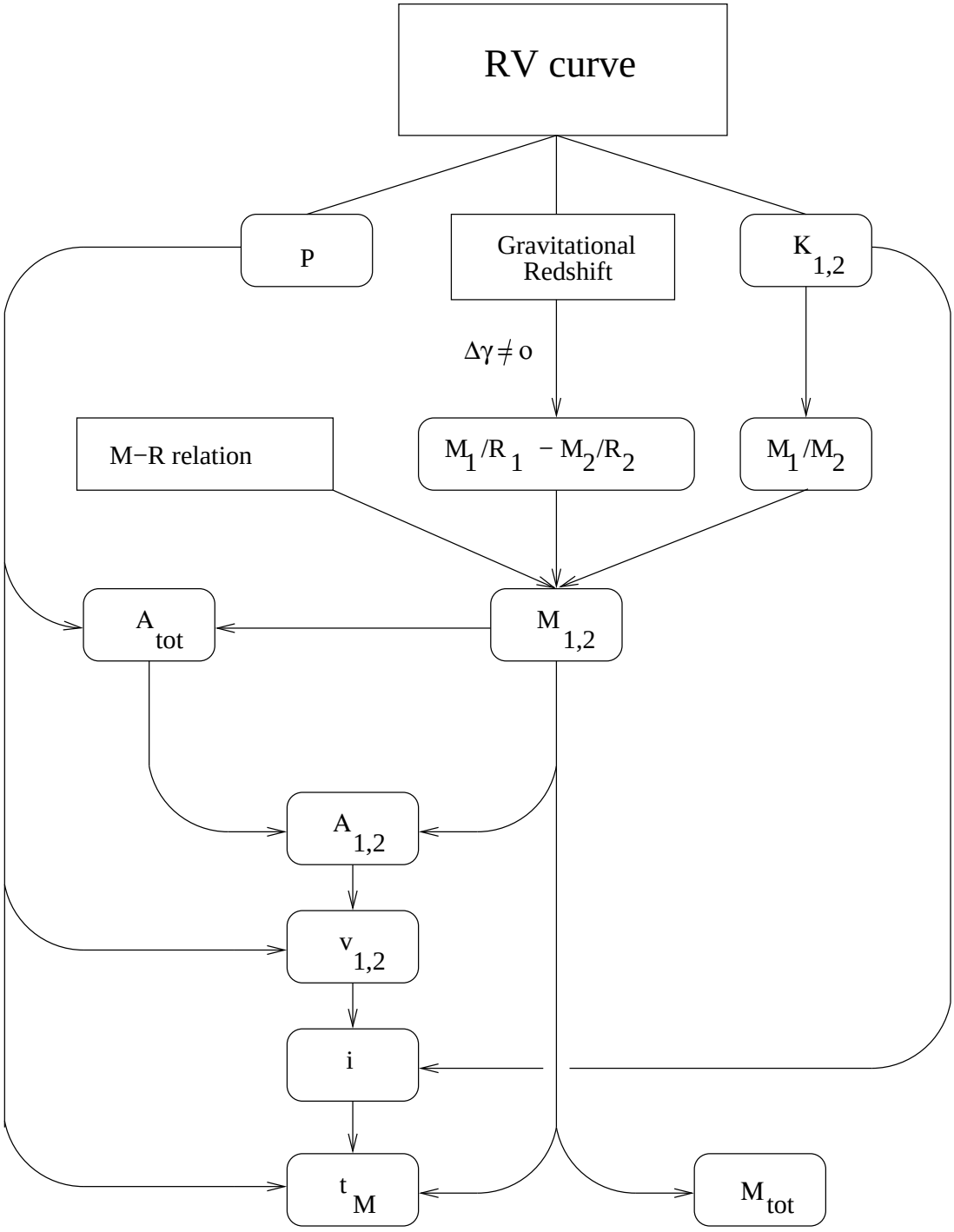

Figure 5.2: Analysis of a double-lined system (schematic).

5.1.1 WD 0028−474

α_{2000}= 00:30:47.16, δ_{2000}= −47:12:36.9, V = 15.24

History

The McCook & Sion catalogue (1999) classified WD 0028−474 as a DA white dwarf. Moreover, it becomes obvious from the survey spectra that this is a double-lined system, and therefore WD 0028−474 became a high-priority object for our follow-up campaign. Observations were done during our September 2002 run at the NTT and again at the VLT in November of the same year.

Radial velocity curve

Both components of WD 0028−474 look sufficiently different in terms of spectral appearance as can be seen from figure 5.3. We assign the stronger Hα line profile to the component called

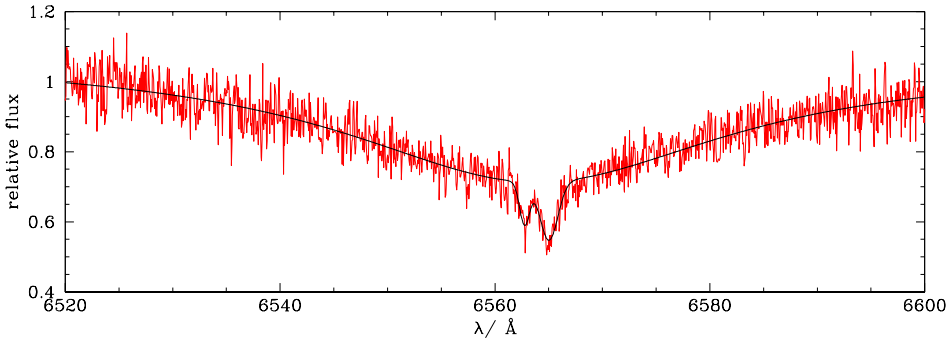

Figure 5.3: Observed Hα line profile and fitted curve of WD 0028−474.

the *primary* henceforth, while the weaker one belongs to the *secondary*. However, the weaker Hα line was hardly visible in some of the spectra. For this reason we excluded ambiguous fits to the observed line profiles from our analysis and concentrated on RV-measurements from the *primary* for the determination of the system's period. The resulting period of 0.389568^{d} ($9^{\mathrm{h}}20^{\mathrm{m}}59^{\mathrm{s}}$) is unequivocal as can be seen from the power spectrum displayed in the lower panel of figure 5.4. The upper panel of figure 5.4 shows the best fit RV curves and yield to the system's velocities and the semi-amplitudes. For the *primary* we derive $\gamma_{\mathrm{prim}} = 38.4 \pm 1.2$ km s^{-1}and a RV semi-amplitude of $\mathrm{K}_{\mathrm{prim}} = 123.4 \pm 1.7$ km s^{-1}. The ephemeris for the time T_0, defined as the conjunction time at which the star moves from the blue shifted part to the red shifted part of the RV curve is

$$HJD(T_0)_{\mathrm{prim}} = 2\,453\,099.815517 \pm 0.389568 \times E. \tag{5.5}$$

The corresponding results for the *secondary* are $\gamma_{\mathrm{sec}} = 22.2 \pm 2.3$ km s^{-1}, $\mathrm{K}_{\mathrm{sec}} = 149.1 \pm 3.7$ km s^{-1}and

$$HJD(T_0)_{\mathrm{sec}} = 2\,453\,100.005863 \pm 0.389568 \times E. \tag{5.6}$$

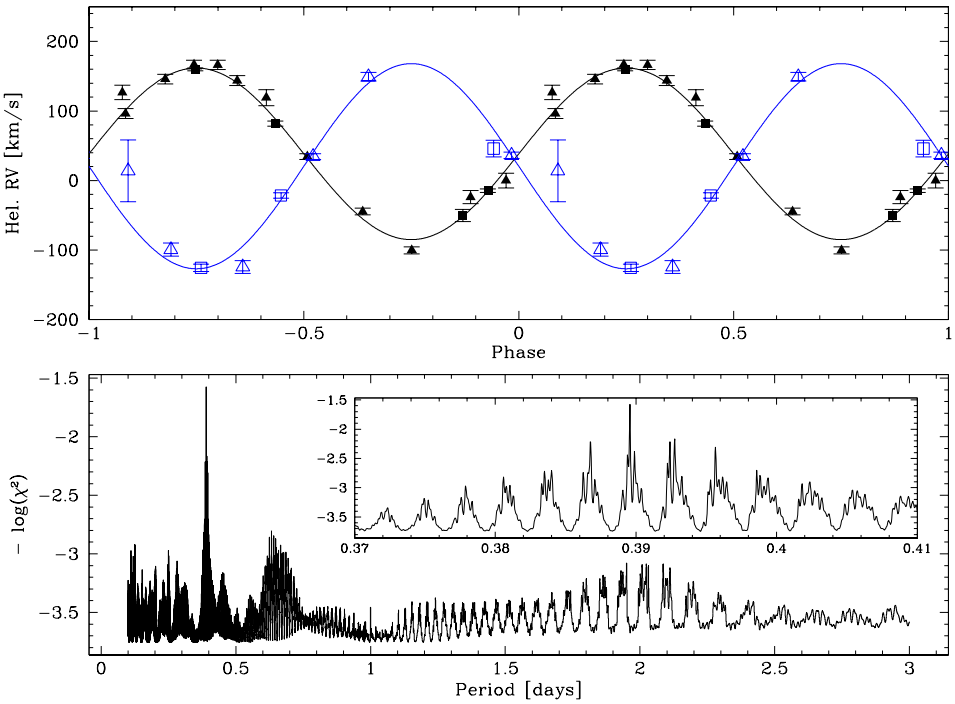

Figure 5.4: Best fit RV curve and power spectrum for WD 0028−474. Upper panel: Measured RVs of both components of WD 0028−474 as a function of orbital phase and fitted sine curves. RVs measurements belonging to the *primary* are marked as filled symbols while open symbols indicate data belonging to the *secondary*. Squares are used for ESO VLT observations and triangles for observations from the ESO NTT. Lower panel: Power spectrum of WD 0028−474. Since fitting the *secondary* was not unambiguous in all cases, the displayed power spectrum was calculated using only data belonging to the *primary*. However, for physical reasons the period has to be the same for the *secondary*. The inset shows the region near the main peak in more detail.

Both ephemerides differ by 0.190346^{d} in terms of $\Delta HJD(T_0)$. This corresponds to $\Delta\Phi = 0.489$ which is close to 0.5 as expected for physical reasons.

System composition

Since WD 0028−474 is a double-lined system we can derive the mass ratio from the semi-amplitudes of the RV curve to be $M_{\mathrm{prim}}/M_{\mathrm{sec}} = 1.21 \pm 0.03$. The system velocities derived for the components differs by $\Delta\gamma = 16.2 \pm 2.6\,\mathrm{km\,s^{-1}}$ due to the mass dependent gravitational redshift. Combining it with the mass-radius relation we compute the masses to be $M_{\mathrm{prim}} = 0.87\,\mathrm{M}_\odot$ and $M_{\mathrm{sec}} = 0.72\,\mathrm{M}_\odot$ respectively. Both components are separated by $A_{\mathrm{tot}} = 2.6\,\mathrm{R}_\odot$ only, thus WD 0028−474 obviously underwent phases of strong binary interaction in its history. The distance from the barycenter and the resulting orbital velocity for the *primary* is $A_{\mathrm{prim}} = 1.2\,\mathrm{R}_\odot$ and $v_{\mathrm{prim}} = 154\,\mathrm{km\,s^{-1}}$. Corresponding results for the *secondary* are $A_{\mathrm{sec}} = 1.4\,\mathrm{R}_\odot$ and $v_{\mathrm{sec}} = 186\,\mathrm{km\,s^{-1}}$. The orbital velocities yield an inclination of $i \approx 53°$, as can be seen from comparison with the radial velocity semi-amplitudes. The merging time of the system can be computed from the orbital period and the components masses to be $t_{\mathrm{m}} = 7.2\,\mathrm{Gyrs}$

only.

This system is a very exciting one as its total mass ($1.59\,M_\odot$) is likely to exceed the Chandrasekhar limit. As it also will merge in less than a Hubble time, WD 0028−474 is a very good candidate for a SN Ia progenitor. Note, however, that the RV curve of the *secondary* lacks some crucial data points, especially at $\Phi = 0.75$ (see figure 5.1.1) to fortify the semi-amplitude and the system velocity. Therefore, the masses derived for both components are somewhat uncertain. Although WD 0028−474 qualifies as an SN Ia precursor within the error margins of $M_{\rm prim}/M_{\rm sec}$ and $\Delta\gamma$ (cf table 5.1), additional observation will be necessary to improve the RV curve and confirm the very important result.

Table 5.1: System composition for WD 0028−474.

Determined from RV curve					
$\Delta\gamma/\mathrm{km\,s^{-1}}$	16.2	13.6	13.6	18.8	18.8
$M_{\rm prim}/M_{\rm sec}$	1.21	1.18	1.24	1.25	1.18
P/d	0.389 568				
Deduced parameters					
$M_{\rm prim}/\mathrm{M}_\odot$	0.87	0.85	0.78	0.89	0.96
$M_{\rm sec}/\mathrm{M}_\odot$	0.72	0.72	0.63	0.72	0.81
$A_{\rm tot}/\mathrm{R}_\odot$	2.6	2.6	2.6	2.6	1.7
i/deg	53	53	58	54	50
$M_{\rm tot}/\mathrm{M}_\odot$	1.59	1.57	1.41	1.61	1.77
$t_{\rm m}/\mathrm{Gyrs}$	7.2	7.4	8.8	7.1	6.0
SN Ia precursor	yes	yes	yes	yes	yes

5.1.2 HE 0315−0118

α_{2000}= 03:18:13.31, δ_{2000}= −01:07:13.1, V = 14.71

History

HE 0315−0118 was first observed in the Hamburg/ESO - survey and classified to be a hydrogen-rich DA white dwarf by Christlieb et al. (2001). Furthermore, from the high-resolution survey spectra taken in August 2001 two Hα line cores become obvious. As a result of this outstanding spectral appearance, we deduced HE 0315−0118 to be a double-lined system composed most probably of two white dwarfs. Follow-up observations were carried out in January 2001 and November 2002 at the ESO VLT. The campaign was complemented by observations done at the ESO NTT during the September 2002 run.

Radial velocity curve

Since both Hα line profiles look very similar, there is no way for HE 0315−0118 to discern the components by visual inspection only. However, to be able to perform a radial velocity analysis, we have to assign the observed lines to the *primary* or to the *secondary*.

Therefore, we computed the separation of the components first and fitted sine curves for a range of periods to the measured RV differences and determined the χ^2 value for each period. Doing this we produced a *difference power spectrum* indicating the quality of our RV fit as a function of period. This way we got a first estimate of the period of the system and were subsequently able to identify the individual components unambiguously for all of our spectra. This enabled us to compute a *power spectrum* for each individual component. To assign the observed absorption lines to the *primary* and *secondary* unambiguously, however, we computed a *difference power spectrum* first not using the absolute radial velocities but the RV-differences of the component. This way we estimated the system's half-period and derived finally the period itself.

Subsequently, independent analyses of both components yield *individual power spectra*. This method finally results in a period of 1.894596^{d} ($1^{\mathrm{d}}21^{\mathrm{h}}28^{\mathrm{m}}13^{\mathrm{s}}$) for the *primary* and the *secondary*'s power spectrum results in the same period, as it should be for a binary system. We finally coadded the χ^2 values of these power spectra, creating a combined power spectrum representing the whole system. As can be seen from the lower panel of figure 5.5, the period is quite well defined. Only one alias at 1.912903^{d} still remains. The upper panel of figure 5.5 shows the best fit RV curves. For the *primary* we derive $\gamma_{\mathrm{prim}} = 72.9 \pm 0.4$ km s^{-1} and $\mathrm{K}_{\mathrm{prim}} = 80.0 \pm 1.3$ km s^{-1}. The ephemeris is

$$HJD(T_0)_{\mathrm{prim}} = 2\,453\,099.326999 \pm 1.894596 \times E. \tag{5.7}$$

The corresponding results for the *secondary* are $\gamma_{\mathrm{sec}} = 62.2 \pm 0.4$ km s^{-1}, $\mathrm{K}_{\mathrm{sec}} = 100.3 \pm 1.2$ km s^{-1} and

$$HJD(T_0)_{\mathrm{sec}} = 2\,453\,100.267090 \pm 1.894596 \times E. \tag{5.8}$$

Both ephemerides differs by 0.940091^{d} in terms of $\Delta HJD(T_0)$ or by $\Delta\Phi = 0.496$.

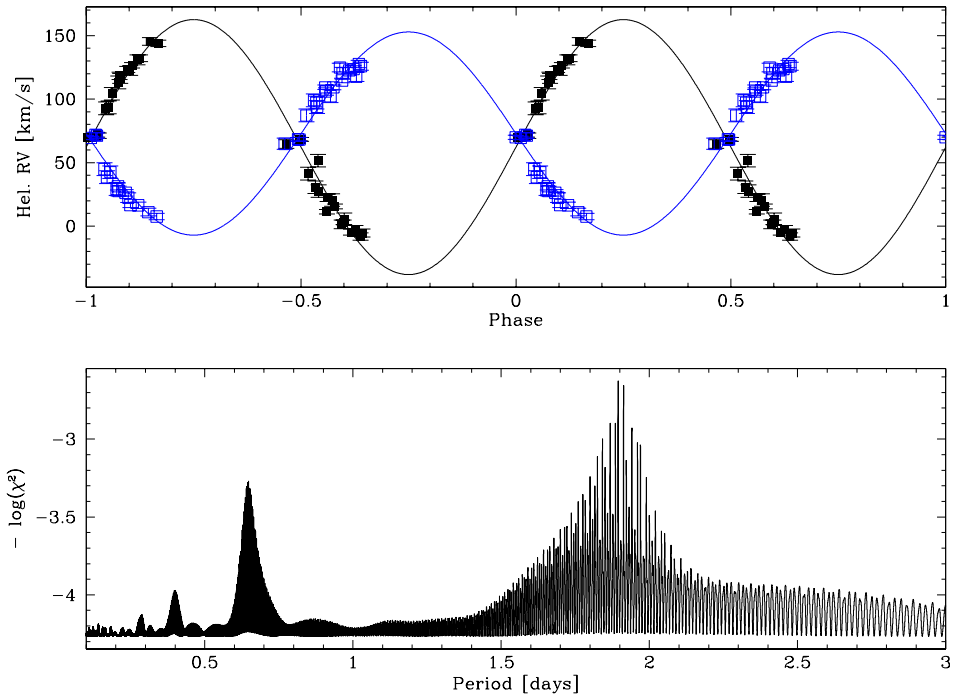

Figure 5.5: Best fit RV curve and power spectrum for HE 0315−0118. Upper panel: Measured RVs of both components of HE 0315−0118 as a function of orbital phase and fitted sine curves. RVs measurements of to the *primary* are marked as filled symbols while open symbols indicate data of the *secondary*. Squares are used for ESO VLT observations and triangles for observations from the ESO NTT. Lower panel: Combined power spectrum of HE 0315−0118.

Table 5.2: System composition for HE 0315−0118.

Determined from RV curve					
$\Delta\gamma/\mathrm{km\,s^{-1}}$	10.7	11.3	11.3	10.1	10.1
$M_{\mathrm{prim}}/M_{\mathrm{sec}}$	1.25	1.27	1.23	1.27	1.24
P/d	1.894 596				
Deduced parameters					
$M_{\mathrm{prim}}/\mathrm{M}_\odot$	0.68	0.69	0.73	0.65	0.68
$M_{\mathrm{sec}}/\mathrm{M}_\odot$	0.54	0.54	0.59	0.51	0.55
$A_{\mathrm{tot}}/\mathrm{R}_\odot$	6.9	6.9	7.1	6.8	6.9
i/deg	78	81	72	—	76
$M_{\mathrm{tot}}/\mathrm{M}_\odot$	1.22	1.23	1.32	1.16	1.23
$t_{\mathrm{m}}/\mathrm{Gyrs}$	760	760	760	830	750
SN Ia precursor	no	no	no	no	no

— : Equation 5.4 runs to $sin\, i > 0$.

System composition

From the semi-amplitudes of the RV curves we calculate the mass ratio of HE 0315−0118 to be $M_{\rm prim}/M_{\rm sec} = 1.25 \pm 0.02$. Due to the fact that both RV curves also differs by $\Delta\gamma = 10.7 \pm 0.6 {\rm km\,s^{-1}}$ in terms of system velocity we can use the mass radius relation for white dwarfs to derive the masses of the individual components. For the *primary*, the analysis results in $M_{\rm prim} = 0.68\,{\rm M_\odot}$ while the *secondary* has $M_{\rm sec} = 0.54\,{\rm M_\odot}$. The orbits are $A_{\rm prim} = 3.1\,{\rm R_\odot}$ and $A_{\rm sec} = 3.8\,{\rm R_\odot}$ respectively. Therefore, the white dwarfs in the HE 0315−0118 system are separated by $A_{\rm tot} = 6.9\,{\rm R_\odot}$. From the size of the orbits and the period orbital velocities can be computed: $v_{\rm prim} = 82\,{\rm km\,s^{-1}}$ for the *primary*and $v_{\rm prim} = 102\,{\rm km\,s^{-1}}$ for the *secondary*. By comparison with the observed radial velocity amplitudes we derive an inclination of $i = 78°$.

Although the total mass ($1.22\,{\rm M_\odot}$) is only 10 % below the Chandrasekhar limit, the large merging time of 760 Gyrs rules it out as a SN Ia progenitor candidate.

5.1.3 WD 1349+144

α_{2000}= 03:18:13.31, δ_{2000}= −01:07:13.1, V = 14.71

History

WD 1349+144 was selected from the the McCook & Sion catalogue (1999) to be a DA3 white dwarf. Thus, the object was observed twice in August 2001 in the course of our survey. From both high-resolution spectra double absorption line cores became obvious, which were clearly separated from each other by 80 $\mathrm{km\,s^{-1}}$ and 70$\mathrm{km\,s^{-1}}$ respectively. Being double-lined, WD 1349+144 became a high-priority object for our follow-up campaigns and was re-observed in July 2001 and February 2002 at the DSAZ. Additional data from January 2003 were obtained at the WHT and provided by Gijs Nelemans.

Radial velocity curve

The spectral spectra of both components is very similar, and thus we cannot distinguish them by visual means only. Therefore, we analyze the system in the same way as we did it in the case of HE 0315−0118 (see section 5.1.2). First of all, we computed a *difference power spectrum* from the radial velocity differences derived from each observation. By means of this, we could estimate the half-period of the system and subsequently assign the observed absorption lines to the components. Although there is no reason to favor one component in front of the other, we call one of them the *primary* and the other *secondary* further on, just to be consistent with previous discussions.

Analyzing the radial velocity data sets of *primary* and *secondary* independently, we computed *individual power spectra*. However, the most likely periods derived from these power spectra slightly differ. For the *primary* we found the main peak at $P_{\mathrm{prim}} = 2.209568^{\mathrm{d}}$ ($2^{\mathrm{d}}5^{\mathrm{h}}1^{\mathrm{m}}47^{\mathrm{s}}$), while the highest peak of the secondary's power spectrum is at $P_{\mathrm{sec}} = 1.984700^{\mathrm{d}}$ ($1^{\mathrm{d}}23^{\mathrm{h}}37^{\mathrm{m}}58^{\mathrm{s}}$). Moreover, both power spectra also show aliases at the period favored by the other component. In some cases, a visual inspection of the corresponding RV curves could help to ruled out aliases. However, for WD 1349+144 this method does not work because neither RV curve show clearly outliers. Thus, we can explain the discrepancy between the periods only by means of insufficient data. Especially radial velocity measurements based on the medium-resolution spectra taken at the DSAZ have relatively large error margins which may be a reason for the problem. Better observations are necessary in order to derive the system's period beyond doubt.

The lower panel of figure 5.6 displays the *combined power spectrum* created by coadding the χ^2 values of the *individual power spectra*. Both peaks discussed above can be reproduced as well as three aliases at $P = 2.106^{\mathrm{d}}$, 2.150^{d} and 2.246^{d}. The strongest peak, however, is at $P = 2.209568^{\mathrm{d}}$, corresponding to the *primary*'s period. The upper panel of figure 5.6 shows the best fit RV curves for this period and result in the most likely system's velocities and the semi-amplitudes. For the *primary* we derive $\gamma_{\mathrm{prim}} = -10.7 \pm 1.1$ $\mathrm{km\,s^{-1}}$ and $\mathrm{K_{prim}} = 60.2 \pm 1.7\,\mathrm{km\,s^{-1}}$. Its ephemeris is

$$HJD(T_0)_{\mathrm{prim}} = 2\,453\,099.886136 \pm 2.209568 \times E. \tag{5.9}$$

The corresponding results for the *secondary* are $\gamma_{\mathrm{sec}} = -16.5 \pm 1.1\,\mathrm{km\,s^{-1}}$, $\mathrm{K_{sec}} = 75.8 \pm 1.8\,\mathrm{km\,s^{-1}}$

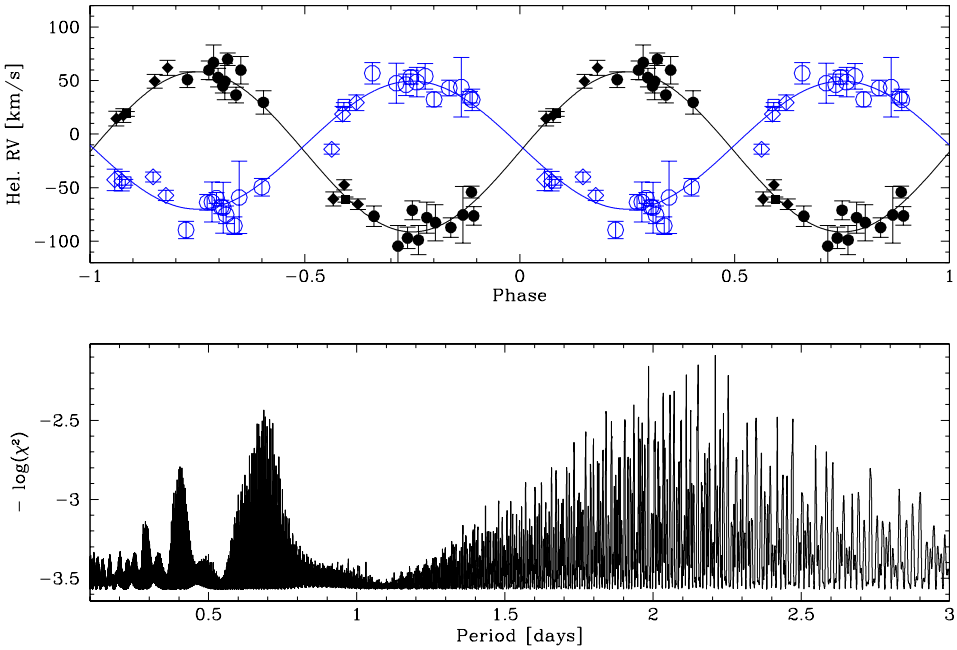

Figure 5.6: Best fit RV curve and power spectrum for WD 1349−144. Upper panel: Measured RVs of both components of WD 1349−144 as a function of orbital phase and fitted sine curves. RVs measurements of to the *primary* are marked as filled symbols while open symbols indicate data of the *secondary*. Squares are used for ESO VLT observations and circles for observations from the DSAZ. Data provided by Gijs Nelemans are marked as diamonds. Lower panel: Combined power spectrum of WD 1349−144.

and

$$HJD(T_0)_{\rm sec} = 2\,453\,101.005294 \pm 2.209568 \times E. \tag{5.10}$$

Both ephemerides differ by $1.119158^{\rm d}$ in terms of $\Delta HJD(T_0)$ or by $\Delta\Phi = 0.507$ consistent with expectation.

System composition

From the semi-amplitudes of the RV curves we calculate the mass ratio of WD 1349−144 to be $M_{\rm prim}/M_{\rm sec} = 1.26 \pm 0.04$. Due to the fact that both RV curves also differs by $\Delta\gamma = 5.8 \pm 1.5\,{\rm km\,s^{-1}}$ in terms of system velocity we can use the mass radius relation for white dwarfs to derive the masses of the individual components. For the *primary*, the analysis results in $M_{\rm prim} = 0.48\,{\rm M_\odot}$ while the *secondary* has $M_{\rm sec} = 0.38\,{\rm M_\odot}$. Therefore, the *primary* is most probably a white dwarf with a C/O while the *secondary* has a core made of helium. The orbits are $A_{\rm prim} = 3.0\,{\rm R_\odot}$ and $A_{\rm sec} = 3.8\,{\rm R_\odot}$ respectively. Therefore, both white dwarfs are separated by $A_{\rm tot} = 6.8\,{\rm R_\odot}$ in total. From the size of the orbits and the period we compute the orbital velocity of the *primary* to be $v_{\rm prim} = 69\,{\rm km\,s^{-1}}$ and $v_{\rm prim} = 87\,{\rm km\,s^{-1}}$ for the *secondary*. By comparison with the observed RV amplitudes we derive the inclination to be $i = 61^{\rm o}$.

Table 5.3: System composition for WD 1349+144.

Determined from RV curve					
$\Delta\gamma/\mathrm{km\,s^{-1}}$	5.8	4.3	4.3	7.3	7.3
$M_{\mathrm{prim}}/M_{\mathrm{sec}}$	1.26	1.30	1.22	1.30	1.22
P/d			2.209 568		
Deduced parameters					
$M_{\mathrm{prim}}/\mathrm{M}_\odot$	0.48	0.38	0.44	0.52	0.59
$M_{\mathrm{sec}}/\mathrm{M}_\odot$	0.38	0.29	0.36	0.40	0.48
$A_{\mathrm{tot}}/\mathrm{R}_\odot$	6.8	6.2	6.6	6.9	7.3
i/deg	61	76	62	61	42
$M_{\mathrm{tot}}/\mathrm{M}_\odot$	0.86	0.67	0.80	0.92	1.07
$t_{\mathrm{m}}/\mathrm{Gyrs}$	2 000	3 150	3 650	3 000	1 450
SN Ia precursor	no	no	no	no	no

Neither the system's merging time of about 2000 Gyrs nor its total mass of $M_{\mathrm{tot}} = 0.87\,\mathrm{M}_\odot$ qualifies WD 1349−144 for being a SN Ia precursor.

5.2 Systems that cannot be solved from their RV curves alone

5.2.1 HE 2209−1444, a system solved through an additional spectral analysis

α_{2000}= 22:12:18.1, δ_{2000}= −14:29:48.0, V = 15.32

History

HE 2209−1444 was discovered by the Hamburg ESO survey as a potential cool white dwarf and, therefore, was included in our SPY project. From the first survey spectrum taken in December 2000 we found HE 2209−1444 to be a double-lined binary system consisting of two DA white dwarfs. The H_α line cores of both components were separated by 4.5 Å in the discovery spectrum, corresponding to a large radial velocity difference of 200 km s^{-1}. Therefore we observed the system during our follow-up observations for the SPY project at the Calar Alto Observatory, Spain. From 2001 July 6$^{\rm th}$ to July 15$^{\rm th}$ a total of 15 medium resolution spectra were obtained with the TWIN spectrograph at the 3.5 m telescope. Figure 5.7 shows a sequence of six Hα spectra taken at Calar Alto Observatory during two hours. The observed spectra are plotted as well as the fit-functions used for RV determination. The rapid change of the spectral appearance due to the orbital motion is obvious. Our follow-up campaign was supplemented by spectra taken with the Isaac Newton Telescope (INT) and by the two SPY spectra taken in December 2000 and October 2001. The INT set of data used for our analysis was taken on October 28$^{\rm th}$ to October 30$^{\rm th}$ 2001 on La Palma. Eight spectra were taken with the Intermediate Dispersion Spectrograph (IDS).

Radial velocity curve

Both components are very similar, but the blue shifted one in figure 5.7 is slightly deeper and broader. This component is called *primary* further on. However, sometimes it was difficult to do an unambiguous identification of the components especially near conjunction phases and in some spectra with relatively low S/N ratio and of lower resolution (from Calar Alto and La Palma). Thus we computed a *difference power spectrum* first in order to estimate the system's period. Thus we were able to allocate the observed line profiles definitely to the *primary* and the *secondary* respectively (cf. section 5.1.2).

Subsequently, an independent analysis of both components yield *individual power spectra*, both showing outstanding peaks at 0.276924$^{\rm d}$ (6$^{\rm h}$38$^{\rm m}$46$^{\rm s}$). An inspection of the phased RV curves created using periods corresponding to other peaks in the power spectra allowed us to rule out aliases, because of one or more strongly deviating radial velocity measurements. This way, the period corresponding to the main peak of the power spectrum remained as an unambiguous solution for the *primary* as well as for the *secondary* – exactly as it should be for a binary system. Finally, adding the χ^2 values of the two individual power spectra we produced a *combined power spectrum* for the whole system (figure 5.8).

To derive accurate orbital parameters for HE 2209−1444 we used in a final step the program FITSB2 developed by Ralf Napiwotzki (cf. section 4.4.2 and Napiwotzki et al. 2003b). In a fashion similar to the method described in Maxted et al. (2002a), a simultaneous fit of all spectra was performed. Two model profiles, one for each star, consisting of a combination of two Gaussians

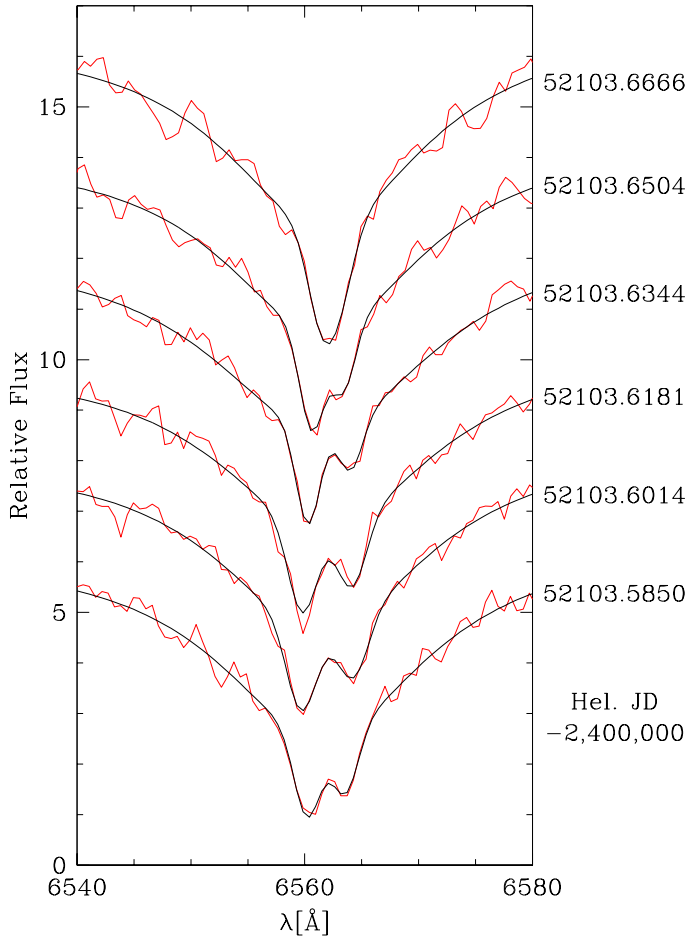

Figure 5.7: Spectra of HE 2209−1444 taken at the 3.5 m telescope of the Calar Alto Observatory during one night. The observed spectra are as well plotted as the fits. The JD is heliocentric corrected and computed for the mid of the exposure.

for the line core and a Lorentzian for the line wings were fitted. The position of each profile is determined from

$$RV_{\mathrm{prim/sec}} = \gamma_{\mathrm{prim/sec}} \pm K_{\mathrm{prim/sec}} \sin\left(\frac{T - T_0}{P}\right). \tag{5.11}$$

Free parameters are the mean velocities (including gravitational redshift) of each component $\gamma_{\mathrm{prim/sec}}$, the (projected) orbital velocities $K_{\mathrm{prim/sec}}$, the zero-point T_0, and the period P, plus the parameters defining the line profiles. The final ephemeris of the system for the time T_0 defined as the conjunction time at which the *primary* moves from the blue side of the RV curve to the red one (i.e. the *primary* is closest to the observer) is

$$HJD(T_0)_{\mathrm{prim}} = 2,452,097.0349 \pm 0.276928 \times E. \tag{5.12}$$

Also from the RV curves (see Fig. 5.8) of the FITSB2 analysis we found the semi-amplitude of the *primary* to be $K_{\mathrm{prim}} = 108.7 \pm 7.5\,\mathrm{km\,s^{-1}}$ ($\gamma_{\mathrm{prim}} = -14.4 \pm 4.5\,\mathrm{km\,s^{-1}}$) whereas for the *secondary* the semi-amplitude is $K_{\mathrm{sec}} = 109.1 \pm 10.8\,\mathrm{km\,s^{-1}}$ ($\gamma_{\mathrm{sec}} = -18.7 \pm 6.8\,\mathrm{km\,s^{-1}}$). The mass

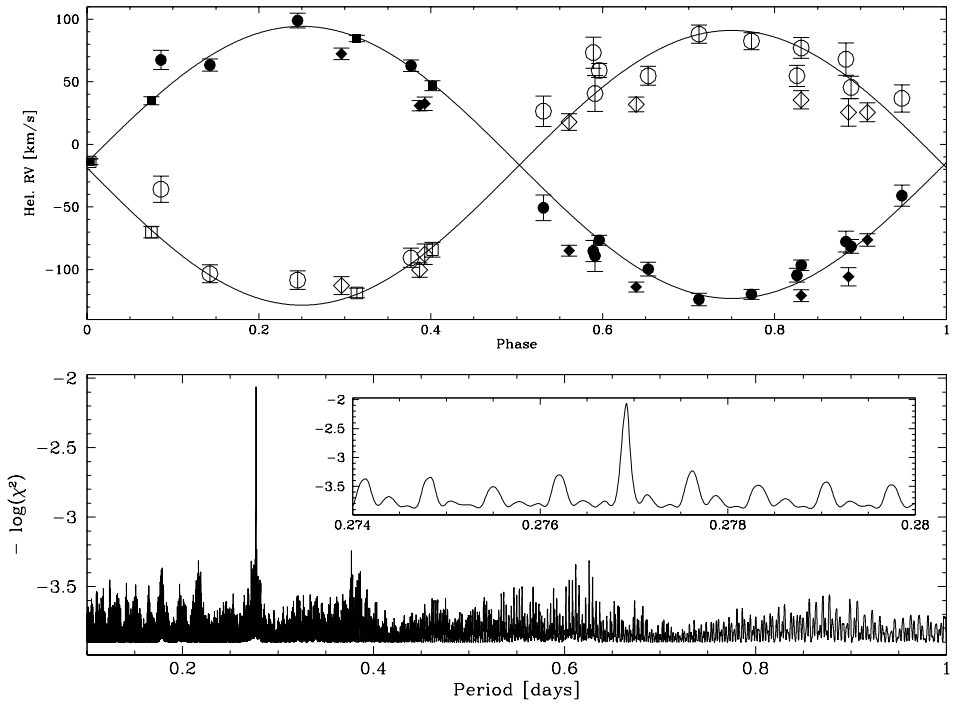

Figure 5.8: Best fit RV curve and power spectrum for HE 2209−1448 Upper panel: Measured RVs of both components of HE 2209−1448 as a function of orbital phase and fitted sine curves. RVs measurements of to the *primary* are marked as filled symbols while open symbols indicate data of the *secondary*. Squares are used for ESO VLT observations, circles for observations from the DSAZ and diamonds for data obtain at the INT. Lower panel: Combined power spectrum of HE 2209−1448.

ratio can be computed from the ratio of the semi-amplitudes to be $M_{\rm prim}/M_{\rm sec} = 1.00 \pm 0.13$, i.e the masses of both white dwarfs are identical within the error limits. As in the cases of the former double-lined systems, the difference of gravitational redshifts can be measured from $\gamma_{\rm prim} - \gamma_{\rm sec}$. If this difference is non zero we obtain an additional constraint equation, which allows to solve for the individual masses. However, since the masses of both components of HE 2209−1444 are very similar, the redshift difference is zero within error limits. Hence we cannot solve for the individual masses from the radial velocity curve alone. The required additional information, however, will be obtained from a quantitative spectral analysis described in the next section.

Spectral analysis

Since in the case of HE 2209−1444 mass estimates from the RV curves alone are impossible, we had to rely on a model atmosphere analysis. Because this system is double-lined the spectra are a superposition of both individual white dwarf spectra. Thus, we used the program FITSB2 (Napiwotzki et al. 2003b), which performs a spectral analysis of both components of double-lined systems (see section 4.4.2).

A large grid of synthetic spectra for DA white dwarfs computed from LTE model atmospheres with a code described in Finley et al. (1997) was used for the analysis. A simultaneous fit of the Balmer lines Hβ to $H8$ (UVES spectra) or Hβ to Hδ (TWIN spectra) was performed. We

Table 5.4: Results of the model atmosphere analysis with FITSB2. The error limits include the uncertainties of orbital parameter determination.

comp.	$T_{\rm eff}$ / K	log g	$M/{\rm M}_\odot$
prim	8490 ± 80	7.97 ± 0.05	0.58 ± 0.03
sec	7140 ± 110	7.97 ± 0.13	0.58 ± 0.08

did not include the INT spectra for the model atmosphere analysis, because these spectra cover only the Hα range. For details refer to Koester et al. (2001 and references therein). The model spectra were convolved with Gaussians with FWHMs corresponding to the resolution of the observed spectra.

The total number of fit parameters (stellar and orbital) is high. Therefore we fixed as many parameters as possible before performing the model atmosphere analysis. We have kept the radial velocities of the individual components fixed according to the radial velocity curve presented in the previous subsection. Since the mass ratio is already accurately determined from the radial velocity curve we fixed the gravity ratio. The remaining fit parameters are the effective temperatures of both components and the gravity of the *primary*. The gravity of the *secondary* is adjusted according to the *primary* value during the fitting procedure. The surface gravities also determine the relative weight of the two model spectra from the radius, obtained from the mass-radius relation of Benvenuto & Althaus (1999). The flux ratio in the V-band is calculated from the actual parameters and the model fluxes are scaled accordingly. The individual contributions are updated consistently as part of the iteration procedure.

Strong NLTE cores are present in Hα and Hβ which cannot be reproduced by our LTE model spectra. In principle, these lines are important for the temperature determination, especially of the cooler and fainter *secondary*. However, due to the large NLTE effects we had to exclude Hα completely and the core of Hβ ($\pm$ 4 Å). The final fit results are summarized in table 5.4 and a sample fit is shown in Fig. 5.9. The fit of the line cores is not perfect, even after excluding Hα. The parameter which is most sensitive to details of the fitting procedure is, as may be expected, the temperature of the fainter *secondary*. If, e.g., we include the wings of the Hα line we increase $T_{\rm eff}$ of the *secondary* by almost 500 K, while the temperature of the *primary* and the gravity are only modified within the error limits. Thus, while the temperature of the *secondary* is less well determined than that of the *primary* the basic properties of the HE 2209−1444 system are reliable. Both components have identical masses ($\rm M_{prim} = M_{sec} = 0.58\,M_\odot$) but different temperatures (8490 K vs. 7140 K). White dwarf masses were computed from the mass - radius relations of Benvenuto & Althaus (1999) with *thick hydrogen envelopes* ($\rm M_H/M_{WD} = 10^{-4}$). This result does not depend much on the choice of a particular model computation. From the thick envelope cooling sequences of Wood (1995) we derived virtually identical results: $0.58\,{\rm M}_\odot$ and $0.57\,{\rm M}_\odot$, respectively. However, since the HE 2209−1444 system is the result of a common envelope evolution it is not clear which envelope layer is the correct one. Using the *thin* envelope models ($\rm M_H = 0$) of Benvenuto & Althaus (1999) as the other extreme would yield slightly lower masses ($0.57\,{\rm M}_\odot$ and $0.56\,{\rm M}_\odot$, resp.). The resulting sum of masses of the HE 2209−1444 system is $1.15 \pm 0.07 M_\odot$. The error limit for the sum of masses is smaller than expected from a simple combination of the individual errors, because the mass errors of the individual components are partially anti-correlated.

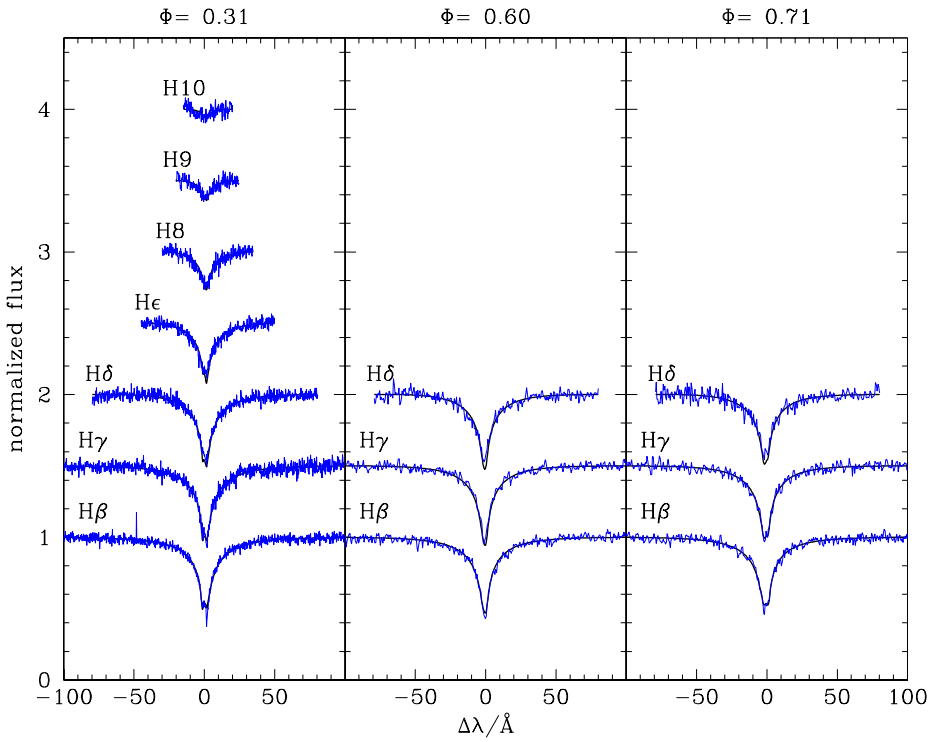

Figure 5.9: Sample Model atmosphere fits of HE 2209−1444 phase spectra taken at different phases: The discovery spectrum ($\Phi = 0.31$) taken with the UVES spectrograph and two TWIN spectra ($\Phi = 0.60$ and $\Phi = 0.71$).

System composition

The separation between both white dwarfs is quite small, only $1.87 R_{\odot}$. Thus HE 2209−1444 obviously underwent phases of strong binary interaction in its history. From the size of the orbits and the period the orbital velocity can be computed to be 171 km/s. The comparison with the observed RV amplitudes allows us to determine the inclination of this system as $i = 40°$. This system will merge within 5 Gyrs due to gravitational wave radiation. Although the merging time of HE 2209−1444 is less than a Hubble time, the system's total mass of $1.15\,M_{\odot}$ will not qualify it for being a SN Ia precursor. Nevertheless, the critical mass limit was missed by about 10 % only, and thus HE 2209−1444 is close to the region where such progenitors are expected.

For a more detailed discussion of HE 2209−1444 we refer to the paper of Karl et al. 2003.

5.2.2 WD 0453−295, a system in need of an additional spectral analysis

α_{2000}= 04:55:35.98, δ_{2000}= −29:29:01.3, V = 15.12

History

Being classified in the McCook & Sion catalogue to be a DAB white dwarf, WD 0453−295 entered our SPY project. This classification implies that HeI lines are present in the spectrum in addition to the Balmer lines. The survey spectra were taken in October and December 2001 reveal two Hα line cores as well as HeI at 4471 Å. Moreover, it became obvious that the Hα line cores changed position from one exposure to the next (cf. figure 5.10). For this reason, we

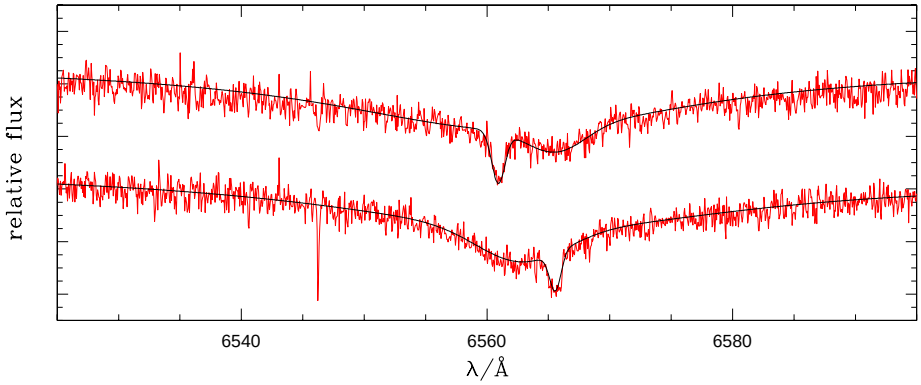

Figure 5.10: Observed line profiles for WD 0453−295 and fitted curves. The change of the line positions is obvious.

classify the system to be a binary composed of a DA white dwarf with a DB companion rather than a DAB star, a scenario already suggested by Bergeron et al. (2002). However, no period was known so far for WD 0453−295 and thus we carried out follow-up observations in order to solve the system's ephemeris. In addition to the survey spectra, three medium-resolution spectra were taken during the September 2002 run at the NTT, and 16 high-resolution spectra at the VLT in November 2002.

Radial velocity curve

In order to measure radial velocities we performed a simultaneous fit of both Hα line profiles within the ESO-MIDAS context. The HeI line was excluded from the radial velocity determination due to its broad line profile. Sample fits can be seen from figure 5.10. It becomes obvious from the spectra, that the Hα line profiles of both components are very different in terms of line-depth and width. Therefore, a simple "by eye" classification was sufficient to allocate the observed line profiles to the individual components.

As we did the cases of the former double-lined systems, we fitted in the first instance the radial velocity sets of both components independently. The resulting power spectra are very similar, both yielding the same period of 0.355918^{d} ($8^{\mathrm{h}}32^{\mathrm{m}}31^{\mathrm{s}}$). Combining these power spectra we obtained the *combined power spectrum* of figure 5.11, representing the complete binary system. Although an alias at 0.361162^{d} that cannot ruled out, which differs by only 7^{m} from

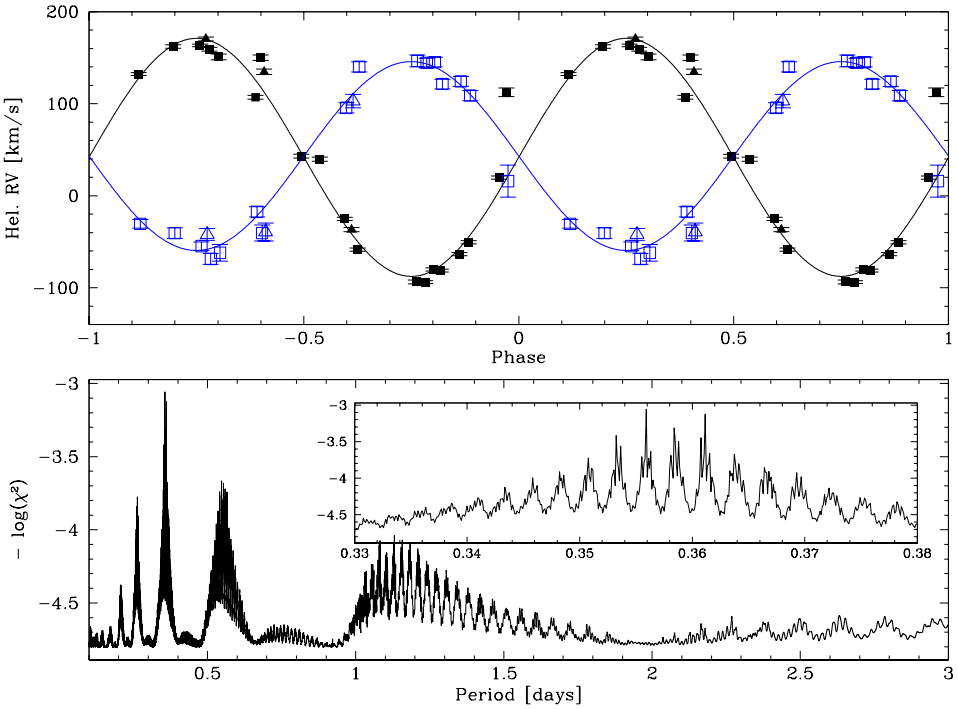

Figure 5.11: Best fit RV curve and power spectrum for WD 0453−295. Upper panel: Measured RVs of both components of WD 0453−295 as a function of orbital phase and fitted sine curves. Data points belonging to the DA white dwarf are marked as filled symbols while open symbols indicates DAB-related data. Squares are used for VLT observations and triangles for observations done at the ESO NTT. Lower panel: Combined power spectrum of WD 0453−295. The inset displays the aliases near the main peak.

the main peak. This, however, is less than the typical exposure time even for VLT data and is therefore insignificant from the discussion that follows. From the fit RV curve based on the DA's data set we derive a system's velocity of $\gamma_{\mathrm{DA}} = 41.7 \pm 0.4\,\mathrm{km\,s^{-1}}$ and a semi-amplitude of $K_{\mathrm{DA}} = 129.3 \pm 0.6\,\mathrm{km\,s^{-1}}$(cf. upper panel of figure 5.11). The ephemeris for the DA is

$$HJD(T_0)_{\mathrm{DA}} = 2\,453\,100.108561 \pm 0.355918 \times E. \tag{5.13}$$

Corresponding results for the DAB are $\gamma_{\mathrm{DAB}} = 43.2 \pm 1.4\,\mathrm{km\,s^{-1}}$ and $K_{\mathrm{DAB}} = 102.6 \pm 1.7\,\mathrm{km\,s^{-1}}$, respectively. Its ephemeris is

$$HJD(T_0)_{\mathrm{DAB}} = 2\,453\,099.929366 \pm 0.355918 \times E. \tag{5.14}$$

Both ephemerides differ by 0.179195^{d} corresponding to $\Delta\Phi = 0.503$, which as in almost perfect agreement with expectations.

System composition

The mass ratio computed from the the RV semi-amplitudes is $M_{\mathrm{DAB}}/M_{\mathrm{DA}} = 1.26 \pm 0.02$. Due to the fact that $\Delta\gamma$ is equal to zero within the error margin ($\Delta\gamma = 1.5 \pm 1.5\,\mathrm{km\,s^{-1}}$), however, an analysis by means of the RV curves only is not possible for WD 0453−295. Thus

we have to perform a quantitative spectral analysis by means of the FITSB2 program in order to determine masses by comparison of the derived stellar parameters $T_{\rm eff}$ and log g with evolutionary calculations (cf. section 4.3). This, however, is much more difficult than for HE 2209−1444 (section 5.2.1) because the components are so dissimilar. This is beyond the scope of this thesis and has still to be done.

If we adopt $\Delta\gamma = 1.5\,\mathrm{km\,s^{-1}}$the resulting masses are very low, i.e. $0.16\,\mathrm{M_\odot}$ and $0.20\,\mathrm{M_\odot}$ respectively, and can be ruled out because the corresponding $\sin i$ (according to equation 5.4) would need to be larger than unity. Even if we assume the largest $\Delta\gamma$ the resulting total mass ($1.16\,\mathrm{M_\odot}$) is below the Chandrasekhar mass (table 5.5). Despite of the merging time being lower than the Hubble, the system does not qualify as a SN Ia progenitor candidate.

Therefore, we conclude that the derived parameters, in particular $\Delta\,\gamma$, are not defined accurately enough. As in the case of HE 2209−1444 we would need an additional spectral analysis to solve the system definitely.

Table 5.5: System parameters and derived results for WD 0453−295. The input parameters mass-ratio and $\Delta\gamma$ are varied by multiples of their error margins. The assumed combination of the proper parameters are displayed in the columns one and two, whereas derivated output parameters are shown in columns three to seven.

Determined from RV curve				
$\Delta\gamma/\mathrm{km\,s^{-1}}$	1.5	3.0	4.5	6.0
$M_{\rm prim}/M_{\rm sec}$	1.26	1.24	1.22	1.20
P/d		0.355 918		
Deduced parameters				
$M_{\rm DAB}/\mathrm{M_\odot}$	0.20	0.33	0.45	0.55
$M_{\rm DA}/\mathrm{M_\odot}$	0.16	0.27	0.37	0.46
$A_{\rm tot}/\mathrm{R_\odot}$	1.5	1.8	2.0	2.1
i/deg	—	65	54	48
$M_{\rm tot}/\mathrm{M_\odot}$	0.36	0.60	0.82	1.01
$t_{\rm m}/\mathrm{Gyrs}$	70	29	17	12
SN Ia precursor	no	no	no	no

— : Equation 5.4 runs to $sin\,i > 0$.

Chapter 6

White dwarfs with M dwarf companions

The main intention of SPY is the search for potential SN Ia precursors by means of checking double degenerates. Obviously, binaries composed of a white dwarf and a M dwarf are not double degenerate and thus do not qualify as SN Ia progenitors. Nevertheless, these objects are interesting with respect to the study of binary evolution. Therefore, we observed three WD + dM systems in the course of the follow-up campaigns in order to create an unbiased sample of white dwarfs in binary systems.

A sample spectrum of a white dwarf plus M dwarf binary can be seen from figure 6.1.

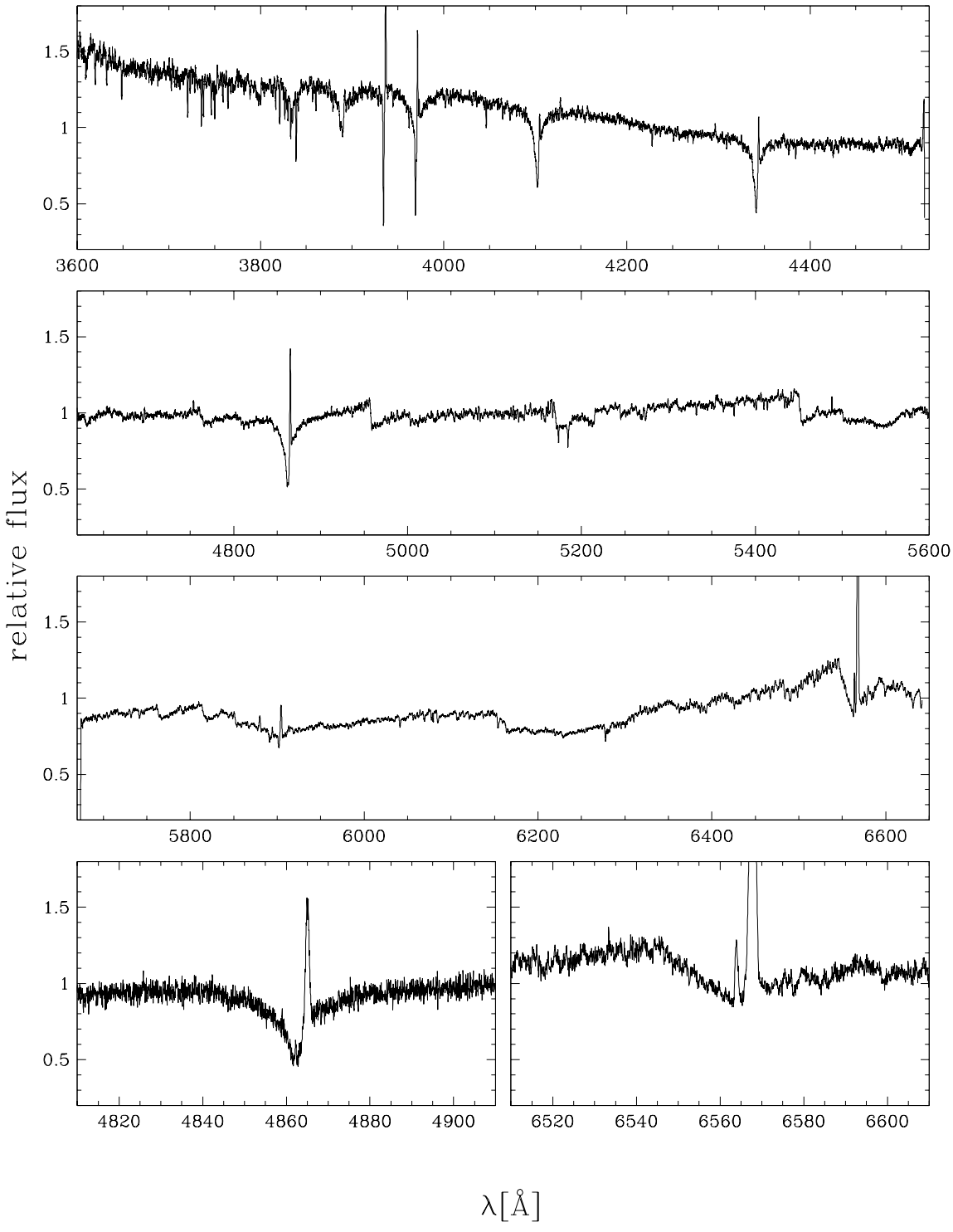

Figure 6.1: Sample UVES spectrum of the white dwarf plus M dwarf system (WD 0419−487, see section 6.1.1). The weaker, blue shifted emission that can be seen in Hα and Hβ is due to a non-LTE effect in the DA's photosphere.

6.1.1 WD 0419−487 alias RR Caeli

α_{2000}= 04:21:05.59, δ_{2000}= −48:39:07.2, V = 14.36

History

Classified as a DA8 white dwarf in the McCook & Sion Catalogue (1999), WD 0419−487 was implemented within our SPY project and observed twice in November 2000 in the course of the SPY project. However, molecular absorption bands and two emission lines in the Balmer series becomes obvious from these survey spectra, as can be seen in figure 6.1. According to the spectral appearance of WD 0419−487, the system has to be classified as a hot DA white dwarf and a M dwarf companion. This classification is consistent with a previous study done by Bruch et al. (1998). Follow-up observations for WD 0419−487, were done in February 2003 at the ESO NTT and in March 2003 at the ESO VLT.

Radial velocity curve

Some spectra lack the weaker DA emission feature seen in figure 6.1 because of low S/N ratios and/or low resolution of the spectra. From the Hα emission lines, however, we were able to determine radial velocities for both components for all but one VLT and for three NTT observations (see figure 5.1).

The analysis was carried out the same way as for HE 0315−0118 (cf. section 5.1.2). By fitting the radial velocities of the DA *primary* and the dM *secondary* independently, we computed a single power spectrum for each component. We finally merge both data sets by coadding the χ^2 values derived from the *individual power spectra*. By means of the *combined power spectrum* produced this way, (cf. lower panel of figure 6.2) we determined a period of 0.303816^{d} ($7^{\mathrm{h}}17^{\mathrm{m}}30^{\mathrm{s}}$). The inset displays the region around the main peak in more detail, revealing some aliases. While we can not rule out any alias by visual inspection of the proper RV curve, however, all of them are within a time interval of less than 30 seconds. For the white dwarf we finally derive a system's velocity of $\gamma_{\mathrm{WD}} = 99.2 \pm 0.6\,\mathrm{km\,s^{-1}}$ and a radial velocity semi-amplitude of $K_{\mathrm{WD}} = 70.7 \pm 0.7\,\mathrm{km\,s^{-1}}$. The ephemeris is

$$HJD(T_0)_{\mathrm{WD}} = 2\,453\,099.869533 \pm 0.303816 \times E.$$

The corresponding results for the dM are $\gamma_{\mathrm{dM}} = 79.4 \pm 0.1\,\mathrm{km\,s^{-1}}$, $K_{\mathrm{dM}} = 189.9 \pm 0.2\,\mathrm{km\,s^{-1}}$ and

$$HJD(T_0)_{\mathrm{dM}} = 2\,453\,100.022449 \pm 0.303816 \times E.$$

Both ephemerides differ by 0.152916^{d}, corresponding to $\Delta\Phi = 0.503$, which is in almost perfect conformance with theory.

System composition

According to the RV curves, we found the mass ratio to be $M_{\mathrm{WD}}/M_{\mathrm{dM}} = 2.69 \pm 0.03$ while the system velocities differs by $\Delta\gamma = 24.8 \pm 0.6\,\mathrm{km\,s^{-1}}$. However, the gravitational redshift of the M dwarf companion can be neglected compared to the redshift caused by the white dwarf. Therefore, equation 4.4 and the mass-radius relation yield $M_{\mathrm{WD}} = 0.56\,\mathrm{M}_\odot$. The companions mass of $M_{\mathrm{dM}} = 0.21\,\mathrm{M}_\odot$ results from the mass ratio. Thus, the companion is most likely a M5

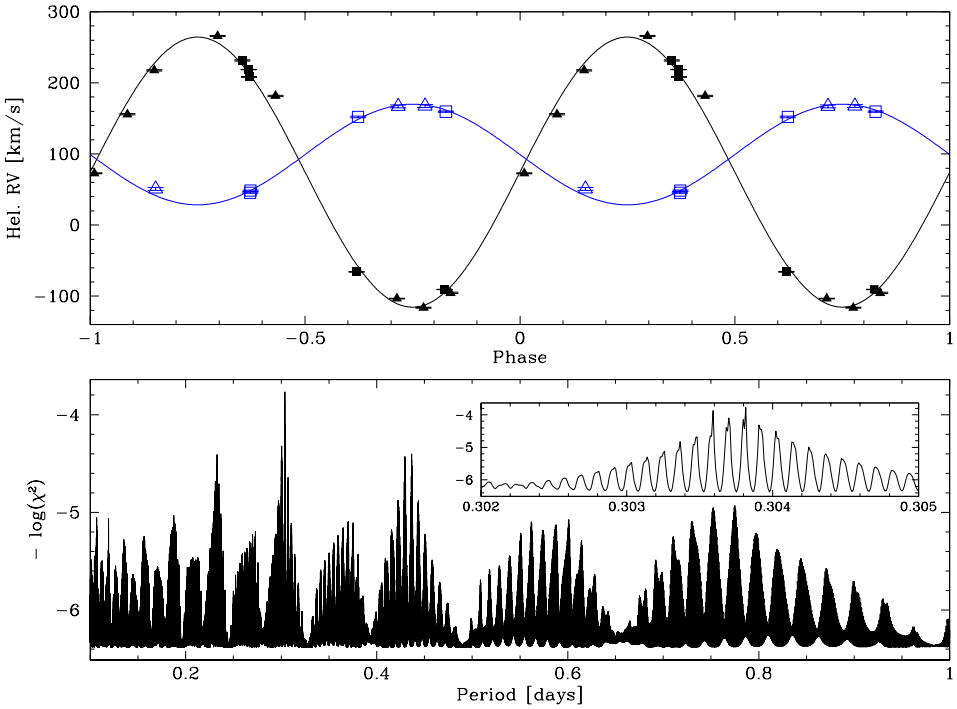

Figure 6.2: Best fit RV curve and power spectrum for WD 0419−487. Upper panel: Measured radial velocities of both components of WD 0419−487 as a function of orbital phase and fitted sine curves. Data points belonging to the M dwarf are marked as filled symbols while open symbols indicates DA-related data. Like within the previous figures, squares are used for VLT observations and triangles for observations from the ESO NTT. Lower panel: Combined power spectrum of WD 0419−487. The inset displays some of the aliases near the main peak.

dwarf (see Drilling et al. 2000). Both components of the WD 0419−487 system are separated by $A_{\rm tot} = 1.8\,{\rm R}_\odot$ which means the white dwarf is at $A_{\rm WD} = 0.5\,{\rm R}_\odot$ from the barycenter and the M dwarf at $A_{\rm dM} = 1.3\,{\rm R}_\odot$. From the orbital velocities of $v_{\rm WD} = 78\,{\rm km\,s^{-1}}$ and $v_{\rm dM} = 211\,{\rm km\,s^{-1}}$ we compute an inclination of $i = 64^{\rm o}$. Due to the radiation of gravitational redshift, both

Table 6.1: System composition for WD 0419−487.

Determined from RV curve					
$\Delta\gamma/{\rm km\,s^{-1}}$	24.8	25.4	25.4	24.2	24.2
$M_{\rm DA}/M_{\rm dM}$	2.69	2.66	2.72	2.66	2.72
$P/{\rm d}$	0.308 816				
Deduced parameters					
$M_{\rm WD}/{\rm M}_\odot$	0.56	0.66	0.66	0.65	0.52
$M_{\rm dM}/{\rm M}_\odot$	0.21	0.25	0.25	0.24	0.19
$A_{\rm tot}/{\rm R}_\odot$	1.8	1.9	1.9	1.8	1.7
$i/{\rm deg}$	64	59	59	59	67

components will merge in $t_{\rm m} = 16\,$Gyrs, but WD 0419−487 will not produce a SN Ia event (because the the dM is not degenerate). This would be a single degenerate scenario.

Comparison with previous results

The period of $0.303816^{\rm d}$ estimated above is in almost perfect agreement with the period of $0.303695^{\rm d}$ derived by Bruch et al. (1998) by means of a light-curve analysis. However, their analysis yields $0.365\,{\rm M}_\odot$ and $0.089\,{\rm M}_\odot$ for the white dwarf and the M dwarf respectively ($M_{\rm WD}/M_{\rm dM} = 4.1$), which can definitely be ruled out by our own analysis.

6.1.2 WD 1013−050

α_{2000}= 10:16:28.76, δ_{2000}= −05:20:33.5, V = 14.30

History

The McCook & Sion (1999) catalogue classified WD 1013−050 as a DAO white dwarf. Vennes et al. (1999), however, found the DAO being only one component of a quadruple system composed of a wide double-binary. In the course of the SPY project, the DAO was observed twice at the VLT in October and November 2000. From these high-resolution spectra, emission features become obvious in the Balmer series and for He I and C II lines (see figure 6.3). The Balmer line emission belongs to the M dwarf companion as do the emission lines which becomes obvious from radial velocity measurements. We also found variation of the line strengths. For instance, the Hα emission feature has $W_\lambda \approx 6.3$Å at $\Phi = 0.39$, while at $\Phi = 0.82$ the line strength is $W_\lambda \approx 2.2$Å only. In a system with gravitational bound rotation, this can be understood if the dM's hemisphere facing toward the white dwarf is heated by the hotter DAO companion. We conclude, that this is the most probable scenario for WD 1013−050.

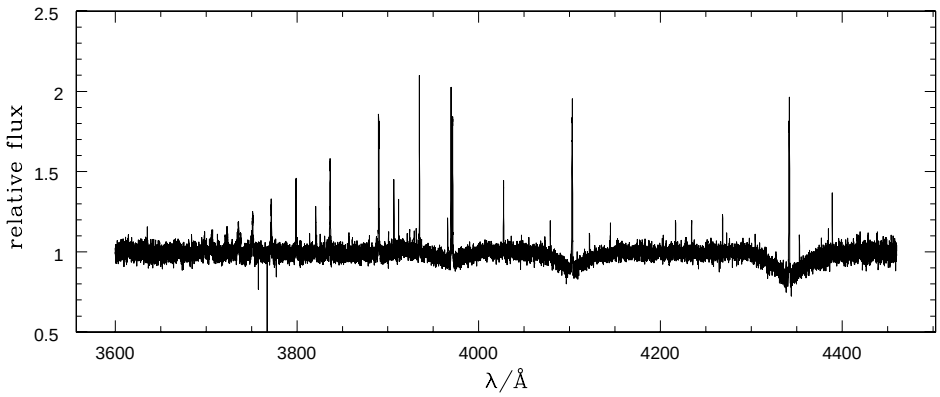

Figure 6.3: UVES spectrum of WD 1013−050, taken at $\Phi = 0.39$. The DAO absorption spectrum is overlayed by the dM's emission lines.

Vennes et al. (1999) already found the Hα emission profile to be split. We detect the same feature for the entire Balmer series as well as for some of the stronger He I lines like 4471 Å. Figure 6.4 shows Hα and Hβ emission for example. The physical reason is most probably a self-absorption effect in the dM's heated atmosphere.

WD 1013−050 was also observed during the January 2004 NTT run.

Radial velocity curve

From the observed emission lines we estimated a set of radial velocities for the dM companion. From the power spectrum calculated by means of this data set we obtain 0.791419^{d} ($18^{\mathrm{h}}59^{\mathrm{m}}39^{\mathrm{s}}$) for the most probable period. Though our result is already close to the period given by Vennes et al. ($\Delta \mathrm{P} = 3^{\mathrm{m}}5^{\mathrm{s}}$), we can improve our analysis if we merge Vennes' data set with our own. This way, the period becomes more accurate: 0.789279^{d} or $18^{\mathrm{h}}56^{\mathrm{m}}34^{\mathrm{s}}$. The ephemeris is

$$HJD(T_0)_{\mathrm{dM}} = 2\,453\,099.746827 \pm 0.789279 \times E. \tag{6.1}$$

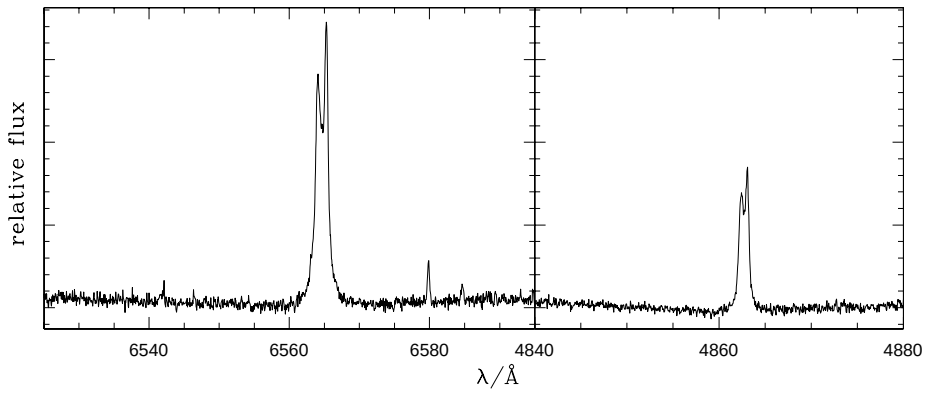

Figure 6.4: UVES spectrum of WD 1013−050 taken at $\Phi = 0.39$. The splitted emission feature in Hα (right) and Hβ (left) is most probably due to self-absorption in the dM's atmosphere.

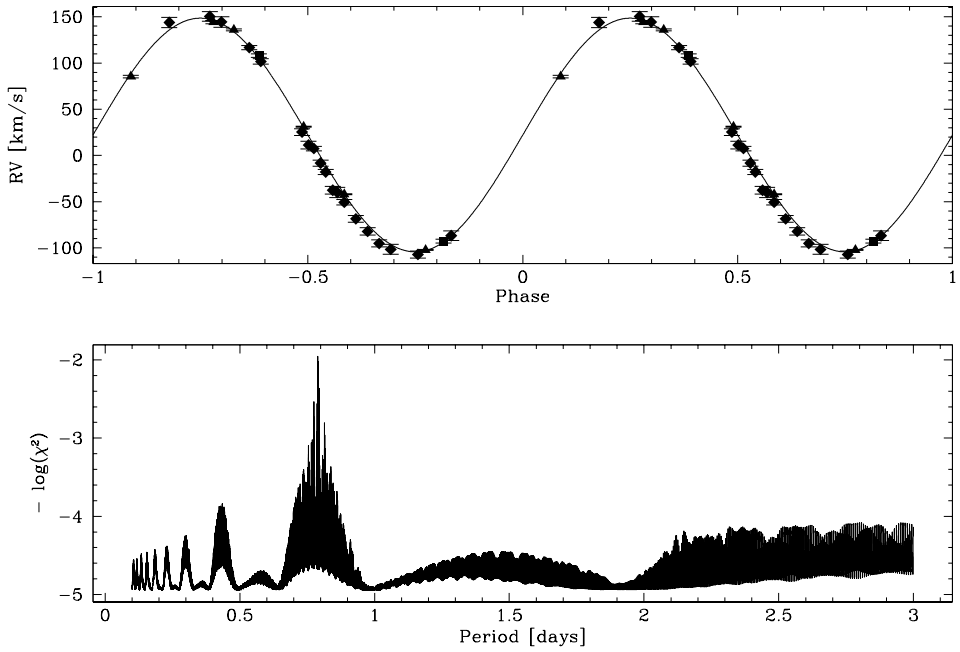

Figure 6.5: Best fit RV curve and power spectrum for WD 1013−050. Upper panel: Measured radial velocities of WD 1013−050 as a function of orbital phase and fitted sine curves. Squares are used for VLT observations, triangles for observations from the ESO NTT and diamonds for data taken from Vennes et al. (1999). Lower panel: Power spectrum of WD 1013−050.

Over a course of 10 years, this ephemeris differs from Vennes' result by less than $0.0001 \times P$. The systems velocity derived from the best fit RV curve (upper panel of figure 6.5) is $\gamma_{\rm dM} = 22.2 \pm 0.4\,{\rm km\,s^{-1}}$ and the radial velocity semi-amplitude is $K_{\rm dM} = 126.4 \pm 0.4\,{\rm km\,s^{-1}}$.

System composition

Vennes et al. (1999) derived a white dwarf with a mass of $0.55\,M_\odot \leq M_{\rm DAO} \leq 0.67\,M_\odot$ and a M5 red dwarf companion of $0.15\,M_\odot$. They found the system's inclination to be $55^\circ \leq i \leq 65^\circ$. For more details on the dM/DAO binary we refer to Vennes et al. (1999). They also give a short discussion about the second binary of the WD 1013−050 quadruple system.

6.1.3 HS 1606+0153

α_{2000}= 16:08:55.22, δ_{2000}= +01:45:48.6, V = 15.00

History

This object was classified as a white dwarf from the Hamburg/Quasar survey. Thus it entered our SPY project and was observed twice at the VLT. From the UVES spectra taken in July 2001, however, strong emission lines superposing the Hα and Hβ lines became evident. Thus, we re-classified HS 1606+0153 to be a white dwarf plus M dwarf binary. Moreover, a radial velocity shift of about 290 km s^{-1}was measured from the survey spectra. Thus, the system was re-observed in the course of our follow-up campaigns in August 2002 at the DSAZ and in March 2003 at the VLT.

Radial velocity curve

By means of fitting the emission feature of the M dwarf, we obtained very accurate radial velocity measurements. Figure 6.6 shows the resulting power spectrum and the best fit RV curve. We derive a most probable period of 2.184164$^{\rm d}$ ($2^{\rm d}4^{\rm h}25^{\rm m}12^{\rm s}$), a system's velocity of $\gamma = -30.8 \pm 2.0\,{\rm km\,s^{-1}}$ and a semi-amplitude of $K = 219.6 \pm 3.7\,{\rm km\,s^{-1}}$ for the M dwarf. Its ephemeris becomes

$$HJD(T_0) = 2\,453\,100.019317 \pm 2.184164 \times E. \tag{6.2}$$

System composition

Although the RV curve looks normal at first glance, we derive a very large mass function of $f_{\rm m} = 2.4\,{\rm M_\odot}$. Following Drilling et al. (2000), we assume a M5 dwarf with a canonical mass of 0.21 M$_\odot$for the visible component. Thus we derive the minimum mass of the companion for an inclination of $i = 90^{\rm o}$ to be $M_{\rm comp} = 2.77{\rm M_\odot}$. Even if we adopt the lowest possible mass of 0.08 M$_\odot$ for the M dwarf, the companion's mass is still 2.55 M$_\odot$. A companion as massive as that has to be either a main sequence star, a neutron star or a black hole. These objects, however, are inconsistent with the spectral appearance of HS 1606+0153, indicating that the companion is a white dwarf, as can be seen from figure 6.7.

The inconsistency of mass function and spectral appearance is caused by the large value of $f_{\rm m}$. We therefore conclude, that either the period or the radial velocity semi-amplitude are falsely determined. There are still more observations necessary to solve HS 1606+0153.

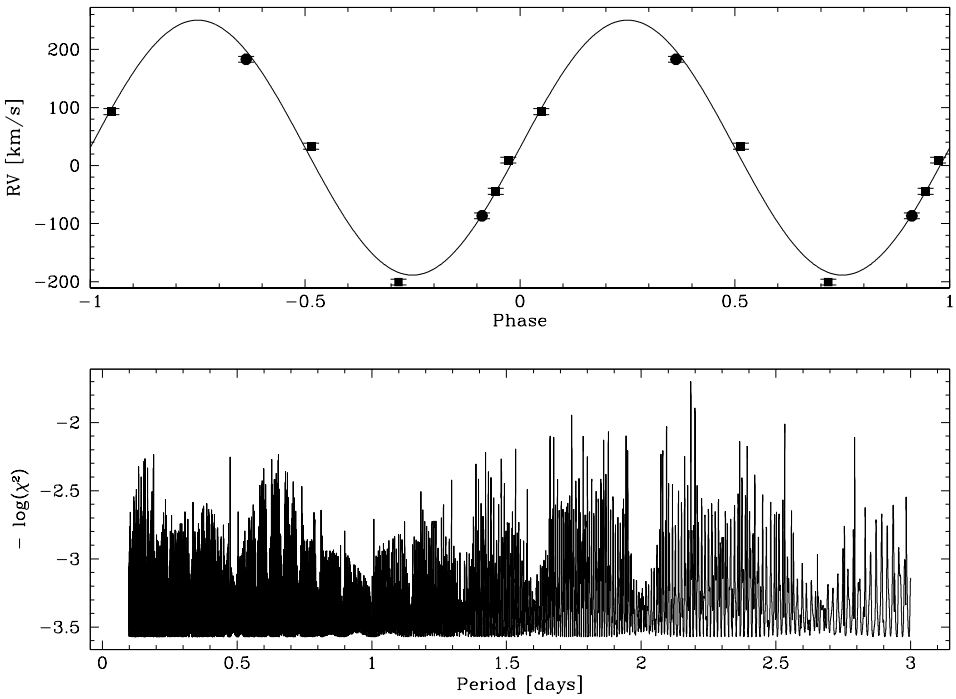

Figure 6.6: Best fit RV curve and power spectrum for HS 1606+0153. Upper part: Measured RVs as a function of orbital phase and fitted sine curve. Squares are used for VLT observations and circles for observations done at the 3.5/,m telescope of the DSAZ. Lower part: Power spectrum of HS 1606+0153.

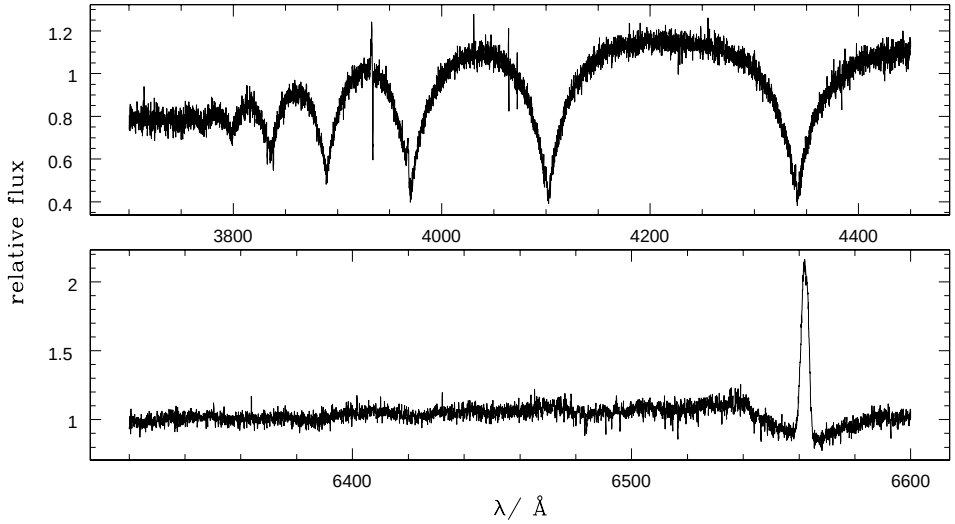

Figure 6.7: Observed line profiles of HS 1606+0153. The displayed wavelength regions are extracted from a UVES spectrum taken in March the 21th 2003. The dM's emission line superposing the Hα profile is obvious, as well as the higher Balmer lines of the white dwarf companion.

Table 6.2: Scenarios for HS 1606+0153. Note that the nature of the companion is inconsistent with the spectral appearance of HS 1606+0153, which suggested a white dwarf companion.

Scenario	i [deg]	$M_{\rm vis}$ [$M_\odot$]	$M_{\rm invis}$ [$M_\odot$]	$M_{\rm tot}$ [$M_\odot$]	$t_{\rm m}$ [Gyrs]	SN Ia - prec.	nature of companion
max. i & $M_{\rm vis} = 0.21\,{\rm M}_\odot$	90	0.21	2.77	2.98	950	no	MS, NS or BH
most likely i & $M_{\rm vis} = 0.21\,{\rm M}_\odot$	52	0.21	5.19	5.40	620	no	MS, or BH
max. i & $M_{\rm vis} = 0.08\,{\rm M}_\odot$	90	0.08	2.55	2.63	2 600	no	MS, NS or BH
most likely i & $M_{\rm vis} = 0.08\,{\rm M}_\odot$	52	0.08	5.05	5.13	1 640	no	MS or BH

6.1.4 HE 2147−1405

α_{2000}= 21:50:03.69, δ_{2000}= −13:51:45.9, V = 15.94

History

HE 2147−1405 was selected from the Hamburg/ESO survey by Norbert Christlieb to be a white dwarf and thus entered our SPY project. The survey spectra of HE 2147−1405 taken in August 2001, however, reveal not only the Balmer series, but also emission features that are characteristic for a M dwarf companion. Not being a double degenerate system, HE 2147−1405 was nevertheless re-observed in the course of our follow-up campaigns because of a large radial velocity shift of more than 140 km s^{-1} evaluated from the the survey spectra. Since the strong emission line of the M dwarf can be easily fitted within the MIDAS context, the DSAZ data taken in August 2002 result in very accurate radial velocities.

Radial velocity curve

Our analysis yields an unequivocal period of $P = 1.500483^{\mathrm{d}}$ or $1^{\mathrm{d}}12^{\mathrm{h}}0^{\mathrm{m}}41^{\mathrm{s}}$. From the best fit RV curve displayed in the upper panel of figure 6.8, a system's velocity of $\gamma = 6.6 \pm 0.2$km s^{-1} and a semi-amplitude of $K = 94.2 \pm 0.2$ km s^{-1} can be derived. The system's ephemeris is

$$HJD(T_0) = 2\,453\,100.136000 \pm 1.500483 \times E. \tag{6.3}$$

System composition

We have no information about the motion of the white dwarf but about the M dwarf companion only. To estimate the white dwarf's mass from the mass function ($f_{\mathrm{m}} = 0.13$ M$_\odot$), we assume the M dwarf to be of spectral type M5 with a mass of 0.21 M$_\odot$ (Drilling et al. 2000). The maximum inclination of $i = 90^{\mathrm{o}}$ yield to the white dwarf's minimum mass of $M_{\mathrm{WD}} = 0.34$ M$_\odot$. Orbits and orbital velocities can be computed from equations 5.2 and to be $A_{\mathrm{dM}} = 2.8$ R$_\odot$ and $v_{\mathrm{dM}} = K = 94$ km s^{-1} respectively. Corresponding results for the white dwarf are $A_{\mathrm{WD}} = 1.7$ R$_\odot$ and $v_{\mathrm{dM}} = 58$ km s^{-1}. Therefore, the total separation of the stars according to this scenario is $A_{\mathrm{tot}} = 4.5$ R$_\odot$.

For the most probable inclination of $i = 52^{\mathrm{o}}$, however, we derive $M_{\mathrm{WD}} = 0.52$ M$_\odot$ for the white dwarf. The orbits are $A_{\mathrm{WD}} = 1.4$ R$_\odot$ and $A_{\mathrm{dM}} = 3.5$ R$_\odot$ respectively. Orbital velocities of $v_{\mathrm{WD}} = 48$ km s^{-1} and $v_{\mathrm{dM}} = 120$ km s^{-1}. Therefore, the system's separation becomes $A_{\mathrm{tot}} = 5.0$ R$_\odot$.

We conclude, that the white dwarf in the HE 2147−1405 system is most probably a DA white dwarf with a C/O core. Table 6.3

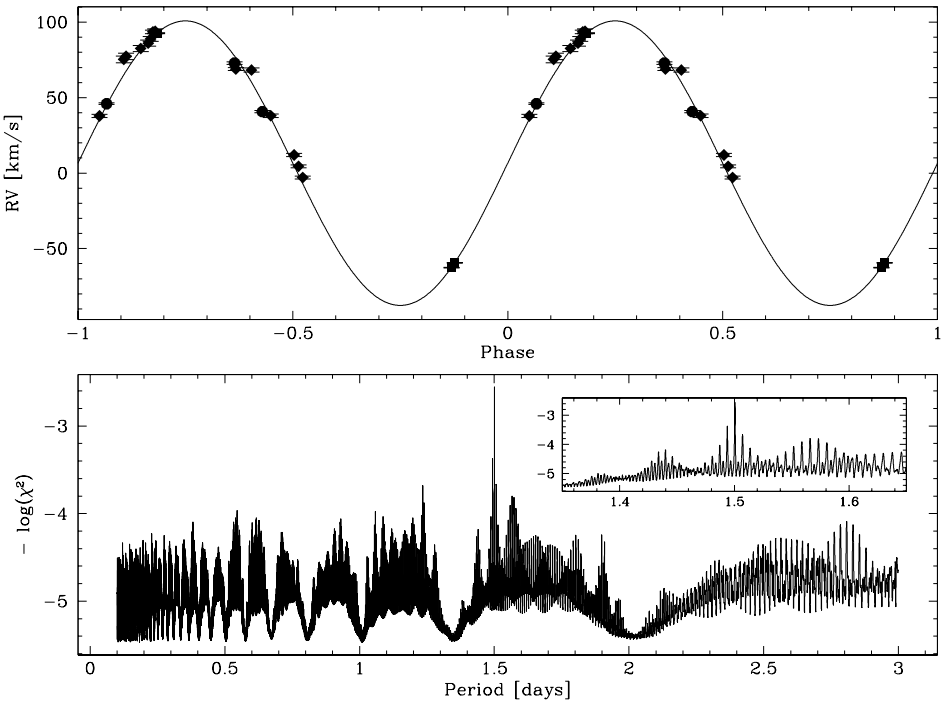

Figure 6.8: Best fit RV curve and power spectrum for HE 2147−1405. Upper panel: Measured radial velocities of HE 2147−1405 a function of orbital phase and fitted sine curves. Squares are used for VLT observations and circles for data based on DSAZ observations. Diamonds mark radial velocity data provided by Gijs Nelemans. Lower panel: Power spectrum of HE 2147−1405.

Table 6.3: Scenarios for HE 2147−1405.

Scenario	i [deg]	$M_{\rm vis}$ [$M_\odot$]	$M_{\rm invis}$ [$M_\odot$]	$M_{\rm tot}$ [$M_\odot$]	$t_{\rm m}$ [Gyrs]	SN Ia-prec.	nature of companion
max. i	90	0.21	0.34	0.55	1 620	no	low mass WD
most likely i	52	0.21	0.52	0.73	1 170	no	C/O core WD
$M_{\rm invis} \approx M_{\rm Chandra}$	≈30	0.21	≈1.40	≈1.61	≈560	no	most massive WD

Chapter 7

Single-lined systems

Most of our objects are single-lined rather than double-lined systems. Thus, only the system's mass function (equation 4.2) can be derived. This, however, is an equation of three unknown parameters. Without additional information to set further constrains on the systems we cannot solve for them.

Nevertheless, by assuming that the observable component has a canonical mass we can decrease the number of free parameters by one. Thus we estimate a white dwarf's mass by means of comparing its stellar parameters $T_{\rm eff}$ and $\log g$ with evolutionary calculations by Blöcker et al. (1997, cf. figure 4.4). For sdBs and sdOs we assume canonical masses of 0.47 $M_{\odot}$. The last free parameter can be eliminated by means of fixing the system's inclination. The statistically most probable inclination angle is $i = 52^{\circ}$, which yields the most probable mass for the invisible component. A lower limit for the component's mass, however, can be derived by assuming the maximum inclination value of $i = 90^{\circ}$. The complete sequence of analyzing a single-lined system is displayed in figure 7.1 in a schematic way.

In section 7.1 we discuss radial velocity variable single-lined systems with a white dwarf primary. Systems with an sdO primary are discussed in section 7.3, whereas sdB systems are discussed in section 7.2.

7.1 White dwarf primaries

A typical UVES spectrum of a hydrogen rich DA white dwarf can be seen from figure 1.4. Most of the DA white dwarfs presented in the following chapter are already analyzed by Detlev Koester by means of a quantitative spectral analysis (Koester et al. 2001 and priv. com.) of the SPY spectra. For these objects, we estimated masses of the visible components by comparison of the determined stellar parameters $T_{\rm eff}$ and $\log g$ with cooling sequences of white dwarfs (Blöcker et al. 1997, cf. section 4.4).

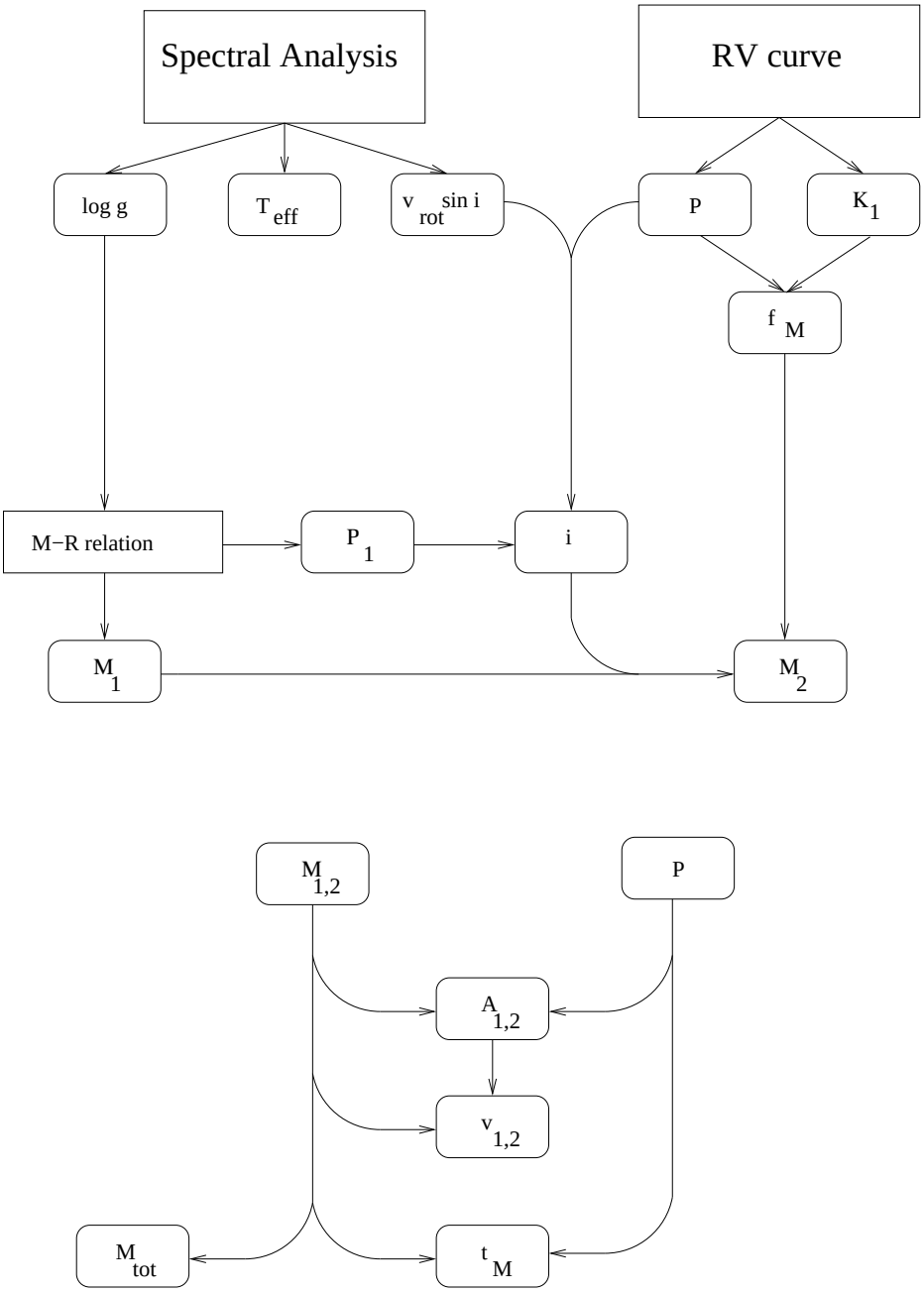

Figure 7.1: Analysis of a single-lined system (schematic).

7.1.1 WD 0326−273

α_{2000}= 03:28:48.81, δ_{2000}= −27:19:01.7, V = 14.0

History

Being classified as a DA5 white dwarf in the McCook & Sion catalogue (1999), WD 0326−273 was observed twice in July 2002 at the VLT. A shift of 180 km s^{-1} was found from the Hα line profiles. In order to solve the system we carried out follow-up observations at the ESO VLT in October 2001 and November 2002 and at the ESO NTT in September 2002.

Radial velocity curve

The resulting power spectrum, displayed in the lower panel of figure 7.2, shows an unambiguous period of 1.875514$^{\rm d}$ ($1^{\rm d}21^{\rm h}0^{\rm m}44^{\rm s}$), while the upper panel of the figure shows the best fit RV curve computed for this period. We derive a system's velocity of $\gamma = 69.0 \pm 0.3$ km s^{-1}, a radial velocity semi-amplitude of $K = 96.3 \pm 0.4$ km s^{-1} and an ephemeris of

$$HJD(T_0) = 2\,453\,099.237222 \pm 1.875514 \times E. \tag{7.1}$$

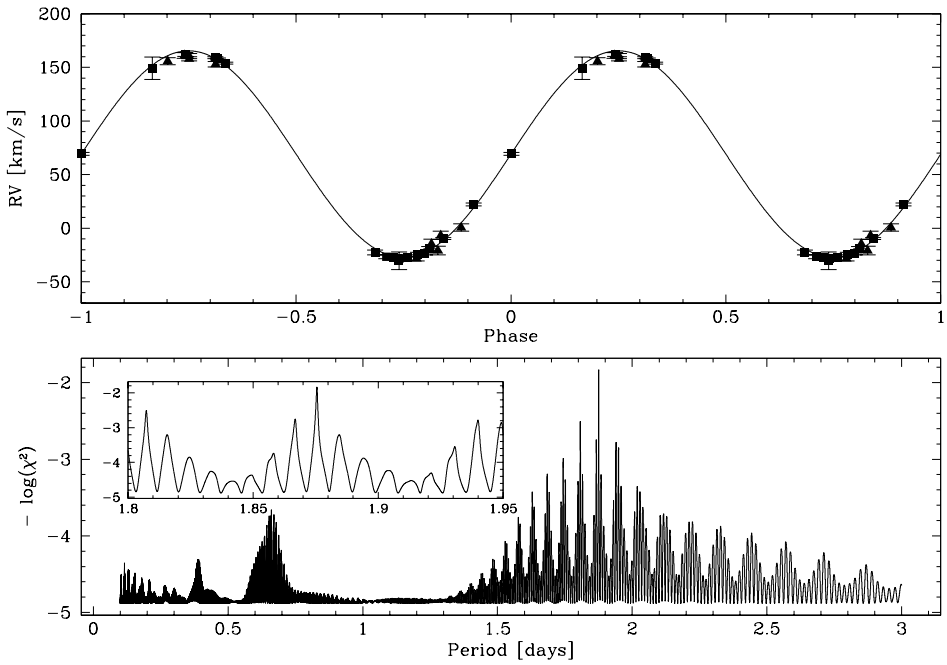

Figure 7.2: Best fit RV curve and power spectrum for WD 0326−273. Upper panel: Measured radial velocities as a function of orbital phase and fitted sine curve. Squares are used for ESO VLT observations and triangles for observations from the ESO NTT. Lower panel: Power spectrum of WD 0326−273.

Spectral analysis and mass determination

WD 0326−273 is one of the objects already analyzed by Detlev Koester in order to derive stellar parameters (cf. section 4.4). By comparison of these parameters ($T_{\rm eff} = 9384\,{\rm K}$ and $\log {\rm g} = 7.8$) with evolutionary tracks by Blöcker et al. (1997) we estimated the white dwarf's mass to be $M_{\rm WD} = 0.50\,{\rm M}_\odot$.

System composition

Assuming an inclination of $i = 90^{\rm o}$, the mass function of $f_{\rm m} = 0.174\,{\rm M}_\odot$ yields a minimum mass of $M_{\rm comp} = 0.59\ {\rm M}_\odot$ for the unseen component. The separation becomes $A_{\rm tot} = 6.6\,{\rm R}_\odot$. Based on this scenario we computed the orbits and orbital velocities by means of equations 5.2 and 6.1.4: For the visible component we derive $A_{\rm WD} = 3.6\,{\rm R}_\odot$ and $v_{\rm WD} = K = 96\,{\rm km\,s^{-1}}$, whereas the corresponding results for unseen component are $A_{\rm comp} = 3.0\,{\rm R}_\odot$ and $v_{\rm comp} = K = 81\,{\rm km\,s^{-1}}$ respectively.

However, the system's most probably inclination is $i = 52^{\rm o}$ which yields the companion's most likely mass of $M_{\rm comp} = 0.88\,{\rm M}_\odot$. The separation becomes $A_{\rm tot} = 7.1\,{\rm R}_\odot$ and the white dwarf's orbit $A_{\rm WD} = 4.5\,{\rm R}_\odot$ ($v_{\rm WD} = 122\,{\rm km\,s^{-1}}$). For the unseen companions we compute $A_{\rm comp} = 2.6\,{\rm R}_\odot$ ($v_{\rm comp} = 69\,{\rm km\,s^{-1}}$) to be most likely.

Although the unseen component is most probably a white dwarf with a C/O core, neither scenario discussed above will quality for a SN Ia precursor. In both cases, the merging time as well as the system's total mass are insufficient, as can be seen from table 7.1. The table shows in addition the inclination angles yielding a total mass equal the Chandrasekhar mass and the most massive white dwarf companion of $1.40\,{\rm M}_\odot$ respectively.

Table 7.1: Scenarios for WD 0326−237.

Scenario	i [deg]	$M_{\rm vis}$ [$M_\odot$]	$M_{\rm invis}$ [$M_\odot$]	$M_{\rm tot}$ [$M_\odot$]	$t_{\rm m}$ [Gyrs]	SN Ia-prec.	nature of companion
max. i	90	0.50	0.59	1.09	890	no	C/O core WD
most likely i	52	0.50	0.88	1.38	650	no	C/O core WD
$M_{\rm tot} \approx M_{\rm Chandra}$	≈51	0.50	≈0.90	≈1.40	≈640	no	C/O core WD
$M_{\rm invis} \approx M_{\rm Chandra}$	≈38	0.50	≈1.40	≈1.90	≈450	no	most massive WD

7.1.2 WD 1210+140

α_{2000}= 12:12:33.89, δ_{2000}= +13:46:25.1, V = 14.67

History

WD 1210+140 is classified as a DA white in the McCook & Sion catalogue (1999) and was analyzed for radial velocity variability by Maxted et al. (1999). However, they observed the system twice and found a radial velocity shift of $10\,\mathrm{km\,s^{-1}}$ only ($\Delta RV = 0$ within the error limits), therefore, they concluded the system to be non variable. We re-observed the system in the course of our SPY program to check this result. Two survey observations were done in January 2003 at the VLT, given a much larger radial velocity shift of $140\,\mathrm{km\,s^{-1}}$. Follow up observation from the NTT run in April and May 2003 provided a data set accurate enough for a radial velocity analysis.

Radial velocity curve

The power spectrum displayed in figure 7.3 is not unequivocal since a large number of aliases can not be ruled out (see inset of figure 7.3). These aliases are concentrated in a time interval of $\approx 29^{\mathrm{m}}$, centered on the main peak. However, for our purposes a perfect determination of the period is desirable, but not necessary. Using the highest peak of the power spectrum we derive the most probable period 0.631691^{d} ($9^{\mathrm{h}}24^{\mathrm{m}}38\mathrm{s}$). The system parameters derived from the best fit RV curve are $\gamma = -0.4 \pm 2.7\,\mathrm{km\,s^{-1}}$ for the system's velocity and $K = 144.6 \pm 4.1\,\mathrm{km\,s^{-1}}$ for the radial velocity semi-amplitude. The ephemeris of WD 1210+140 is

$$HJD(T_0) = 2\,453\,099.913719 \pm 0.631691 \times E. \tag{7.2}$$

Spectral analysis and mass determination

Ralf Napiwotzki (priv.com.) determined the stellar atmospheric parameters of WD 1210+140 to be T_{eff} =32 340 K and $\log g = 6.97$. Thus, we estimated a mass of $M_{\mathrm{WD}} = 0.37\,\mathrm{M_\odot}$ by means of the Blöcker evolutionary tracks (cf. figure 4.4).

System composition

The mass function computed from these parameters is $f_{\mathrm{m}} = 0.198\,\mathrm{M_\odot}$. Using the mass we estimated above for the visible companion, we derive the minimum mass of the unseen companion to be $M_{\mathrm{comp}} = 0.55\,\mathrm{M_\odot}$ for $i = 90^{\mathrm{o}}$. The companion is therefore most likely a late type main sequence star. The separation of the two components becomes $A_{\mathrm{tot}} = 3.0\,\mathrm{R_\odot}$ which yields the orbits of the components: For the white dwarf we compute $A_{\mathrm{WD}} = 1.8\,\mathrm{R_\odot}$ and for the unseen component $A_{\mathrm{comp}} = 1.2\,\mathrm{R_\odot}$. The orbital velocities determined by means of equation 6.1.4 are $v_{\mathrm{WD}} = K = 145\,\mathrm{km\,s^{-1}}$ and $v_{\mathrm{comp}} = K = 97\,\mathrm{km\,s^{-1}}$ respectively.

The most probable system composition, however, results for an inclination of $i = 52^{\mathrm{o}}$. The companion's mass becomes $M_{\mathrm{comp}} = 0.84\,\mathrm{M_\odot}$, which makes it a C/O core white dwarf. The orbits are $A_{\mathrm{WD}} = 2.3\,\mathrm{R_\odot}$ for the visible white dwarf and $A_{\mathrm{comp}} = 1.0\,\mathrm{R_\odot}$ for the unseen

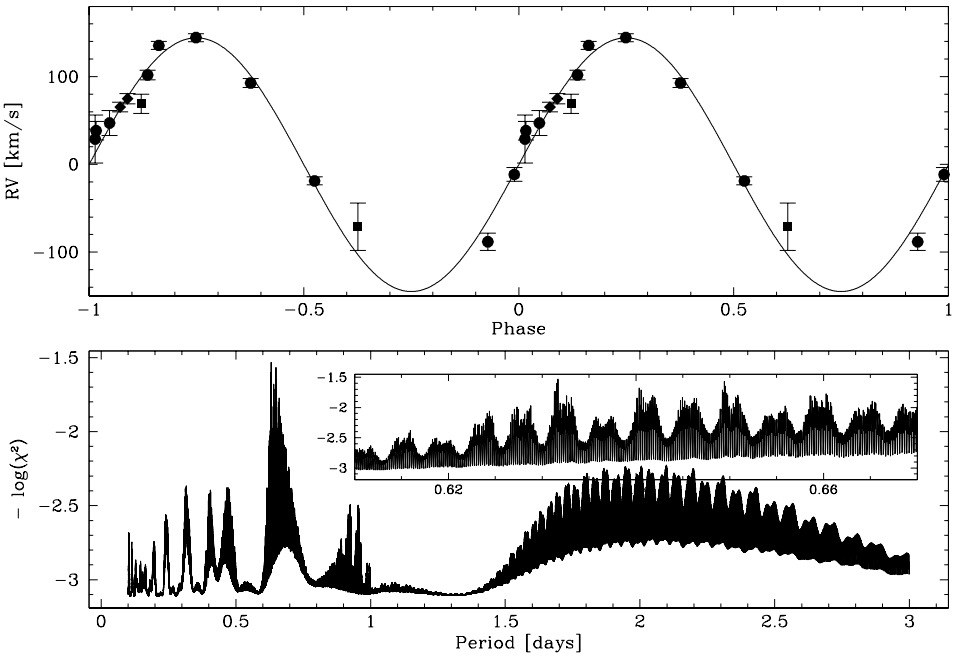

Figure 7.3: Best fit RV curve and power spectrum for WD 1210+140. Upper panel: Measured radial velocities as a function of orbital phase and fitted sine curves. Squares are used for ESO VLT observations and circles for observations done at the DSAZ. Diamonds mark data taken from Maxted et al. (1999). Lower panel: Power spectrum of WD 1210+140. The inset shows the region near the main peak in more detail.

companion. Thus, the system's total expansion becomes $A_{\rm tot} = 3.3\,{\rm R}_\odot$. Orbital velocities of both components can be computed to be $v_{\rm WD} = 184\,{\rm km\,s^{-1}}$ and $v_{\rm comp} = 81\,{\rm km\,s^{-1}}$ respectively.

As can be seen from table 7.2, WD 1210+140 will not qualify as a SN Ia precursor due to its large merging time. Even for the most massive white dwarf companion of about $1.40\,{\rm M}_\odot$ the merging time will still exceeds the Hubble time.

Table 7.2: Scenarios for WD 1210+140.

Scenario	i [deg]	$M_{\rm vis}$ $[M_\odot]$	$M_{\rm invis}$ $[M_\odot]$	$M_{\rm tot}$ $[M_\odot]$	$t_{\rm m}$ [Gyrs]	SN Ia-prec.	nature of companion
max. i	90	0.37	0.55	0.92	67	no	C/O core WD
most likely i	52	0.37	0.84	1.21	48	no	C/O core WD
$M_{\rm tot} \approx M_{\rm Chandra}$	$\approx$45	0.37	$\approx$1.03	$\approx$1.40	$\approx$41	no	C/O core WD
$M_{\rm invis} \approx M_{\rm Chandra}$	$\approx$41	0.37	$\approx$1.40	$\approx$1.77	$\approx$33	no	most massive WD

7.1.3 HS 1334+0701

α_{2000}= 13:36:33.67, δ_{2000}= +06:46:26.8, V = 15.00

History

HS 1334+0701 was selected from the Hamburg Quasar Survey to be a DA white dwarf. The first survey observation was done in June 2001, followed by another VLT observation in April 2002. Though we found a radial velocity shift of only $13\,\mathrm{km\,s^{-1}}$ from these spectra, the expected radial velocity semi-amplitude seemed to be very small, and therefore we expected HS 1334+0701 not to be a SN Ia candidate. Since it is sufficient bright, the system was re-observed in July 2002 at the DSAZ in order to create an unbiased sample of double degenerates for probing binary evolution theory.

Radial velocity curve

The power spectrum yields a most probable period of 0.229486^{d} ($5^{\mathrm{h}}30^{\mathrm{m}}28^{\mathrm{s}}$), but the result is not unambiguous. There are some aliases at $P = 0.157363^{\mathrm{d}}$, 0.186757^{d} and 0.297905^{d} that can not be ruled out by visual inspection of the corresponding RV curves. The power spectrum of HS 1334+0701 is displayed in the lower panel of figure 7.4, while the upper panel shows the best fit RV curve computed for the most probable period of 0.229486^{d}. The ephemeris is

$$HJD(T_0) = 2\,453\,100.100063 \pm 0.229486 \times E. \tag{7.3}$$

The system velocity and semi-amplitude derived from the RV curve are $\gamma = -30.3 \pm 1.3\,\mathrm{km\,s^{-1}}$ and $K = 29.2 \pm 2.0\,\mathrm{km\,s^{-1}}$ respectively.

Spectral analysis and mass determination

Like WD 0326−273, HS 1334+0701 was spectroscopically analyzed by Detlev Koester. By means of this results ($T_{\mathrm{eff}} = 16\,190\,\mathrm{K}$ and $\log g = 7.3$) we estimated a white dwarf's mass of $M_{\mathrm{WD}} = 0.37\,\mathrm{M_\odot}$ from the tracks of Blöcker et al. (1997).

System composition

Assuming an inclination of $i = 90^{\mathrm{o}}$ we determined the companion's minimum mass to be $M_{\mathrm{comp}} = 0.05\,\mathrm{M_\odot}$. Thus, the white dwarf circles around the barycenter at a distance of $A_{\mathrm{WD}} = 0.1\,\mathrm{R_\odot}$ and at a orbital velocity equal to the semi-amplitude K. The companion is at $A_{\mathrm{comp}} = 1.0\,\mathrm{R_\odot}$ from the system's barycenter at an orbital velocity of $v_{\mathrm{comp}} = 230\,\mathrm{km\,s^{-1}}$. The total separation of both components becomes $A_{\mathrm{tot}} = 1.1\,\mathrm{R_\odot}$.

For the most probable inclination of $i = 52^{\mathrm{o}}$, however, the companion has $M_{\mathrm{comp}} = 0.06\,\mathrm{M_\odot}$, $A_{\mathrm{comp}} = 1.0\,\mathrm{R_\odot}$ and $v_{\mathrm{comp}} = 226\,\mathrm{km\,s^{-1}}$. Orbital size and velocity for the white dwarf are $A_{\mathrm{WD}} = 0.2\,\mathrm{R_\odot}$ and $v_{\mathrm{WD}} = 37\,\mathrm{km\,s^{-1}}$, yielding $A_{\mathrm{tot}} = 1.2\,\mathrm{R_\odot}$ for the system's total extend.

The companion of the visible white dwarf is most probable a massive brown dwarf. However, for a system's inclination below 38^{o}, the companions mass exceeds $0.08\,\mathrm{M_\odot}$ which is the minimum mass for central hydrogen burning. Thus, a late type M star can not be ruled out either. Table 7.3 summarizes different scenarios for HS 1334+0701.

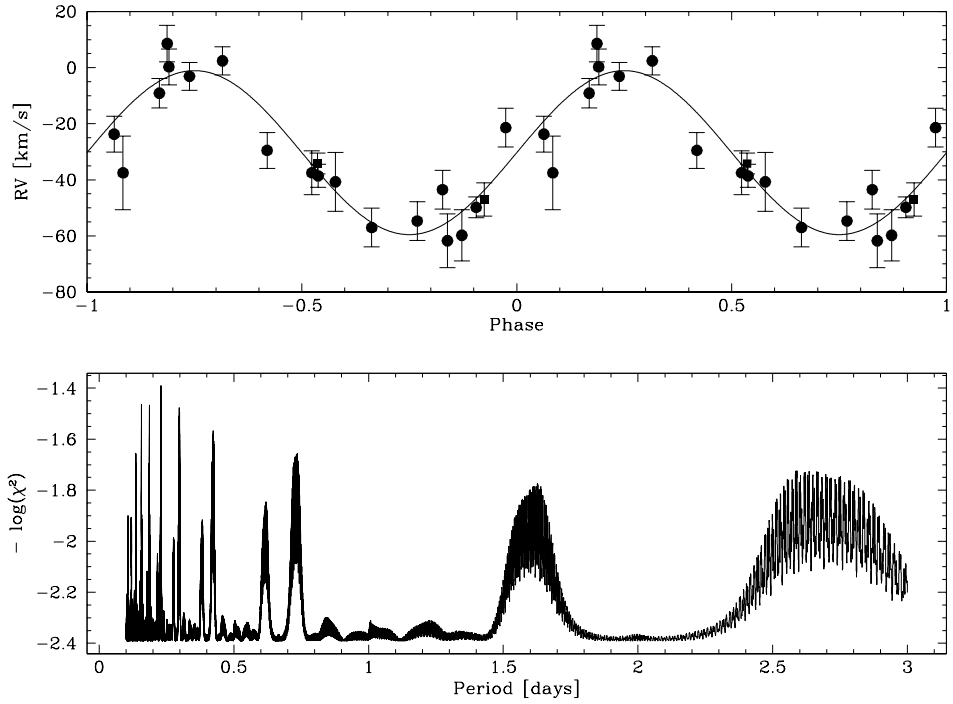

Figure 7.4: Best fit RV curve and power spectrum for HS 1334+0701. Upper panel: Measured RVs of HS 1334+0701 as a function of orbital phase and fitted sine curve. The data points are phase according to the most probable period of 0.229486^{d}. Squares are used for VLT observations and squares for observations from the DSAZ. Lower panel: Power spectrum of HS 1334+0701.

Table 7.3: Scenarios for HS 1334+0701.

Scenario	i [deg]	M_{vis} $[M_\odot]$	M_{invis} $[M_\odot]$	M_{tot} $[M_\odot]$	t_{m} [Gyrs]	SN Ia - prec.	nature of companion
max. i	90	0.37	0.05	0.42	38	no	brown dwarf
most likely i	52	0.37	0.06	0.43	32	no	brown dwarf
$M_{\mathrm{tot}} \approx M_{\mathrm{Chandra}}$	$\approx$8	0.37	$\approx$0.60	$\approx$0.97	$\approx$4	no	typical C/O core WD
$M_{\mathrm{invis}} \approx M_{\mathrm{Chandra}}$	$\approx$5	0.37	$\approx$1.40	$\approx$1.77	$\approx$2	yes	most massive WD

7.1.4 WD 1824+040

α_{2000}= 18:27:13.13, δ_{2000}= +04:03:45.9, V = 13.90

History

WD 1824+040 was first detected to be a radial velocity variable white dwarf by Saffer et al. (1998). However, since it is found in the McCook and Sion catalogue (1999), this system was independently observed at the VLT in May 2000 in the course of the SPY project. The first survey spectra already reveal an unequivocal radial velocity shift of about 50 $\mathrm{km\,s^{-1}}$, confirming the variability found by Saffer et al. (1998). Additional medium-resolution spectra were taken with TWIN at the DSAZ in March and July 2001 and in February 2002. The data set was complemented by five high-resolution spectra taken over the course of 2001 at the VLT.

Radial velocity curve

The resulting power spectrum is displayed in the lower panel of figure 7.5. The unambiguous period of $P = 6.266079^{\mathrm{d}}$ ($6^{\mathrm{d}}6^{\mathrm{h}}23^{\mathrm{m}}9^{\mathrm{s}}$) is obvious. From the best fit RV curve we derive a system's velocity of $\gamma = 47.3 \pm 0.4 \mathrm{km\,s^{-1}}$ and a radial velocity semi-amplitude of $K = 62.2 \pm 0.7\,\mathrm{km\,s^{-1}}$. Maxted et al. (1999) has already found a period of 6.266^{d} and a semi-amplitude of $59\,\mathrm{km\,s^{-1}}$ for WD 1824+040, which is in almost perfect agreement with our own analysis. The ephemeris of is

$$HJD(T_0) = 2\,453\,100.824021 \pm 6.266079 \times E. \tag{7.4}$$

Spectral analysis and mass determination

The spectral analysis performed by means of our high-resolution UVES spectra gives $T_{\mathrm{eff}} = 13723\,\mathrm{K}$ and $\log g = 7.94$ (Koester, priv.com.). Therefore, we estimated the white dwarf's mass to be $M_{\mathrm{WD}} = 0.55\,\mathrm{M_\odot}$. Although these results differs slightly form a previous study of low resolution spectra (Bragaglia et al. 1995; $T_{\mathrm{eff}} = 14795\,\mathrm{K}$, $\log g = 7.61$ and $M_{\mathrm{WD}} = 0.39\,\mathrm{M_\odot}$) we rely on our own results for the ongoing discussion.

System composition

For an inclination of $i = 90°$, the mass function of $f_{\mathrm{m}} = 0.156\,\mathrm{M_\odot}$ results in the companion's minimum mass of $M_{\mathrm{comp}} = 0.59\,\mathrm{M_\odot}$. The separation of the two components is $A_{\mathrm{tot}} = 14.9\,\mathrm{R_\odot}$. Orbit and orbital velocity of the visible white dwarf can be computed from equations 5.2 and 6.1.4 to be $A_{\mathrm{WD}} = 7.7\,\mathrm{R_\odot}$ and $v_{\mathrm{WD}} = K = 62.2\,\mathrm{km\,s^{-1}}$. Corresponding results for the companion are $A_{\mathrm{comp}} = 7.2\,\mathrm{R_\odot}$ and $v_{\mathrm{comp}} = 58.3\,\mathrm{km\,s^{-1}}$.

For the most probable inclination of $i = 52°$, however, the mass function yields a companion with a mass of $M_{\mathrm{comp}} = 0.86\,\mathrm{M_\odot}$ and a orbit of $A_{\mathrm{comp}} = 6.2\,\mathrm{R_\odot}$ ($v_{\mathrm{comp}} = 50.5\,\mathrm{km\,s^{-1}}$). According to this scenario, the distance of the white dwarf to the barycenter can be computed to be $A_{\mathrm{WD}} = 9.8\,\mathrm{R_\odot}$ ($v_{\mathrm{WD}} = 78.9\,\mathrm{km\,s^{-1}}$). This results in a total separation of $R_{\mathrm{tot}} = 16.0\,\mathrm{R_\odot}$.

On the basis of these results we conclude that the unseen companion in the WD 1824+040 system is most likely a C/O core white dwarf. Although the system's total mass reaches the

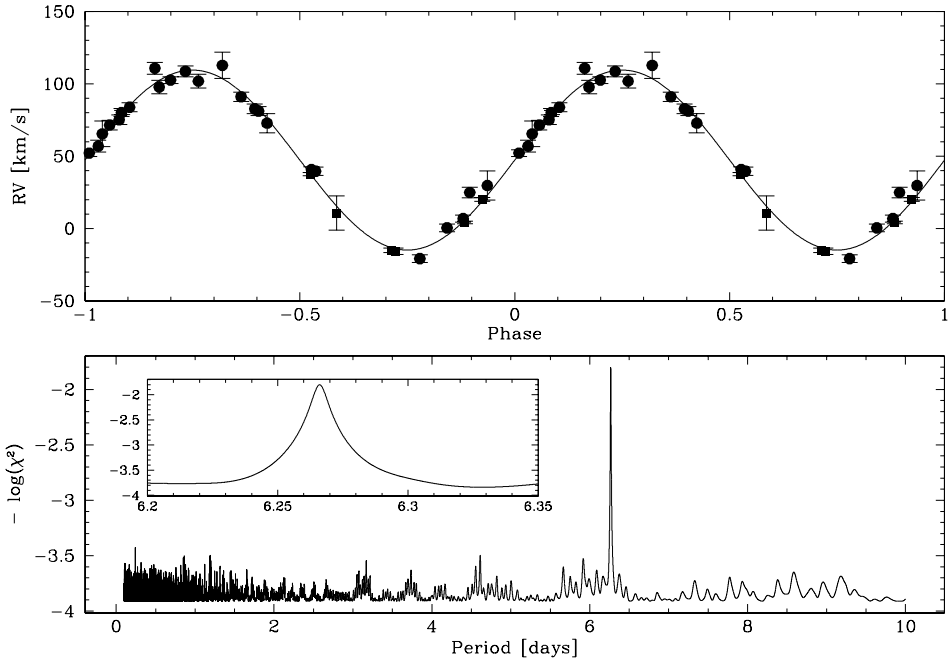

Figure 7.5: Best fit RV curve and power spectrum for WD 1824+040. Upper panel: Measured radial velocities as a function of orbital phase and fitted sine curves. Squares are used for VLT observations and circles for data based on DSAZ observations. Lower panel: Power spectrum of WD 1824+040.

Chandrasekhar limit in the case of the $i = 52^{\circ}$ scenario, its merging time is too large to qualify WD 1824+040 as a SN Ia precursor (15 100 Gyrs and 20 600 Gyrs respectively, cf. table 7.4).

Table 7.4: Scenarios for WD 1824+040.

Scenario	i [deg]	$M_{\rm vis}$ [$M_\odot$]	$M_{\rm invis}$ [$M_\odot$]	$M_{\rm tot}$ [$M_\odot$]	$t_{\rm m}$ [Gyrs]	SN Ia - prec.	nature of companion
max. i	90	0.55	0.59	1.14	20 600	no	C/O core WD
most likely i	52	0.55	0.86	1.41	15 100	no	C/O core WD
$M_{\rm invis} \approx M_{\rm Chandra}$	≈37	0.55	≈1.40	≈1.95	≈10 400	no	most massive WD

7.2 Subdwarf B primary

Subluminous B stars are generally considered to be core helium-burning stars with thin hydrogen envelopes of less than $0.02\,M_\odot$ and total masses of about $0.5\,M_\odot$. In the Hertzsprung Russell diagram they populate a very narrow area which lies on the blue-ward extension of the horizontal branch, the so called *Extreme Horizontal Branch*. From there they evolve directly to the white dwarf graveyard without reaching the *Asymptotic Giant Branch* previously, because their thin envelope cannot sustain hydrogen shell burning. According to standard stellar evolution theory, however, sdB star should not exist. Their detailed evolution is still unclear and several scenarios are still under debate (cf. Han et al. 2003). Figure 7.6 shows a typical example for an sdB's spectrum taken with UVES.

Although not being degenerate, sdB stars are immediate progenitors of white dwarfs and thus promising objects with respect to our search for supernova Ia precursors. The only likely SN Ia progenitor according to the merging scenario known so far is not a double degenerate, but the sdB plus white dwarf binary KPD 1930+2752 (Maxted et al. 2000c). Its period is $2^{\rm h}17^{\rm m}$, which yields a white dwarf companion of at least $0.97\,M_\odot$ which is almost certainly a white dwarf. Since the sdB will evolve directly to a white dwarf and merge in less than 0.2 Gyrs with the companion, KPD 1930+2752 is indeed a very good candidate for a SN Ia event. However, this result is still discussed since evolutionary calculations show that KPD 1930+2752 will form a ONeMg white dwarf rather than a SN/,Ia precursor (Ergma et al. 2001).

Unlike white dwarfs, sdB stars display a large variety of metal lines in their spectra. These lines can be used in order to estimate the projected rotational velocities $v_{\rm rot}\,sin\,i$ from quantitative spectral analyses of the objects (cf. section 4.4.3). Finally, the systems' inclination i themselves could be derived from equation 4.6 by means of P and R. The analysis has been performed in three steps:

Creating high S/N templates

In preparation for further analysis, a *high S/N template* was created for each object first. For that purpose, all available UVES spectra were weighted by their S/N ratio and shifted to laboratory wavelengths. Subsequently they were coadded in order to increase the S/N ratio of the template.

Atmospheric parameters

Although Lisker et al. (2004) already determined stellar atmospheric parameters for sdB stars by means of the SPY spectra, we performed an independent analysis by means of the high S/N coadded UVES templates. Effective temperatures ($T_{\rm eff}$), surface gravities ($\log g$) and helium abundances ($n_{\rm He} = \log[n_{\rm He}/n_{\rm H}]$) were determined by fitting simultaneously each observed hydrogen and helium line to a grid of synthetic model spectra. Therefore, a procedure developed by Napiwotzki et al. (1999) based on Saffer et al. (1994) was used. The model grid was composed of metal-line blanked LTE model atmospheres (Heber et al. 2000) with solar metal abundances. Figure 7.7 shows a typical fit result.

For each line the continuum level was determined and normalized to one, in order to compare it to the synthetic spectrum. The Hα line was never used for the parameter determination because its line core is sensitive to non-LTE effects and thus a LTE model has to fail reproducing the line. However Hα was kept in the plot for examining possible deviations from the model Hα line.

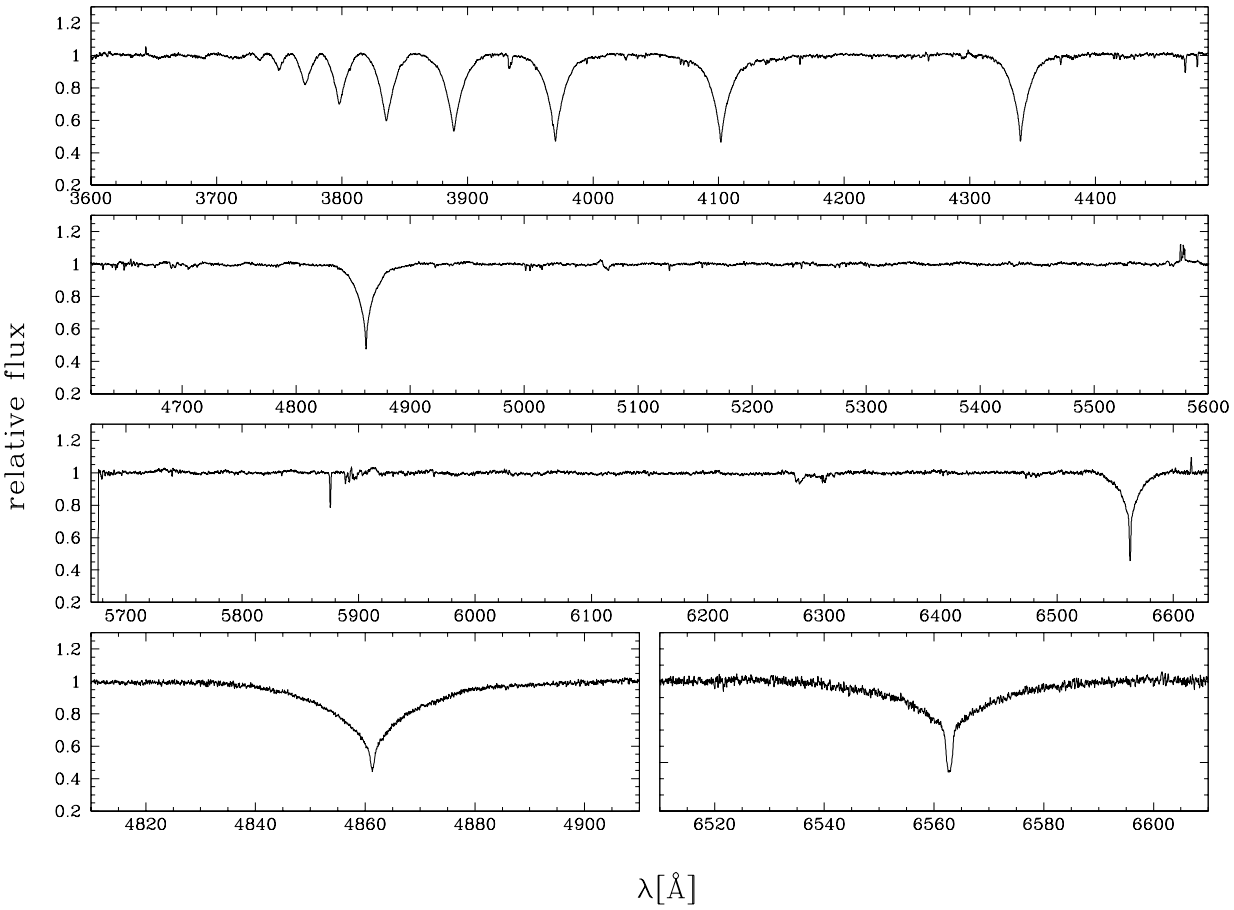

Figure 7.6: Sample UVES spectrum of an subdwarf B star (HE 0929−0424, see section 7.2.3).

Metal abundance patterns

The equivalent widths were measured by means of fitting Gaussians to the high S/N templates within the MIDAS context (see Herrmann 2000). The central intensity and the full-width-at-half-maximum (FWHM) were adjustable parameters, which were subsequently used to compute equivalent widths. Results can be seen from table D.1 in the appendix.

Thereafter, model atmospheres were generated with the *ATLAS9* code of Kurucz (1992) using the atmospheric parameters derived above and solar abundances. These models were used to calculate curve-of-growth for the observed metal lines. Blends from different analysis were omitted from the analysis. Finally, the abundances were determined from a detailed spectrum synthesis by means of *LINFOR*[1] using all metal lines.

The atomic data used for this analysis were taken from the lists of Wiese et al. (1996), Kurucz (1992), Ekberg (1993) and Hirata & Horaguchi (1995).

Closely connected to the determination of metal abundances is the measurement of microscopical turbulences in the star's atmosphere. These turbulences broadens the observed spectral

[1]LINFOR was originally developed by Holweger, Steffen and Steenbok at Kiel University. It has been enhanced and maintained by Lemke and was recently modified by Przybilla. For a description see: `http://www.sternwarte.uni-erlangen.de/~ai26/linfit/linfor.html`

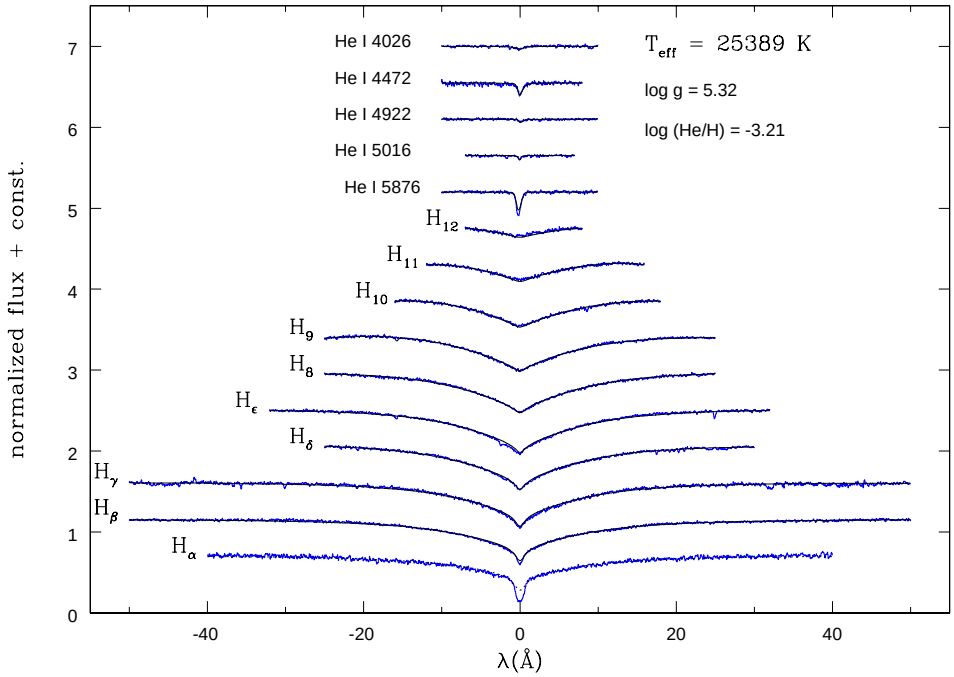

Figure 7.7: Sample model fit of an subdwarf B star (HE 0532−4503, see section 7.2.2).

lines due to the Doppler effect. However, if a sufficient number of lines of one ion over a wide range of strength is measured the microturbulence ξ can be estimated. Lines at the flat part of the curve-of-growth are very sensitive to ξ, whereas lines at the linear part are insensitive. By varying ξ, a different slope of the linear regression fitted to the determined abundances versus the equivalent widths results. Figure 7.8 demonstrates this effect on the example of the oxygen abundances determined from the O II lines of He 0532−4503. A vanishing slope of the linear regression is the means to determine the value of ξ.

Projected rotational velocity and inclination

Using the *LINFOR*[1] program package we computed synthetic spectra over a small wavelength range. In order to do this, we had to consider the previously determined parameters $T_{\rm eff}$, $\log g$, $n_{\rm He}$, ξ, and ε. These profiles were subsequently folded with an adopted rotational velocity and fitted to the observed line profiles given by the template. The quality of the fit was estimated by means of a χ^2 test. This way, the best fit and the proper projected rotational velocity was derived. An example for the determination of $v_{\rm rot}$ sin i is shown in figure 7.9 for HE 2135−3749.

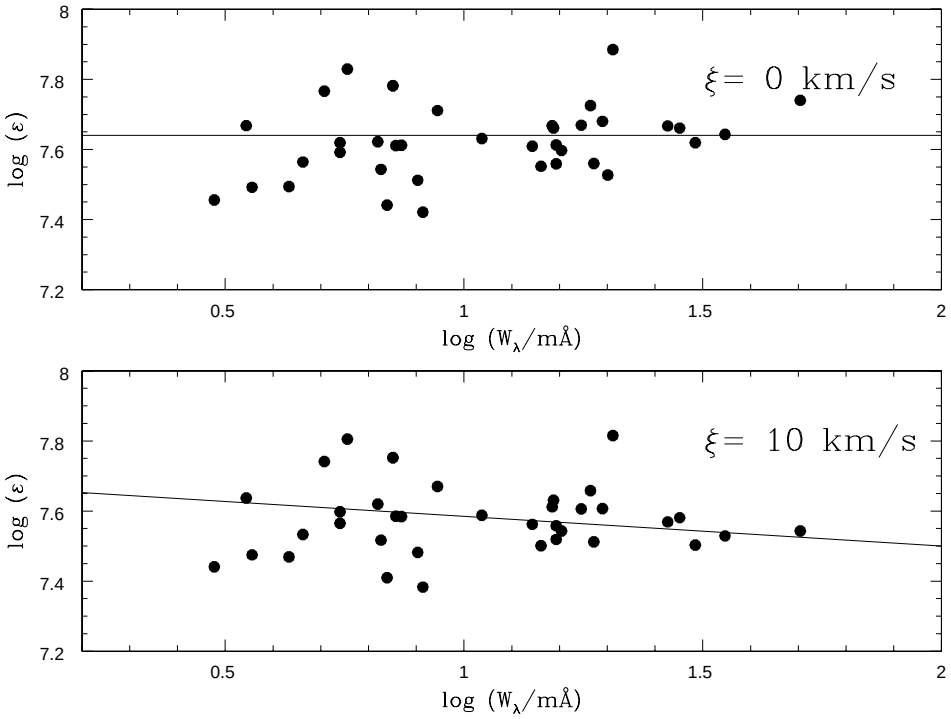

Figure 7.8: Determination of the microturbulence ξ for HE 2135−3749 by means of the N II results. Values of 0 km/s (upper panel) and 10 km/s are applied (lower panel). For $\xi = 0$ km/s the slope of the regression line vanishes as expected if the choice of ξ is correct.

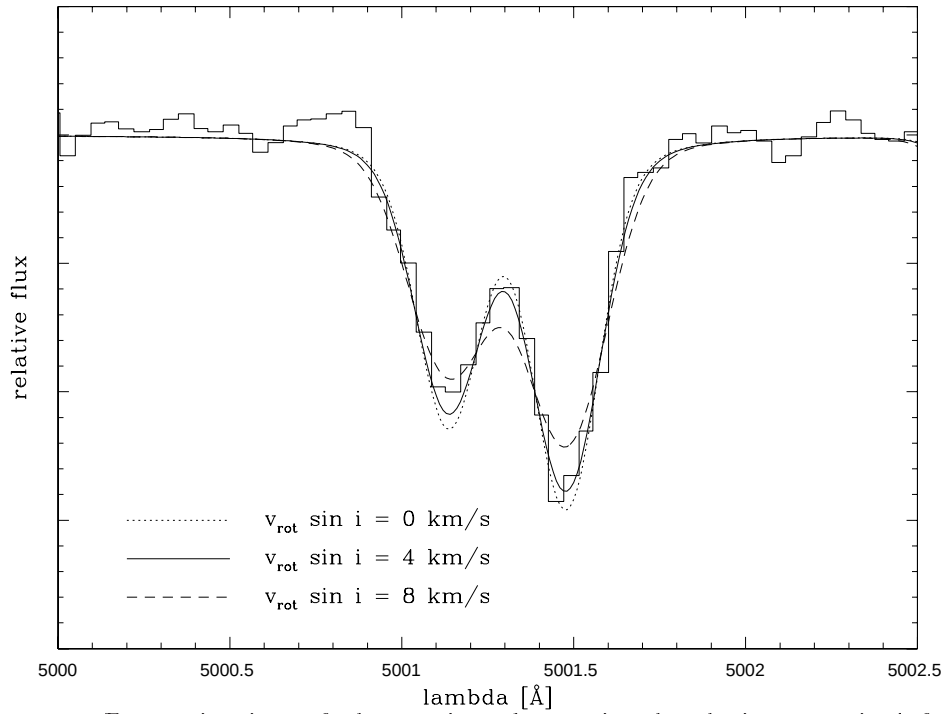

Figure 7.9: Determination of the projected rotational velocity $v_{\rm rot} \sin i$ for the sdB star HE 2135−3749. The lines used therefore are the N II lines at 5001.136 Å and 5001.447 Å respectively. $\xi = 0$ was adopted.

7.2.1 WD 0048−202

α_{2000}= 00:51:03.97, δ_{2000}= −20:00:00.3, V = 14.85

History

Classified as a DA1 white dwarf in the McCook & Sion catalogue (1999), high-resolution UVES spectra were taken of WD 0048−202 in July 2000 for the SPY project. From these spectra, however, it became obvious that WD 0048−202 is a subdwarf B star rather than a white dwarf. Moreover, a radial velocity shift of 80 km s^{-1} was measured, although a previous study by Bragaglia et al. (1990) derived no variation for this object from low resolution spectra. Since the star is bright and varies at a sufficiently large radial velocity amplitude we included WD 0048−202 into our follow-up campaign. Numerous observations were done at the VLT (October 2001 and November 2002), the DSAZ 3.5 m telescope (August and October 2002) and the NTT (September 2002). The data set was complemented by WHT observations done in October 2001 and in August 2003 done by Gijs Nelemans.

Radial velocity curve

The lower panel of figure 7.10 shows the resulting power spectrum with the main peak at 7.443571$^{\mathrm{d}}$ ($7^{\mathrm{d}}10^{\mathrm{h}}38^{\mathrm{m}}45^{\mathrm{s}}$). The best fit RV curve for the main period can be seen from the upper panel of figure 7.10. We derive a system's velocity of $\gamma = -26.5 \pm 0.4$ km s^{-1}, a radial velocity semi-amplitude of K = 47.9 ± 0.4 km s^{-1} and an ephemeris of

$$HJD(T_0) = 2\,453\,097.556906 \pm 7.443571 \times E. \tag{7.5}$$

Spectral analysis

A total of nine high-resolution UVES spectra allows a more detailed analysis of the visible components of WD 0048−202. By means of a spectral analysis an effective temperature of $T_{\mathrm{eff}} = 29960$ K, a surface gravity of $\log g = 5.50$ and a helium abundance of $n_{\mathrm{He}} \leq -4.00$ was derived. The helium abundance, however, is below the lower boundary of the used model grid and thus only an upper limit can be determined. These results are in almost perfect agreement with the stellar parameters derived by Lisker et al. (2004) from the survey spectra only.

The coadded spectrum furthermore reveals lines of several ions: N II, O II, Mg II, Al III, Si III and IV, S III, Ti III and Fe III. The abundances derived for these ions are shown in table 7.5. and displayed in figure 7.11 with respect to the solar value. Regarding prior studies (e.g. Edelmann 2003) WD 0048−202 shows no peculiar abundance patterns except for the unusual titanium abundance. The curve-of-growth of nitrogen, oxygen and iron are consistent with $\xi \leq 3$.

A detailed analysis in order to determine the projected rotational velocity by means of the Mg II doublet yields an upper limit of 5 km s^{-1} for $v_{\mathrm{rot}} \, sin \, i$ only. This result is not astonishing because former studies (e.g. Edelmann 2003) already showed that single-star sdBs are usually slow rotators. The same, however, can be expected for sdB stars in wide binaries without tidal locking, like WD 0048−202.

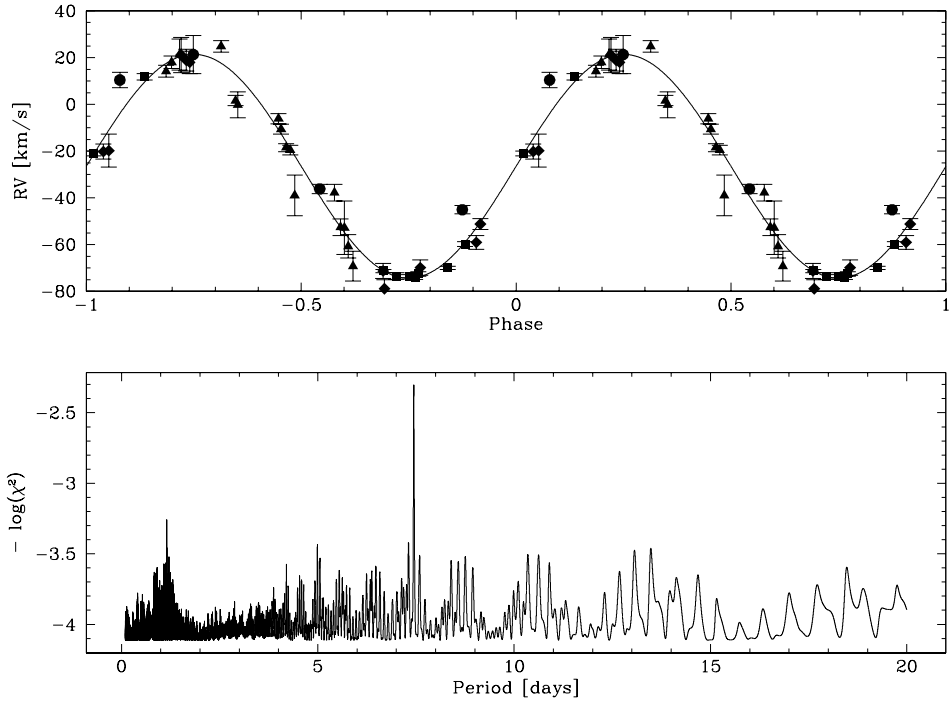

Figure 7.10: Best fit RV curve and power spectrum for WD 0048−202. Upper panel: Measured radial velocities as a function of orbital phase and fitted sine curve. Squares are used for ESO VLT observations, triangles for observations from the ESO NTT and observations done at the DSAZ 3.5 m telescope are marked as circles. Lower panel: Power spectrum of WD 0048−202.

Table 7.5: LTE metal abundances for WD 0048−202. The ion is given in the first column, n is the number of lines used for the analysis and $\log \varepsilon$ is the derived abundance.

ion	n	$\log \varepsilon$
N II	31	7.32±0.34
O II	49	7.54±0.21
Mg II	2	6.53±0.17
Al III	3	5.72±0.26
Si III	2	6.00±0.29
Si IV	1	5.52
S III	2	5.79±0.27
Ti III	11	6.72±0.39
Fe III	37	7.19±0.25

System composition

The mass function of $f_{\rm m} = 0.085\,{\rm M}_\odot$ results in a minimum mass of $M_{\rm comp} = 0.40$ M$_\odot$ for the unseen component, assuming a canonical mass of $0.47\,{\rm M}_\odot$ for the visible component and an inclination of $i = 90^{\rm o}$. The total separation becomes $A_{\rm tot} = 15.3$ R$_\odot$, which means the visible subdwarf is at $A_{\rm sdB} = 7.0$ R$_\odot$ from the barycenter whereas the unseen companion is at $A_{\rm comp} = 8.3$ R$_\odot$. The orbital velocities of both components are $v_{\rm sdB} = K = 47.9\,{\rm km\,s^{-1}}$ and

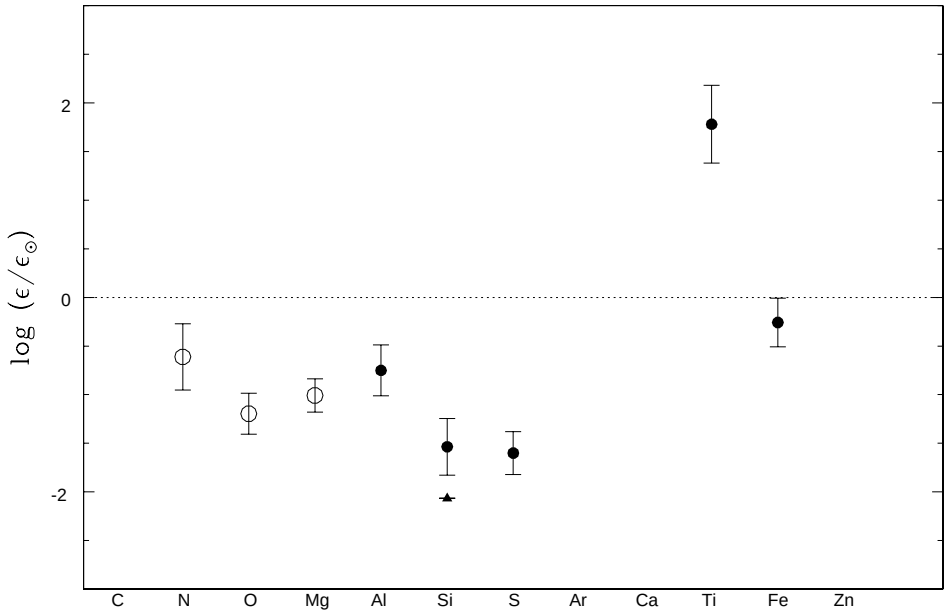

Figure 7.11: LTE abundances with error bars for WD 0048−202 relative to solar values (dashed horizontal line). Abundances derived from single ionized ions are marked as open circles, from double ionized ions as filled circles and from triple ionized ions as filled triangles.

$v_{\rm comp} = 56.2\,{\rm km\,s^{-1}}$ respectively.

However, the most probable value of the inclination is $i = 52°$, which gives a companion mass of $M_{\rm comp} = 0.57$ M$_\odot$ and a system's total separation of $A_{\rm tot} = 16.3\,{\rm R}_\odot$. Orbital size and orbital velocity of the subdwarf become $A_{\rm sdB} = 8.9$ R$_\odot$ and $v_{\rm sdB} = 60.8\,{\rm km\,s^{-1}}$ respectively. The corresponding results for the unseen companion are $A_{\rm comp} = 7.3$ R$_\odot$ and $v_{\rm comp} = 49.8\,{\rm km\,s^{-1}}$.

Based on the results derived above we finally conclude that the unseen component is most likely a white dwarf with a C/O core composition. The system, however, will not qualify as a SN Ia precursor because its total mass will neither exceeds the Chandrasekhar mass nor will it merge within a Hubble time, as can be seen from table 7.6. Even for the most massive $1.4\,{\rm M}_\odot$ white dwarf companion the system's merging time will not be below a Hubble time.

Table 7.6: Scenarios for WD 0048−202.

Scenario	i [deg]	$M_{\rm vis}$ [$M_\odot$]	$M_{\rm invis}$ [$M_\odot$]	$M_{\rm tot}$ [$M_\odot$]	$t_{\rm m}$ [Gyrs]	SN Ia-prec.	nature of companion
max. i	90	0.47	0.47	0.94	44 900	no	C/O core WD
most likely i	52	0.47	0.57	1.14	38 300	no	C/O core WD
$M_{\rm tot} \approx M_{\rm Chandra}$	≈36	0.47	≈0.93	≈1.40	≈25 900	no	massive C/O core WD
$M_{\rm invis} \approx M_{\rm Chandra}$	≈29	0.47	≈1.40	≈1.87	≈19 400	no	most massive WD

7.2.2 HE 0532−4503

α_{2000}= 05:33:40.51, δ_{2000}= −45:01:35.3, V = 16.02

History

Being selected from the Hamburg/ESO survey, HE 0532−4503 was observed twice for SPY at the VLT in April 2001. These spectra revealed helium lines at 5876 Å and 4471 Å and therefore the star seemed to be a subdwarf rather than a white dwarf. A classification that was confirmed later on by means of a quantitative spectral analysis. Nevertheless, a large radial velocity shift of about 200 km s^{-1} became obvious as well, and therefore the star was a very promising candidate for follow-up observation. However, its location in the southern hemisphere rules out most of the observational sites used for SPY follow-ups – only the ESO telescopes qualify for re-observation. In fact, HE 0532−4503 was re-observed at the ESO VLT during our runs in October 2001, in November 2002 and in March 2003.

Radial velocity curve

The power spectrum derived for HE 0532−4503 is unambiguously and yields a period of $P = 0.265584^{\mathrm{d}}$ ($6^{\mathrm{h}}22^{\mathrm{m}}26^{\mathrm{s}}$). From the best fit RV curve that can be seen in the upper panel of figure 7.12 we estimated a system's velocity of $\gamma = 8.5 \pm 0.1 \mathrm{km\,s^{-1}}$ and a semi-amplitude of $K = 101.5 \pm 0.2\,\mathrm{km\,s^{-1}}$. The ephemeris becomes

$$HJD(T_0) = 2\,453\,099.997536 \pm 0.265584 \times E. \tag{7.6}$$

Power spectrum and best fit RV curve for HE 0532−4503 can be seen from figure 7.12.

Spectral analysis

HE 0532−4503 was observed 47 times at the VLT, providing a large number of high quality spectra yielding a coadded template with an S/N ratio of 80. A quantitative spectral analysis results in very accurate stellar parameters of $T_{\mathrm{eff}} = 25389\,\mathrm{K}$, $\log g = 5.32$ and $n_{\mathrm{He}} \leq -3.21$, which are consistent with the results of Lisker et al. (2004).

We found spectral lines of C II, N II, O II, Mg II, Si III, S II and S III and Fe III. The abundances derived for these ions are shown in table 7.7 and shown in figure 7.13 with respect to the solar value. As can be seen from this plot, HE 0532−4503 shows no unexpected peculiarities among its abundance patterns but looks like an ordinary subdwarf B type star. The curve-of-growth analyses of nitrogen, oxygen and iron reveal no hint for microturbulence. Thus we assume $\xi = 0$ further on.

A detailed analysis in order to determine the projected rotational velocity by means of the N II lines between 5000 Å and 5010 Å results in $v_{\mathrm{rot}} \sin i = 9 \pm 1\,\mathrm{km\,s^{-1}}$.

System composition

Assuming a canonical mass of 0.47 $M_\odot$ for the sdB, the radius of the star became 0.25 $R_\odot$ (cf. equation 4.7). For bounded rotation, this finally yields a system's inclination of $i = 11^{\mathrm{o}}$ by means of comparison of the computed rotational velocity with the measured one. However, the

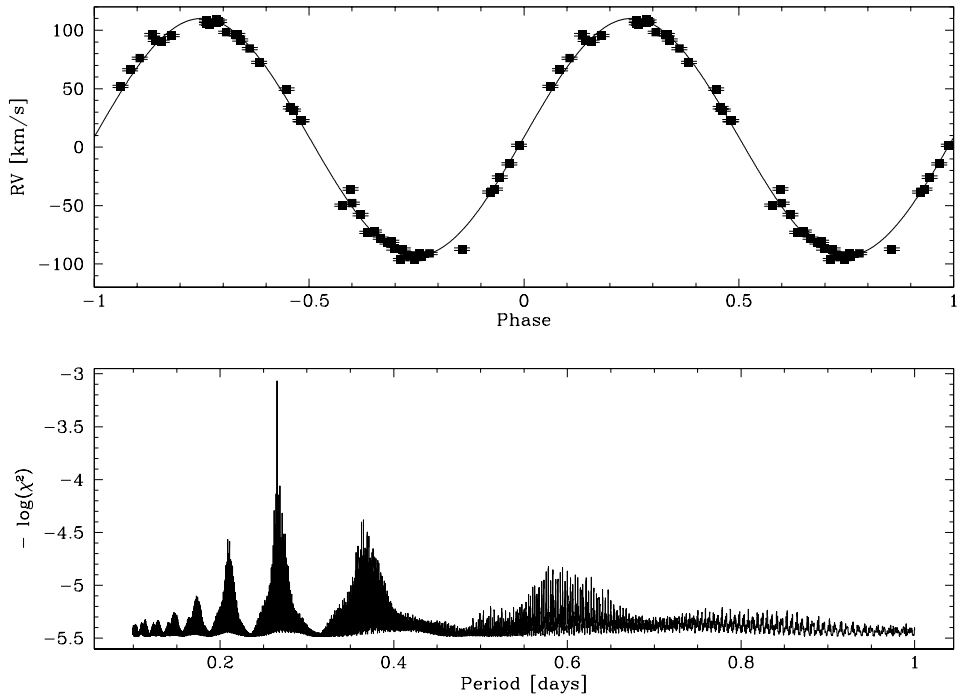

Figure 7.12: Best fit RV curve and power spectrum for HE 0532−4503. Upper panel: Measured radial velocities as a function of orbital phase and fitted sine curve. All measurements are based on ESO VLT observations. Lower panel: Power spectrum of HE 0532−4503.

Table 7.7: LTE metal abundances for HE 0532−4503. The ion is given in the first column, n is the number of lines used for the analysis and $\log\varepsilon$ is the derived abundance.

ion	n	$\log\varepsilon$
C II	4	6.38±0.83
N II	18	7.20±0.27
O II	31	7.75±0.21
Mg II	5	6.81±0.27
Si III	2	6.28±0.52
S II	1	6.92
S III	2	6.38±0.31
Fe III	55	7.62±0.36

mass function of $f_{\rm m} = 0.029\ {\rm M}_\odot$ results in $M_{\rm comp} = 5.0\ {\rm M}_\odot$ for the companion, which therefore has to be a black hole. The separation between the sdB and the black hole become $A_{\rm tot} = 3.0\ {\rm R}_\odot$, and the orbital size and velocity of the sdB are $A_{\rm sdB} = 2.8\ {\rm R}_\odot$ and $v_{\rm sdB} = 530\ {\rm km\,s^{-1}}$ respectively.

Although a sdB plus black hole binary is not impossible, it is still unlikely. In order to discuss the evolutionary status of HE 0532−4503 in more detail we therefore adopted a post-RGB evolutionary scenario for HE 0532−4503 instead of the usual post-EHB evolution (cf. the discussion for HD 188122 in Heber et al. 2003). Thus, we derive a mass of $0.25\ {\rm M}_\odot$ by means of comparison of the stars position in the ($T_{\rm eff}$,log g) plane with evolutionary track computed for post-RGB

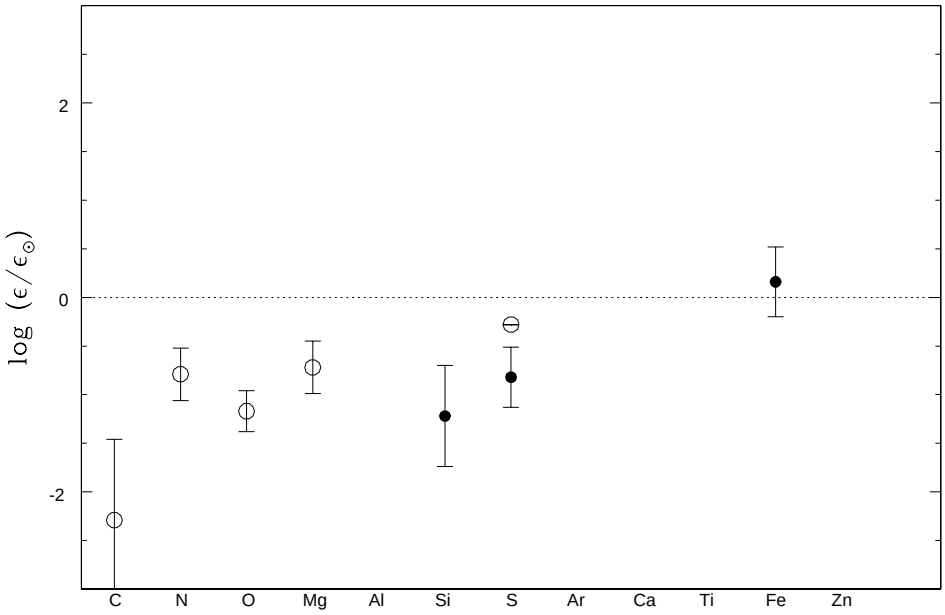

Figure 7.13: LTE abundances with error bars for HE 0532−4503 relative to solar values (dashed horizontal line). Abundances derived from single ionized ions are marked as open circles, from double ionized ions as filled circles and from triple ionized ions as filled triangles.

evolution. This can be seen graphically from figure 7.14. Thus, the star's radius and subsequently the system's inclination change to $R_{\rm sdB} = 0.18\,{\rm R}_\odot$ and $i = 15^{\rm o}$. The companion's mass, however, is still $M_{\rm comp} = 2.1\,{\rm M}_\odot$. which means the companion has to be a neutron star therefore. For the post-RGB scenario, the separation of the system becomes $A_{\rm tot} = 2.3\,{\rm R}_\odot$, whereas the orbital size and velocity of the sdB are $A_{\rm sdB} = 2.1\,{\rm R}_\odot$ and $v_{\rm sdB} = 392\,{\rm km\,s^{-1}}$ respectively.

Both scenarios exemplified above results in very massive companions. In the following, we abandon the assumption of bounded rotation and discuss the nature of the companion for the maximum and the most probable inclination angle. Assuming the sdB star having a canonical mass of $0.47\,{\rm M}_\odot$, the companion's minimum mass computed for $i = 90^{\rm o}$ becomes $M_{\rm comp} = 0.25\,{\rm M}_\odot$, which is either a low mass He-core white dwarf or a late type main sequence star. The separation of the system can be calculated to be $A_{\rm tot} = 1.6\,{\rm R}_\odot$, and the orbital parameters for the components are $A_{\rm sdB} = 0.5\,{\rm R}_\odot$ and $v_{\rm sdB} = K = 101\,{\rm km\,s^{-1}}$ for the sdB and $A_{\rm comp} = 1.1\,{\rm R}_\odot$ and $v_{\rm comp} = 195\,{\rm km\,s^{-1}}$ for the companion respectively.

The most probable inclination, however, is $i = 52^{\rm o}$ which yields $M_{\rm comp} = 0.34\,{\rm M}_\odot$for the companion's mass. Thus, the companion is again either a low mass white dwarf or a late type main sequence star. The orbital parameters for the components are $A_{\rm sdB} = 0.7\,{\rm R}_\odot$ and $A_{\rm comp} = 0.9\,{\rm R}_\odot$ for the orbital sizes and $v_{\rm sdB} = 129\,{\rm km\,s^{-1}}$ and $v_{\rm comp} = 179\,{\rm km\,s^{-1}}$ for the orbital velocities. The total extend of the system is $A_{\rm tot} = 1.6\,{\rm R}_\odot$.

Table 7.8 summarizes the results of different scenarios for HE 0532−4503.

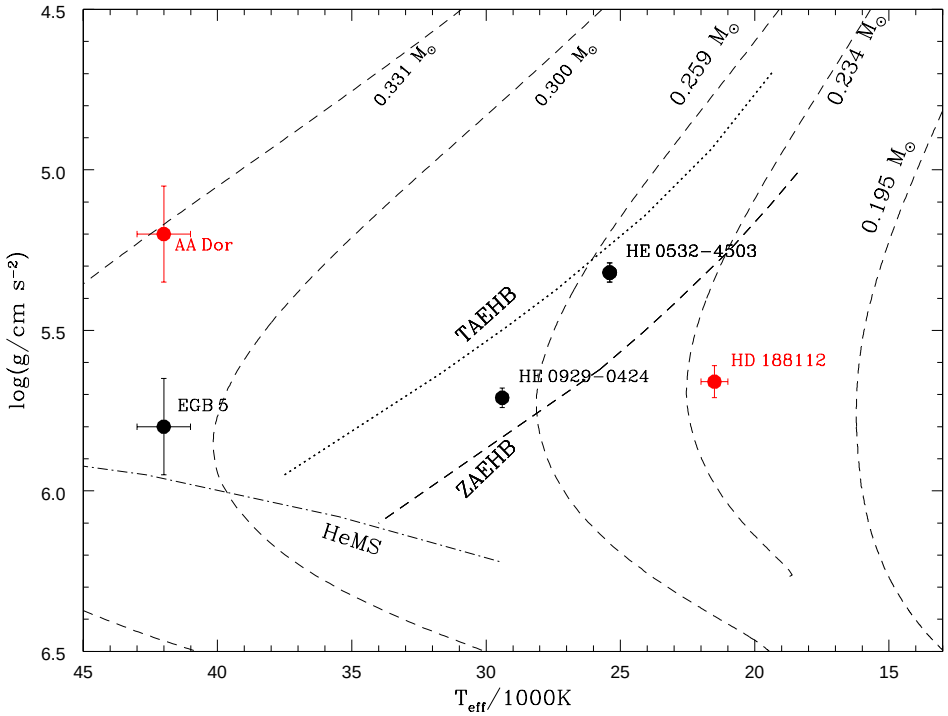

Figure 7.14: Position of HE 0532−4503 in the ($T_{\rm eff}$,log g) plane and comparison with the low mass evolutionary tracks computed by Driebe et al. (1998) for post red giant branch (post-RGB) evolution. These tracks represent the evolution of stars whose hydrogen-rich envelope was stripped away by a companion during the first red giant branch phase. The remaining mass is too low for the ignition of helium burning and the star will eventually become a low mass white dwarf with a helium core.

Table 7.8: Scenarios for HE 0532−4503.

Scenario	i [deg]	$M_{\rm vis}$ [$M_\odot$]	$M_{\rm invis}$ [$M_\odot$]	$M_{\rm tot}$ [$M_\odot$]	$t_{\rm m}$ [Gyrs]	SN Ia - prec.	nature of companion
bd. rot. & post-EHB	11	0.47	5.0	5.47	1.0	no	black hole
bd. rot. & post-RGB	15	0.25	2.1	2.35	3.5	no	neutron star
max. i	90	0.47	0.25	0.72	10.6	no	Low mass WD or late type MS
most likely i	52	0.47	0.34	0.81	8.1	no	Low mass WD or late type MS
$M_{\rm tot} \approx M_{\rm Chandra}$	≈24	0.47	≈0.93	≈1.40	≈3.6	yes	massive C/O core WD
$M_{\rm invis} \approx M_{\rm Chandra}$	≈19.5	0.47	≈1.40	≈1.87	≈2.6	yes	most massive WD

7.2.3 HE 0929−0424

α_{2000}= 09:32:02.15, δ_{2000}= −04:37:37.8, V = 15.53

History

HE 0929−0424 was selected from the Hamburg/ESO survey by Norbert Christlieb (priv.com.) to be a hydrogen rich DA white dwarf. The high-resolution spectra taken in the course of SPY, however, reveal that this object is in fact a subdwarf of spectral type B. Although one of the survey spectra was of low quality only, a radial velocity shift of more than 200 km s^{-1} was estimated. Thus, HE 0929−0424 was re-observed in January 2003 at the WHT, in February at the NTT and in March at the VLT.

Radial velocity curve

From the power spectrum, a period of $P = 0.440046^{\rm d}$ ($10^{\rm h}33^{\rm m}40^{\rm s}$) results, whereas the system's velocity was determined to be $\gamma = 41.4 \pm 1.0$km s^{-1} and the RV semi-amplitude to be $K = 114.3 \pm 1.4$ km s^{-1}. The ephemeris of HE 0929−0424 becomes

$$HJD(T_0) = 2\,453\,100.058523 \pm 0.440046 \times E. \tag{7.7}$$

Power spectrum and best fit RV curve can be seen from figure 7.15.

Spectral analysis

HE 0929−0424 was observed eight times totally at the VLT. Even after discarding the low S/N survey observation, seven high-resolution UVES spectra remain to be coadded in order to obtain a high S/N template. By means of a spectral analysis we derive $T_{\rm eff} = 29470$ K, $\log g = 5.71$ and $n_{\rm He} = -1.99$, which is in almost perfect agreement with the results of Lisker et al. (2004) based on the survey spectra only.

Furthermore, we identified spectral lines of the C II, N II, O II, Ne II, Mg II, Al III, Si III, S III and Fe III. ions. The abundances are shown in table 7.9 in more detail. In addition, figure 7.16 displays the derived abundance patterns with respect to solar values. The derived neon abundance is regarded as an upper limit, because the equivalent width measurements yield values only slightly above the detection limit. However, the two lines are among the strongest lines expected in the Ne-line-spectrum. The microturbulence was deduced from the curve-of-growth of the N II and O II lines to be $\xi = 0$ km s^{-1}.

The projected rotational velocity was determined by means of fitting synthetic line profiles to the Ne,II lines 5001.136 Å, 5001.447 Å, 5002.703 Å, 5005.149 Å and 5007.325 Å. Thus, $v_{\rm rot}$ sin $i = 6 \pm 1$ km s^{-1} was derived.

System composition

From the projected rotation velocity a stellar radius of $R_{\rm sdb} = 0.16\,{\rm R}_\odot$ was determined for an assumed canonical sdB mass of $0.47\,{\rm M}_\odot$ (cf. equation 4.7). Thus, the inclination becomes $i = 19^{\rm o}$. The mass function of $f_{\rm m} = 0.068\,{\rm M}_\odot$ yields a companion's mass of $M_{\rm comp} = 2.7\,{\rm M}_\odot$. Therefore, the companion is a neutron star or black hole. The separation of both components

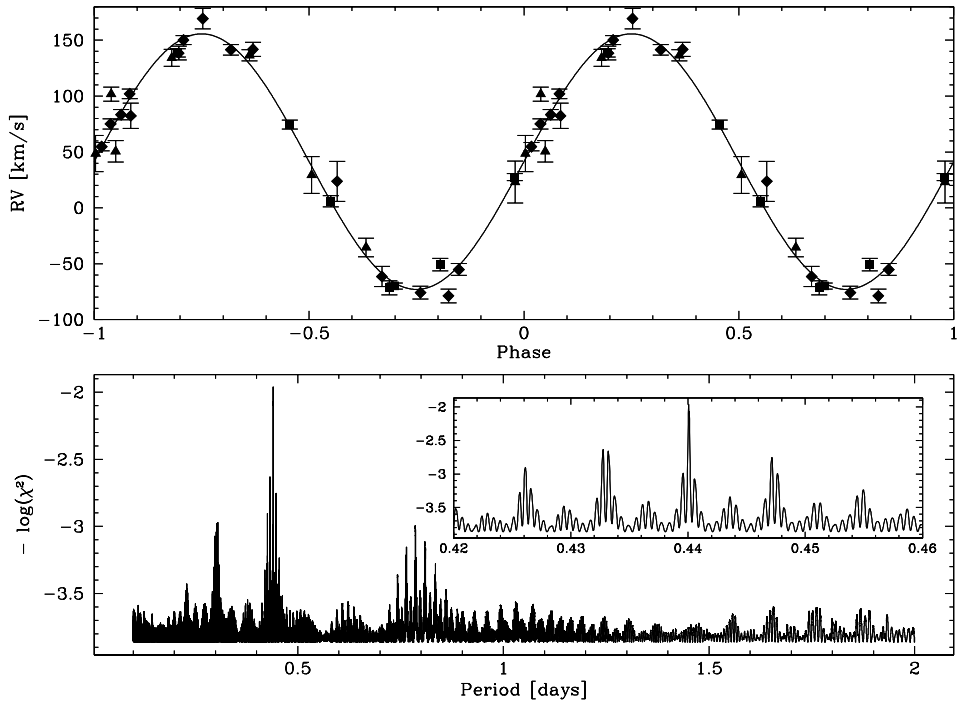

Figure 7.15: Best fit RV curve and power spectrum for HE 0929−0424. Upper panel: Measured radial velocities as a function of orbital phase and fitted sine curve. Squares are used for ESO VLT observations and triangles for observations from the ESO NTT. Data taken at the WHT are provided from Gijs Nelemans and are marked as diamonds. Lower panel: Power spectrum of HE 0929−0424.

Table 7.9: LTE metal abundances for HE 0929−0424. The ion is given in the first column, n is the number of lines used for the analysis and $\log\varepsilon$ is the derived abundance.

ion	n	$\log\varepsilon$
C II	3	6.86±0.53
N II	43	7.85±0.47
O II	33	7.85±0.29
Ne II	2	≤7.23
Mg II	1	6.73
Al III	2	5.90±0.13
Si III	4	6.57±0.31
S III	2	6.40±0.07
Ar II	4	7.62±0.58
Fe III	7	7.46±0.16

is $A_{\rm tot} = 3.6\,{\rm R}_\odot$. The orbital velocity of the subdwarf is $v_{\rm sdB} = 350\,{\rm km\,s^{-1}}$ and its orbital size $A_{\rm sdB} = 3.1\,{\rm R}_\odot$.

Like in the case of HE 0532−4503, we alternatively consider post-RGB evolution for HE 0929−0424. By means of comparison of the determined stellar atmospheric parameters

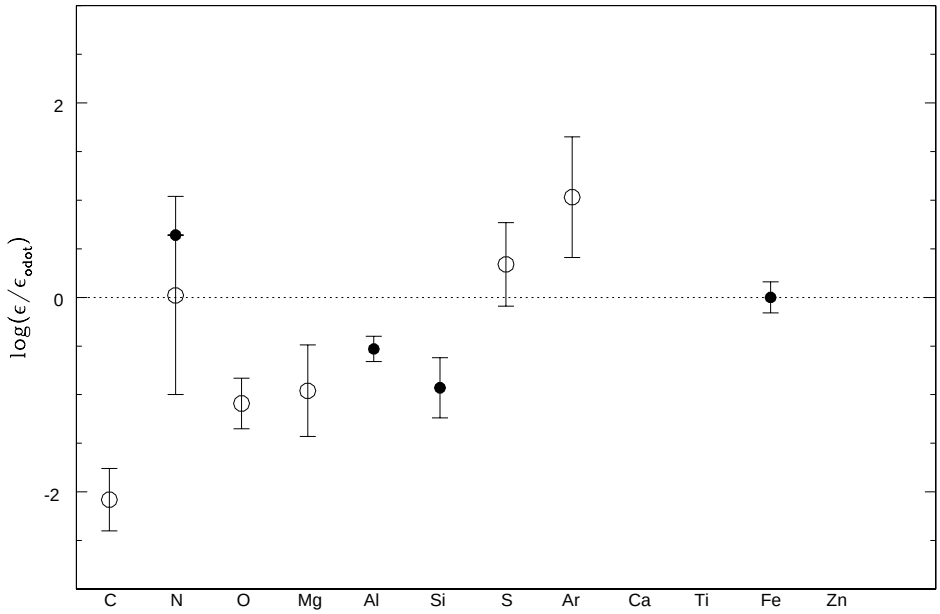

Figure 7.16: LTE abundances with error bars for HE 0929−0424 relative to solar values (dashed horizontal line). Abundances derived from single ionized ions are marked as open circles, from double ionized ions as filled circles and from triple ionized ions as filled triangles.

with the evolutionary tracks in a ($T_{\rm eff}$,log g) plane, we derive $M_{\rm sdB} = 0.26\,{\rm M}_\odot$. This yields a stellar radius of $R_{\rm sdb} = 0.12\,{\rm R}_\odot$ and subsequently an inclination angle of $i = 26^\circ$. From the mass function, a companion's mass of $M_{\rm comp} = 1.2\,{\rm M}_\odot$ can be derived which indicates a high mass white dwarf companion. The systems total expansion becomes $A_{\rm tot} = 2.7\,{\rm R}_\odot$, whereas orbit and orbital velocity of the subdwarf are $A_{\rm sdB} = 2.2\,{\rm R}_\odot$ and $v_{\rm sdB} = 260\,{\rm km\,s^{-1}}$. Corresponding results for the white dwarf are $A_{\rm WD} = 0.5\,{\rm R}_\odot$ and $v_{\rm WD} = 57\,{\rm km\,s^{-1}}$. Although the system's merging time is close to the Chandrasekhar mass limit, the system will not qualify for a SN Ia precursor due to its large merging time.

Table 7.10: Scenarios for HE 0929−0424.

Scenario	i [deg]	$M_{\rm vis}$ [$M_\odot$]	$M_{\rm invis}$ [$M_\odot$]	$M_{\rm tot}$ [$M_\odot$]	$t_{\rm m}$ [Gyrs]	SN Ia - prec.	nature of companion
bd. rot. & post-EHB	19	0.47	2.7	2.37	6.1	no	neutron star
bd. rot. & post-RGB	26	0.26	1.2	1.46	19.5	no	massive WD
max. i	90	0.47	0.36	0.83	29.8	no	low mass WD or late type MS
most likely i	52	0.47	0.51	0.98	22.2	no	C/O-core WD
$M_{\rm tot} \approx M_{\rm Chandra}$	≈33	0.47	≈0.93	≈1.40	≈13.7	yes	most massive WD
$M_{\rm invis} \approx M_{\rm Chandra}$	≈26	0.47	≈1.40	≈1.87	≈10.0	yes	most massive WD

In addition, we also want to discuss the situation if rotation is not tidally locked to the orbit. Assuming a canonical sdB mass for the visible component of HE 0929−0424 and an inclination angle of $i = 90^{o}$ we derive a minimum mass of $M_{\rm comp} = 0.36\,{\rm M}_{\odot}$ for the companion. Thus it is either a late type main sequence star or a low mass white dwarf. The systems separation becomes $A_{\rm tot} = 2.3\,{\rm R}_{\odot}$. Both components are at $A_{\rm sdB} = 1.0\,{\rm R}_{\odot}$ and $A_{\rm comp} = 1.3\,{\rm R}_{\odot}$ respectively. Their orbital velocities are $v_{\rm sdB} = K = 114\,{\rm km\,s^{-1}}$ and $v_{\rm comp} = 148\,{\rm R}_{\odot}$.

For the most probable inclination of $i = 52^{o}$, however, the invisible companion becomes $M_{\rm comp} = 0.51\,{\rm M}_{\odot}$, which is most likely a C/O core white dwarf. The separation of the system can be computed to be $A_{\rm tot} = 2.4\,{\rm R}_{\odot}$. In this scenario, the sdB circles around the barycenter at $A_{\rm sdB} = 1.3\,{\rm R}_{\odot}$ ($v_{\rm sdB} = 145\,{\rm km\,s^{-1}}$) whereas the companion is at $A_{\rm comp} = 1.2\,{\rm R}_{\odot}$ ($v_{\rm comp} = 133\,{\rm R}_{\odot}$).

An overview about different scenarios for HE 0929−0424 is given in table 7.10.

7.2.4 HE 1421−1206

α_{2000}= 14:24:08.81, δ_{2000}= −12:20:21.5, V = 15.21

History

HE 1421−1206 was miss-classified to be an DA white dwarf from the Hamburg/ESO survey (Christlieb et al. 2001) and thus entered our SPY project. These spectra did not only show evidence for a large radial velocity shift about of $50\,\mathrm{km\,s^{-1}}$, but furthermore reveal that HE 1421−1206 is an sdB star rather than a white dwarf. Nevertheless, in order to probe binary evolution theory by means of an unbiased sample, the star was included into our follow-up campaigns. Observations were carried out at the WHT in January 2003 by Gijs Nelemans and at the VLT in March 2003 by Ralf Napiwotzki.

Radial velocity curve

Radial velocity measurements are based on the Hα line since there is no evidence for helium in HE 1421−1206. Figure 7.17 shows the resulting power spectrum and the best fit RV curve. A period of $P = 1.188062^{\mathrm{d}}$ ($1^{\mathrm{d}}4^{\mathrm{h}}31^{\mathrm{m}}35^{\mathrm{s}}$), a system's velocity of $\gamma = -86.2 \pm 1.1\mathrm{km\,s^{-1}}$ and a semi-amplitude of $K = 55.5 \pm 2.0\,\mathrm{km\,s^{-1}}$ can be derived. As can be seen from the inset of figure 7.17, an alias at $P = 1.189308^{\mathrm{d}}$ cannot be ruled out. This alias, however, is only at $\Delta P = +1^{\mathrm{m}}48\mathrm{s}$ to the main peak, corresponding to a relative error for the period of about 0.1 %. The ephemeris of HE 1421−1206 is

$$HJD(T_0) = 2\,453\,099.471101 \pm 1.188062 \times E. \tag{7.8}$$

Spectral analysis

We did not perform a spectral analysis for HE 1421−1206 because no additional high-resolution spectra have been taken and thus we refer to the results of Lisker et al.(2004). This study yields $T_{\mathrm{eff}} = 29570\,\mathrm{K}$, $\log g = 5.55$ and $n_{\mathrm{He}} \leq$-4.00.

System composition

By means of the mass function, we can estimate the system parameters for a given scenario. Assuming a canonical mass of 0.47 $\mathrm{M_\odot}$ for the sdB and an inclination of $i = 90^{\mathrm{o}}$, the mass function ($f_{\mathrm{m}} = 0.021\,\mathrm{M_\odot}$) results in $M_{\mathrm{comp}} = 0.21$ $\mathrm{M_\odot}$ for the minimum mass of the unseen companion. Subdwarf and companion are at $A_{\mathrm{sdB}} = 2.9\,\mathrm{R_\odot}$ and $A_{\mathrm{comp}} = 1.3\,\mathrm{R_\odot}$, respectively, from the barycenter. The system's total extension becomes $A_{\mathrm{tot}} = 4.2\,\mathrm{R_\odot}$. The orbital velocities of the component is $v_{\mathrm{comp}} = 122\,\mathrm{km\,s^{-1}}$ while the sdB has a velocity equal to the radial velocity semi-amplitude.

The most probable composition for the system results from an inclination of $i = 52^{\mathrm{o}}$. The companion's mass becomes $M_{\mathrm{comp}} = 0.29$ $\mathrm{M_\odot}$. The separation of the components increases to $A_{\mathrm{tot}} = 4.3\,\mathrm{R_\odot}$, whereas the orbital velocities decrease to $v_{\mathrm{sdB}} = 70\,\mathrm{km\,s^{-1}}$ (at $A_{\mathrm{sdB}} = 1.6\,\mathrm{R_\odot}$) and $v_{\mathrm{comp}} = 113\,\mathrm{km\,s^{-1}}$ (at $A_{\mathrm{comp}} = 2.7\,\mathrm{R_\odot}$), respectively.

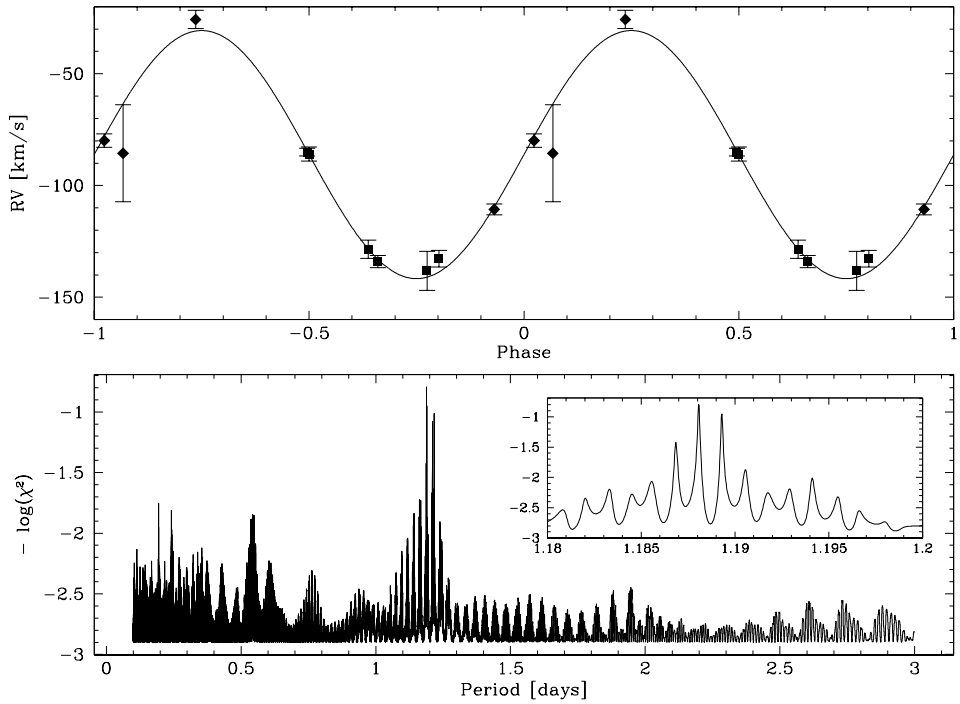

Figure 7.17: Best fit RV curve and power spectrum for HE 1421−1206. Upper panel: Measured radial velocities as a function of orbital phase and fitted sine curves. Squares are used for VLT observations and diamonds for data provided by Gijs Nelemans. Lower panel: Power spectrum of HE 1421−1206.

The results for the companion's mass yields the conclusion that it is either a late type main sequence star or a very low mass He-core white dwarf. Table 7.11 summarizes different scenarios for HE 1421−1206.

Table 7.11: Scenarios for HE 1421−1206.

Scenario	i [deg]	$M_{\rm vis}$ [$M_\odot$]	$M_{\rm invis}$ [$M_\odot$]	$M_{\rm tot}$ [$M_\odot$]	$t_{\rm m}$ [Gyrs]	SN Ia-prec.	nature of companion
max. i	90	0.47	0.21	0.68	680	no	low mass WD or late type MS
most likely i	52	0.47	0.29	0.76	510	no	low mass WD or late type MS
$M_{\rm tot} \approx M_{\rm Chandra}$	≈22	0.47	≈0.93	≈1.40	≈190	no	massive C/O core WD
$M_{\rm invis} \approx M_{\rm Chandra}$	≈17.5	0.47	≈1.40	≈1.87	≈140	no	most massive WD

7.2.5 HE 1448−0510

α_{2000}= 14:51:13.13, δ_{2000}= −05:23:16.9, V = 14.42

History

This is another object miss-classified as a white dwarf from the Hamburg/ESO survey. The first survey spectra taken in July 2000 already reveal the true nature of the visible component in the HE 1448−0510 system which is an sdB star. Although not a white dwarf, a radial shift of about 90 km s^{-1} made HE 1448−0510 a promising object for follow-up observations. Thus the system was re-observed at the DSAZ in February 2002, and during all 2003 runs in (April, May and July).

Radial velocity curve

The high-resolution UVES spectra reveal weak He I (5876 Å) and He II (4686 Å) lines, however, no helium lines can be seen in spectra taken with the TWIN instrument due to low S/N ratios. Thus the radial velocity measurements were done by means of the Hα line core.

Figure 7.18 shows the resulting power spectrum of HE 1448−0510. The outstanding peak corresponds to a period of $P = 7.158756^{\mathrm{d}}$ ($7^{\mathrm{d}}3^{\mathrm{h}}48^{\mathrm{m}}37^{\mathrm{s}}$). The best fit RV curve displayed in the upper panel of the figure yields a system's velocity of $\gamma = -45.5 \pm 0.8 \mathrm{km\,s^{-1}}$ and a semi-amplitude of $K = 53.7 \pm 1.1 \mathrm{km\,s^{-1}}$. The ephemeris of HE 1448−0510 become

$$HJD(T_0) = 2\,453\,097.070275 \pm 7.158756 \times E. \tag{7.9}$$

Spectral analysis

Our spectral analysis was based on a template created from three survey spectra and yields $T_{\mathrm{eff}} = 34690$ K, $\log g = 5.59$ and $n_{\mathrm{He}} = -3.06$. This is in good agreement with the previous study of Lisker et al. (2004) except for the helium abundance, where a difference of $\Delta n_{\mathrm{He}} = 0.35$ becomes obvious.

Although the S/N ratio (≈30) of the template was sufficient, no spectral features except for the Balmer series, He I (5876 Å), He II (4686 Å), Mg II (4481 Å) and probably Si IV (4089 Å) were detected. Nevertheless, we performed a metal abundance analysis in order to derive upper limits at least. Therefore, the line detection limit was estimated by means of measuring "fake" absorption from the noise level. The average noise level – in terms of equivalent width – was subsequently assumed for those lines that are predicted to be strongest in sdB stars. As a reference, the study of Edelmann (2003) was used. Table 7.12 summarizes the results of our study and figure 7.19 displays them with respect to the solar value. Due to the lack of suitable metal lines, neither the microturbulence ξ nor the projected rotational velocity $v_{\mathrm{rot}} \sin i$ could be derived.

System composition

From the semi-amplitude and the period we compute a mass function of $f_{\mathrm{m}} = 0.115\ \mathrm{M}_{\odot}$. Supposing the sdB to have a canonical mass of 0.47 $\mathrm{M}_{\odot}$ and the system's inclination to be

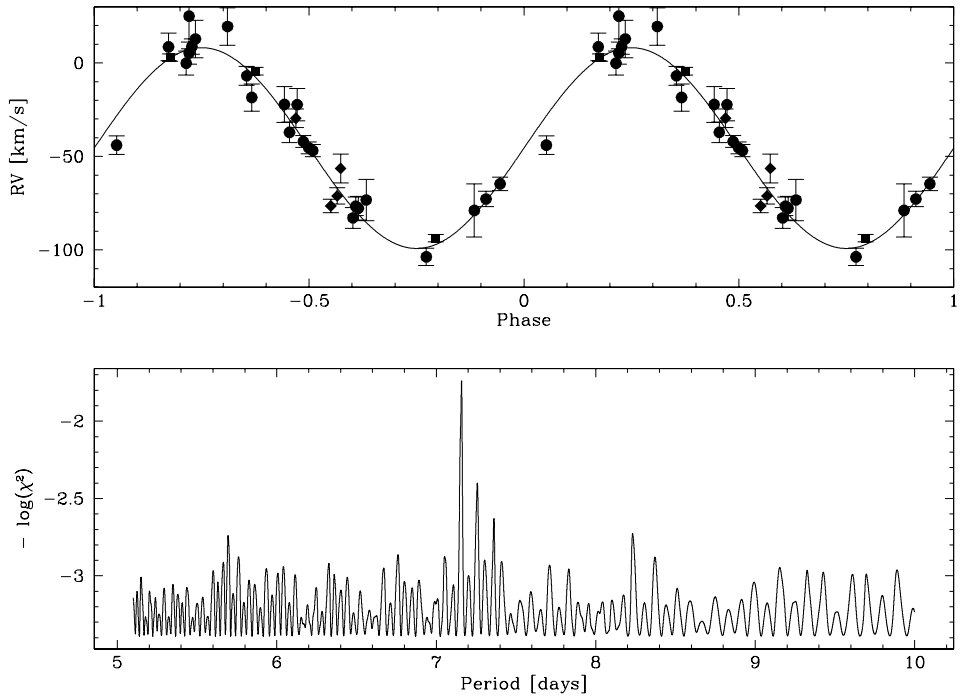

Figure 7.18: Best fit RV curve and power spectrum for HE 1448−0510. Upper panel: Measured radial velocities as a function of orbital phase and fitted sine curves. Squares are used for VLT observations and circles for data based on DSAZ observations. Lower panel: Power spectrum of HE 1448−0510.

Table 7.12: LTE metal abundances for HE 1448−0510. The ion is given in the first column, n is the number of lines used for the analysis and $\log \varepsilon$ is the derived abundance.

ion	n	$\log \varepsilon$
C II	0	$\leq$6.50
N II	0	$\leq$6.75
O II	0	$\leq$6.75
Mg II	1	6.94
Al III	0	$\leq$5.50
Si IV	1	6.36
S III	0	$\leq$8.00
Ar II	0	$\leq$7.50
Fe III	0	$\leq$7.00

$i = 90°$, the minimum mass for the unseen companion becomes $M_{\rm comp} = 0.46\ {\rm M}_\odot$. Both components are separated by $A_{\rm tot} = 15.28\,{\rm R}_\odot$. The orbits and the orbital velocities can also be computed. For the companion we found $A_{\rm comp} = 7.68\,{\rm R}_\odot$ and $v_{\rm comp} = 54.3\,{\rm km\,s^{-1}}$, while the corresponding results for the sdB are $A_{\rm sdB} = 7.59\,{\rm R}_\odot$ and $v_{\rm sdB} = K = 54\,{\rm km\,s^{-1}}$.

The most probable inclination of $i = 52°$, however, yields a slightly different system composition. Now, we compute the companion's mass to be $M_{\rm comp} = 0.68\ {\rm M}_\odot$. Whereas the or-

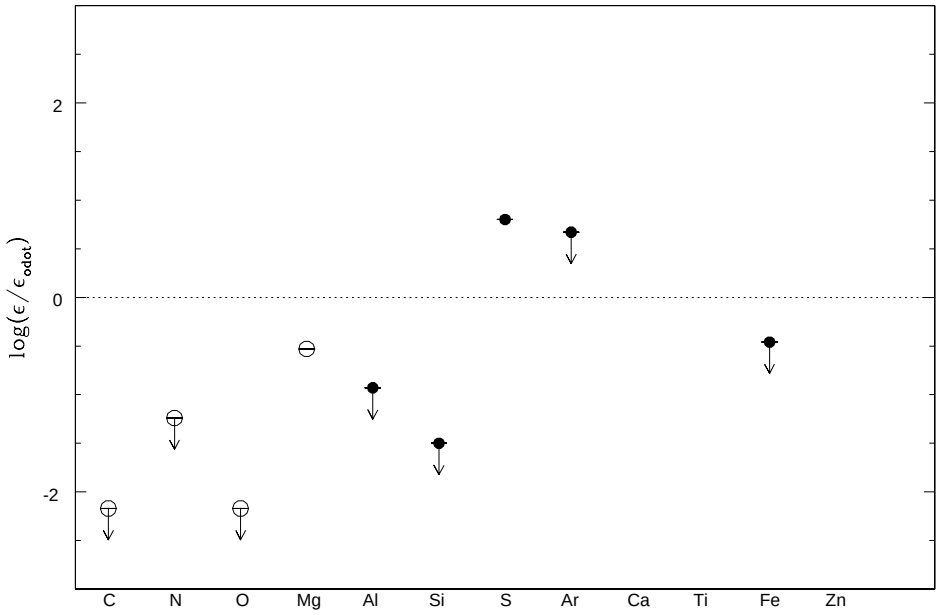

Figure 7.19: LTE abundances with error bars for HE 1448−0510 relative to solar values (dashed horizontal line). Abundances derived from single ionized ions are marked as open circles and from double ionized ions as filled circles.

bit of the sdB increases to $A_{\rm sdB} = 9.63\,{\rm R}_\odot$ ($v_{\rm sdB} = 68.1\,{\rm km\,s^{-1}}$), the orbit of the companion shrinks to $A_{\rm comp} = 6.71\,{\rm R}_\odot$ ($v_{\rm comp} = 47.4\,{\rm km\,s^{-1}}$). Finally, the system's total expansion becomes $A_{\rm tot} = 16.34\,{\rm R}_\odot$ for this scenario.

According to the results for the companions mass we conclude, that the unseen star in the HE 1448−0510 system is most probable a white dwarf with a C/O core. Different scenarios for HE 1448−0510 are summarized in table 7.13.

Table 7.13: Scenarios for HE 1448−0510.

Scenario	i [deg]	$M_{\rm vis}$ [$M_\odot$]	$M_{\rm invis}$ [$M_\odot$]	$M_{\rm tot}$ [$M_\odot$]	$t_{\rm m}$ [Gyrs]	SN Ia - prec.	nature of companion
max. i	90	0.47	0.56	1.03	35 000	no	C/O core WD
most likely i	52	0.47	0.68	1.15	30 000	no	C/O core WD
$M_{\rm tot} \approx M_{\rm Chandra}$	≈41	0.47	≈0.93	≈1.40	≈23 300	no	most massive WD
$M_{\rm invis} \approx M_{\rm Chandra}$	≈32	0.47	≈1.40	≈1.87	≈17 000	no	most massive WD

7.2.6 HE 2135−3749

α_{2000}= 21:38:44.18, δ_{2000}= −37:36:15.1, V = 13.77

History

Like the other sdB stars discussed in this chapter, HE 2135−3749 was miss-classified from the Hamburg/ESO survey as a DA white dwarf. From the UVES spectra taken in August 2001, however, strong helium lines become obvious and thus the star was re-classified to be a subdwarf B rather than a white dwarf. Despite of this, HE 2135−3749 became part of our follow-up campaigns because of its large radial velocity shift of about $140\,\mathrm{km\,s^{-1}}$ found from the survey spectra. The observations were carried out at the VLT and the NTT in June respectively in September 2002.

Radial velocity curve

Within the high-resolution UVES spectra, a large number of He I lines can be seen, e.g. at 4472 Å, 4713 Å, 4922 Å, 5016 AA and 5876 Å. The observations done at the NTT, however, are restricted to the wavelength region centered on Hα. Thus no helium lines can be seen in the medium-resolution spectra taken with EMMI.

Figure 7.20 (lower panel) displays the resulting power spectrum that reveal an outstanding peak at $P = 0.924041^{\mathrm{d}}$ ($22^{\mathrm{h}}10^{\mathrm{m}}37^{\mathrm{s}}$). From the best fit RV curve shown in the upper panel of the figure, a system's velocity of $\gamma = 45.0 \pm 0.5\mathrm{km\,s^{-1}}$ and a semi-amplitude of $K = 90.5 \pm 0.6\,\mathrm{km\,s^{-1}}$ could be derived. The system's ephemeris becomes

$$HJD(T_0) = 2\,453\,099.652040 \pm 0.924041 \times E. \tag{7.10}$$

Spectral analysis

By means of 14 high-resolution UVES spectra a template with an S/N ratio of about 70 was created. The spectral analysis performed thereof results in very accurate stellar atmospheric parameters: $T_{\mathrm{eff}} = 30\,000$ K, $\log g = 5.84$ and $n_{\mathrm{He}} = -2.54$. A comparison with Lisker et al. (2004) yields an almost perfect agreement between the two studies.

The spectrum reveals a large number of species: N II, S II, S III, Ar II, Ar III, Ca III, Ti III, and also two lines we allocate to Zn III. The abundances derived for individual ions are shown in table 7.14. Figure 7.21 displays them with respect to solar values. It became obvious, that the α-process elements Ar, Ca, Ti (and Zn) are enriched, similarly to the "peculiar" sdB to UVO 1758+36 (Edelmann 2003). The microturbulence was estimated from the curve-of-growth of N II lines. Thus $\xi = 0\,\mathrm{km\,s^{-1}}$ was determined.

In order to derive the projected rotational velocity, we fitted synthetic line profiles to our template. Concentrating on the strong N II lines between 5000 Å and 5010 Å, the best fit results in $v_{\mathrm{rot}} \sin i = 4 \pm 1\,\mathrm{km\,s^{-1}}$.

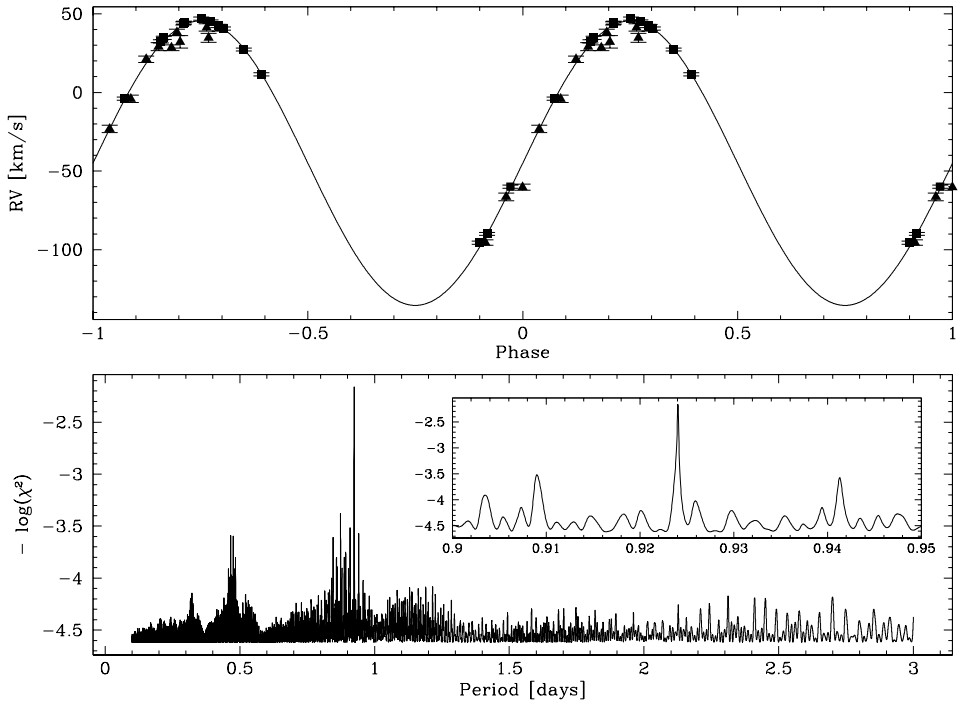

Figure 7.20: Best fit RV curve and power spectrum for HE 2135−3749. Upper panel: Measured radial velocities of HE 2135−3749 as a function of orbital phase and fitted sine curves. Squares are used for VLT observations and triangles for data based on NTT observations. Lower panel: Power spectrum of HE 2135−3749.

Table 7.14: LTE metal abundances for HE 2135−3749. The ion is given in the first column, n is the number of lines used for the analysis and $\log \varepsilon$ is the derived abundance.

ion	n	$\log \varepsilon$
N II	52	7.63±0.17
S II	19	7.08±0.26
S III	15	6.62±0.62
Ar II	43	7.57±0.55
Ar III	7	7.33±0.64
Ca III	5	8.25±0.21
Ti III	29	6.49±0.51
Fe III	17	6.59±0.24
Zn III	2	6.54±0.18

System composition

Assuming the sdB to have the canonical mass of 0.47 $M_\odot$, we can estimate the stars radius to be $R_{\rm sdb} = 0.14\,R_\odot$. For bounded rotation, this yields an inclination of $i = 32°$.

From the mass function of $f_{\rm m} = 0.071\,M_\odot$ we deduce a companion's mass of $M_{\rm comp} = 1.02\ M_\odot$ which is most probably a massive C/O core white dwarf. The systems total extend can be computed to be $A_{\rm tot} = 5.5\,R_\odot$. Orbit and orbital velocity for the sdB becomes $A_{\rm sdB} = 3.1\,R_\odot$

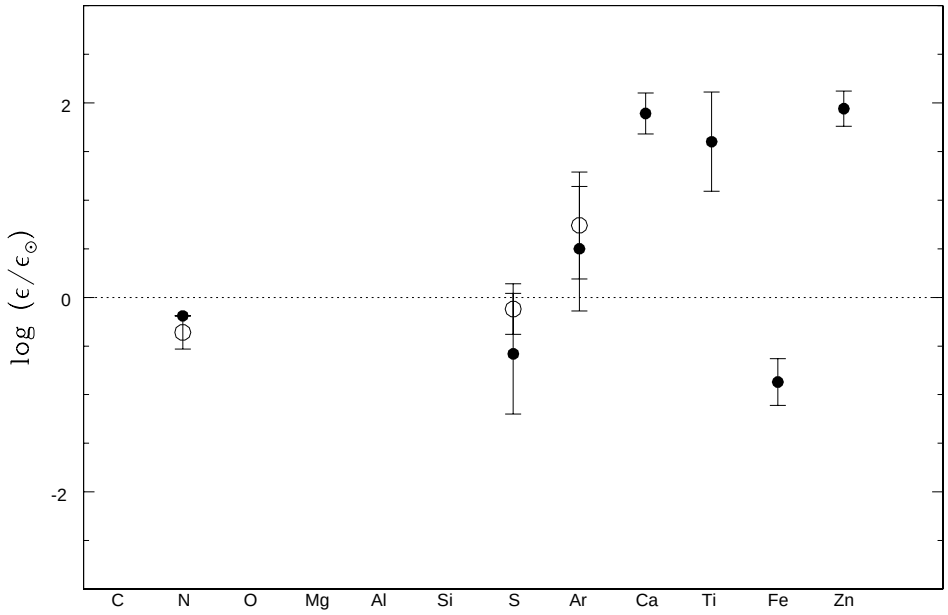

Figure 7.21: LTE abundances with error bars for HE 2135−3749 relative to solar values (dashed horizontal line). Abundances derived from single ionized ions are marked as open circles, from double ionized ions as filled circles and from triple ionized ions as filled triangles.

and $v_{\rm sdB} = 171\,{\rm km\,s^{-1}}$ respectively, Corresponding results for the companion are $A_{\rm comp} = 1.4\,{\rm R}_\odot$ and $v_{\rm comp} = 79\,{\rm km\,s^{-1}}$. Although the system's total mass will exceeds the Chandrasekhar limit, it will not merge within a Hubble time and therefore not qualify as a SN Ia precursor.

Like for the previous systems, we want to discuss the case of unbound rotation as well. The maximum inclination of $i = 90^{\rm o}$ yields the companions minimum mass of $M_{\rm comp} = 0.37\ {\rm M}_\odot$, which indicates either a late type main sequence star or a low mass white dwarf. The separation of both components becomes $A_{\rm tot} = 3.76\,{\rm R}_\odot$, and the orbits are $A_{\rm sdB} = 1.65\,{\rm R}_\odot$ and $A_{\rm comp} = 2.11\,{\rm R}_\odot$ respectively. The orbital velocities can be computed to be $v_{\rm sdB} = K = 90.5{\rm km\,s^{-1}}$

Table 7.15: Scenarios for HE2135−3749.

Scenario	i [deg]	$M_{\rm vis}$ [$M_\odot$]	$M_{\rm invis}$ [$M_\odot$]	$M_{\rm tot}$ [$M_\odot$]	$t_{\rm m}$ [Gyrs]	SN Ia-prec.	nature of companion
bd. rot. & post-EHB	32	0.47	1.02	1.49	92	no	massive white dwarf
max. i	90	0.47	0.36	0.83	30	no	low mass WD or late type MS
most likely i	52	0.47	0.51	0.98	22	no	C/O core WD
$M_{\rm tot} \approx M_{\rm Chandra}$	≈34	≈0.47	≈0.93	≈1.40	≈99	no	massive C/O core WD
$M_{\rm invis} \approx M_{\rm Chandra}$	≈27	≈0.47	≈1.40	≈1.87	≈72	no	most massive WD

and $v_{\rm comp} = 115.6\,{\rm km\,s^{-1}}$.

For the most probable scenario, however, we assume an inclination of $i = 52^{\rm o}$. This results in $M_{\rm comp} = 0.52\ {\rm M}_{\odot}$ for the unseen companion, which is a hint for a white dwarf. The orbits are $A_{\rm sdB} = 2.10\,{\rm R}_{\odot}$ and $A_{\rm comp} = 1.88\,{\rm R}_{\odot}$ respectively, and the orbital velocities are $v_{\rm sdB} = 114.8\,{\rm km\,s^{-1}}$ and $v_{\rm comp} = 103.2\,{\rm km\,s^{-1}}$. Thus, the system's separation becomes $A_{\rm tot} = 3.98\,{\rm R}_{\odot}$. Different scenarios for HE 2135−3749 are summarized in table 7.15.

7.2.7 HE 2150−0238

α_{2000}= 21:52:35.81, δ_{2000}= −02:24:31.6, V = 15.91

History

Like the previous objects, HE 2150−0238 was selected from the Hamburg/ESO survey as a DA white dwarf and subsequently entered our survey. By means of visual inspection of the first UVES spectra taken in August 2001, however, it became evident that HE 2150−0238 is a sdB star rather than a white dwarf. Nevertheless, the object was included in our follow-up campaign because of the radial velocity shift of about 70 km s^{-1} that was determined from the survey spectra. Therefore, additional medium resolution spectra were taken during our August 2002 run at the DSAZ.

Radial velocity curve

From the power spectrum of HE 2150−0238 we derive a period of $P = 1.320880^{\rm d}$ ($1^{\rm d}7^{\rm h}42^{\rm m}4^{\rm s}$), as can be seen from the lower panel of figure 7.22. The inset reveal some aliases at $\Delta P \approx \pm 7^{\rm m}$ which are nearly as likely as the period defined by the main peak. However, the relative error caused by these aliases is less than 0.3 % and will therefore not influence the further discussion. From the best fit RV curve displayed in the upper panel of figure 7.22 a system's velocity of $\gamma = -32.5 \pm 0.9$km s^{-1} and a semi-amplitude of $K = 96.3 \pm 1.4$ km s^{-1} was derived. The ephemeris of HE 2150−0238 becomes

$$HJD(T_0) = 2\,453\,100.608050 \pm 1.320880 \times E. \tag{7.11}$$

Spectral analysis

Due to the fact that HE 2150−0238 was observed at the VLT only in the course of the survey, our template used for the following analysis relys on two high-resolution UVES spectra only. A quantitative spectral analysis done by means of the coadded high-resolution spectra results in the stellar parameters: $T_{\rm eff} = 30200$ K, $\log g = 5.83$ and $n_{\rm He} = -2.44$. These parameters are almost consistent with the results derived by Lisker et al. (2004) who measured $T_{\rm eff} = 29850$ K, $\log g = 5.90$ and $n_{\rm He} = -2.36$.

Despite a low S/N ratio of 25 of the coadded spectrum N II, S III and Ar II lines becomes obvious. For these lines abundances were derived, whereas for C II, O II, Mg II, Al III, Si III and Fe III upper limits were determined by means of the noise level (see HE 1448−0510, section 7.18). The results are summarized in table 7.16 and displayed with respect to solar values in figure 7.23.

The microturbulence was estimated from the curve-of-growth of the N II lines to be $\xi \leq 5$ km s^{-1}. Moreover, in order to obtain the projected rotational velocity we fitted the observed N II lines in the spectral range from 5000 Å to 5010 Å to synthetic profiles. From the best fit we estimate $v_{\rm rot} \sin i = 8 \pm 1$ km s^{-1}.

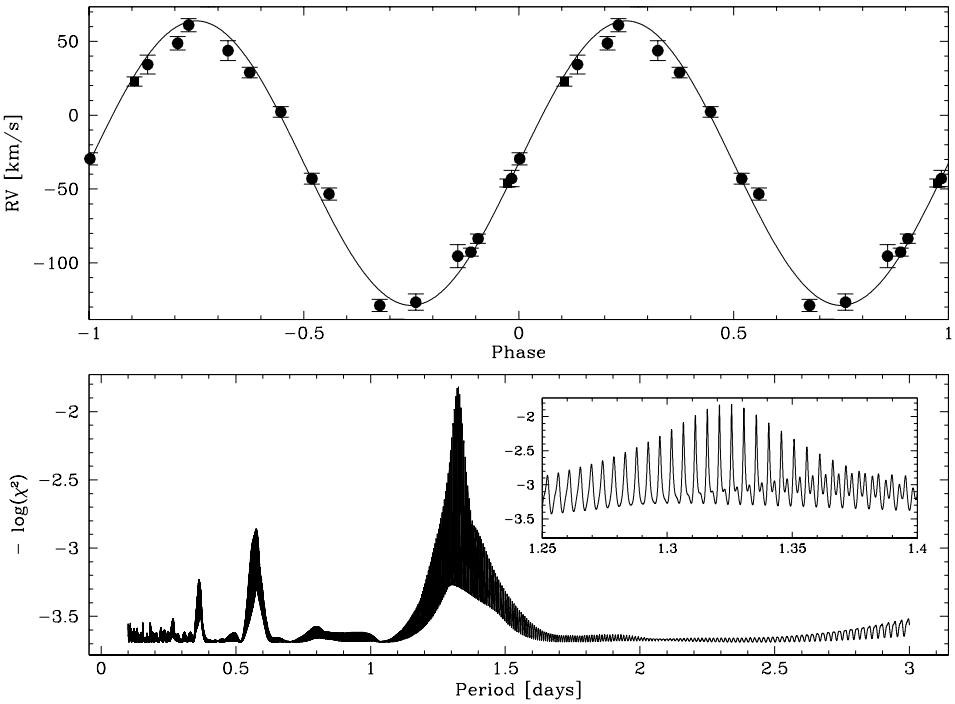

Figure 7.22: Best fit RV curve and power spectrum for HE 2150−0238. Upper panel: Measured radial velocities as a function of orbital phase and fitted sine curves. Squares are used for VLT observations and circles for data based on DSAZ observations. Lower panel: Power spectrum of HE 2150−0238.

Table 7.16: LTE metal abundances for HE 2150−0238. The ion is given in the first column, n is the number of lines used for the analysis and $\log\varepsilon$ is the derived abundance.

ion	n	$\log\varepsilon$
O II	0	$\leq$6.00
N II	20	7.74±0.23
O II	0	$\leq$6.75
Mg II	0	$\leq$6.00
Al III	0	$\leq$5.25
Si III	0	$\leq$5.50
S III	4	6.94±0.11
Ar II	4	7.75±0.13
Fe III	0	$\leq$6.75

System composition

The radius computed for a canonical mass of $0.47\,M_\odot$ is $R_{\rm sdb} = 0.14\,R_\odot$. However, for bounded rotation this results in $\sin i > 1$ (equation 4.6), unless the star has a mass of $1.08\,M_\odot$ (for which $\sin i$ becomes unity) or more. Therefore, a tidally locked scenario can be ruled out for HE 2150−0238.

Nevertheless, we want to discuss the case of non bounded rotation for $i = 90°$ and $i = 52°$.

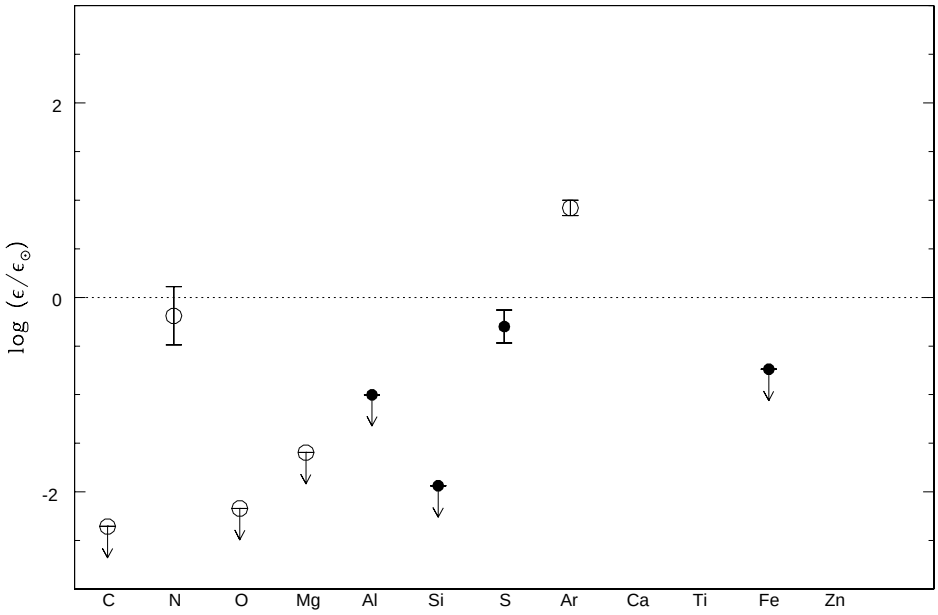

Figure 7.23: LTE abundances with error bars for HE 2150−0238 relative to solar values (dashed horizontal line). Abundances derived from single ionized ions are marked as open circles, from double ionized ions as filled circles and from triple ionized ions as filled triangles.

as we did for the previous systems. The mass function becomes $f_{\rm m} = 0.122\,{\rm M}_\odot$. Assuming a canonical sdB mass of $0.47\,{\rm M}_\odot$ for the sdB and $i = 90^{\rm o}$, we determine the minimum mass of the companion to be $M_{\rm comp} = 0.48\ {\rm M}_\odot$. Because both components have almost the same mass, their orbits and orbital velocities are quite similar. The orbits are $A_{\rm sdB,comp} = 2.5\,{\rm R}_\odot$ whereas the orbital velocities becomes $v_{\rm sdB,comp} = K = 96\,{\rm R}_\odot$. The total separation of the components is $A_{\rm tot} = 5.0\,{\rm R}_\odot$.

The most probable inclination of $i = 52^{\rm o}$ yields $M_{\rm comp} = 0.70\ {\rm M}_\odot$ for the unseen companion. Orbits and orbital velocity of the visible sdB star are $A_{\rm sdB} = 3.2\,{\rm R}_\odot$ and $v_{\rm sdB} = 122\,{\rm km\,s^{-1}}$ respectively. For the unseen component we estimate $A_{\rm comp} = 3.2\,{\rm R}_\odot$ and $v_{\rm comp} = 82\,{\rm km\,s^{-1}}$. The system's total extension becomes $A_{\rm tot} = 5.4\,{\rm R}_\odot$.

Table 7.17: Scenarios for HE 2150−0238.

Scenario	i [deg]	$M_{\rm vis}$ [$M_\odot$]	$M_{\rm invis}$ [$M_\odot$]	$M_{\rm tot}$ [$M_\odot$]	$t_{\rm m}$ [Gyrs]	SN Ia-prec.	nature of companion
max. i	90	0.47	0.48	0.95	440	no	C/O core WD
most likely i	52	0.47	0.70	1.17	320	no	C/O core WD
$M_{\rm tot} \approx M_{\rm Chandra}$	≈38	0.47	≈0.93	≈1.40	≈260	no	massive C/O core WD
$M_{\rm invis} \approx M_{\rm Chandra}$	≈33	0.47	≈1.40	≈1.87	≈190	no	most massive WD

Based on the masses determined above for the unseen companion, we conclude that it is most likely a white dwarf with a C/O core. Table 7.17 gives an overview about different scenarios for HE 2150−0238.

7.3 Subdwarf O primary

Subdwarfs of the spectral type O are hot stars with effective temperatures that ranges from about 30 000 K up to 100 000 K at logarithmic surface gravities of $4.3 \leq \log g \leq 6.5$. From their spectra broad Balmer lines become obvious, accombined by He II absorption (Moehler et al. 1990). The helium abundances varies between $-4.0 \leq n_{\mathrm{He}} \leq 0.3$ (Ströer 2004). Moreover, He-rich sdO stars (He-sdOs) show a large variety of metal lines like carbon, nitrogen, oxygen, neon, magnesium and silicon.

Some sdO stars were classified as DA white dwarfs from the Hamburg/ESO survey (Christlieb et al. 2001) and thus entered our SPY project. The true nature of these objects, however, became obvious by means of visual inspection of the high-resolution UVES spectra taken at the VLT (cf. figure 7.24). Nevertheless, the survey spectra also reveal some highly radial velocity variable objects among the sdO stars.

In the following section, the result of our analysis for three sdO stars is presented.

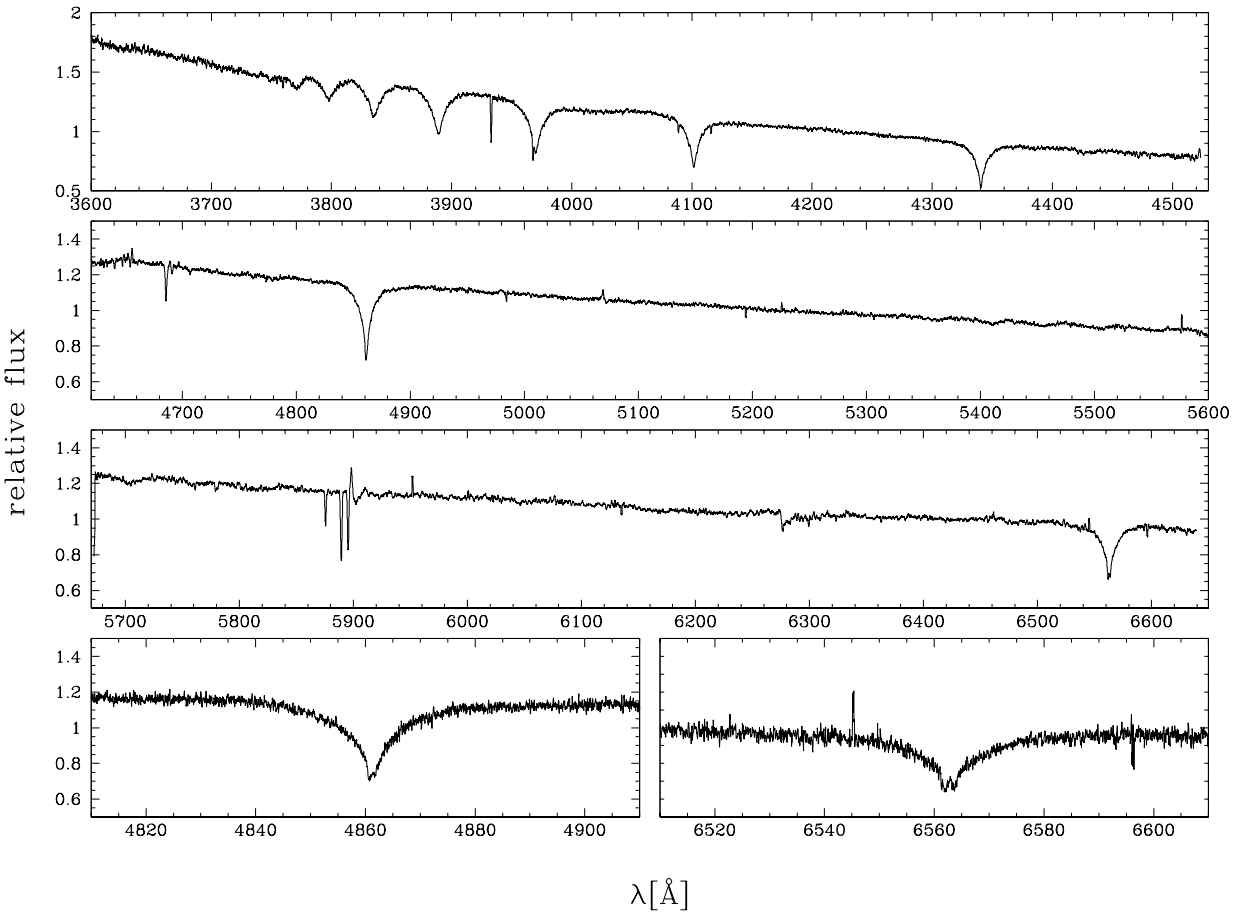

Figure 7.24: Sample UVES spectrum of an subdwarf O star (HE 1318−2111, see section 7.3.3).

7.3.1 HE 1059−2735

α_{2000}= 11:01:24.95, δ_{2000}= −27:51:42.9, V = 15.21

History

Selected to be a DA white dwarf from the Hamburg/ESO survey (Christlieb et al. 2001), HE 1059−2735 was observed five times in the course of our SPY project. However, from the spectra not only the Balmer series but also a strong HeII absorption line at 4686 Å become evident. Thus we classified HE 1059−2735 to be either a DAO white dwarf or a subdwarf of type O. Since a large radial velocity shift of about $100\,\mathrm{km\,s^{-1}}$ was detected from the survey spectra, HE 1059−2735 was re-observed in the course of our follow-up campaigns. Observation were carried out at the ESO VLT in June 2002 and March 2003, and at the NTT in February 2003.

Radial velocity curve

From the sharp, well defined HeII line we made very accurate radial velocity measurements. Our analysis results in an unequivocal period of 0.555624^{d} ($13^{\mathrm{h}}20^{\mathrm{m}}6^{\mathrm{s}}$). The power spectrum can be seen in the lower panel of figure 7.25, whereas the best fit RV curve is displayed in the upper panel. This RV curve gives a system's velocity of $\gamma = -44.7 \pm 0.6\ \mathrm{km\,s^{-1}}$ and a radial velocity semi-amplitude of $K = 87.7 \pm 0.8\ \mathrm{km\,s^{-1}}$. The ephemeris of HE 1059−2735 is

$$HJD(T_0) = 2\,453\,099.835319 \pm 0.555624 \times E. \tag{7.12}$$

Spectral analysis

Recently, a model fit to the observed spectra resulted in $T_{\mathrm{eff}} = 41\,200\,\mathrm{K}$, $\log g = 5.39$ and $n_{\mathrm{He}} = -3.00$ (Ströer 2004). The visible component of HE 1059−2735 has to be a sdO rather than a DAO white dwarf because of the low surface gravity.

System composition

The mass function of $f_{\mathrm{m}} = 0.039\ \mathrm{M_\odot}$ allows a more detailed insight in the HE 1059−2735 system. Assuming the sdO to have a canonical mass of 0.47 $\mathrm{M_\odot}$, we compute a minimum mass for the unseen companion of $M_{\mathrm{comp}} = 0.28\ \mathrm{M_\odot}$ for an inclination of $i = 90^{\mathrm{o}}$. The system's total extend becomes $A_{\mathrm{tot}} = 2.58\,\mathrm{R_\odot}$. Subdwarf and companion are at $A_{\mathrm{sdO}} = 0.96\,\mathrm{R_\odot}$ and $A_{\mathrm{comp}} = 1.62\,\mathrm{R_\odot}$ respectively from the barycenter. Whereas the orbital velocity of the sdO is equal to the radial velocity semi-amplitude for $i = 90^{\mathrm{o}}$, the companion's velocity becomes $v_{\mathrm{comp}} = 147.3\,\mathrm{km\,s^{-1}}$.

The most probable composition for the system results from an inclination of $i = 52^{\mathrm{o}}$. The companion's mass becomes $M_{\mathrm{comp}} = 0.39\ \mathrm{M_\odot}$. The separation of the two components increase to $A_{\mathrm{tot}} = 2.70\,\mathrm{R_\odot}$, whereas the orbital velocities decrease to $v_{\mathrm{sdO}} = 111.3\,\mathrm{km\,s^{-1}}$ (at $A_{\mathrm{sdO}} = 1.22\,\mathrm{R_\odot}$) and $v_{\mathrm{comp}} = 134.8\,\mathrm{km\,s^{-1}}$ (at $A_{\mathrm{comp}} = 1.48\,\mathrm{R_\odot}$), respectively.

For both scenarios, the companion could be either a low mass white dwarf or a late type main sequence star. Infrared photometry could help to distinguish between these options. Therefore

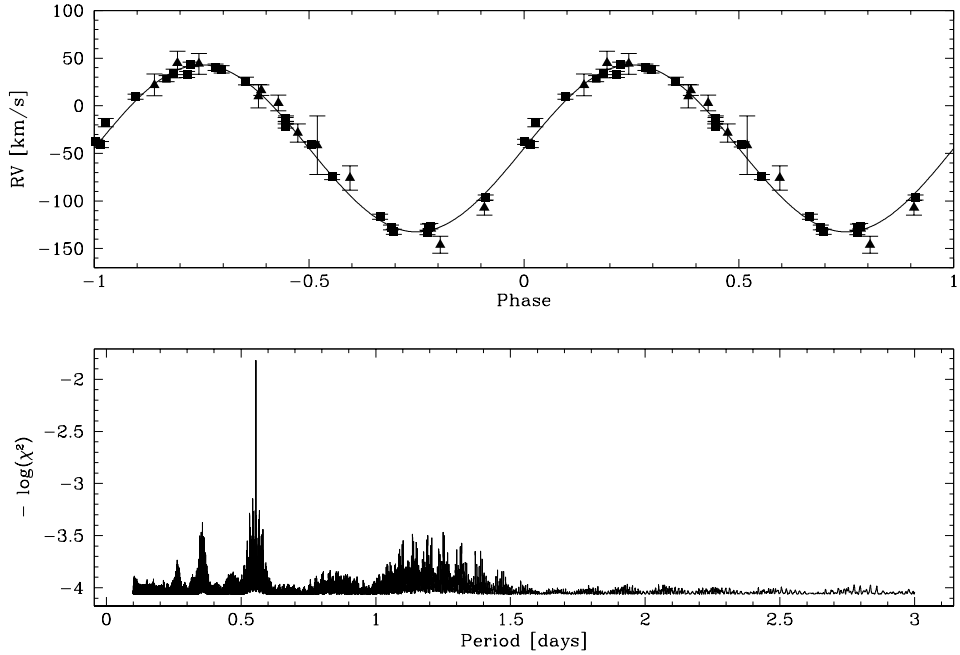

Figure 7.25: Best fit RV curve and power spectrum for HE 1059−2735. Upper panel: Measured radial velocities as a function of orbital phase and fitted sine curves. Squares are used for VLT observations and triangles for observations done at the ESO NTT. Lower panel: Power spectrum of HE 1059−2735.

we checked the *2MASS* database. Unfortunately, the listed error margins are too large to be useful (see Stark & Wade 2003).

Although a late type main sequence star cannot be ruled out, the system companion is probably a low-mass white dwarf with a helium core. This means HE 1059−2735 is indeed a double degenerate system, but it will not qualify as a SN Ia precursor due to its low total mass and its merging time exceeding the Hubble time (cf. table 7.18). Even for a $1.4\,M_\odot$ white dwarf companion – the most massive white dwarf possible – the merging time would still be larger than the current age of the universe.

Table 7.18: Scenarios for HE 1059−2735.

Scenario	i [deg]	$M_{\rm vis}$ [$M_\odot$]	$M_{\rm invis}$ [$M_\odot$]	$M_{\rm tot}$ [$M_\odot$]	$t_{\rm m}$ [Gyrs]	SN Ia-prec.	nature of companion
max. i	90	0.47	0.28	0.75	69	no	low mass WD or late type MS
most likely i	52	0.47	0.39	0.86	52	no	low mass WD or late type MS
$M_{\rm tot} \approx M_{\rm Chandra}$	≈27	0.47	≈0.93	≈1.40	≈26	no	massive C/O core WD
$M_{\rm invis} \approx M_{\rm Chandra}$	≈22	0.47	≈1.40	≈1.87	≈19	no	most massive WD

7.3.2 HE 1115−0631

α_{2000}= 11:18:11.69, δ_{2000}= −06:47:33.2, V = 14.70

HE 1115−0631 was observed for SPY in July 2000 at the ESO VLT. As in the former case of HE 1059−2735 (cf. section 7.3.1), the survey spectra show not only narrow Balmer lines up to $H8$ but also the He II line at 4686 Å. Therefore, we classified HE 1115−0631 to be a sdO star in agreement with the most common classification system described by Moehler et al. (1990). This result is in good agreement with an older study by Kilkenny et al. (1988), classifying HE 1115−0631 alias PG 1115−065 to be a sdB-O star.

The survey spectra reveals a radial velocity shift of 70 km s^{-1}. Nevertheless, being brighter than 15.5 mag HE 1059−2735 qualified for our subsample two and thus entered the follow-up program. Spectra were taken at the DSAZ in February 2002 and April 2003, at the ESO NTT in February 2003 and at the ESO VLT in March 2003. The set of radial velocity measurements was complemented by data provided by Gijs Nelemans. These measurements are based on WHT observation from January and March 2003.

Radial velocity curve

Our radial velocity analysis results in an unambiguous period of 5.868095$^{\mathrm{d}}$ ($5^{\mathrm{d}}20^{\mathrm{h}}50^{\mathrm{m}}3^{\mathrm{s}}$), as can be seen from the power spectrum in the lower panel of figure 7.26. The upper panel of the figure displays the best fit RV curve. A system's velocity of $\gamma = 87.1 \pm 1.3\,\mathrm{km\,s^{-1}}$ and a semi-amplitude of $K = 61.9 \pm 1.1\,\mathrm{km\,s^{-1}}$ were derived. The ephemeris of the visible component of the HE 1115−0631 system is

$$HJD(T_0) = 2\,453\,100.952092 \pm 5.868095 \times E. \tag{7.13}$$

Spectral analysis

A spectral analysis performed by Ströer (2004) results in $T_{\mathrm{eff}} = 40400\,\mathrm{K}$, $\log g = 5.80$ and $n_{\mathrm{He}} = -2.60$.

System composition

From the system's parameter we compute the mass function to be $f_{\mathrm{m}} = 0.144\ \mathrm{M}_{\odot}$. Assuming a canonical mass of 0.47 $\mathrm{M}_{\odot}$ for the sdO and a inclination of $i = 90°$, the minimum mass of the unseen component becomes $M_{\mathrm{comp}} = 0.52\,\mathrm{M}_{\odot}$. Orbit extension and velocity for the companion are $A_{\mathrm{comp}} = 6.5\,\mathrm{R}_{\odot}$ and $v_{\mathrm{comp}} = 56\,\mathrm{km\,s^{-1}}$, respectively. The corresponding results for the sdO are $A_{\mathrm{sdO}} = 7.2\,\mathrm{R}_{\odot}$ for an orbital velocity equal to the radial velocity semi-amplitude. The total expansion of the system becomes $A_{\mathrm{tot}} = 13.7\,\mathrm{R}_{\odot}$.

For the most probable inclination of $i = 52°$, however, we derive $M_{\mathrm{comp}} = 0.77\,\mathrm{M}_{\odot}$, $A_{\mathrm{comp}} = 5.6\,\mathrm{R}_{\odot}$ and $v_{\mathrm{comp}} = 48\,\mathrm{km\,s^{-1}}$. The results for the sdO are $A_{\mathrm{sdO}} = 9.1\,\mathrm{R}_{\odot}$ and $v_{\mathrm{sdO}} = 79\,\mathrm{km\,s^{-1}}$, which means that both components are separated by $A_{\mathrm{tot}} = 14.7\,\mathrm{R}_{\odot}$ totally.

From the companion's masses derived above we finally conclude that it is most likely a white dwarf with a C/O core. As in the case of HE 1059−2735, the system's merging time is many times larger than the Hubble time, and thus HE 1115−0631 will not qualify as a SN Ia progenitor (cf. table 7.19).

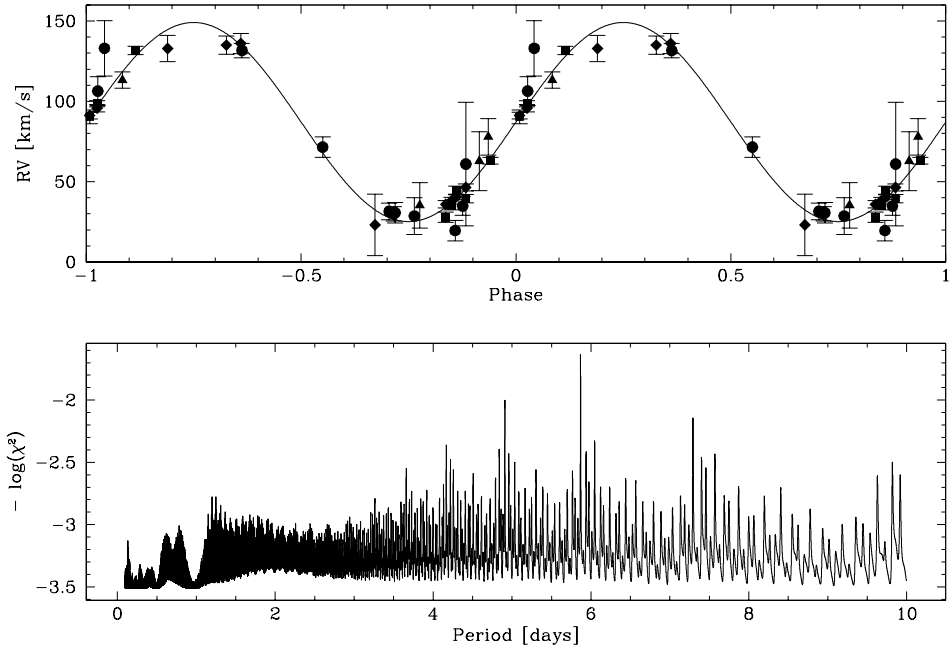

Figure 7.26: Best fit RV curve and power spectrum for HE 1115−0631. Upper panel: Measured radial velocities as a function of orbital phase and fitted sine curve. Squares are used for VLT observations, triangles for observations taken at the NTT and squares for observations from the DSAZ. Data provided by Gijs Nelemans are marked as diamonds. Lower panel: Power spectrum of HE 1115−0631.

Table 7.19: Scenarios for HE 1115−0631.

Scenario	i [deg]	$M_{\rm vis}$ [$M_\odot$]	$M_{\rm invis}$ [$M_\odot$]	$M_{\rm tot}$ [$M_\odot$]	$t_{\rm m}$ [Gyrs]	SN Ia-prec.	nature of companion
max. i	90	0.47	0.52	0.99	21 800	no	C/O core WD
most likely i	52	0.47	0.77	1.24	15 900	no	C/O core WD
$M_{\rm tot} \approx M_{\rm Chandra}$	≈45	0.47	≈0.93	≈1.40	≈13 400	no	massive C/O core WD
$M_{\rm invis} \approx M_{\rm Chandra}$	≈34	0.47	≈1.40	≈1.87	≈10 000	no	most massive WD

7.3.3 HE 1318−2111

α_{2000}= 13:21:15.66, δ_{2000}= −21:27:18.5, V = 14.60

History

Selected from the Hamburg ESO Survey by Norbert Christlieb to be a DA white dwarf (Christlieb et al. 2001), HE 1318−2111 was observed in April and May 2000 and once more in June 2001 and in April 2003. From the spectral appearance, however, it became evident that HE 1318−2111 is not a white dwarf but a subdwarf of type O. (cf. figure 4.1, panels g and h). The spectra reveal moreover radial velocity shift of $40\,\mathrm{km\,s^{-1}}$, which becomes obvious from measurements done by means of the He II lines at 4686 Å. Thus, follow-up observations were performed at the ESO NTT (February 2003), at the VLT (March 2003) and at the DSAZ (February 2000 and May 2003) in order to solve the system's RV curve.

Radial velocity curve

The radial velocity analysis results in an unambiguous period of 0.487502^{d} or $11^{\mathrm{h}}42^{\mathrm{m}}0^{\mathrm{s}}$. The proper power spectrum can be seen in the lower panel of figure 7.27, whereas the upper panel displays the best fit RV curve. The system's velocity and its semi amplitude are $\gamma = 48.9 \pm 0.7\,\mathrm{km\,s^{-1}}$ and $K = 48.5 \pm 1.2\,\mathrm{km\,s^{-1}}$ respectively. The ephemeris of the visible component is

$$HJD(T_0) = 2\,453\,099.857070 \pm 0.487502 \times E. \tag{7.14}$$

Spectral analysis

A spectral analysis of the high-resolution UVES spectra results in $T_{\mathrm{eff}} = 36400\,\mathrm{K}$, $\log g = 5.41$ and $n_{\mathrm{He}} = -2.29$ (Ströer 2004).

System composition

From the system's parameter we compute the mass function to be $f_{\mathrm{m}} = 0.006\ \mathrm{M_\odot}$. Assuming a canonical mass of 0.47 $\mathrm{M_\odot}$ for the sdO and a inclination of $i = 90°$, the minimum mass of the unseen component becomes $M_{\mathrm{comp}} = 0.13\,\mathrm{M_\odot}$. Orbit extension and velocity for the companion are $A_{\mathrm{comp}} = 1.7\,\mathrm{R_\odot}$ and $v_{\mathrm{comp}} = 179\,\mathrm{km\,s^{-1}}$, respectively. The corresponding results for the sdO are $A_{\mathrm{sdO}} = 0.5\,\mathrm{R_\odot}$ for an orbital velocity equal to the RV semi-amplitude. The total extend of the system becomes $A_{\mathrm{tot}} = 2.2\,\mathrm{R_\odot}$.

For the most probable inclination of $i = 52°$, however, we derive $M_{\mathrm{comp}} = 0.17\,\mathrm{M_\odot}$, $A_{\mathrm{comp}} = 1.7\,\mathrm{R_\odot}$ and $v_{\mathrm{comp}} = 171\,\mathrm{km\,s^{-1}}$. The results for the sdO are $A_{\mathrm{sdO}} = 0.6\,\mathrm{R_\odot}$ and $v_{\mathrm{sdO}} = 62\,\mathrm{km\,s^{-1}}$, which means that both components are separated by $A_{\mathrm{tot}} = 2.3\,\mathrm{R_\odot}$ totally.

The companion is most probably a late type main sequence star. Thus, HE 1318−2111 is not a double degenerate system and will therefore not qualify as a SN Ia precursor. Nevertheless, a double degenerate scenario and even a SN Ia precursor can not be ruled out definitely, because for a very low inclination of $i \approx 11°$ the companion's mass is $1.4\,\mathrm{M_\odot}$ and the system's merging time becomes less than a Hubble time (cf. table 7.20).

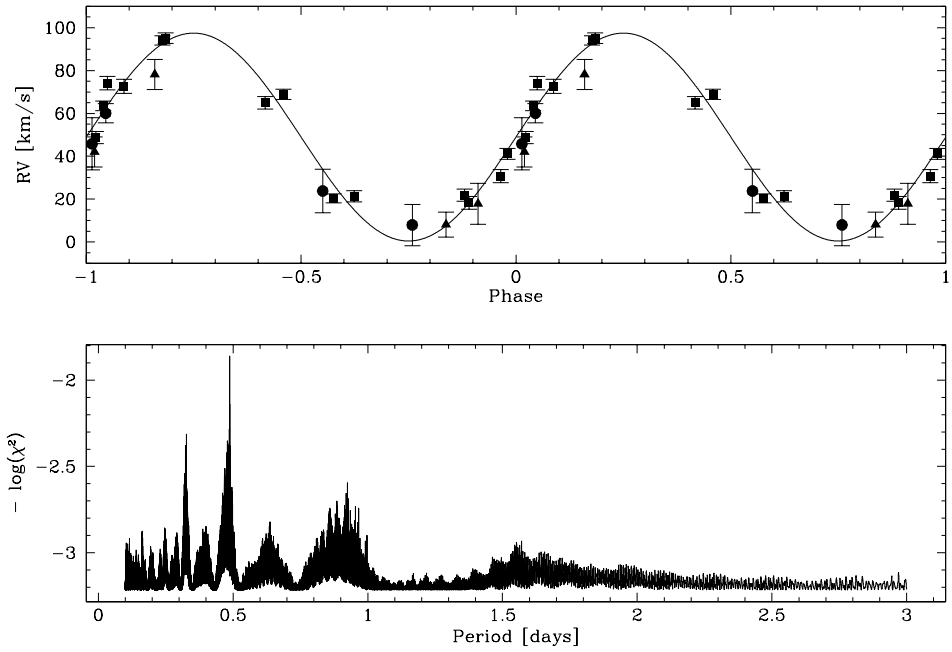

Figure 7.27: Best fit RV curve and power spectrum for HE 1318−2111. Upper panel: Measured radial velocities as a function of orbital phase and fitted sine curve. Squares are used for VLT observations, triangles for observations taken at the NTT and squares for observations from the DSAZ. Lower panel: Power spectrum of HE 1318−2111.

Table 7.20: Scenarios for HE 1318−2111.

Scenario	i [deg]	$M_{\rm vis}$ [$M_\odot$]	$M_{\rm invis}$ [$M_\odot$]	$M_{\rm tot}$ [$M_\odot$]	$t_{\rm m}$ [Gyrs]	SN Ia-prec.	nature of companion
max. i	90	0.47	0.13	0.60	97	no	late type MS
most likely i	52	0.47	0.17	0.64	76	no	late type MS
$M_{\rm tot} \approx M_{\rm Chandra}$	≈14	0.47	≈0.97	≈1.40	≈18	no	massive C/O core WD
$M_{\rm invis} \approx M_{\rm Chandra}$	≈11	0.47	≈1.40	≈1.87	≈13	yes	most massive WD

Chapter 8

Peculiar objects

8.1.1 PN G 2119+226 alias EGB 5, a central star of a planetary nebula

α_{2000}= 08:11:12.77, δ_{2000}= +10:57:16.8, V = 13.83

History

Not a white dwarf but the central star of the planetary nebulae PN G 2119+226, EGB 5 is an immediate precursor of a white dwarf. Mendez et al. (1988) derived $T_{\rm eff} = 42000\,{\rm K}$, $\log g = 5.80$ and $n_{\rm He} = -2.52$ the central star of the nebula (CSPN). Figure 8.1 (Napiwotzki 1999) displays this object in a $T_{\rm eff}$-log g diagram. The dashed lines mark post-RGB evolutionary tracks computed by Driebe et al. (1998; cf. figure 7.14). Therefore, EGB 5 is the result of post-RGB evolution, as becomes obvious from the diagram.

Over the course of three years we obtained more than 50 spectra of this object, taken at the ESO VLT and ESO NTT as well as at the 3.5m telescope of the DSAZ. The sample was complemented by data taken at the WHT in October 2001 and in January 2003.

Radial velocity curve

The spectra reveal lines from the Balmer series as well as He I at 4471 Å and the He II line at 4686 Å. No hint for any other element can be found, even not in the high-resolution spectra taken at the VLT using UVES. Thus we fitted all available helium lines as well as Hα in order to determine the radial velocities. From the power spectrum displayed in the lower panel of figure 8.2 we deduce a period of either $1.111037^{\rm d}$ ($1^{\rm d}2^{\rm h}39^{\rm m}54^{\rm s}$). There are some aliases, however, that we cannot rule out by visual inspection of the proper RV curve. The most significant of these aliases are at $0.547250^{\rm d}$, $1.062039^{\rm d}$ and $1.153744^{\rm d}$. From the best fit RV curve, displayed in the upper panel of figure 8.2, we derive a system's velocity of $\gamma = 65.7 \pm 0.5\,{\rm km\,s^{-1}}$ and a radial velocity semi amplitude of $K = 12.1 \pm 0.8\,{\rm km\,s^{-1}}$. The ephemeris of EGB 5 is

$$HJD(T_0) = 2\,453\,100.250615 \pm 1.111037 \times E. \qquad (8.1)$$

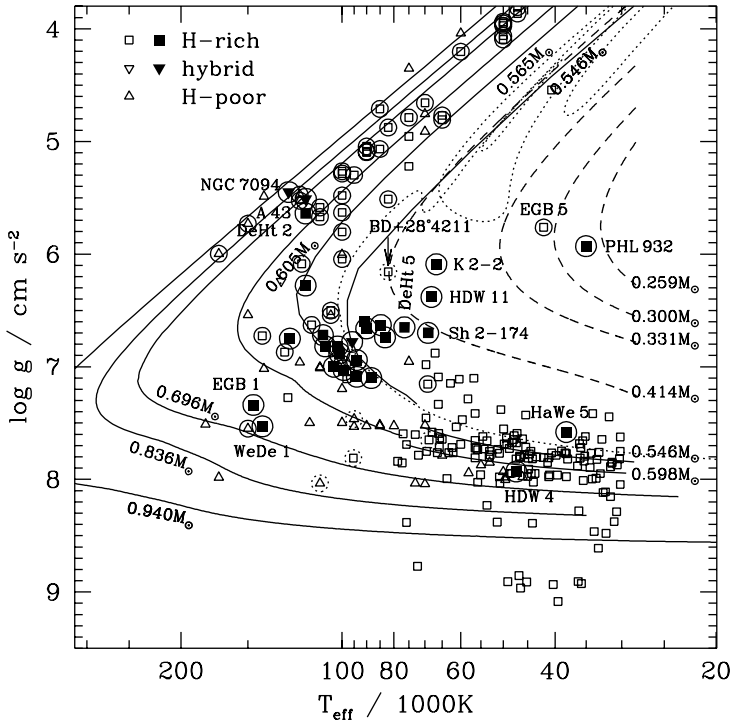

Figure 8.1: $T_{\rm eff}$ - $\log g$ - diagram of hydrogen-rich DA and DAO white dwarfs (squares) and hydrogen-poor objects (triangles) like PG 1159 stars, DO white dwarfs and O(He) post-AGB stars. CSPNe are encircled. Also plotted are evolutionary tracks of post-AGB stars (solid lines), post-RGB stars (dashed lines) and post-early-AGB stars (dotted lines). The figure is taken from Napiwotzki (1999).

System composition

From figure 8.1 we can estimate the mass of the sdB binary to be about $0.31\,{\rm M}_\odot$. The mass function of $f_{\rm m} = 0.0002\,{\rm M}_\odot$ and an inclination of $i = 90^{\rm o}$ yield the minimum mass of the companion of $M_{\rm comp} = 0.03\,{\rm M}_\odot$. The system's total extend, computed by means of equation 5.1, becomes $A_{\rm tot} = 3.2\,{\rm R}_\odot$. Thus, the planetary nebula's central star is at $A_{\rm CSPN} = 0.3\,{\rm R}_\odot$ ($v_{\rm CSPN} = K = 12.1\,{\rm km\,s^{-1}}$) whereas the unseen companion is at $A_{\rm comp} = 2.9\,{\rm R}_\odot$ ($v_{\rm comp} = 131\,{\rm km\,s^{-1}}$).

The most probable inclination of $i = 52^{\rm o}$, however, gives $M_{\rm comp} = 0.04\,{\rm M}_\odot$ and $A_{\rm tot} = 3.2\,{\rm R}_\odot$. Orbit and orbital velocity of the visible companion become $A_{\rm CSPN} = 0.3\,{\rm R}_\odot$ and $v_{\rm CSPN} = 15\,{\rm km\,s^{-1}}$ respectively. Corresponding results for the companion are $A_{\rm comp} = 2.8\,{\rm R}_\odot$ and $v_{\rm comp} = 129\,{\rm km\,s^{-1}}$.

We finally conclude that the companion of the central star is most probably a brown dwarf. If the system's inclination is below 23°, however, also a low mass ($0.08\,{\rm M}_\odot$) late type main sequence star would be possible. The system's composition is very similar to AA Dor, a well known sdOB plus brown dwarf system (cf. Rauch 2000, Rauch & Werner 2003), but the period is much larger. Table 8.1 summarizes different scenarios for EGB 5.

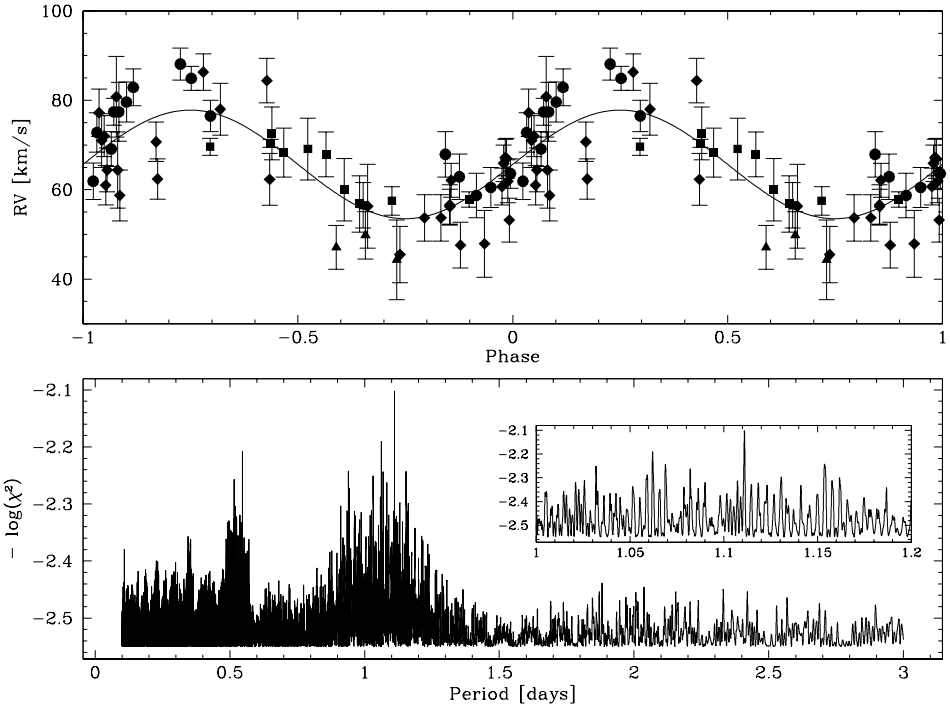

Figure 8.2: Best fit RV curve and power spectrum for PN G 2119+226 or EGB 5. Upper panel: Measured RVs of PN G 2119+226 alias EGB 5 as a function of orbital phase and fitted sine curve. VLT observations are marked as squares, circles indicate 3.5 m DSAZ data, and triangles are used for data taken at the NTT. Diamonds represent RV-data provided by Gijs Nelemans. The observations were done at the WHT. Lower panel: Power spectrum of PN G 2119+226. The inset shows the region near the main peak in more detail.

Table 8.1: Scenarios for PN G 2119+226 alias EGB 5.

Scenario	i [deg]	$M_{\rm vis}$ [$M_\odot$]	$M_{\rm invis}$ [$M_\odot$]	$M_{\rm tot}$ [$M_\odot$]	$t_{\rm m}$ [Gyrs]	SN Ia-prec.	nature of companion
max. i	90	0.31	0.03	0.34	4 800	no	brown dwarf
most likely i	52	0.31	0.04	0.35	3 600	no	brown dwarf
$M_{\rm invis} \approx 0.08\,{\rm M}_\odot$	≈23	0.31	≈0.08	≈0.39	≈1 900	no	minimum mass MS
$M_{\rm tot} \approx M_{\rm Chandra}$	≈4	0.31	≈1.09	≈1.40	≈210	no	massive C/O core WD
$M_{\rm invis} \approx M_{\rm Chandra}$	≈3.5	0.31	≈1.40	≈1.71	≈170	no	most massive WD

8.1.2 WD 1914+094, a white dwarf with a peculiar Hα profile?

α_{2000}= 19:16:50.53, δ_{2000}= +09:34:46.5, V = 15.43

History

Because this object is classified as a DA white dwarf in the actual version of the McCook & Sion Catalogue (1999), WD 1914+094 entered our SPY survey. Four high-resolution spectra were taken at the VLT, revealing a radial velocity shift of up to 60 km s^{-1}. Thus, WD 1914+094 was re-observed during our DSAZ runs in August and October 2002 and in April and May 2003. The data set was complemented by four spectra taken at the NTT in September 2002.

Variable Hα line profile ?

Figure 8.3 displays five medium-resolution TWIN spectra taken in August 18$^{\text{th}}$ 2002 and their best mathematical fit. It seems that the shape of the Hα line profile is temporally variable. Up to now it is not clear, if this time-dependent spectral appearance is due to observational constrains or based on a real physical process. Although an unresolved double-lined system can explain flat line profiles like the top and bottom ones of figure 8.3, this scenario can be ruled out because even the high-resolution UVES spectra show no hint for a companion except the RV shift.

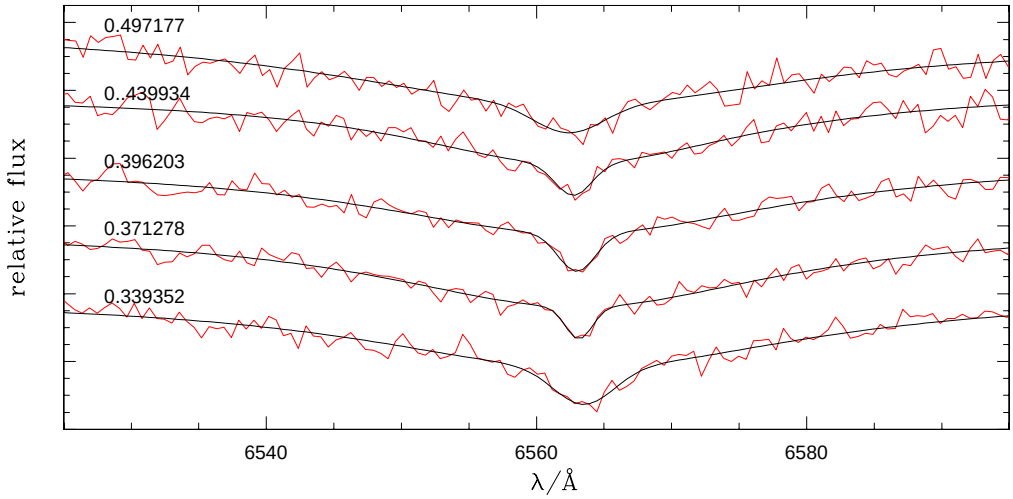

Figure 8.3: Observed Hα line profiles of WD 1914+094 and their best mathematical fit results. All displayed spectra were taken in the night 18th to 19th of August 2002 at the DSAZ 3.5 m telescope equipped with the TWIN instrument. The HJDs (−2,452,505) can be seen on the left hand.

Radial velocity curve

If we include all available RV measurements into our analysis, we derive a power spectrum that yield to 0.218477$^{\text{d}}$ ($5^{\text{h}}14^{\text{m}}36^{\text{s}}$). This result, however, is not very convincing because of the large number of aliases in the periodogram. Moreover, a large number of observed data points match

the best fit RV curve insufficiently. Therefore, we checked the quality of the mathematical fit used for the radial velocity determination and classified all spectra by this means. This was done by a visual inspection. In order to improve our analysis we discarded subsequently all data points classified to be insufficient. This, however, includes also radial velocity measurements based on "peculiar", "flat" Hα line profiles.

The resulting power spectrum and RV curve are much more unambiguously than the previous ones computed for all data points. Moreover, no outliers remains within the RV curve. The system's most probably period is 0.193381^{d} or $4^{\mathrm{h}}38^{\mathrm{m}}28^{\mathrm{s}}$ as can be seen from the lower panel of figure 8.4. From the best fit RV curve (upper panel of figure 8.4) we estimate the system's velocity to be $\gamma = +3.8 \pm 2.3\ \mathrm{km\,s^{-1}}$ and the semi-amplitude to be $K = 21.6 \pm 4.4\ \mathrm{km\,s^{-1}}$. The ephemeris becomes

$$HJD(T_0) = 2\,453\,099.922111 \pm 0.193381 \times E. \tag{8.2}$$

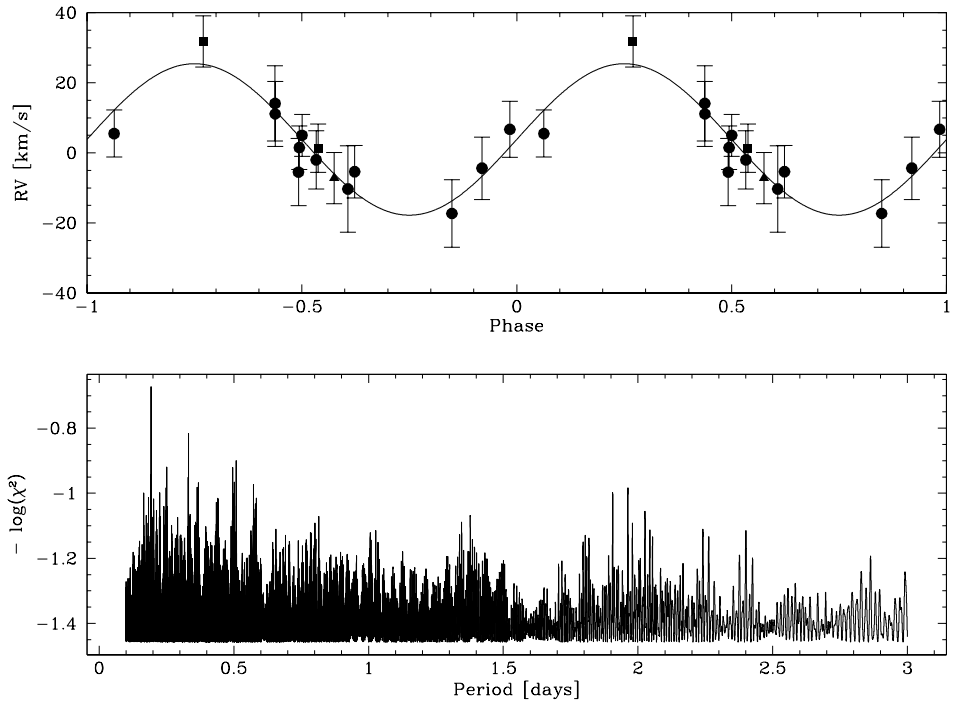

Figure 8.4: Best fit RV curve and power spectrum for WD 1914+094. Upper panel: Measured RVs as a function of orbital phase and fitted sine curves. Squares are used for VLT observations and circles for data based on DSAZ observations. The triangle, however, marks an observation done at the NTT. Lower part: Power spectrum of WD 1914+094.

Spectral analysis

Detlev Koester (priv.com.) already analyzed WD 1914+094 in order to obtain stellar atmospheric parameters. His study results in $T_{\mathrm{eff}} = 32\,000\,\mathrm{K}$ and $\log g = 7.92$. Therefore, we estimate a mass of $M_{\mathrm{WD}} = 0.61\,\mathrm{M}_{\odot}$ for the white dwarf from the Blöcker tracks (cf. figure 4.4).

System composition

The mass function of $f_{\rm m} = 0.0002\,{\rm M}_\odot$ results for an inclination of $i = 90^{\rm o}$ in the companion's minimum mass of $M_{\rm comp} = 0.04\ {\rm M}_\odot$. Its most probable mass is $M_{\rm comp} = 0.06\ {\rm M}_\odot$ (for $i = 52^{\rm o}$). The orbits are quite similar for both scenarios: $A_{\rm WD} \approx 0.1\,{\rm R}_\odot$ and $A_{\rm comp} \approx 1.1\,{\rm R}_\odot$ respectively. The system's total separation become $A_{\rm tot} \approx 1.2\,{\rm R}_\odot$. Orbital velocities of the white dwarf are $v_{\rm WD} = K = 21.6\,{\rm km\,s^{-1}}$ ($i = 90^{\rm o}$) and $v_{\rm WD} = 27\,{\rm km\,s^{-1}}$ ($i = 52^{\rm o}$) respectively. The companion's velocity is nearly constant for both scenarios at $v_{\rm comp} \approx 300\,{\rm km\,s^{-1}}$.

Due to the masses found above for the unseen companion, we conclude that it is most probable a brown dwarf. Table 8.2 gives an overview about the scenarios discussed above.

Table 8.2: Scenarios for WD 1914+094.

Scenario	i [deg]	$M_{\rm vis}$ [$M_\odot$]	$M_{\rm invis}$ [$M_\odot$]	$M_{\rm tot}$ [$M_\odot$]	$t_{\rm m}$ [Gyrs]	SN Ia-prec.	nature of companion
max. i	90	0.61	0.04	0.65	21.2	no	brown dwarf
most likely i	52	0.61	0.06	0.67	14.3	no	brown dwarf
$M_{\rm invis} = 0.08\,{\rm M}_\odot$	$\approx$35	0.61	$\approx$0.08	$\approx$0.69	$\approx$10.8	no	minimum mass MS
$M_{\rm tot} = M_{\rm Chandra}$	$\approx$5.5	0.61	$\approx$0.79	$\approx$1.40	$\approx$1.5	yes	massive C/O core WD
$M_{\rm invis} = M_{\rm Chandra}$	$\approx$4	0.61	$\approx$1.40	$\approx$2.01	$\approx$0.9	yes	most massive WD

Chapter 9

Stars with small RV amplitudes

Although it is unlikely to find a merger candidate among stars that show small radial velocity amplitudes only, we nevertheless re-observed these objects as backup-targets in the course of our follow-up campaigns. In addition, they are useful in order to build an unbiased sample of double degenerates for probing binary evolution theory (e.g. Nelemans et al 2001). For this purpose, it is important to avoid observational biases, i.e. by selecting against long periods and low amplitude systems. Our observations are a the first step toward this sample.

The analyses of objects with small radial velocity amplitudes is difficult and not straight forward, as it has been shown for WD 1914+094 (section 8.1.2). The following section will concentrate on these systems. Therefore we will discuss HE 2208+0126 as an example in more detail, whereas objects with similar characteristics are shown in an overview.

9.1.1 HE 2208+0126

α_{2000}= 22:10:45.57, δ_{2000}= +01:41:35.4, V = 15.26

History

Being classified as a white dwarf from the Hamburg/ESO survey, HE 2208+0126 entered our SPY project and was observed at the VLT in September 2001 and 2002 at the VLT. Although the first UVES spectrum was nearly useless due to a very low S/N ratio, it became obvious that the object was miss-classified, since HE 2208+0126 is not a white dwarf but a sdB star. Regardless of the bad quality of the first UVES spectra, a radial velocity shift of about 30 km s^{-1} was determined by a first analysis of the spectra. Therefore, HE 2208+0126 was re-observed during our July 2003 run at the DSAZ. The routine used to determine the radial velocity shifts from the UVES spectra, however, was improved recently, and thus the former shift was corrected to 2 km s^{-1}.

Radial velocity curve

In the course of our analysis we found that the determination of the system parameters was not simply straight forward. Some of the follow-up observations yield spectra of very low S/N ratios. This results finally in large errors of the radial velocity determination. The resulting power spectrum and RV curve are therefore equivocal with a large number of aliases and outliers respectively. We found that the semi-amplitude is in the same order of magnitude than some of the error margins. Thus we excluded all data points with error limits as large or even larger than the semi-amplitude. Data points lying clearly outside the radial velocity range covered by the RV curve were discarded as "fake" measurements as well.

Figure 9.1 shows the best results for HE 2208+0126 derived this way. For these power spectrum and RV curve, however, we had to discard 14 data points totally. As can be seen from the lower panel of the figure, even this is not an unambiguous result because some aliases still remain. We can also not rule out that HE 2208+0126 is not variable at all. A straight line instead of a time-dependent sine-function fits the observed data points also very well, as can be seen from the dashed line in the upper panel of figure 9.1. Results of all RV measurements – even the discarded ones – are given in table C.1. Although the variability is not given for sure, the best result derived by the method described above yield a period of 0.194545$^{\mathrm{d}}$ or $4^{\mathrm{h}}40^{\mathrm{m}}9^{\mathrm{s}}$. The system parameters obtained by means of the best fitting RV curve are $\gamma = -2.7 \pm 0.9\,\mathrm{km\,s^{-1}}$ and $K = 11.5 \pm 1.2\,\mathrm{km\,s^{-1}}$. The most probable ephemeris is

$$HJD(T_0) = 2\,453\,099.9591 \pm 0.1945 \times E. \tag{9.1}$$

Spectral analysis

By means of a quantitative spectroscopic analysis of the second high-resolution spectrum taken at the VLT, Lisker et al. (2004) determined the stellar parameters of the visible component to be $T_{\mathrm{eff}} = 24277\,\mathrm{K}$, $\log g = 5.67$ and $n_{\mathrm{He}} =$ -2.98.

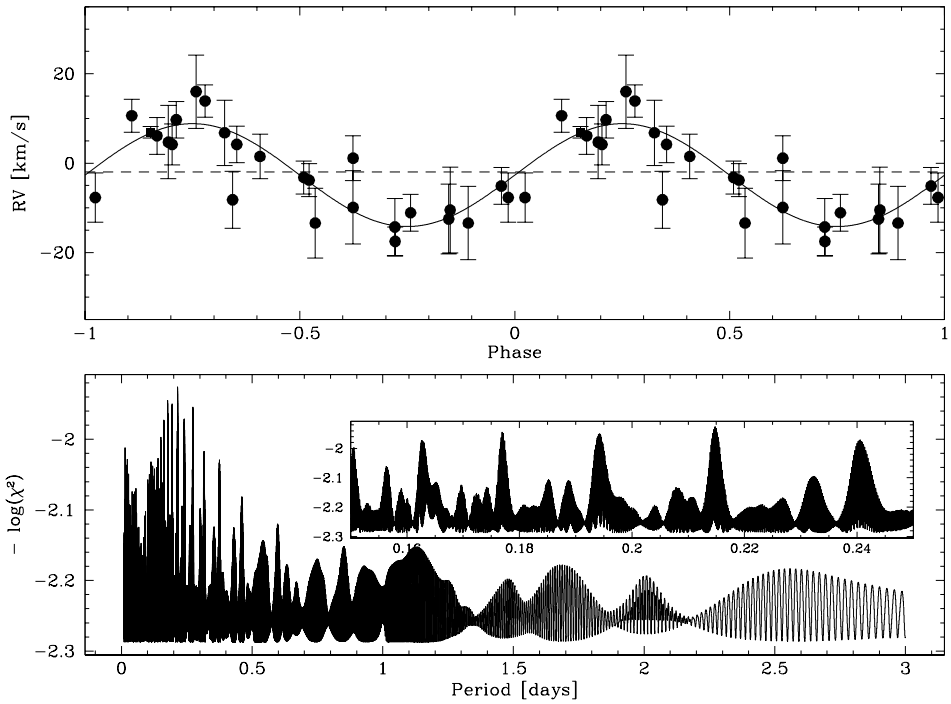

Figure 9.1: Best fit RV curve and power spectrum for HE 2208+0126. Upper panel: Measured RVs as a function of orbital phase and fitted sine curve (solid line). Squares are used for VLT observations and circles for observations done at the DSAZ. The dashed line marks the average radial velocity of $-2.0\,\mathrm{km\,s^{-1}}$. Note that this velocity differs slightly from the system's velocity derived by means of a sine-fit. Lower panel: Power spectrum of HE 2208+0126. The inset displays the region around the main peak in more detail.

System composition

Assuming a canonical sdB mass of $0.47\,\mathrm{M}_\odot$, the mass function of $f_\mathrm{m} = 0.0000307\,\mathrm{M}_\odot$ yields a companion's minimum mass of $M_\mathrm{comp} = 0.02\,\mathrm{M}_\odot$ for an inclination of $i = 90^\mathrm{o}$. The most probable mass (for $i = 52^\mathrm{o}$) is the same due to the small mass functions. Deviations are placed at the third decimal. Thus, a probable companion (if it really exist) is most likely a brown dwarf.

Table 9.1: Scenarios for HE 2208+0126.

Scenario	i [deg]	M_vis [$M_\odot$]	M_invis [$M_\odot$]	M_tot [$M_\odot$]	t_m [Gyrs]	SN Ia - prec.	nature of companion
max. i	90	0.47	0.02	0.49	51	no	brown dwarf
most likely i	52	0.47	0.02	0.49	51	no	brown dwarf
$M_\mathrm{invis} \approx 0.08\,\mathrm{M}_\odot$	≈15	0.47	≈0.08	≈0.55	≈13	no	minimum mass MS
$M_\mathrm{tot} \approx M_\mathrm{Chandra}\,\mathrm{M}_\odot$	≈2.5	0.47	≈0.93	≈1.40	≈1.5	yes	massive C/O core WD
$M_\mathrm{invis} \approx M_\mathrm{Chandra}$	≈2	0.47	≈1.40	≈1.87	≈1	yes	most massive WD

Thus, the sdB is located almost in the system's barycenter, whereas the companion circle at an orbit of $A_{\rm tot} \approx 1.1\,{\rm R}_\odot$. Its orbital velocity is $v_{\rm comp} \approx 280\,{\rm km\,s}^{-1}$

Except for the unlikely case of pole on view this system does definitely not qualify as a SN Ia progenitor. The maximum inclination for a $1.4\,{\rm M}_\odot$ neutron star companion, for example, is below 2°. Table 9.1 summarizes the scenarios discussed above for a probable binary.

9.1.2 WD 0710+216

α_{2000}= 07:13:21.61, δ_{2000}= +21:34:06.8, V = 15.29

History

Being classified as a DA5 white dwarf in the Mc Cook & Sion Catalogue (1999) WD 0710+216 entered our SPY project and was observed twice at the VLT with UVES. In addition, four medium-resolution spectra were taken at the NTT during our January 2004 run.

Radial velocity curve

The power spectrum derived from these six data points formally results in a period of $0.556^{\rm d}$ or $13^{\rm h}20^{\rm m}38^{\rm s}$. The best fit RV curve gives a system's velocity of $\gamma = 36.9 \pm 2.2\,{\rm km\,s^{-1}}$ and a very small semi-amplitude of only $K = 9.8 \pm 4.5\,{\rm km\,s^{-1}}$. Its ephemeris becomes

$$HJD(T_0) = 2\,453\,099.753 \pm 0.556 \times E. \tag{9.2}$$

However, within the error margins almost all individual RV measurements are consistent with each other as can be seen from figure 9.2. Therefore it is possible that WD 0710+216 is not radial velocity variable.

Spectral analysis and system composition

Detlev Koester determined $T_{\rm eff} = 10\,200\,{\rm K}$ and $\log g = 7.97$ for WD 0710+216. Thus, we estimate a mass of $M_{\rm WD} = 0.57\,{\rm M}_\odot$ by means of the Böcker tracks. Table 9.2 summarizes the most important characteristics for WD 0710+216, assuming $i = 90^{\rm o}$, $i = 52^{\rm o}$, the minimum mass main sequence star companion, and the most massive white dwarf companion.

Table 9.2: Scenarios for WD 0710+216.

Scenario	i [deg]	$M_{\rm vis}$ [$M_\odot$]	$M_{\rm invis}$ [$M_\odot$]	$M_{\rm tot}$ [$M_\odot$]	$t_{\rm m}$ [Gyrs]	SN Ia - prec.	nature of companion
max. i	90	0.57	0.02	0.59	740	no	brown dwarf
most likely i	52	0.57	0.03	0.60	490	no	brown dwarf
$M_{\rm invis} \approx 0.08\,{\rm M}_\odot$	≈19	0.57	≈0.08	≈0.65	≈190	no	minimum mass MS
$M_{\rm tot} \approx M_{\rm Chandra}$	≈3.5	0.57	≈0.83	≈1.40	≈24	no	massive C/O core WD
$M_{\rm invis} \approx M_{\rm Chandra}$	≈2.5	0.57	≈1.40	≈1.97	≈16	no	most massive WD

9.1.3 WD 1058−129

α_{2000}= 11:01:12.28, δ_{2000}= −13:14:42.7, V = 14.93

History

Also selected from the McCook & Sion Catalogue (1999), the UVES survey spectra reveal a radial velocity shift of about $10\,\mathrm{km\,s^{-1}}$ only. Nevertheless, the initial VLT observations were complemented over the course of two years by additional observations taken at the NTT, the DSAZ and at the WHT.

Radial velocity curve

However, we found no unambiguous period from the resulting power spectrum, and therefore a non variable scenario can not be ruled out for WD 1058−129. The most probable period is 0.727^{d} or $17^{\mathrm{h}}26^{\mathrm{m}}52^{\mathrm{s}}$. From the best fit RV curve given in figure 9.2 we estimate a semi-amplitude of $K = 11.6 \pm 1.8\,\mathrm{km\,s^{-1}}$ and a system's velocity of $\gamma = 74.8 \pm 1.2\,\mathrm{km\,s^{-1}}$. The ephemeris becomes

$$HJD(T_0) = 2\,453\,099.888 \pm 0.727 \times E. \tag{9.3}$$

However, six data points with error margin up to three times larger than the derived semi-amplitude had been discarded.

Spectral analysis and system composition

Detlev Koester determined $T_{\mathrm{eff}} = 24\,250\,\mathrm{K}$ and $\log g = 8.67$. Because of its high surface gravity, however, the star lies outside the range of the tracks by Blöcker at el. (1997, cf figure 4.4). Thus, we have to extrapolate in order to derive the mass of the white dwarf ($M_{\mathrm{WD}} = 1.00\,\mathrm{M}_\odot$). Table 9.3 summarizes the most important characteristics for WD 1058−129, assuming $i = 90°$, $i = 52°$, the minimum mass main sequence star companion, and the most massive white dwarf companion.

Table 9.3: Scenarios for WD 1058−129.

Scenario	i [deg]	M_{vis} [$M_\odot$]	M_{invis} [$M_\odot$]	M_{tot} [$M_\odot$]	t_{m} [Gyrs]	SN Ia - prec.	nature of companion
max. i	90	1.00	0.05	1.05	420	no	brown dwarf
most likely i	52	1.00	0.06	1.06	350	no	brown dwarf
$M_{\mathrm{invis}} \approx 0.08\,\mathrm{M}_\odot$	≈40	1.00	≈0.08	≈1.08	≈260	no	minimum mass MS
$M_{\mathrm{tot}} \approx M_{\mathrm{Chandra}}$	≈9	1.00	≈0.40	≈1.40	≈60	no	low mass WD
$M_{\mathrm{invis}} \approx M_{\mathrm{Chandra}}$	≈3.5	1.00	≈1.40	≈2.40	≈20	no	most massive WD

9.1.4 WD 1229−012

α_{2000}= 12:31:34.46, δ_{2000}= −01:32:08.5, V = 14.24

History

Maxted et al. (2000a) already found this system to be RV variable. Due to the fact that no period was known so far, we took additional spectra in order to solve the system parameters. Two observations were done in the course of SPY at the VLT, one at the NTT in February 2003 and two more during our March 2003 run at the WHT.

Radial velocity curve

The additional radial velocity measurements based on these observations did not result in an unambiguous solution for the period and the RV curve. Figure 9.2 displays the best fit RV curve derived for the most probable period of 0.187^{d} ($4^{\mathrm{h}}29^{\mathrm{m}}17^{\mathrm{s}}$). A semi-amplitude of $K = 9.4 \pm 2.2\,\mathrm{km\,s^{-1}}$ and a system's velocity of $\gamma = 14.4 \pm 1.0\,\mathrm{km\,s^{-1}}$ can be derived. The ephemeris is

$$HJD(T_0) = 2\,453\,099.938 \pm 0.187 \times E. \tag{9.4}$$

The RV variability found by Maxted et al. (2000a) seems to depend heavily on the data point at $-27.9\,\mathrm{km\,s^{-1}}$. After discarding it, however, the radial velocities can also be fitted very well by a straight line. Thus, the systems variability is not for sure at all.

Spectral analysis and system composition

The spectra analysis performed by Detlev Koester yields $T_{\mathrm{eff}} = 18\,870\,\mathrm{K}$ and $\log g = 7.50$. Thus, we determine the white dwarf's mass to be $M_{\mathrm{WD}} = 0.41\,\mathrm{M}_{\odot}$. Table 9.4 summarizes the most important characteristics for WD 1229−012, assuming $i = 90^{\mathrm{o}}$, $i = 52^{\mathrm{o}}$, the minimum mass main sequence star companion, and the most massive white dwarf companion.

Table 9.4: Scenarios for WD 1229−012.

Scenario	i [deg]	M_{vis} [$M_{\odot}$]	M_{invis} [$M_{\odot}$]	M_{tot} [$M_{\odot}$]	t_{m} [Gyrs]	SN Ia - prec.	nature of companion
max. i	90	0.41	0.01	0.42	100	no	brown dwarf
most likely i	52	0.41	0.02	0.43	50	no	brown dwarf
$M_{\mathrm{invis}} \approx 0.08\,\mathrm{M}_{\odot}$	≈11	0.41	≈0.08	≈0.49	≈13	no	minimum mass MS
$M_{\mathrm{tot}} \approx M_{\mathrm{Chandra}}$	≈2	0.41	≈0.99	≈1.40	≈1.5	yes	massive C/O core WD
$M_{\mathrm{invis}} \approx M_{\mathrm{Chandra}}$	≈1.5	0.41	≈1.40	≈1.81	≈1	yes	most massive WD

9.1.5 WD 1449+168

α_{2000}= 14:52:11.37, δ_{2000}= +16:38:03.5, V = 15.44

History

For being classified as a DA white dwarf in the Mc Cook & Sion Catalogue (1999), WD 1449+168 entered our survey and was observed twice at the VLT. The maximum radial velocity shift found was only about 40 km s^{-1}. Nevertheless, follow-up observations were done at the DSAZ in April and May 2003.

Radial velocity curve

We found a period of 0.328$^{\rm d}$ ($7^{\rm h}52^{\rm m}19^{\rm s}$). The best fit RV curve displayed in figure 9.2 gives a semi-amplitude of $K = 12.9 \pm 2.5\,{\rm km\,s^{-1}}$ only. Therefore, we cannot rule out definitely that the system is not variable at all. The system's velocity we derived by our analysis is $\gamma = 50.4{\rm km\,s^{-1}}$. The ephemeris is

$$HJD(T_0) = 2\,453\,099.976 \pm 0.328 \times E. \tag{9.5}$$

Spectral analysis and system composition

Detlev Koester derived $T_{\rm eff} = 21\,850\,{\rm K}$ and $\log g = 7.68$. Thus, we estimate the white dwarf's mass to be $M_{\rm WD} = 0.48\,{\rm M}_\odot$. Table 9.5 summarizes the most important characteristics for WD 1449+168, assuming $i = 90^{\rm o}$, $i = 52^{\rm o}$, the minimum mass main sequence star companion, and the most massive white dwarf companion.

Table 9.5: Scenarios for WD 1449+168.

Scenario	i [deg]	$M_{\rm vis}$ [$M_\odot$]	$M_{\rm invis}$ [$M_\odot$]	$M_{\rm tot}$ [$M_\odot$]	$t_{\rm m}$ [Gyrs]	SN Ia-prec.	nature of companion
max. i	90	0.48	0.03	0.51	140	no	brown dwarf
most likely i	52	0.48	0.03	0.51	140	no	brown dwarf
$M_{\rm invis} \approx 0.08\,{\rm M}_\odot$	≈21	0.48	≈0.08	≈0.56	≈52	no	minimum mass MS
$M_{\rm tot} \approx M_{\rm Chandra}$	≈3.75	0.48	≈0.92	≈1.40	≈6	yes	massive C/O core WD
$M_{\rm invis} \approx M_{\rm Chandra}$	≈2.5	0.48	≈1.40	≈1.88	≈4.5	yes	most massive WD

9.1.6 WD 1736+052

α_{2000}= 17:38:41.72, δ_{2000}= +05:16:06.3, V = 15.89

History

WD 1736+052 is classified as DA6 white dwarf in the actual version of the McCook & Sion Catalogue (1999) and thus entered our survey. From the survey spectra taken at the VLT, a small radial velocity shift of about $10\,\mathrm{km\,s^{-1}}$ became obvious. Nevertheless, the object was re-observed as a backup-object during our follow-up runs at the DSAZ in 2003.

Radial velocity curve

The power spectrum of WD 1736+052 reveals a large number of aliases that are almost as likely than the main peak at 2.090^{d} or $2^{\mathrm{d}}2^{\mathrm{h}}9^{\mathrm{m}}36^{\mathrm{s}}$. Moreover, these aliases are not concentrated but rather scattered over the full range covered by the periodogram. Thus, the resulting period is equivocal, and a non variable scenario cannot be ruled out either. Nevertheless, the most likely ephemeris

$$HJD(T_0) = 2\,453\,099.268 \pm 2.090 \times E. \tag{9.6}$$

The best fit RV curve can be seen from figure 9.2. This yields a system's velocity of $\gamma = 46.7 \pm 1.0\ \mathrm{km\,s^{-1}}$ and a semi-amplitude of $K = 10.4 \pm 2.1\,\mathrm{km\,s^{-1}}$. Although the RV curve looks not so bad, seven RV measurements have been discarded because of large error margins.

Spectral analysis and system composition

By means of a quantitative spectral analysis, Detlev Koester determined $T_{\mathrm{eff}} = 9\,030\,\mathrm{K}$ and $\log g = 8.20$. Thus, we estimate the white dwarf's mass to be $M_{\mathrm{WD}} = 0.70\,\mathrm{M}_\odot$. Table 9.6 summarizes the most important characteristics WD 1736+052 for assuming $i = 90^\circ$, $i = 52^\circ$, the minimum mass main sequence star companion, and the most massive white dwarf companion.

Table 9.6: Scenarios for WD 1736+052.

Scenario	i [deg]	M_{vis} [$M_\odot$]	M_{invis} [$M_\odot$]	M_{tot} [$M_\odot$]	t_{m} [Gyrs]	SN Ia-prec.	nature of companion
max. i	90	0.70	0.05	0.75	8 900	no	brown dwarf
most likely i	52	0.70	0.07	0.57	6 400	no	brown dwarf
$M_{\mathrm{invis}} \approx 0.08\,\mathrm{M}_\odot$	≈41	0.70	≈0.08	≈0.78	≈5 600	no	minimum mass MS
$M_{\mathrm{tot}} \approx M_{\mathrm{Chandra}}$	≈6.5	0.70	≈0.70	≈1.40	≈780	no	C/O core WD
$M_{\mathrm{invis}} \approx M_{\mathrm{Chandra}}$	≈4	0.70	≈1.40	≈2.10	≈450	no	most massive WD

9.1.7 HS 2108+1734

α_{2000}= 21:10:59.52, δ_{2000}= +17:46:32.8, V = 15.20

History

One of the few objects selected from the Hamburg/Quasar survey HS 2108+1734 reveals a radial velocity shift of about 15 km s^{-1} from the survey spectra. For a definite test of the apparent variability, we re-observed this objects during our July 2003 run at the DSAZ.

Radial velocity curve

Some spectra have a very low S/N ratio. Thus, we classified all data "bye eye" prior to our analysis and discarded those radial velocity measurements based on insufficient spectra. The resulting power spectrum yields a most probable period of $0.355^{\rm d}$ or $8^{\rm h}31^{\rm m}12^{\rm s}$. This result is based on an outstanding peak of the power spectrum. No striking alias becomes evident from the periodogram. However, 17 spectra were discarded for the reasons mentioned above and thus the analysis is based on the remaining 14 ones only. From the best fit RV curve (figure 9.2), we derive a system's velocity of $\gamma = 45.5 \pm 3.1$ km s^{-1} and a semi-amplitude of $K = 29.5 \pm 6.7$ km s^{-1}.

$$HJD(T_0) = 2\,453\,099.968 \pm 0.355 \times E. \tag{9.7}$$

If we try to improve our first "bye eye" classification ("good" and "poor" quality) by means of a third ("in between") category, we found that the results change dramatically. Therefore, we conclude that we need more observations with a good S/N level in order to test the systems variability definitely.

Spectral analysis and system composition

The stellar parameters derived by Koester (priv.com.) are $T_{\rm eff} = 27\,800$ K and logg = 8.57. This yields a dwarf's mass of $M_{\rm WD} = 0.95\,{\rm M}_\odot$ from the Blöcker tracks cf. figure 4.4). Table 9.7 summarizes the most important characteristics HS 2108+1734 for assuming $i = 90^{\rm o}$, $i = 52^{\rm o}$, the minimum mass main sequence star companion, and the most massive white dwarf companion.

Table 9.7: Scenarios for HS 2108+1734.

Scenario	i [deg]	$M_{\rm vis}$ [$M_\odot$]	$M_{\rm invis}$ [$M_\odot$]	$M_{\rm tot}$ [$M_\odot$]	$t_{\rm m}$ [Gyrs]	SN Ia - prec.	nature of companion
max. i	90	0.95	0.10	1.05	32	no	low mass MS star
most likely i	52	0.95	0.13	1.08	25	no	low mass MS
$M_{\rm tot} \approx M_{\rm Chandra}$	≈16	0.95	≈0.45	≈1.40	≈8	yes	low mass WD
$M_{\rm invis} \approx M_{\rm Chandra}$	≈7	0.95	≈1.40	≈2.35	≈3	yes	most massive WD

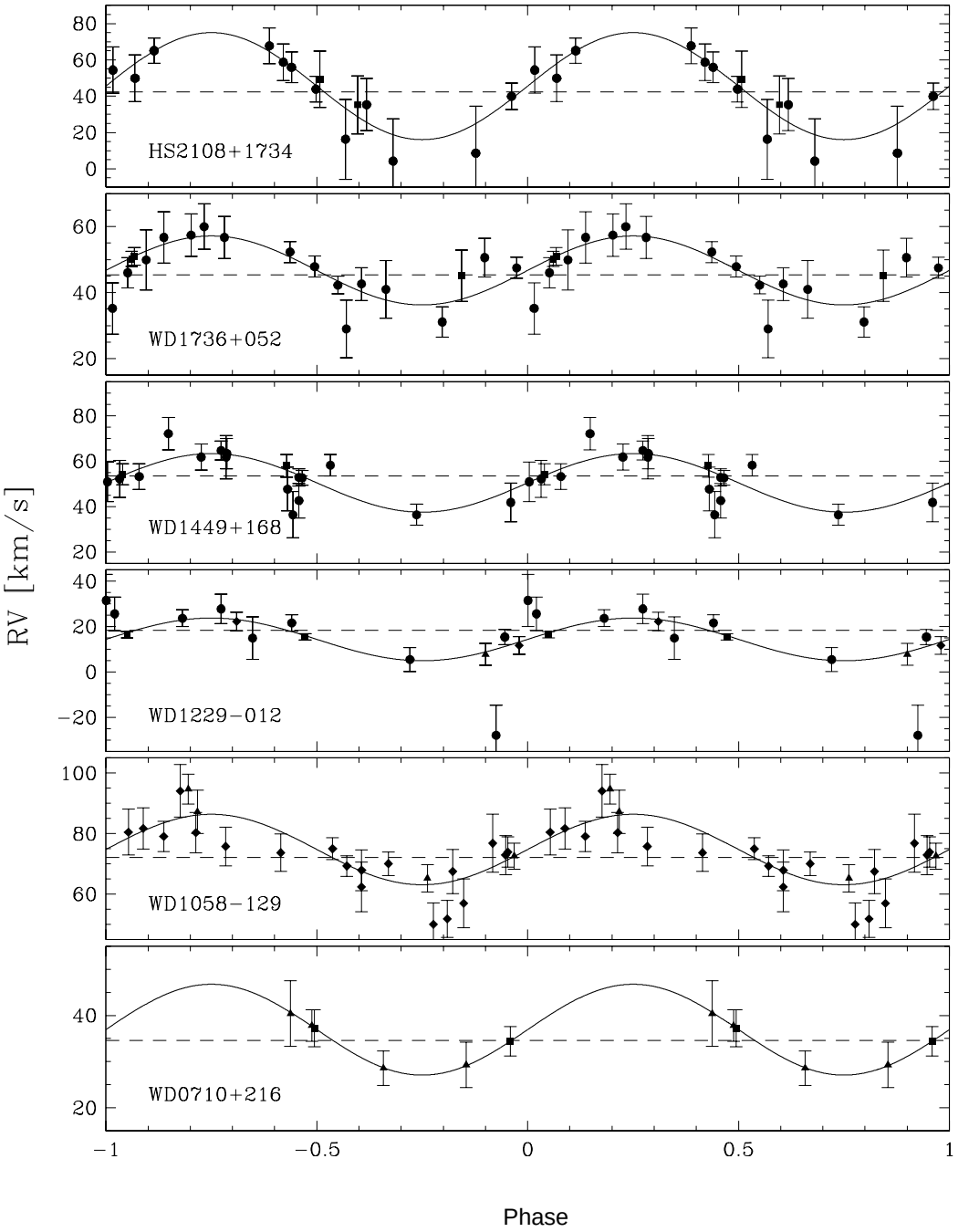

Figure 9.2: Best fit RV curves of WD 0710+216, WD 1058−129, WD 1229−012, WD 1449+168, WD 1736+052 and HS 2108+1734. Squares are used for VLT observations, triangles for NTT observations and circles for observations done at the 3.5 m telescope of the DSAZ. Diamonds are either data points provided by Gijs Nelemans (priv. com.) or taken from Maxted et al. (2000b). The dashed lines mark the average radial velocities. Note that these differ slightly from the system's velocities derived by means of a sine-fit.

Chapter 10

Conclusion and outlook

10.1 Conclusion

In this thesis results are presented from follow-up campaigns of radial velocity variable white dwarfs and hot subdwarfs discovered in the course of the SPY (**S**upernova Ia **P**rogenitor Surve**Y**) project.

Supernovae of type Ia (SN Ia) play an outstanding role for our understanding of galactic evolution and the determination of the extragalactic distance scale. In one of two possible scenarios SNe Ia result from the merging of two white dwarfs (double degenerates) in a close binary system via gravitational wave radiation. According to this scenario, a system qualifies as a SN Ia precursor if its components will merge in less than the Hubble time ($T_{\rm M} \leq T_{\rm H}$) and their total mass exceeds a critical mass limit (which is most likely the Chandrasekhar mass at $M_{\rm Chandra} \approx 1.40\,{\rm M}_{\odot}$). However, theoretical model calculations predict that only $\approx$1/400 white dwarf systems fulfill these criteria (see e.g. Iben et al. 1997, Nelemans et al. 2001).

The intention of SPY is to fortify the double degenerate (or merger) scenario for the evolution of SN Ia events by observational means. Thus, more than 1000 white dwarfs were observed for SPY at the VLT (**V**ery **L**arge **T**elescope) and 137 degenerate stars were identified to be radial velocity (RV) variable. SPY is the largest project searching for radial velocity variations among white dwarfs. The number of examined systems was quintupled and the number of known double degenerates increased by a factor of seven. Most important are 16 so-called double-lined systems, already revealing evidence for a companion in their spectra. Only six of these objects were known before SPY started.

In parallel with the survey, follow-up spectroscopic observations have been started to obtain radial velocity curves from which periods P and RV semi-amplitude K have been determined. Both parameters are crucial for the determination of the merging time $t_{\rm m}$ and the total mass $M_{\rm tot}$ of a binary system, which are the criteria to decide whether or not the system qualifies as a SN Ia precursor. First results were presented by Napiwotzki (HE 1047−0436, Napiwotzki et al. 2001b and HE 1414−0848, Napiwotzki et al. 2002). In this thesis we discussed additional 32 radial velocity variable systems found by SPY. In order to derive their radial velocity curves, these objects were re-observed over the course of three years with 4 to 8 m telescopes.

Six of the observed objects are double-lined systems. Thus, radial velocity analyses provide information not only about the motion of the primary, but also of the secondary. This results in the mass ratio $M_{\rm prim}/M_{\rm sec}$. In addition we made use of the different gravitational redshift of the components to determine the masses of the components of four double-lined binaries

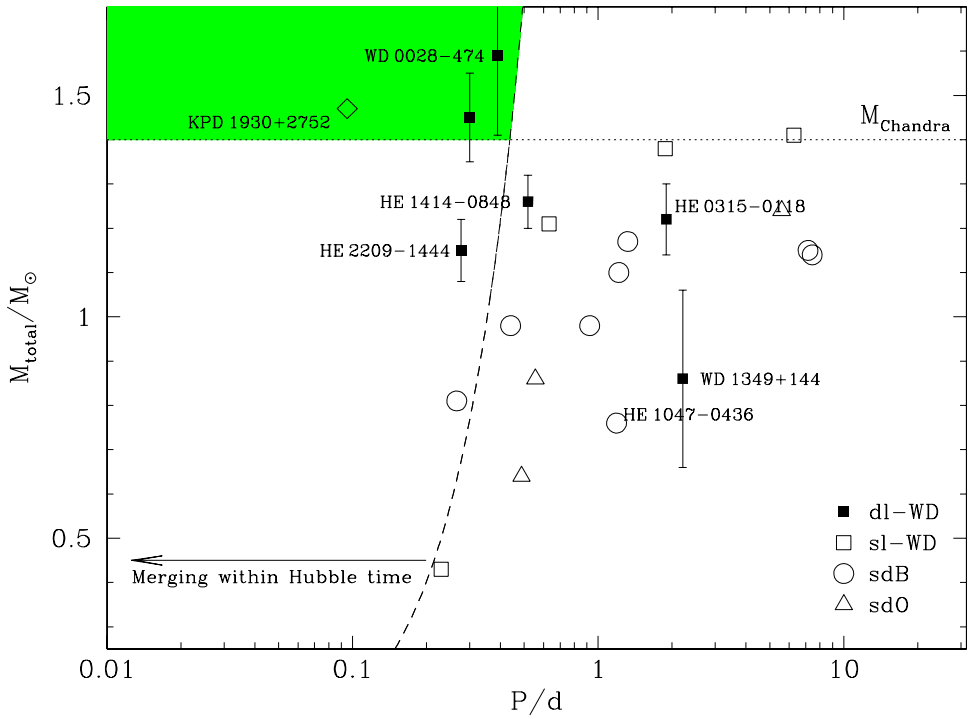

Figure 10.1: System parameters period (P) and masses ($M_{\rm tot}$) of the systems discussed in the chapters 5 (except for WD 0453−295, see text) and 7. The masses of the unseen companions of the single-lined systems (open symbols) are estimated from the mass function for the expected average inclination angle of $i = 52^{\rm o}$. In addition, KPD 1930+2752 (Maxted et al. 2000) is marked as an open diamond. HE 1047−0436 and HE 1414−0848 (Napiwotzki et al. 2001b and 2002, respectively), two binaries discovered in the course of SPY, are marked as well a newly discovered SN Ia precursor candidate (Napiwotzki et al. 2003a). The shaded area in the upper left part of the plot marks the region where SN Ia precursors are expected.

as well as their merging time. The remaining systems were in need of additional spectral analysis by means of a model fit. However, this is usually complicated for double-lined objects because their observed spectra are always a superposition of two individual white dwarf spectra. Nevertheless, a model fit was possible for HE 2209−1444, because both components are quite similar. Therefore, the number of free fit-parameters could be reduced. For the last system WD 0453−295 this turned out to be impossible to do with the spectral analysis tools at hand.

In addition to the double-lined systems, we analyzed a sample of 26 single-lined objects classified as radial velocity variable from SPY. For 17 we derived very accurate orbital solutions, whereas for the remaining systems the solutions are still ambiguous and more observations are needed to solve them definitely.

Since these systems are single-lined, radial velocity analyses reveal less information than for double-lined systems. Only the mass function could be derived, which is an equation of three unknown parameters: The masses $M_{\rm vis}$ and $M_{\rm invis}$ of the two components and the system's inclination angle i. In order to set further constrains to this equation, we have to determine the masses of the visible (primary) components. For the white dwarf primaries, this can be done with the aid of the mass-radius relation and a quantitative spectral analysis. For subdwarf (sd) B and O primaries, we assumed a canonical mass of $0.47\,{\rm M}_{\odot}$ predicted by evolutionary

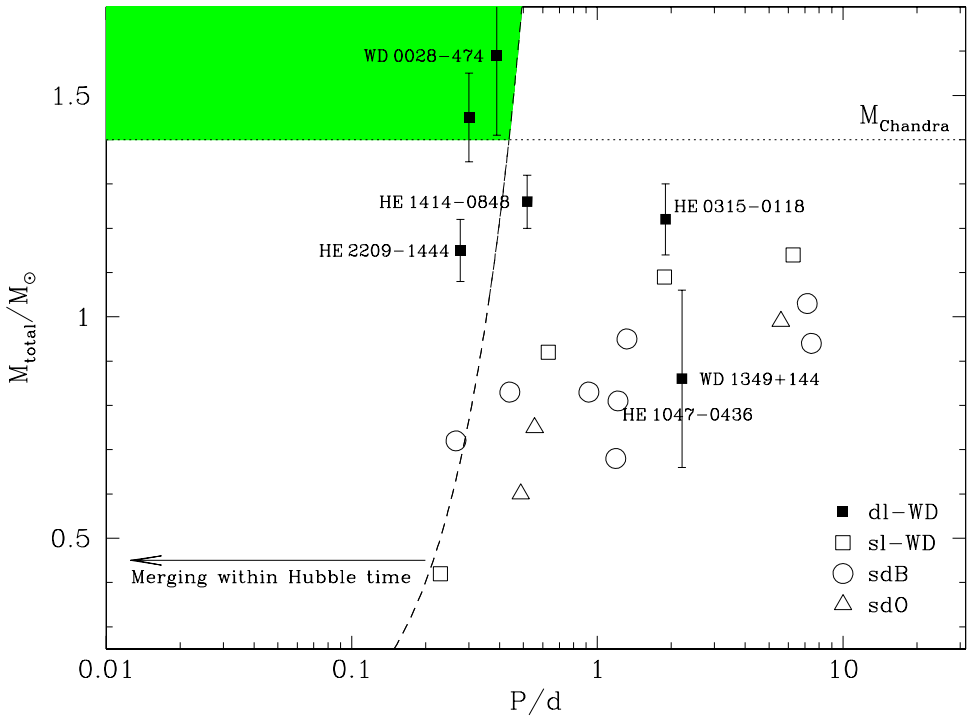

Figure 10.2: The same as in figure 10.1, but for an inclination of $i = 90^{\circ}$ for the single-lined systems.

calculation. Subsequently, we derived the most likely system compositions out of the mass functions and the statistically most probable inclination ($i = 52^{\circ}$). Figure 10.1 displays our results for the double-lined systems from section 5 as well as for the white dwarf primaries from section 7.1, the sdB primaries from section 7.2 and the sdO primaries from section 7.3. The shaded area in the upper left corner marks the region where SN Ia progenitors are expected according to the merger scenario. Whereas the total masses for the double-lined systems are determined (filled symbols), results for the single-line systems (open symbols) are not due to the uncertainty of the inclination. At least the minimum masses of the unseen companions and thus the minimum masses of the systems themselves can be derived if we assume $i = 90^{\circ}$ (figure 10.2). The displayed symbols are therefore lower limits only.

We want to highlight WD 0028−474, a binary system composed of two DA white dwarfs merging in less than a Hubble time. Since the total mass of the system is super-Chandrasekhar within the error margins, the system will most likely explode in an SN Ia event. Thus, it is one of the most promising SN Ia progenitor candidates known so far, besides a further binary discovered in the course of SPY (Napiwotzki et al. 2003a) and KPD 1930+2752 (Maxted et al. 2000c). The latter system, however, is a subdwarf plus white dwarf binary rather than a real double degenerate, and thus some doubts have been raised if it really qualifies as a SN Ia precursor (see Ergma et al. 2001). For WD 0028−474, the error margin is still somewhat large and thus more observations are necessary in order to improve our result.

As can be seen from the figure 10.1 and 10.2, three SN Ia precursor candidates are known so far and two additional systems (HE 1047−0436 and HE 1414−0848) are only 10 - 20 % below the limit. Therefore, the relevance of the merger scenario is strongly enforced, all the more if one considers that only about 30 % of the radial velocity variable objects found by SPY have

been re-observed and investigated as probable SNe Ia precursors up to now. Model calculations have to examine whether or not the fraction of super-Chandrasekhar SN Ia events produced via the merger channel is significant enough to challenge the role of SNe Ia as "standard-candles" for cosmological distance determination.

Simulations of stellar populations forming double degenerates need several input parameters which describe the formation of stars, stellar evolution and the outcome of close binary interactions. One rather uncertain ingredient for the formation of double degenerates is the parameter $\alpha_{\rm CE}$ governing the outcome of the common envelope (CE) evolution. This parameter is defined as the fraction of orbital energy released in the orbital contraction, which is used to eject the envelope. Since this parameter is only weakly constrained by present theoretical calculations, it is essential to calibrate $\alpha_{\rm CE}$ empirically. A precise knowledge of $\alpha_{\rm CE}$ is essential for our understanding of the results of common envelope evolution, namely cataclysmic binaries, very low mass and very high mass white dwarfs and close binary central stars of planetary nebulae. Once the analysis of all double degenerates found by SPY is completed our binary sample will provide an ideal laboratory for this task.

10.2 Outlook

Our analysis for HE 0532−4503, HE 1059−2735, HE 1421−1206 and HE 2135−3749 did not allow us to prove that the invisible companion is a white dwarf. A late type main sequence star cannot be ruled out. This uncertainty could be solved by searching for periodic light variations, because main sequence companions may give rise to reflection effects, whereas white dwarfs are too small to show a measurable reflection (see e.g. Heber et al. 2004 and Maxted et al. 2002c). This method, however, will only work for close binaries ($P \lesssim 1^{\rm d}$) at intermediate inclination angles ($i \gtrsim 30^{\rm o}$). Thus, HE 1421−1206 is probably not suited for such an analysis because of its large period. Nevertheless, photometric monitoring of the remaining objects is urgently need to rule out main sequence companions.

Since the rotation of close binary systems can be assumed to be tidally locked to the orbital motion, we investigated the projected rotational velocities for six sdB stars. This offered the possibility to set constraints to the systems' inclination angles and therefore (via the mass function) to the masses of the unseen companions. However, it had turned out that only for HE 2135−3749 $M_{\rm invis}$ yields a reasonable value. For WD 0048−202 and HE 1448−0510 this could be explained by their rather large periods and separations. Their rotation is most likely decoupled from their orbit therefore. HE 0532−4503, HE 0929−0424 and HE 2150−0238, however, cannot be explained this way since their periods are in between $0.26^{\rm d} \leq P \leq 1.32^{\rm d}$. Thus, we finally conclude that our determinations of the projected rotational velocities are insufficient because the resolution of our spectra was not known for certain. Observations with optimum spectral resolution are needed to improve this study.

Appendix A

Selected DB candidates from the Hamburg ESO Survey

Table A.1: Selected DB candidates from the HES. The Name is given in the first column, whereas the coordinates are displayed in column two and three. Columns four to seven list the luminosity in the V-band and the $B-V$, $U-B$ and the Strömgren $c1$ colour indices. Comments are given in the last column.

Name	α_{2000}	δ_{2000}	V	$B-V$	$U-B$	$c1$	comments
HE 0001−2443	00 04 31.0	−24 26 21	13.7	−0.06	−1.01	−0.26	
HE 0016−3212	00 18 53.2	−31 56 03	14.3	−0.07	−0.68	−0.17	
HE 0017−4419	00 20 11.3	−44 02 37	16.9	−0.15	−0.91	−0.04	
HE 0031−1837	00 33 40.9	−18 20 32	16.8	−0.29	−0.92	−0.01	
HE 0031−5607	00 34 07.7	−55 51 06	15.7	−0.33	−1.13	−0.08	
HE 0048−0343	00 50 45.8	−03 26 56	16.9	−0.38	−1.13	−0.06	
HE 0052−3401	00 54 26.1	−33 45 36	17.1	−0.14	−0.90	−0.14	Friedrich et al. (2000)
HE 0100−0648	01 03 24.4	−06 32 09	13.9	−0.04	−0.89	−0.07	Sion et al. (1999)
HE 0104−4053	01 06 35.8	−40 37 33	16.9	0.04	−0.77	−0.01	
HE 0110−5630	01 12 21.2	−56 14 27	16.0	−0.18	−0.94	−0.06	
HE 0111−1526	01 13 38.2	−15 11 02	14.4	−0.07	−0.97	−0.11	
HE 0119−0026	01 21 48.4	−00 10 52	16.0	−0.07	−0.83	0.01	Sion et al. (1999)
HE 0131−3925	01 33 49.6	−39 09 44	17.0	−0.03	−0.90	−0.32	
HE 0140−0205	01 43 23.6	−01 49 59	16.7	−0.14	−1.02	−0.29	
HE 0142−4710	01 44 17.5	−46 55 45	16.8	−0.28	−1.17	−0.30	
HE 0149−2518	01 51 59.5	−25 03 15	17.2	−0.11	−0.87	−0.03	Friedrich et al. (2000)
HE 0155−3710	01 58 01.4	−36 56 22	15.2	−0.18	−1.05	−0.14	
HE 0202−3914	02 04 43.5	−39 00 12	17.3	0.04	−0.72	−0.03	
HE 0215−0225	02 17 32.6	−02 11 15	16.3	−0.19	−0.80	−0.09	
HE 0249−0514	02 52 15.4	−05 02 34	16.1	−0.14	−0.86	0.01	Sion et al. (1999)
HE 0300−0120	03 02 53.2	−01 08 33	15.4	−0.10	−0.88	−0.06	
HE 0301−3039	03 03 43.9	−30 27 48	15.8	−0.27	−1.15	−0.20	

Name	α_{2000}	δ_{2000}	V	$B-V$	$U-B$	$c1$	comments
HE 0308−5635	03 09 47.7	−56 23 51	14.1	−0.09	−0.96	−0.26	
HE 0335−3925	03 37 45.7	−39 15 51	16.8	0.35	−0.79	−0.15	
HE 0342−1702	03 44 58.8	−16 52 44	14.9	−0.22	−1.05	−0.09	
HE 0414−5429	04 15 30.3	−54 21 59	14.7	−0.12	−0.99	−0.17	
HE 0414−0434	04 16 52.6	−04 27 23	15.7	−0.04	−0.86	−0.05	
HE 0417−5357	04 19 10.1	−53 50 43	15.2	−0.17	−1.14	−0.21	
HE 0420−4748	04 22 11.4	−47 41 43	14.6	0.01	−0.85	−0.04	
HE 0423−0616	04 25 42.2	−06 09 35	17.1	−0.40	−1.19	−0.02	
HE 0423−1434	04 25 51.7	−14 27 52	16.4	−0.27	−0.99	−0.02	
HE 0429−1651	04 32 13.8	−16 45 10	15.8	0.07	−0.81	−0.18	
HE 0433−0700	04 36 19.1	−06 54 13	15.1	−0.11	−1.00	−0.06	
HE 0948+0118	09 51 02.2	+01 04 32	15.8	−0.17	−1.01	−0.23	
HE 0956−1121	09 59 01.3	−11 35 24	16.9	−0.13	−0.98	−0.17	Friedrich et al. (2000)
HE 1026−0539	10 29 02.0	−05 54 27	16.5	−0.22	−1.08	−0.19	
HE 1045−0145	10 48 32.6	−02 01 10	15.8	0.10	−0.92	−0.09	
HE 1149−1320	11 51 50.5	−13 37 14	16.1	0.07	−0.46	−0.20	Friedrich et al. (2000)
HE 1207−2349	12 09 36.7	−24 06 19	16.0	−0.25	−0.88	−0.10	
HE 1326−0343	13 29 16.3	−03 58 52	15.6	0.18	−0.89	−0.14	
HE 1352+0026	13 55 32.4	+00 11 24	15.9	0.17	−0.80	−0.03	Friedrich et al. (2000)
HE 1421−0108	14 24 29.1	−01 22 17	16.3	0.19	−0.70	−0.01	
HE 2026−6000	20 30 20.3	−59 50 39	13.8	0.14	−0.89	−0.21	
HE 2249−5813	22 52 15.1	−57 57 43	16.6	−0.08	−0.82	0.07	
HE 2253−0616	22 55 47.3	−06 00 50	15.2	−0.13	−0.93	−0.10	
HE 2301−6031	23 04 19.3	−60 15 12	15.7	−0.15	−0.77	0.29	
HE 2305−1155	23 08 30.3	−11 38 46	15.9	−0.26	−1.01	−0.04	
HE 2334−4127	23 37 38.4	−41 10 30	15.8	−0.28	−1.06	−0.10	
HE 2347−4130	23 50 19.7	−41 14 01	15.2	0.00	−1.13	−0.25	
HE 2350−3908	23 53 00.7	−38 51 45	16.3	0.16	−0.71	−0.21	

Appendix B

Follow-up campaigns

Table 4.1 gives an overview about all follow-up campaigns performed in the course of our SPY project so far. In addition, the telescopes, instruments, setups and techniques used in order to obtain and reduce the data are described below in more detail.

B.1 Campaigns at the DSAZ 3.5m telescope

We performed 8 follow-up runs totally at the Deutsch - Spanisches Astronomisches Zentrum (DASZ) at Calar Alto, Spain. Over the course of 57 nights, medium resolution spectra were taken with the TWIN spectrograph at the the 3.5 m telescope. Since this instrument allows to observe in two wavelength ranges, a dicroic mirror divided the incomming light at 5500 Å. For the blue arm, we used grating T05, while T06 was used in the red. Both gratings have 1200 lines/mm, resulting in a dispersion of 0.54 Å/pix. The wavelength coverage range from 3900 Å to 5000 Å in the blue at a medium resolution of 1.3 Å. In the red part, the wavelength scale ranges from 6000 Å to 7000 Å at a mean resolution of 1.2 Å.

The data were reduced with a semi-automated program based on a set of standard routines for long slit spectra from the ESO MIDAS package. A two dimensional bias correction was done for the object data as well as for the dome flats. After flatfield correction, the spectra were extracted from the two dimensional images with respect to the sky background. Finally we performed the wavelength calibration using ThAr calibration spectra taken at the same position of the telescope and extracted at the same pixel space on the CCD as the object spectra. For the purpose of normalization, we observed at least one DC white dwarf each night. Since these spetral type does not show any lines in the observed wavelength range, normalization could be done easily for the DC and thereafter assigned to the spectra of the remaining program stars.

The exposure time typically range from 15 minutes for bright stars ($V \leq 13$ mag) up to 30 minutes or more for fainter objects ($V \geq 15$ mag). Objects with outstanding spectral appearance like double lined DA's are given a longer exposure, while stars showing strong features – i.e. emission lines – are less exposed.

B.2 Campaigns at the ESO NTT

Over the course of three runs we had a total of 13 nights of observation at the New Technnology Telescope (NTT) with the ESO Multi Mode Instrument (EMMI). Long slit medium-resolution

spectra were taken in REMD and BLMD mode, respectively.

We used two different setup. In the red, grating No 6 covers a wavelength range from 6160 Å to 6960 Å at a dispersion of 0.39 Å/pix and at a resolution of $R = 5500$. Two MIT/LL CCDs of 2048 x 4096 pixel totally and 0.15 μm pixel-size were used as detectors. This setup was used for objects whoose most interesting feature is the Hα line, i.e. DA white dwarfs or white dwarfs with M dwarf companions.

A second setup optimized for the blue region used grating No 3, centered on 4670 Å. The wavelength scale ranges from 4418 Å to 4919 Å at a dispersion of 0.45 Å/pix and a resolution of $R = 4100$. The detector was also a MIT/LL CCD, but of 1024 x 1024 pixel only. This setup was used for observing Hβ as well as the He I and He II lines at 4471 Å and 4686 Å respectively – i.e. for sdB and sdO stars and for DB and DO white dwarfs.

Exposure times varies between 15 and 45 minutes, depending on luminosity and spectral appearance of the target. For data reduction purposes, the ESO MIDAS program already used for DSAZ 3.5 m data was modified to match NTT conditiones. For more details on the data reduction, we therefore refer to section B.1.

B.3 Campaigns at the ESO VLT

Between 2001 and 2003 we carried out a total of 4 follow-up runs for 12 nights at Paranal observatory. Like for the survey observations, UVES at the UT2 (Kueyen) of the Very Large Telescope (VLT) was used to obtain high-resolution spectra of adequate S/N. The instrumental setup was nearly the same as for SPY except for a smaller slit width. A 0.6" to 1.5" slit, optimized for seeing conditions, was used instead of the larger 2.1" slit used in the survey. For more details on the spectrograph and the data reduction, we refer to section 3.

B.4 Campaigns at the WHT and INT

In October 2001 we had 7 nights at the 2.5 m Isaac Newton Telescope (INT) equipped with the Intermediate Dispersion Spectrograph (IDS). We used the 500 mm camera and R1200R grating for a dispersion of 0.37 Å/pix from 6300 Å to 6700 Å at a resolution of 1 Å. The spectra were reduced (using the overscan bias level and a tungsten flat field) with standard IRAF tasks, using optimal extraction (Horne 1986). To perform the wavelength calibration, CuAr and CuNe were taken at the same position of the telescope and extracted at the same place on the CCD as the object spectra. This typically gives a rms scatter less than 0.015 Å.

In the course of 2003, we also observed 12 nights at the 4.2 m William Herschel Telescope (WHT) equipped with the double-armed, medium-resolution spectrograph ISIS. We used the instrument with a 5700 Å dichroic and a 1.0" slit. In the red channel, grating R1200R was centered on 6550 Å, giving the spectra a mean resolution of 0.74 Å. The dispersion on the MARCONI2 CCD (4k $\times$ 2k, 13.5 μm) was 0.23 Å/pix. In the blue arm, grating R600B was centered on 4700 Å, yielding to a mean resolution of 1.44 Å and a dispersion of 0.45 Å/pix. The detector was a blue sensitive EEV CCD of 4k $\times$ 2k (13.5 μm). The ISIS data reduction was performed in the same way as for the IDS data.

Appendix C

Radial velocity measurements

Table C.1: Radial velocity measurements for all program stars.

Run	mid HJD [−2 450 000]	$RV_{\rm primary}$ [km s^{-1}]	$RV_{\rm secondary}$ [km s^{-1}]
WD 0028−474			
SPY	2212.7189	−50.2±8.9	90.3±64.4 [b]
	2272.5422	82.0±3.7	-21.6±3.9
NTT 09 - 02	2540.5940	34.5±4.0	34.5±4.0
	2540.7419	−23.7±9.4	129.8±5.3
	2540.8547	145.8±6.8	-99.3±9.6
	2540.8807	166.7±6.3	-59.2±32.4 [a]
	2541.5978	96.2±7.1	-51.1±12.2 [a]
	2541.7254	119.1±11.5	-89.5±36.9 [a]
	2542.5920	−44.6±4.9	149.3±6.1
	2542.7218	−0.1±10.8	36.2±4.5
	2542.8677	143.9±7.2	-124.3±9.1
	2543.5428	126.6±10.4	13.9±44.5
	2543.6293	166.3±6.6	-100.1±59.0 [b]
	2543.8052	−100.4±5.2	194.7±24.7 [b]
VLT 11 - 02	2591.5258	160.1±2.1	-125.6±5.3
	2592.5702	−14.7±2.6	46.0±11.9
WD 0048−202			
SPY	1740.7585	−71.1±1.4	
	1743.8381	8.0±1.6	
VLT 10 - 01	2194.5859	−71.3±0.7	
	2195.7036	−70.0±0.7	
WHT 10 - 01	2209.4705	−71.3±3.2	
	2209.4926	−78.9±3.9	
	2213.5032	18.9±4.6	

Run	mid HJD [−2 450 000]	$RV_{\rm primary}$ [km s^{-1}]	$RV_{\rm secondary}$ [km s^{-1}]
	2213.5621	18.0±4.8	
DSAZ 08 - 02	2498.6698	−36.2±2.0	
	2501.1399	−45.1±1.8	
	2502.6523	10.4±3.3	
NTT 09 - 02	2540.6713	14.2±2.5	
	2540.7672	18.0±2.7	
	2540.9020	21.3±6.7	
	2541.6220	24.8±2.5	
	2541.8743	1.6±2.2	
	2541.9132	−0.2±5.5	
	2542.6191	−6.1±2.2	
	2542.6637	−10.6±2.1	
	2542.7486	−18.5±1.7	
	2542.8190	−19.6±2.1	
	2542.8969	−39.0±8.7	
	2543.5863	−37.8±3.6	
	2543.6920	−52.6±3.6	
	2543.7608	−52.8±11.4	
	2543.8271	−60.7±5.0	
	2543.9097	−69.2±6.4	
DSAZ 10 - 02	2563.4734	21.3±8.2	
VLT 11 - 02	2589.5406	−73.6±0.7	
	2589.6436	−74.2±0.7	
	2589.6975	−72.6±1.0	
	2590.5094	−59.8±1.0	
	2591.5198	−21.0±1.0	
WHT 08 - 03	2857.7040	−69.9±3.3	
	2858.6745	−59.1±2.9	
	2858.7452	−51.2±2.3	
	2859.6602	−20.2±3.2	
	2859.7532	−19.8±7.0	
HE 0315−0118			
SPY	1947.5839	1.3±3.4	124.9±3.4
	1949.5505	10.0±3.6	117.5±3.6
VLT 10 - 02	2194.6562	69.9±1.6	conjunction
	2194.7052	71.2±2.2	conjunction
	2194.7376	92.8±5.0	44.9±5.0
	2194.7641	104.2±5.0	42.5±5.0
	2194.8006	116.3±3.8	27.6±3.8
	2194.8432	122.4±3.8	22.4±3.8
	2194.8763	130.9±4.0	20.3±4.0
	2195.6722	51.5±5.0	97.2±5.0
	2195.7142	22.4±2.9	106.0±2.9

Run	mid HJD [−2 450 000]	$RV_{\rm primary}$ [km s^{-1}]	$RV_{\rm secondary}$ [km s^{-1}]
	2195.7470	15.4±1.9	109.3±1.9
	2195.7879	5.6±4.7	120.3±4.7
	2195.8179	−4.7±2.4	122.6±2.4
	2195.8366	−2.2±2.7	123.6±2.7
	2195.8684	−5.4±3.2	125.9±3.2
NTT 09 - 02	2541.7572	65.1±2.7	conjunction
	2541.8480	65.0±4.6	conjunction
	2542.7729	69.7±2.2	conjunction
VLT 11 - 02	2589.6081	64.6±3.4	conjunction
	2589.6734	68.2±1.5	conjunction
	2589.7375	30.6±5.0	99.1±5.0
	2589.7874	11.3±1.7	109.3±1.7
	2590.6488	69.4±1.3	conjunction
	2590.7624	113.2±5.0	29.2±5.0
	2590.8231	126.6±2.1	16.6±2.1
	2591.5619	68.4±1.3	conjunction
	2591.5987	41.4±5.0	87.1±5.0
	2591.6459	27.6±5.0	93.8±5.0
	2591.7048	20.5±5.0	102.3±5.0
	2591.7556	3.0±1.8	114.7±1.8
	2591.8297	−8.2±2.9	127.6±2.9
	2592.5639	71.9±1.9	conjunction
	2592.6148	93.4±5.0	38.6±5.0
	2592.6630	118.3±2.8	31.3±2.8
	2592.6966	123.4±2.4	26.2±2.4
	2592.7524	132.1±2.6	16.4±2.6
	2592.7969	145.3±3.0	11.0±3.0
	2592.8334	143.9±2.5	7.6±2.5
WD 0326−273			
SPY	1737.9246	149.2±10.5	
	1740.8767	−30.4±8.2	
VLT 10 - 01	2194.6468	−22.7±2.3	
	2194.6960	−26.6±1.8	
	2194.7281	−27.1±2.3	
	2194.7547	−28.1±1.8	
	2194.7899	−27.3±2.3	
	2194.8335	−24.7±2.3	
	2194.8833	−18.8±1.8	
	2195.6945	162.1±1.8	
	2195.8255	159.1±0.9	
NTT 09 - 02	2540.7119	155.8±3.3	
	2540.7859	161.1±2.6	
	2540.8050	160.6±2.4	

Run	mid HJD [−2 450 000]	$RV_{\rm primary}$ [km s^{-1}]	$RV_{\rm secondary}$ [km s^{-1}]
	2541.7982	−28.4±2.1	
	2541.8911	−20.8±4.1	
	2542.6806	158.0±1.9	
	2542.7960	152.8±2.6	
	2543.6692	23.6±2.7 [a]	
	2543.7380	−14.6±4.5	
	2543.7790	−6.7±3.9	
	2543.8676	0.6±3.4	
VLT 11 - 02	2589.7266	154.0±0.9	
	2590.5974	−24.0±0.9	
	2591.5699	157.9±0.9	
	2592.5530	−9.5±0.9	
	2592.6857	22.1±1.3	
	2592.8507	69.3±1.2	
WD 0419−487			
SPY	1889.7314	45.5±1.0	218.7±0.2
	1891.5497	hardly visible	231.5±1.0
	1891.6927	159.5±1.0	−90.4±0.2
NTT 02 - 03	2689.5177	hardly visible	−95.4±0.9
	2689.5932	hardly visible	155.7±0.9
	2690.5237	50.9±2.0[b]	217.6±0.9
	2690.5686	hardly visible	265.9±0.5
	2691.5208	hardly visible	181.6±0.9
	2692.5181	167.0±2.0[b]	−103.4±0.5
	2692.5370	167.5±2.0[b]	−116.2±0.5
	2692.6082	hardly visible	72.8±0.5
VLT 03 - 03	2718.5419	48.4±0.9	208.2±0.2
	2719.5293	152.0±1.0	−65.9±0.3
WD 0453−295			
SPY	2213.8638	112.6±4.7	16.0±17.3
	2247.8281	150.0±2.9	−40.5±8.7
	2260.6749778	43.0±2.1	conjunction
NTT 09 - 02	2540.8237	−36.8±2.2	103.0±7.3
	2541.8190	134.7±3.1	−39.3±9.7
	2542.8384	170.3±2.0	−42.1±6.4
VLT 11 - 02	2589.6521	−80.1±1.7	145.2±5.2
	2589.7064	19.7±1.8	conjunction
	2589.7640	132.2±1.5	−30.6±4.7
	2589.8147	163.4±1.5	−54.7±4.7
	2589.8224	159.3±2.0	−68.6±6.0
	2589.8301	150.9±3.0	−62.0±9.2
	2589.8608	107.0±2.0	−17.5±5.6

Run	mid HJD $[-2\,450\,000]$	$RV_{\rm primary}$ [km s^{-1}]	$RV_{\rm secondary}$ [km s^{-1}]
	2590.6571	−58.4±1.8	140.2±5.5
	2590.7261	−81.3±1.7	121.4±5.2
	2590.7414	−63.4±1.8	124.3±5.4
	2590.7490	−50.5±1.8	108.9±5.6
	2590.8603	162.1±1.9	−40.6±5.9
	2591.7142	−25.0±1.7	95.6±5.5
	2591.7732	−93.7±2.0	146.5±6.3
	2591.7809	−93.8±1.7	144.4±5.2
	2592.7614	39.7±2.2	conjunction
HE 0532−4503			
SPY	2006.5077	−80.7±1.0	
	2008.5258	107.7±1.0	
VLT 10 - 03	2194.8205	−93.7±1.0	
	2194.8503	−87.4±1.0	
	2195.7331	95.4±1.0	
	2195.7736	96.2±1.0	
	2195.8041	49.6±1.0	
	2195.8438	−35.9±1.0	
	2195.8759	−87.2±1.0	
VLT 11 - 03	2589.8493	91.4±1.0	
	2590.7795	−73.0±1.0	
	2591.6525	−36.0±1.0	
	2591.7415	105.0±1.0	
	2591.7986	22.7±1.0	
	2591.8351	−57.8±1.0	
	2591.8392	−72.9±1.0	
	2591.8434	−71.9±1.0	
	2591.8475	−77.9±1.0	
	2591.8517	−82.0±1.0	
	2591.8559	−87.1±1.0	
	2591.8600	−96.2±1.0	
	2591.8641	−93.1±1.0	
	2591.8683	−96.3±1.0	
	2591.8724	−93.5±1.0	
	2592.6206	−49.8±1.0	
	2592.6265	−48.0±1.0	
	2592.6685	−90.6±1.0	
	2592.6744	−91.0±1.0	
	2592.7120	−38.5±1.0	
	2592.7179	−25.7±1.0	
	2592.7238	−14.4±1.0	
	2592.7297	1.6±1.0	
	2592.7687	96.2±1.0	

Run	mid HJD $[-2\,450\,000]$	$RV_{\rm primary}$ $[{\rm km\,s^{-1}}]$	$RV_{\rm secondary}$ $[{\rm km\,s^{-1}}]$
	2592.7746	90.6±1.0	
	2592.8024	105.7±1.0	
	2592.8083	106.7±1.0	
	2592.8143	98.3±1.0	
	2592.8202	96.4±1.0	
	2592.8558	31.6±1.0	
VLT 03 - 03	2716.5111	51.9±1.0	
	2716.5170	66.1±1.0	
	2716.5229	76.1±1.0	
	2716.5849	91.6±1.0	
	2716.5908	84.3±1.0	
	2716.5967	72.4±1.0	
	2717.6268	108.0±1.0	
	2717.6327	108.9±1.0	
	2719.5377	33.7±1.0	
	2719.5436	22.7±1.0	
WD 0710+216			
SPY	2322.6880	37.2±4.0	
	2324.6158	34.4±3.2	
NTT 01 - 04	3006.7475	29.3±4.9	
	3007.6565	37.8±3.4	
	3007.7511	28.6±3.7	
	3008.7413	40.4±7.1	
PN 2119+226 alias EGB 5			
SPY	2008.5864	70.4±0.9	
	2033.5419	57.8±1.7	
WHT 10 - 01	2211.7321	86.3±4.1	
	2211.7757	78.0±5.8	
	2213.6844	77.2±5.3	
	2213.6914	71.0±6.0	
	2213.7293	80.8±9.0	
	2213.7328	64.4±8.5	
	2213.7381	58.7±5.7	
	2209.6742	84.4±5.0	
	2209.6814	62.3±5.8	
DSAZ 02 - 02	2328.3597	84.9±2.7	
	2329.3032	79.6±4.5	
	2329.4426	88.1±3.6	
	2329.5204	76.5±3.5	
	2330.3379	72.8±4.4	
	2330.3815	77.4±3.0	
	2330.3945	77.4±6.6	

Run	mid HJD $[-2\,450\,000]$	$RV_{\rm primary}$ $[{\rm km\,s^{-1}}]$	$RV_{\rm secondary}$ $[{\rm km\,s^{-1}}]$
	2330.4319	82.9±4.1	
	2331.3563	60.5±4.5	
	2331.4069	63.6±3.3	
	2331.4392	61.9±4.1	
	2331.4859	69.1±3.9	
	2332.3496	67.9±5.1	
	2332.3859	62.9±5.1	
	2332.4298	58.7±5.0	
WHT 01 - 03	2662.4743	60.7±4.1	
	2662.4785	65.9±4.1	
	2662.4822	67.2±4.1	
	2662.4859	67.0±4.5	
	2662.4895	61.9±4.8	
	2662.4932	53.2±4.9	
	2662.5571	72.0±4.6	
	2662.5607	61.0±4.4	
	2662.5644	64.4±4.9	
	2662.6910	70.7±4.4	
	2662.6946	62.4±4.5	
	2663.4504	56.2±3.9	
	2663.4540	62.1±3.8	
	2664.5611	56.6±4.5	
	2664.5889	47.6±5.1	
	2664.6511	47.9±7.5	
	2665.4597	56.3±9.4	
	2665.4760	51.0±14.4 [c]	
	2665.4867	80.4±12.0 [c]	
	2665.5434	45.5±6.3	
	2665.6068	53.7±5.2	
	2665.6497	53.7±5.2	
VLT 03 - 03	2716.5068	60.0±7.0	
	2716.5555	56.5±5.1	
	2716.6302	57.5±3.2	
	2717.5713	67.9±5.0	
	2717.6576	56.8±6.3	
	2718.5730	68.3±5.5	
	2718.6352	69.1±6.9	
	2719.4937	69.6±1.9	
	2719.6530	72.6±5.9	
NTT 01 - 04	3008.7649	49.8±5.3	
	3008.8458	44.3±8.9	
	3009.8007	47.1±4.9	
HE 0929−0424			

Run	mid HJD [−2 450 000]	$RV_{\rm primary}$ [km s^{-1}]	$RV_{\rm secondary}$ [km s^{-1}]
SPY	2327.6449	−69.9±2.7	
WHT 01 - 03	2662.5751	−78.8±6.2	
	2662.5858	−55.2±5.3	
	2662.6693	75.2±4.6	
	2662.6799	83.4±4.5	
	2662.7438	150.1±4.1	
	2663.5402	54.8±3.7	
	2663.5688	102.0±4.3	
	2663.6190	138.5±6.1	
	2663.6726	141.4±4.7	
	2664.4500	82.3±11.3	
	2664.5237	169.3±9.1	
	2664.5751	141.8±6.4	
	2664.6391	23.7±17.9	
	2665.5873	−61.4±9.1	
	2665.6268	−75.9±5.7	
NTT 02 - 03	2688.6371	50.6±9.6	
	2689.5748	134.2±7.7	
	2689.6543	136.5±5.0	
	2690.5981	29.4±16.6	
	2690.6538	−35.5±8.4	
	2690.8169	48.7±16.2	
	2692.5665	23.1±18.8	
	2692.5929	101.8±6.3	
VLT 03 - 03	2716.5385	74.5±4.1	
	2716.5803	5.8±5.0	
	2716.6404	−71.6±6.4	
	2716.6923	−50.8±5.5	
	2717.6488	27.6±3.2	
	2719.5040	138.7±3.6	
WD 1013−050			
SPY	1888.8475	−92.7±2.0	
	1920.8691	108.0±2.0	
NTT 01 - 03	3006.8331	144.2±1.7	
	3006.8707	135.9±1.1	
	3007.7882	31.1±0.6	
	3007.8629	−41.9±0.5	
	3008.8012	−102.1±0.5	
	3009.8388	85.4±1.3	
WD 1058−129			
SPY	1683.5079	94.1±8.7	
	1920.8751	67.9±6.8	

Run	mid HJD [−2 450 000]	$RV_{\rm primary}$ [km s^{-1}]	$RV_{\rm secondary}$ [km s^{-1}]
	2087.5520	67.5±7.3	
	2387.7117	62.4±8.2	
WHT 01 - 03	2662.7022	50.0±7.1	
	2662.7546	57.0±8.1	
	2663.5538	72.9±6.5	
	2663.6307	80.5±7.6	
	2663.6561	81.7±6.8	
	2664.6670	114.7±22.0 [c]	
	2664.7590	85.4±15.6 [c]	
	2665.6616	47.2±22.0 [c]	
NTT 02 - 03	2688.6678	70.6±34.9 [c]	
	2688.7935	53.9±14.0 [c]	
	2689.7094	76.8±9.6	
DSAZ 02 - 02	2328.4706	79.1±5.0	
	2329.5427	39.9±26.2 [c]	
	2330.5183	73.9±5.0	
WHT 03 - 03	2720.4657	80.3±6.7	
	2720.5167	75.8±6.4	
	2720.6120	73.7±6.2	
	2721.4285	75.0±3.6	
	2721.4532	69.3±3.4	
	2721.5246	70.1±3.9	
	2721.6260	51.8±6.1	
NTT 01 - 04	3006.7885	72.6±4.3	
	3008.8201	65.3±4.5	
	3009.8623	94.7±4.9	
	3009.8779	87.2±7.2	
HE 1059−2735			
SPY	1655.6458	−128.1±3.7	
	1681.5758	−21.3±2.2	
	2044.5380	−132.3±2.8	
	2069.5375	−127.9±2.5	
	2087.4904	−37.9±2.7	
VLT 06 - 02	2430.5564	−14.4±2.2	
	2430.6164	−74.7±2.7	
	2431.5447	43.6±2.4	
NTT 02 - 03	2690.7881	−145.9±9.0	
	2690.8451	−107.0±7.7	
	2692.6410	21.9±11.5	
	2692.6708	44.9±12.2	
	2692.6986	44.1±10.9	
	2692.7756	10.0±12.2	
	2692.8015	3.0±8.3	

Run	mid HJD $[-2\,450\,000]$	$RV_{\rm primary}$ $[{\rm km\,s^{-1}}]$	$RV_{\rm secondary}$ $[{\rm km\,s^{-1}}]$
	2692.8266	−28.5±9.6	
	2692.8518	−41.4±30.7	
	2692.8939	−75.9±12.8	
VLT 03 - 03	2716.5485	28.6±3.2	
	2716.6120	40.4±3.3	
	2716.6513	26.1±4.0	
	2716.7030	−13.5±3.0	
	2717.5812	−17.7±4.4	
	2717.6689	33.8±4.6	
	2717.7311	38.3±4.0	
	2718.5566	−126.4±2.8	
	2718.6281	−96.4±2.6	
	2718.6864	−40.6±3.2	
	2718.7976	32.9±3.2	
	2719.5146	−40.6±2.8	
	2719.6027	−116.5±2.8	
	2719.6641	−132.9±2.4	
	2719.8424	9.6±2.7	
NTT 01 - 04	3007.8177	16.4±5.4	
HE 1115−0631			
SPY	1727.4715	63.0±2.1	
	1728.4930	131.6±2.6	
DSAZ 02 - 02	2328.4905	131.6±4.5	
	2329.5925	71.5±6.4	
	2330.4994	31.5±5.1	
	2330.5647	30.0±4.5	
	2330.5815	30.7±6.4	
	2331.5038	34.8±5.8	
	2331.5474	61.0±38.4	
	2332.4804	133.0±17.3	
WHT 01 - 03	2663.6043	64.3±12.9[a]	
	2664.6902	87.9±21.0[a]	
	2688.8195	92.4±6.4[a]	
	2688.7399	139.9±18.9[a]	
	2664.7897	23.1±19.1	
NTT 02 - 03	2688.8719	35.3±14.2	
	2689.6847	62.8±18.3	
	2689.8073	77.9±11.4	
	2690.6808	113.3±5.1	
VLT 03 - 03	2718.5676	27.9±3.2	
	2718.6469	35.3±2.8	
	2718.7096	44.6±2.7	
	2718.8405	39.4±2.6	

Run	mid HJD [−2 450 000]	$RV_{\rm primary}$ [km s^{-1}]	$RV_{\rm secondary}$ [km s^{-1}]
	2719.5740	90.4±4.3	
	2719.6760	98.6±1.9	
WHT 03 - 03	2718.5676	35.9±2.3	
	2718.6469	38.2±2.1	
	2718.7096	40.5±1.7	
	2718.8405	46.4±2.2	
	2719.5741	91.2±2.1	
	2719.6760	95.8±2.3	
	2720.6391	132.9±8.2	
	2721.4401	135.0±5.7	
	2721.6380	136.0±6.3	
DSAZ 04 - 03	2747.4788	28.6±11.4	
	2749.3765	−17.4±43.5[a]	
DSAZ 05 - 03	2777.3766	19.6±6.4	
	2778.3659	106.4±9.0	
WD 1210+140			
SPY	2657.8068	69.0±11.0	
	2658.7568	−71.0±27.0	
DSAZ 04 - 03	2747.4390	28.5±27.4	
	2747.5327	135.5±4.6	
	2748.3933	−18.9±4.6	
	2749.3355	38.4±10.5	
	2749.4113	101.7±5.5	
	2749.4823	144.4±4.6	
	2749.5628	92.6±5.0	
	2750.5431	−88.3±10.0	
	2750.5818	−11.5±7.8	
DSAZ 05 - 03	2773.3597	47.0±14.2	
Maxted et al. (1999)	0969.8965	65.2±5.4	
	0969.9073	74.8±5.8	
WD 1229−012			
SPY	1684.5779	15.5±1.4	
	1686.5580	16.5±1.4	
NTT 02 - 03	2688.8195	7.8±4.9	
WHT 03 - 03	2720.6590	11.7±3.9	
	2720.7208	22.3±4.1	
Maxted et al. (2000a)	1238.6209	27.8±6.5	
	1238.6349	14.9±9.4	
	1238.7430	−27.9±13.3	
	1238.7571	31.5±11.5	
	1240.6630	23.7±3.7	
	1240.7640	5.5±5.3	

Run	mid HJD $[-2\,450\,000]$	$RV_{\rm primary}$ $[{\rm km\,s^{-1}}]$	$RV_{\rm secondary}$ $[{\rm km\,s^{-1}}]$
	1243.6141	15.4±3.4	
	1268.0433	21.6±3.6	
	1268.1519	25.6±7.4	
HE 1318−2111			
SPY	1657.5627	68.9±2.4	
	1683.6468	30.7±3.1	
	2069.5823	21.3±2.6	
	2387.6278	48.7±2.8	
DSAZ 02 - 02	2328.6512	60.1±4.5	
	2329.6108	45.8±12.2	
NTT 02 - 03	2689.8776	42.0±7.0	
	2690.7635	8.1±5.8	
	2692.7499	17.8±9.6	
	2692.8707	78.2±7.0	
VLT 03 - 03	2716.6224	21.8±2.8	
	2716.6709	41.1±2.6	
	2716.7234	72.6±3.3	
	2717.6022	18.3±3.0	
	2717.6796	74.1±3.1	
	2717.7419	94.1±2.2	
	2717.8587	64.9±2.9	
	2719.6249	63.5±2.2	
	2719.6956	95.1±2.5	
	2719.8864	20.4±2.1	
DSAZ 05 - 03	2777.3991	23.8±10.2	
	2778.4757	7.9±9.6	
HS 1334+0701			
SPY	2078.5501	−34.2±3.7	
	2387.7572	−47.0±5.9	
DSAZ 07 - 03	2822.3820	-43.5±6.9	
	2823.3833	0.3±6.4	
	2824.3810	-38.6±4.1	
	2825.3833	-49.8±3.7	
	2826.3777	-3.1±5.0	
	2827.3736	-40.7±10.5	
	2827.4333	-61.7±9.6	
	2828.3824	-21.4±6.9	
	2829.3786	2.4±5.0	
	2829.4024	-29.5±6.4	
	2829.4263	-37.5±7.8	
	2830.3762	-57.0±6.9	
	2830.4005	-54.7±6.9	

Run	mid HJD [−2 450 000]	$RV_{\rm primary}$ [km s^{-1}]	$RV_{\rm secondary}$ [km s^{-1}]
	2830.4243	-59.8±9.1	
	2831.3909	-37.5±13.1	
	2831.4145	8.6±6.5	
	2834.3694	-23.7±6.4	
	2834.3936	-9.1±5.2	
HE 1349+144			
SPY	1948.8907	−45.1±2.7	−61.1±2.3
	1947.8050	27.1±2.3	18.8±2.3
DSAZ 07 - 01	2106.4372	38.0±15.5	−25.5±15.5
	2098.3993	53.2±6.4	−71.1±8.6
	2099.4531	−89.5±8.2	50.8±7.3
	2100.4120	56.8±10.0	−76.6±9.6
	2097.4354	−68.8±23.7	49.1±16.9
DSAZ 02 - 02	2328.5100	32.0±10.0	−76.3±8.6
	2329.6384	−49.5±8.2	29.6±11.0
	2330.6024	43.0±7.3	−87.2±9.1
	2330.6643	43.8±27.9	−75.4±26.4
	2330.7082	34.5±5.4	−54.1±5.5
	2331.5679	−63.7±7.3	59.7±8.6
	2331.5915	−63.3±18.7	66.9±16.4
	2331.6149	−59.7±5.0	52.7±8.7
	2331.6394	−68.0±6.4	44.9±6.4
	2331.6639	−75.3±8.2	69.9±5.9
	2331.7075	−85.5±8.2	36.4±7.3
	2331.7322	−59.1±33.8	59.6±12.8
	2332.7331	32.4±6.8	−82.7±16.9
	2332.6884	53.9±11.8	−78.0±14.6
	2332.6447	48.6±13.7	−98.9±13.7
	2332.5889	46.1±10.0	−96.9±10.0
	2332.5399	47.5±18.7	−104.6±19.4
WHT 01 - 03	2662.7242	−40.0±4.6	49.3±6.4
	2662.7980	−57.3±4.8	61.8±7.0
	2663.6428	−14.1±4.6	−60.5±6.6
	2663.6987	18.8±6.8	−47.5±4.7
	2663.7693	29.3±7.3	−65.5±5.0
	2664.7366	−42.7±9.9	14.5±6.8
	2664.7732	−44.0±9.2	17.4±6.4
	2665.6801	64.2±14.5	−17.6±10.0
HE 1421−1206			
SPY	1755.5051	−138.2±8.7	
	2136.5413	−85.1±1.7	
WHT 01 - 03	2663.7327596	−25.7±4.1	

Run	mid HJD $[-2\,450\,000]$	$RV_{\rm primary}$ $[{\rm km\,s^{-1}}]$	$RV_{\rm secondary}$ $[{\rm km\,s^{-1}}]$
VLT 03 - 03	2716.6804	−132.7±3.7	
	2717.6994	−134.0±2.7	
	2718.6971	−85.9±3.1	
	2718.8608	−128.5±4.1	
WHT 03 - 03	2721.5852	−110.7±2.4	
	2721.6954	−79.9±3.0	
	2721.7472	−85.6±21.7	
HE 1448−0510			
SPY	1739.5929	−4.4±2.0	
	1742.5967	−93.7±2.0	
	2718.9230	−9.1±2.0	
DSAZ 02 - 02	2330.6854	−64.7±3.6	
	2332.6163	−0.1±6.4	
	2332.6641	5.3±5.9	
	2332.7104	8.8±4.1	
WHT 01 - 03	2663.7447	−29.6±4.9	
VLT 03 - 03	2718.9230	2.9±2.0	
WHT 03 - 03	2721.5981	−76.5±3.6	
	2721.7042	−71.1±4.3	
	2721.7601	−56.4±7.7	
DSAZ 04 - 03	2749.4592	−22.2±9.6	
	2749.5438	−37.1±5.5	
	2749.6718	−22.3±8.7	
	2750.6025	−82.9±5.5	
	2750.6466	−76.7±5.0	
	2750.6907	−77.7±6.4	
DSAZ 05 - 03	2776.5079	25.0±17.4	
	2776.6135	12.8±10.0	
	2777.4670	−6.9±5.0	
	2777.5523	−18.5±7.3	
	2778.4102	−42.0±3.2	
	2778.4997	−45.4±3.2	
	2778.5670	−46.9±3.2	
DSAZ 07 - 03	2822.4104	−73.3±11.0	
	2823.4107	−103.7±4.6	
	2824.4064	−72.8±4.1	
	2825.4110	−44.0±5.0	
	2831.3693	−78.9±14.2	
	2833.4348	8.6±7.3	
	2834.4183	19.5±10.0	
WD 1449+168			
SPY	2387.7490	54.2±4.7	

Run	mid HJD [−2 450 000]	$RV_{\rm primary}$ [km s^{-1}]	$RV_{\rm secondary}$ [km s^{-1}]
	2393.7762	57.9±5.0	
DSAZ 04 - 03	2747.6267	50.9±8.7	
	2749.5058	36.4±4.6	
	2749.6180	53.2±5.7	
	2750.6239	72.1±7.2	
	2750.6693	63.3±6.6	
DSAZ 05 - 03	2773.6127	61.7±9.6	
	2773.6604	47.7±9.6	
	2774.4397	55.5±17.2 [c]	
	2774.4895	41.8±8.6	
	2774.5131	52.2±8.2	
	2774.6243	26.7±15.0 [c]	
	2774.6478	36.4±10.2	
	2775.6357	52.9±3.8	
	2775.6603	58.2±4.7	
	2776.6358	32.3±16.3 [c]	
	2777.5264	61.8±5.8	
	2777.6025	42.6±7.6	
	2778.5253	64.7±4.1	
	2778.5883	52.6±3.2	
HS 1606+0153			
SPY	2116.5280	−200.9±0.8	
	2108.5174	94.6±1.1	
DSAZ 08 - 02	2501.3660	−86.6±1.7	
	2502.3513	182.9±1.5	
VLT 03 - 03	2718.9140	−5.0±0.8	
	2719.8519	−44.4±1.1	
	2719.9160	15.8±1.0	
WD 1736+052			
SPY	1688.9114	51.0±2.7	
	1696.8023	45.1±7.8	
	1730.6909	50.2±2.3	
DSAZ 04 - 03	2747.6524	21.5±14.6 [c]	
	2749.5857	44.4±22.8 [c]	
DSAZ 05 - 03	2773.5738	56.7±7.8	
	2774.5527	42.6±5.0	
	2774.6740	41.0±8.7	
	2776.5671	29.0±8.7	
	2776.6690	9.6±10.0 [c]	
	2777.4976	35.2±7.8	
	2777.5737	46.0±4.6	
	2777.6650	49.9±9.1	

Run	mid HJD $[-2\,450\,000]$	$RV_{\rm primary}$ $[{\rm km\,s^{-1}}]$	$RV_{\rm secondary}$ $[{\rm km\,s^{-1}}]$
	2778.6146	42.3±2.7	
DSAZ 07 - 03	2824.4714	47.9±3.2	
	2825.4723	47.5±3.2	
	2826.4397	52.3±3.2	
	2827.4034	50.6±5.9	
	2833.4625	31.1±4.6	
	2834.4726	56.7±6.4	
	2835.4157	74.2±10.5 [c]	
	2836.4614	60.0±6.9	
	2838.4101	43.4±10.0 [c]	
	2838.4864	57.4±6.4	
	2838.5637	26.6±23.3 [c]	
	2747.6524	21.5±14.6 [c]	
WD 1824+040			
SPY	1681.71652	37.6±1.0	
	1682.89334	−15.0±1.6	
	2033.85144	−15.6±2.2	
	2078.72655	4.3±0.9	
	2116.57473	20.2±1.3	
	2117.59390	80.2±1.5	
	2139.51631	10.7±11.8	
DSAZ 03 - 01	1979.69473	75.1±3.3	
	1979.72742	80.1±2.8	
	1980.66044	108.6±3.7	
	1981.67179	82.7±3.4	
	1981.72575	81.2±3.1	
DSAZ 07 - 01	2097.49905	6.9±2.5	
	2097.59516	24.9±3.6	
	2098.44468	56.9±4.1	
	2098.50502	65.4±8.8	
	2098.61031	71.5±3.3	
	2099.49840	102.5±2.3	
	2100.52795	91.0±3.2	
	2101.55330	40.7±2.0	
	2101.61393	39.6±2.9	
	2103.52965	0.5±2.7	
	2104.58011	52.1±2.4	
	2105.53698	110.7±4.1	
	2105.59991	97.7±4.6	
	2106.52128	112.7±9.1	
DSAZ 02 - 02	2329.69601	29.7±10.1	
	2330.74766	83.8±3.1	
	2331.74892	101.8±4.7	

Run	mid HJD [−2 450 000]	$RV_{\rm primary}$ [km s^{-1}]	$RV_{\rm secondary}$ [km s^{-1}]
	2332.75050	72.8±6.6	
	2328.71197	−20.8±2.7	
WD 1914+094			
SPY	1689.9170	−18.1±8.8 [d]	
	1690.9000	−30.6±28.4 [d]	
	2033.8653	31.8±7.3	
	2065.8249	1.3±6.9	
DSAZ 08 - 02	2498.4171	−2.0±8.3	
	2499.4060	16.5±8.5 [d]	
	2500.5259	11.1±9.3	
	2501.3925	−4.4±8.9	
	2502.3781	−13.1±11.3 [d]	
	2502.4718	5.0±6.0	
	2503.3542	5.5±6.7	
	2503.5322	6.7±8.0	
	2505.3394	19.0±9.3 [d]	
	2505.3713	1.5±6.2	
	2505.3962	−5.4±7.5	
	2505.4399	−17.3±9.6	
	2505.4972	−33.0±14.7 [d]	
NTT 09 - 02	2540.4997	28.3±16.7 [d]	
	2540.5467	1.3±12.6 [d]	
	2541.5493	−7.2±7.3	
	2543.4956	16.3±23.6 [d]	
DSAZ 10 - 02	2563.2949	0.4±12.7 [d]	
DSAZ 04 - 03	2747.6772	−5.5±9.6	
	2747.6933	−44.1±16.6 [d]	
	2749.6416	9.6±14.6 [d]	
	2773.5339	−15.6±22.8 [d]	
	2773.6350	9.5±15.0 [d]	
DSAZ 05 - 03	2774.5794	−10.3±12.3	
	2774.5965	−22.5±14.5 [d]	
	2775.5570	−15.2±12.9 [d]	
	2775.5747	35.7±13.7 [d]	
	2775.5914	19.1±22.2 [d]	
	2775.6100	−36.6±22.6 [d]	
	2776.5884	−38.7±12.6 [d]	
	2777.6239	−13.4±6.9 [d]	
	2777.6407	14.1±10.7	
HS 2108+1734			
SPY	2465.7845	49.3±15.5	
	2527.5498	35.3±16.0	

Run	mid HJD $[-2\,450\,000]$	$RV_{\rm primary}$ $[{\rm km\,s^{-1}}]$	$RV_{\rm secondary}$ $[{\rm km\,s^{-1}}]$
DSAZ 07 - 03	2822.4792	8.6±26.0	
	2822.5287	54.4±12.8	
	2823.4740	4.2±23.4	
	2824.4984	16.3±22.0	
	2825.4987	67.7±9.9	
	2826.4660	65.1±6.9	
	2826.5201	53.2±14.2 [d]	
	2827.4632	11.9±14.2 [d]	
	2827.5144	49.9±12.9	
	2828.4892	74.5±12.8 [d]	
	2828.5407	39.9±7.3	
	2829.4682	18.5±19.6 [d]	
	2829.4930	8.4±36.6 [d]	
	2829.5494	48.4±12.7 [d]	
	2830.4690	27.7±38.9 [d]	
	2830.4925	52.3±40.4 [d]	
	2830.5476	35.4±14.3	
	2831.4560	89.4±22.6 [d]	
	2831.4946	53.5±19.1 [d]	
	2831.5487	55.9±8.5	
	2832.5562	132.2±45.4 [d]	
	2832.5798	47.6±25.3 [d]	
	2832.6336	43.9±7.1	
	2833.4920	61.3±11.3 [d]	
	2833.6006	41.4±12.9 [d]	
	2834.4986	43.5±20.3 [d]	
	2835.4562	54.1±18.9 [d]	
	2836.5089	58.7±10.0	
	2838.4407	44.8±23.7 [d]	
HE 2135−3749			
SPY	2138.5565	−95.6±1.0	
	2142.5979	45.2±1.0	
VLT 04 - 02	2430.8405	43.9±1.0	
	2430.8788	46.9±1.0	
	2430.9257	40.6±1.0	
	2431.7160	32.5±1.0	
	2431.7662	44.4±1.0	
	2431.8396	42.3±1.0	
	2431.8947	27.3±1.0	
	2431.9324	11.5±1.0	
	2589.5046	−90.0±1.0	
	2589.5547	−60.0±1.0	
	2591.4979	−3.9±1.0	

Run	mid HJD [−2 450 000]	$RV_{\rm primary}$ [km s^{-1}]	$RV_{\rm secondary}$ [km s^{-1}]
	2592.5058	34.7±1.0	
NTT 09 - 02	2540.5266	−95.5±1.8	
	2540.5714	−66.5±2.5	
	2540.6428	−23.2±2.3	
	2540.6884	−4.1±2.3	
	2541.5310	−60.3±1.9	
	2541.6459	21.1±2.1	
	2541.7001	28.4±1.8	
	2541.7799	34.7±2.8	
	2542.6357	38.2±2.0	
	2542.6998	41.3±2.3	
	2543.5202	29.1±2.5	
	2543.5665	32.2±3.9	
	2543.6517	41.1±2.1	
HE 2147−1405			
SPY	2141.6042	92.8±0.3	
	2145.6329	−62.7±0.2	
	2145.6438	−59.4±0.2	
DSAZ 08 - 02	2498.5425	46.0±0.5	
	2500.5870	40.7±0.8	
	2503.4906	72.9±0.8	
HE 2150−0238			
SPY	2141.6146	−46.0±2.7	
	2145.7520	22.8±3.2	
DSAZ 08 - 02	2498.5932	61.0±4.5	
	2499.4604	−92.7±2.8	
	2499.5854	−42.9±5.5	
	2500.5014	−128.8±4.1	
	2500.5530	−142.6±4.5	
	2500.6119	−126.6±5.5	
	2501.4226	28.9±3.6	
	2501.5181	2.3±3.6	
	2501.6138	−43.0±3.6	
	2501.6663	−53.3±4.1	
	2502.4297	34.3±6.4	
	2502.5218	48.7±4.5	
	2502.6159	77.0±3.6	
	2502.6767	43.7±6.8	
	2503.3826	−95.4±7.8	
	2503.4452	−83.6±3.2	
	2503.5730	−29.6±4.1	

Run	mid HJD [−2 450 000]	$RV_{\rm primary}$ [km s^{-1}]	$RV_{\rm secondary}$ [km s^{-1}]
HE 2200−1341			
SPY	1885.5317	162.2±3.6	
	2172.6046	125.6±11.7	
	2540.6967	10.3±3.6	
	2540.7071	−0.7±4.6	
DSAZ 07 - 03	2822.5694	−50.8±6.1	
	2822.6435	−30.3±6.9	
	2823.5856	163.7±6.9	
	2823.6101	132.4±7.5	
	2823.6351	118.5±7.0	
	2824.5252	6.0±37.4 [a]	
	2824.6118	−16.6±6.7	
	2824.6357	−16.8±7.3	
	2825.5512	148.6±6.7	
	2825.6226	109.5±9.1	
	2826.5455	−35.9±7.2	
	2826.6125	12.9±8.1	
	2826.6354	108.5±8.0 [a]	
	2827.5394	116.8±9.4	
	2827.6419	100.5±6.8	
	2828.5665	−25.6±7.3	
	2828.6289	47.0±5.5	
	2829.5780	118.7±8.1	
	2830.5752	0.7±8.7	
	2831.5762	60.2±10.1	
	2833.5743	26.5±6.6	
	2834.5654	75.4±12.8	
	2834.6146	93.2±10.0	
HE 2208+0126			
SPY	2527.6384900	6.9±1.3	
DSAZ 07 - 03	2822.6071	4.2±4.1	
	2823.5030	6.8±12.8 [c]	
	2823.5587	−13.8±10.0 [c]	
	2824.5252	9.7±4.1	
	2824.5853	−3.8±3.7	
	2825.5245	−26.3±11.4 [c]	
	2825.5780	1.1±5.0	
	2826.4925	6.8±7.3	
	2826.5696	−14.3±6.4	
	2827.4884	13.8±17.8 [c]	
	2827.5674	−10.5±9.6	
	2827.5905	−5.1±4.1	

Run	mid HJD $[-2\,450\,000]$	$RV_{\rm primary}$ $[{\rm km\,s^{-1}}]$	$RV_{\rm secondary}$ $[{\rm km\,s^{-1}}]$
	2828.5152	−17.5±3.2	
	2828.5905	10.6±3.7	
	2828.6088	4.2±4.6	
	2829.5210	−13.4±8.2	
	2829.6213	1.5±5.0	
	2829.6411	−3.2±3.7	
	2830.5194	−7.7±5.5	
	2830.6190	−13.4±7.8	
	2830.6361	−9.9±8.2	
	2830.6565	−35.0±6.4 [a]	
	2831.5218	6.6±14.2 [c]	
	2831.6183	3.1±4.6 [a]	
	2831.6349	−11.1±4.1	
	2831.6521	−12.5±7.8	
	2832.6067	1.4±5.9 [a]	
	2833.5184	25.1±12.3 [c]	
	2833.6245	−7.7±5.5	
	2833.6418	1.5±28.3 [c]	
	2834.5376	20.1±16.4 [c]	
	2834.6380	4.7±8.2	
	2834.6546	13.9±3.6	
	2836.5453	19.9±14.2 [c]	
	2836.5782	6.1±4.1	
	2836.5960	16.0±8.2	
	2836.6125	−8.2±6.4	
	2836.6297	−23.8±16.4 [c]	
	2836.6458	−25.2±5.9 [a]	
HE 2209−1444			
SPY	1885.5488	85±3	−119±4
	2172.6372	−14±2	−14±2
DSAZ 07 - 01	2097.5404	−105±6	55±9
	2097.6125	67±8	−36±10
	2101.5702	63±5	−91±8
	2101.6309	−77±4	59±6
	2102.5410	−78±8	68±13
	2103.5514	−51±10	27±12
	2103.5678	−89±12	41±14
	2103.5850	−100±6	55±8
	2103.6014	−124±5	88±7
	2103.6182	−120±4	83±7
	2103.6344	−97±4	77±8
	2103.6504	−82±5	45±9
	2103.6666	−41±8	37±11

Run	mid HJD $[-2\,450\,000]$	$RV_{\rm primary}$ $[{\rm km\,s^{-1}}]$	$RV_{\rm secondary}$ $[{\rm km\,s^{-1}}]$
	2104.6750	-85 ± 8	73 ± 12
	2105.6591	63 ± 5	-103 ± 7
	2106.5183	99 ± 6	-108 ± 7
VLT 10 - 01	2194.5343	35 ± 3	-70 ± 5
	2194.6249	47 ± 4	-84 ± 6
WHT 10 - 01	2211.3592	-121 ± 5	36 ± 7
	2211.3807	-76 ± 5	26 ± 8
	2212.3189	72 ± 5	-112 ± 7
	2212.3440	31 ± 4	-100 ± 6
	2212.3921	-85 ± 4	18 ± 7
	2212.4138	-114 ± 4	32 ± 6
	2212.4822	-106 ± 7	26 ± 11
	2213.4533	32 ± 5	-88 ± 8

conjunction: Only one component is visible in the doublelined spectra. We therefore assume that this observation was be done at conjunction. The measured RV were used for both components

a: This data point lies clearly outside the best fit RV curve and was therefore discarded as an outlier from the final analysis

b: The spectra has a low S/N ratio which makes the component hardly visible. Thus, the data point was discarded from the final analysis.

c: The measured RV errors are larger than the RV semi-amplitude. We therefore discarded this data point from the final analysis.

d: Visual inspection of the MIDAS fit reveals a poor fit quality. We therefore discarded this data point from the final analysis.

Appendix D

Equivalent widths measurements

Table D.1: Equivalent width measurements for sdB stars. 01 = WD 0048−202; 02 = HE 0532−4503; 03 = HE 0929−0424; 04 = HE 1448−0510; 05 = HE 2135−3749; 06 = HE 2150−0238.

Ion			W_λ/mA					
Mult.	λ/Å	$\log(gf)$	01	02	03	04	05	06
C II								
74	4267.003	0.562	-	31	7	-	-	-
74	4267.258	−0.584	-	3	28	-	-	-
74	4267.261	0.717	-	3	-	-	-	-
101	5145.160	0.189	-	5	-	-	-	-
-	3920.681	−0.212	-	7	-	-	-	-
C III								
74	4647.420	0.070	-	3	-	-	-	-
N II								
38	4035.080	0.600	-	-	-	-	17	17
38	4073.042	−0.410	3	-	-	-	5	-
38	4082.270	−0.410	-	-	-	-	5	-
39	4041.311	0.830	-	-	-	-	32	50
39	4043.529	0.710	13	6	32	-	16	23
39	4044.777	−0.460	4	-	-	-	4	-
43	4176.161	0.600	8	6	18	-	15	-
43	4171.607	0.280	-	-	-	-	10	-
48	4236.910	0.400	12	9	44	-	26	24
48	4241.240	−0.340	-	-	-	-	3	-
48	4241.784	0.210	11	14	58	-	55	27
48	4241.784	0.730	11	14	-	-	55	27
49	4181.100	−1.310	-	6	-	-	-	-

Ion			W_λ/mA					
Mult.	λ/Å	$\log(gf)$	01	02	03	04	05	06
49	4199.980	0.030	-	-	11	-	-	-
50	4157.010	−0.650	-	3	-	-	-	12
50	4165.770	−1.300	8	-	-	-	-	-
50	4173.572	−0.460	-	-	-	-	3	-
50	4179.674	−0.200	3	-	14	-	6	-
55	4417.070	−0.340	27	-	-	-	-	-
55	4427.236	−0.010	-	-	-	-	8	20
55	4427.964	−0.150	-	-	32	-	7	-
55	4431.816	−0.150	-	-	7	-	4	-
55	4432.735	0.600	-	-	34	-	20	-
55	4433.475	−0.030	-	-	13	-	6	-
55	4442.018	0.300	-	-	-	-	9	23
61	4678.140	0.470	-	-	7	-	8	-
72	6379.615	−6.746	-	-	21	-	-	-
73	5676.019	−0.368	-	-	44	-	-	-
73	5679.562	0.250	16	25	50	-	49	-
73	5686.213	−0.549	-	-	-	-	12	-
73	5710.766	−0.518	-	-	-	-	15	15
74	5002.703	−1.021	-	2	14	-	6	-
74	5010.620	−0.606	6	4	10	-	13	15
74	5045.100	−0.407	9	11	25	-	19	-
75	4607.157	−0.507	-	-	-	-	-	48
75	4613.866	−0.665	-	-	-	-	-	18
75	4621.394	−0.514	6	-	36	-	14	19
75	4630.543	0.094	25	23	59	-	43	47
75	4643.085	−0.359	15	18	42	-	23	47
76	3955.851	−0.813	3	-	9	-	5	-
85	6482.053	−0.245	-	-	25	-	12	-
87	5073.590	−1.523	6	1	-	-	4	-
88	4667.206	−1.533	3	-	-	-	-	-
89	3994.988	0.208	29	18	64	-	47	55
104	4447.033	0.230	19	-	35	-	31	30
107	3918.999	−0.331	9	-	-	-	13	-
114	5001.136	0.263	14	10	35	-	28	56
114	5001.477	0.439	17	22	46	-	35	35
114	5005.149	0.592	23	-	62	-	43	-
114	5016.387	−0.515	4	-	12	-	8	-
114	5025.662	−0.546	-	-	15	-	8	-
116	4779.722	−0.587	-	-	11	-	4	-
116	4788.131	−0.363	5	-	-	-	10	-
116	4803.289	−0.113	8	-	19	-	16	17
117	4477.691	−1.098	-	-	-	-	4	-
127	4994.363	−0.069	7	-	39	-	13	-
127	5007.325	0.171	8	14	32	-	22	21

Ion			W_λ/mA					
Mult.	λ/Å	$\log(gf)$	01	02	03	04	05	06
142	5927.811	−0.293	-	-	-	-	10	-
142	5931.779	0.052	12	-	38	-	16	-
142	5941.653	0.313	-	10	51	-	22	-
143	5495.666	−0.266	-	-	14	-	7	-
159	4227.742	−0.060	-	-	21	-	10	18
175	6170.166	−0.311	11	-	-	-	-	-
232	5535.350	0.398	-	-	11	-	-	-
233	5011.300	−0.181	-	-	-	-	2	-
233	5012.029	0.136	-	-	9	-	-	-
234	4145.776	−0.023	-	-	12	-	-	-
8	3934.430	−0.128	36	-	-	-	-	-
102	4640.640	0.168	-	-	-	-	8	-
-	4003.578	0.611	-	-	9	-	-	-
O II								
5	4416.973	−0.020	17	-	-	-	-	-
10	4078.842	−0.250	7	-	-	-	-	-
28	4924.531	0.150	7	-	-	-	-	-
32	5206.650	−0.030	4	-	-	-	-	-
48	4089.288	0.870	9	-	10	-	-	-
50	4035.461	−1.130	-	3	-	-	-	-
53	4303.825	0.670	8	9	37	-	-	-
64	4638.855	−0.332	18	13	19	-	-	-
64	4641.810	0.054	31	25	38	-	-	-
64	4649.135	0.308	51	35	43	-	-	-
64	4650.839	−0.361	18	11	25	-	-	-
64	4661.633	−0.278	20	15	21	-	-	-
64	4676.235	−0.395	15	10	22	-	-	-
65	4319.628	−0.380	13	11	22	-	-	-
65	4349.426	0.060	-	6	-	-	-	-
65	4366.888	−0.348	15	10	16	-	-	-
67	4275.551	0.760	9	7	19	-	-	-
72	4414.901	0.172	35	10	38	-	-	-
72	4452.374	−0.789	5	4	-	-	-	-
73	3945.038	−0.726	7	4	-	-	-	-
73	3954.362	−0.396	14	16	8	-	-	-
78	4285.687	−2.230	7	-	-	-	-	-
90	4069.623	0.150	16	13	12	-	-	-
90	4069.886	0.344	20	11	24	-	-	-
90	4072.157	0.552	-	22	-	-	-	-
90	4075.862	0.692	-	24	37	-	-	-
100	4351.257	0.226	11	-	-	-	-	-
101	3911.957	0.000	5	4	-	-	-	-
101	3912.107	−0.886	5	7	-	-	-	-

Ion			W_λ/mA					
Mult.	λ/Å	$\log(gf)$	01	02	03	04	05	06
101	3919.285	−0.248	7	4	-	-	-	-
101	4253.895	0.920	4	11	-	-	-	-
101	4254.121	0.840	6	-	-	-	-	-
107	4121.462	−0.544	6	6	-	-	-	-
107	4132.800	−0.065	8	-	16	-	-	-
107	4153.298	0.053	21	10	11	-	-	-
107	4156.530	−0.696	-	-	12	-	-	-
107	4169.222	−0.409	4	5	11	-	-	-
108	4119.215	0.451	28	-	25	-	-	-
108	4120.280	−0.463	3	11	-	-	-	-
108	4120.544	−0.522	5	4	-	-	-	-
117	4710.012	−0.226	7	3	-	-	-	-
118	4699.220	0.270	8	-	26	-	-	-
118	4705.350	0.476	19	12	21	-	-	-
120	4395.942	−0.168	2	-	-	-	-	-
148	4941.069	−0.054	6	-	15	-	-	-
148	4942.999	0.239	11	-	23	-	-	-
161	4185.449	0.604	15	8	-	-	-	-
161	4189.592	−0.828	-	3	20	-	-	-
161	4189.789	0.716	16	11	-	-	-	-
172	4699.003	0.262	9	-	8	-	-	-
172	4703.163	0.262	5	-	15	-	-	-
-	4257.549	−0.280	6	-	-	-	-	-
-	4701.184	0.100	4	-	-	-	-	-
O III								
26	3934.808	0.070	7	-	-	-	-	-
165	4081.040	0.217	5	-	-	-	-	-
Ne II								
-	3694.212	0.090	-	-	7	-	-	-
-	3713.080	0.260	-	-	15	-	-	-
Mg II								
4	4481.129	−0.560	16	43	11	35	-	-
4	4481.130	0.740	16	43	11	-	-	-
4	4481.327	0.590	19	21	31	-	-	-
Al III								
2	5696.603	0.235	21	-	27	-	-	-
2	5722.728	−0.069	14	-	-	-	-	-
8	4479.892	0.900	10	-	23	-	-	-
8	4479.973	1.020	10	-	23	-	-	-

Ion			W_λ/mA					
Mult.	λ/Å	$\log(gf)$	01	02	03	04	05	06
Si II								
3	4128.067	0.380	-	-	30	-	-	-
4	5739.734	−0.110	6	-	-	-	-	-
5	3806.544	−0.080	8	-	-	-	-	-
Si III								
1	4088.854	0.195	5	-	8	47	-	-
4	5739.734	−0.110	-	29	37	-	-	-
5	3806.544	0.670	-	12	39	-	-	-
8	3924.468	0.690	-	-	25	-	-	-
8	4716.651	0.820	-	5	-	-	-	-
9	4819.718	0.750	-	-	8	-	-	-
9	4828.968	1.090	-	5	-	-	-	-
-	3791.439	−0.093	-	6	-	-	-	-
-	3924.522	0.480	-	6	-	-	-	-
S II								
6	5428.667	−0.130	-	-	-	-	3	-
6	5432.815	0.260	-	-	-	-	5	-
6	5453.828	0.480	-	-	-	-	10	-
7	4924.110	−0.059	-	-	-	-	4	-
7	5032.447	0.270	-	-	-	-	5	-
9	4815.549	0.090	-	-	-	-	5	-
9	4716.271	−0.319	-	-	-	-	3	-
12	4792.007	0.306	-	-	-	-	1	-
15	4917.212	−0.320	-	-	-	-	3	-
15	5014.069	0.100	-	-	-	-	15	-
15	5047.295	−0.560	-	-	-	-	4	-
38	5320.732	0.490	-	-	-	-	4	-
38	5345.721	0.350	6	-	-	-	6	-
44	4153.064	0.620	-	-	-	-	5	-
44	4162.665	0.780	-	-	-	-	7	-
49	4267.762	0.256	-	-	-	-	2	-
49	4294.402	0.549	-	-	-	-	3	-
55	3923.460	0.440	-	-	-	-	3	-
-	4463.581	0.134	-	-	-	-	3	-
S III								
4	4332.692	−0.240	-	-	-	-	4	-
4	4253.593	0.360	17	12	27	-	46	54
4	4284.991	0.090	5	7	20	-	35	35
5	3838.312	0.170	-	-	-	-	10	-
5	3860.695	−0.410	-	-	-	-	5	-

Ion			W_λ/mA					
Mult.	λ/Å	$\log(gf)$	01	02	03	04	05	06
7	4354.560	−1.610	-	-	-	-	9	21
7	4364.730	−0.710	-	4	-	-	8	-
8	3983.770	−0.440	-	-	-	-	10	16
8	3985.970	−0.790	-	-	-	-	6	16
10	4677.657	−0.790	-	-	-	-	6	-
-	3662.008	−0.380	-	-	-	-	12	-
-	3717.771	−0.190	-	-	-	-	17	-
-	3778.903	−0.290	-	-	-	-	4	-
-	3831.861	−0.410	-	-	-	-	3	-
-	3928.595	−0.190	-	12	-	-	-	-
Ar II								
1	4013.857	−0.680	-	-	-	-	5	-
1	4400.986	−0.330	-	-	-	-	9	-
1	4430.996	−0.790	-	-	-	-	6	-
2	4013.857	−0.880	-	-	-	-	5	-
6	4735.906	−0.120	-	-	-	-	15	20
6	4806.021	0.210	-	-	13	-	25	-
6	4972.160	−1.120	-	-	-	-	2	-
6	5009.334	−0.460	-	-	-	-	10	-
6	5062.037	−0.460	-	-	-	-	5	-
7	4266.527	−0.550	-	-	-	-	6	-
7	4331.200	−0.220	-	-	15	-	5	-
7	4426.001	0.170	-	-	-	-	21	30
7	4430.189	−0.170	-	-	-	-	11	-
7	4439.879	−1.630	-	-	-	-	7	-
7	4228.158	−0.680	-	-	-	-	4	-
7	4266.527	−0.420	-	-	-	-	6	-
7	4379.667	−0.170	-	-	-	-	13	-
10	3850.581	−0.240	-	-	-	-	4	-
10	3928.623	−0.640	-	-	-	-	-	-
13	5145.308	−0.570	-	-	-	-	4	-
14	4726.868	−0.170	-	-	-	-	9	21
14	4879.864	0.220	-	-	14	-	12	-
14	4965.079	−0.290	-	-	-	-	7	-
13	5145.308	−0.900	-	-	-	-	4	-
15	4657.901	−0.280	-	-	-	-	12	-
15	4764.865	−0.110	-	-	-	-	10	14
32	4277.528	0.000	-	-	13	-	8	-
33	4042.894	0.140	-	-	-	-	2	-
33	4072.005	−0.070	-	-	-	-	8	-
39	4481.811	−0.050	-	-	-	-	13	-
39	4370.753	−0.130	-	-	-	-	6	-
52	4072.385	−0.110	-	-	-	-	3	-

Ion			W_λ/mA					
Mult.	λ/Å	$\log(gf)$	01	02	03	04	05	06
53	3933.187	−1.380	-	19	-	-	-	-
54	3911.576	−1.160	-	-	-	-	10	-
63	4379.229	−1.220	-	-	-	-	3	-
79	4191.040	−1.190	-	-	-	-	5	-
81	3855.161	−1.740	-	-	-	-	3	-
86	4372.095	−1.700	-	22	-	-	-	-
90	3868.529	0.290	-	-	-	-	6	-
90	3932.547	0.010	-	52	-	-	11	-
101	3994.763	−1.780	-	-	28	-	-	-
101	4052.921	0.200	-	-	-	-	3	-
-	3935.282	−1.840	-	28	-	-	-	-
-	4367.831	0.575	-	-	-	-	3	-
-	4385.056	0.761	-	-	-	-	3	-
Ar III								
4	4361.530	−0.390	-	-	20	-	-	-
-	3503.586	0.041	-	-	-	-	10	-
-	3509.326	−0.473	-	-	-	-	4	-
-	3511.117	0.217	-	-	-	-	20	-
-	3511.696	−0.609	-	-	-	-	6	-
-	3514.176	−0.003	-	-	-	-	19	-
-	3756.307	−0.783	-	-	-	-	7	-
-	3858.287	−1.590	-	-	-	-	3	-
Ca III								
-	4201.113	0.302	-	-	-	-	3	-
-	4240.742	0.637	-	-	-	-	4	-
-	4296.004	0.578	-	-	-	-	3	-
-	4302.803	0.587	-	-	-	-	4	-
-	4431.290	0.273	-	-	-	-	4	-
Ti III								
-	3872.495	0.505	-	-	-	-	4	-
-	3881.209	0.656	-	-	-	-	3	-
-	3893.633	0.365	8	-	-	-	-	-
-	3915.471	−0.415	-	-	-	-	10	-
-	3921.387	0.031	5	-	-	-	-	-
-	3921.609	0.204	8	-	-	-	7	-
-	3922.958	0.263	8	-	-	-	3	-
-	3924.962	0.010	8	-	-	-	2	-
-	4060.196	0.068	-	-	-	-	2	-
-	4079.958	−0.353	-	-	-	-	2	-
-	4180.219	−0.649	-	-	-	-	2	-
-	4200.067	0.211	12	-	-	-	-	-

Ion			W_λ/mA					
Mult.	λ/Å	$\log(gf)$	01	02	03	04	05	06
-	4201.695	−0.411	4	-	-	-	-	-
-	4204.919	−0.136	9	-	-	-	4	-
-	4207.491	0.083	-	-	-	-	11	-
-	4214.929	−0.993	-	-	-	-	4	-
-	4215.525	−0.917	18	-	-	-	13	-
-	4243.873	−0.433	5	-	-	-	-	-
-	4269.833	−0.823	-	-	-	-	3	-
-	4285.497	0.385	-	-	-	-	8	-
-	4286.504	−0.339	-	-	-	-	3	-
-	4288.672	−0.982	-	-	-	-	6	-
-	4289.254	−0.178	-	-	-	-	7	-
-	4295.432	−0.613	-	-	-	-	3	-
-	4304.492	0.752	-	-	-	-	15	-
-	4327.611	0.544	-	-	-	-	2	-
-	4348.035	−0.787	4	-	-	-	-	-
-	4378.933	0.415	-	-	-	-	3	-
-	4424.304	−0.425	-	-	-	-	4	-
-	4652.856	−0.829	-	-	-	-	3	-
-	4971.194	−0.976	-	-	-	-	5	-
-	5278.120	−0.414	-	-	-	-	5	-
-	5301.213	−0.112	-	-	-	-	3	-
-	6621.596	0.355	-	-	-	-	25	-
Fe III								
4	4382.502	−3.092	-	5	-	-	-	-
4	4395.751	−2.703	12	-	-	-	-	-
4	4419.599	−2.335	11	19	11	-	-	-
4	4431.001	−2.710	9	19	-	-	-	-
5	5063.459	−3.139	-	7	-	-	-	-
5	5073.896	−2.741	11	8	-	-	-	-
5	5086.718	−2.767	6	12	-	-	-	-
5	5127.352	−2.404	10	25	-	-	-	-
5	5127.638	−2.018	5	-	-	-	-	-
5	5156.111	−2.018	16	23	-	-	-	-
5	5193.883	−3.084	-	9	-	-	-	-
45	4005.022	−1.755	5	9	-	-	2	-
46	4022.326	−2.720	-	6	-	-	-	-
53	4025.000	−2.454	-	8	-	-	-	-
68	5485.568	−1.693	-	6	-	-	-	-
113	5235.658	−0.107	-	14	-	-	-	-
113	5243.306	0.405	19	24	26	-	4	-
113	5272.369	−0.421	4	6	-	-	-	-
113	5276.476	−0.001	8	17	-	-	1	-
113	5282.297	0.108	11	15	-	-	4	-

Ion			W_λ/mA					
Mult.	λ/Å	$\log(gf)$	01	02	03	04	05	06
113	5299.926	−0.166	5	14	16	-	2	-
113	5302.602	−0.120	5	13	-	-	-	-
114	5833.938	0.616	18	19	31	-	9	-
114	5929.685	0.351	10	15	15	-	3	-
118	4122.025	0.406	8	9	-	-	-	-
118	4122.780	0.360	7	7	-	-	-	-
118	4139.350	0.520	11	15	-	-	-	-
118	4140.482	0.101	7	-	-	-	-	-
118	4164.731	0.923	23	4	27	-	6	-
118	4166.840	0.409	11	13	-	-	2	-
118	4168.449	−0.323	7	-	-	-	2	-
119	4053.112	0.261	8	12	-	-	4	-
121	4273.372	0.252	-	7	-	-	-	-
121	4286.091	−0.512	7	12	-	-	-	-
121	4296.814	−0.512	15	9	-	-	-	-
121	4304.767	1.027	9	-	-	-	-	-
121	4310.337	−1.072	17	16	-	-	-	-
-	3586.072	−1.313	-	13	-	-	-	-
-	3600.943	−1.367	-	18	-	-	-	-
-	3603.890	−1.395	-	13	-	-	-	-
-	3778.716	0.648	-	3	-	-	-	-
-	3845.171	0.849	-	2	-	-	-	-
-	3869.137	0.680	-	5	-	-	-	-
-	3874.922	−0.789	-	4	-	-	-	-
-	3900.070	1.052	-	2	-	-	-	-
-	3916.858	0.970	-	2	-	-	-	-
-	3949.086	0.814	-	2	-	-	-	-
-	4003.227	0.624	4	-	-	-	-	-
-	4081.007	0.372	-	-	-	-	2	-
-	4120.903	0.184	5	-	-	-	-	-
-	4145.648	0.806	-	6	-	-	-	-
-	4154.963	0.891	9	4	-	-	-	-
-	4174.260	1.113	9	9	-	-	-	-
-	4186.828	0.105	4	-	-	-	-	-
-	4210.674	0.676	-	4	-	-	-	-
-	4222.271	0.272	10	14	-	-	-	-
-	4238.619	0.127	6	6	-	-	-	-
-	4240.670	0.652	-	4	-	-	-	-
-	4243.408	0.527	-	4	-	-	-	-
-	4249.733	−0.547	6	-	-	-	-	-
-	4357.204	−2.179	-	3	-	-	-	-
-	4372.746	−1.369	18	-	-	-	-	-
-	5156.111	−2.018	-	-	14	-	-	-
-	5192.013	−2.689	-	2	-	-	-	-

Ion			W_λ/mA					
Mult.	λ/Å	$\log(gf)$	01	02	03	04	05	06
-	5218.103	0.537	-	5	-	-	-	-
-	5272.975	0.598	6	9	-	-	-	-
-	5298.114	0.367	-	7	-	-	-	-
-	5309.922	0.344	-	3	-	-	-	-
-	4455.391	−3.751	5	-	-	-	-	-
-	5756.394	0.545	-	-	-	-	2	-
-	5854.622	0.801	-	-	-	-	2	-
-	5999.543	0.355	-	6	-	-	-	-
Zn III								
-	4818.883	0.492	-	-	-	-	7	-
-	4970.769	0.339	-	-	-	-	8	-

Appendix E

List of abbreviations

Table E.1: Abbreviations

$\odot$	Solar
γ	Systemic velocity
λ	Wavelength
ξ	Microturbulent velocity
$^\circ$	Degree
’	Arc-Minute
”	Arc-Second
Å	Ångström
A	Distance from barycenter
$A_{\rm tot}$	System’s total separation
AGB	Asymptotic Giant Branch
AGN	Active Galactic Nucleus
Al	Aluminum
Apr	April
Ar	Argon
Aug	August
bd. rot.	Bounded rotation
BH	Black hole
C	Carbon
Ca	Calcium
CA	Calar Alto
CCD	Charged Coupled Device
CE	Common Envelope
CNO	Carbon, Nitrogen, & Oxygen
comp	Companion
CSPN	Central star of a planetary nebula
CV	Cataclysmic Variable
$^{\rm d}$	Day
DA	Hydrogen-rich white dwarf (Degenerate type A)

DAO	Very hot hydrogen-rich white dwarf (Degenerate type AO)
DAZ	Cool hydrogen-rich white dwarf (Degenerate type AZ)
DB	Helium-rich white dwarf (Degenerate type B)
DBA	Helium-rich white dwarf with traces of hydrogen (Degenerate type BA)
DC	Cool white dwarf wit no spectral features (Degenerate type C)
Dec	December
deg	Degree
DFG	Deutsche Forschungsgemeinschaft
dl	Double-lined (system)
dM	M dwarf
DO	Very hot helium-rich white dwarf (Degenerate type O)
DSAZ	Deutsch-Spanisches Astronomisches-Zentrum
EC	Edinburgh-Cape
EHB	Extended (Extreme) Horizontal Branch
EMMI	ESO Multi Mode Instrument
ESO	European Southern Observatory
$f_{\rm m}$	Mass-Function
Fe	Iron (Ferrum)
Feb	February
FWHM	Full Width Half Maximum
g	Gravity
G	Gravitational Constant $G = 6.673 \cdot 10^{-8}$dyne cm^{-2} g$^{-}2$
Gyrs	Giga-years
h	Hour
H	Hydrogen
He	Helium
HE	Hamburg ESO
HeMS	Helium-Main-Sequence
He-sdB	Helium-rich subdwarf B
He-sdO	Helium-rich subdwarf O
HES	Hamburg ESO Survey
HJD	Heliocentric corrected Julian date
HQS	Hamburg Quasar Survey
HR	Hertzsprung-Russell
HRD	Hertzsprung-Russell-Diagram
HS	Hamburg Schmidt
i	Inclination
IDS	Intermediate Dispersion Spectrograph
INT	Isaac Newton Telescope
invis	Invisible (component)
Jan	January
JD	Julian Date
Jun	June
Jul	July
K	Radial Velocity Semi-Amplitude

K	Kelvin
km	Kilometer
KPD	Kitt-Peak-Downes
LINFOR	LINLTE.FOR
LTE	Local ThermoEquilibrium
M	Mass
M_{Chandra}	Chandrasekhar mass ($\approx 1.40\,\mathrm{M}_{\odot}$)
M_{tot}	Total mass
Mar	March
max.	Maximum
Mg	Magnesium
MIDAS	Munich Image Data Analysis System
MS	Main Sequence (star)
n	By number
N	Nitrogen
n_{He}	Logarithmic helium abundance ($\log[n_{\mathrm{He}}/n_{\mathrm{H}}]$)
Ni	Nickel
NLTE	Non-Local ThermoEquilibrium
Nov	November
NS	Neutron star
NTT	New Technology Telescope
Oct	October
O	Oxygen
P	Period
PG	Palomar Green
Q	Quality
prec	Precursor
prim	Primary
R	Radius
RGB	Red Giant Branch
RV	Radial velocity
RVV	Radial velocity variable
s	Second
S	Sulfur
sl	Single-lined (system)
S/N	Signal to Noise
sdB	Subdwarf B
sdO	Subdwarf O
sdOB	Subdwarf OB
sec	Secondary
Sep	September
Si	Silicon
SN	Supernova
SPY	SN Ia Progenitor Survey
SVD	Singular Value Decomposition

$T_{\rm eff}$	Effective temperature
$T_{\rm H}$	Hubble time
$t_{\rm m}$	Merging time
TAEHB	Terminal Age Extended (Extreme) Horizontal Branch
Ti	Titanium
UV	Ultra Violet
v	Orbital velocity
$v_{\rm rot} \sin i$	Projected rotational velocity
vis	Visual (component)
VLT	Very Large Telescope
WD	White Dwarf
WHT	William Herschel Telescope
y	Year
ZAEHB	Zero Age Extreme (Extreme) Horizontal Branch
Zn	Zinc

References

Benvenuto O.G., Althaus L.G., 1999, MNRAS 303, 30

Bergeron P., Liebert J., 2002, ApJ 566, 1091

Blöcker T., Herwig F., Driebe T., et al., 1997, in *White dwarfs*, eds. J. Isern, M. Hernanz, E. Garcia-Berro, Kluwer, Dordrecht, p. 57

Bragaglia A., Greggio L., Renzini A., D'Odorico S., 1990, ApJ 365, L13

Bragaglia A., Renzini A., Bergeron P., 1995, ApJ 443, 735

Branch D., Fisher A., Nugent P., 1993, AJ 106, 2383

Branch D., Tammann G.A., 1992, ARA&A 30, 359

Bruch A., Diaz M.P., 1998, AJ 116, 908

Chandrasekhar S., 1939, *An Introduction to the Study of Stellar Structure*, University of Chicago Press

Christlieb N., Wisotzki L., Reimers D., et al., 2001, A&A 366, 898

D'Odorico S., 2000, ESO Msngr 99, 1

D'Odorico S., Kaper L., Kaufer A., 2000, *UVES user manual*, Doc. No. VLT-MAN-ESO-13200-1825

Dorman B., Rood R.T., O'Connell R.W., 1993, ApJ 419, 596

Driebe T., Schönberner D., Blöcker T., Herwig F., 1998, A&A 339, 123

Drilling J.S., Landolt A.U., 2000, in *Allen's Astrophysical Quantities (4th edition)*, ed. Arthur N. Cox, AIP Press, Springer, New York

Edelmann H., 2003, *PhD - Thesis*, Friedrich Alexander Universität Erlangen - Nürnberg

Ekberg J.O., 1993, A&AS 101, 1

Ergma E., Fedorova A.V., Yungelson L.R., 2001, A&A 376, L9

Finley D.S., Koester D., Basri G., 1997, ApJ 488, 375

Friedrich S., Koester D., Christlieb N., et al., 2000, A&A 363, 1040

Hachisu I., Kato M., 2001, ApJ 558, 323

Hagen H.-J., Groote D., Engels D., Reimers D., 1995, A&AS 111, 195

Han Z., Podsiadlowski P., Maxted P.F.L., Marsh T.R., 2003, MNRAS 341, 669

Heber, U., Drechsel H., Østensen R., Karl C., et al., 2004, A&A 420, 251

Heber U., Edelmann H., Lisker T., Napiwotzki R., 2003, A&A 411, L477

Heber, U., Napiwotzki R., Reid I.N., 1997, A&A 323, 819

Heber U., Reid I.N., Werner K., 2000, A&A 363, 198

Herrmann M., 2000, *Zulassungsarbeit*, Friedrich Alexander Universität Erlangen - Nürnberg

Hilditch R.W., Kilkenny D., Lynas-Gray A.E., Hill G., 2003, MNRAS 344, 644

Hirata R., Horaguchi T., 1995, *Atomic spectral line list*, Department of Astronomy, Kyoto University and National Science Museum

Höflich P., Wheeler J.C., Thielemann F.K., 1998, ApJ 495, 617

Horne K., 1986, PASP 98, 609

Iben I.Jr., Tutukov A.V., 1984, ApJS 54, 335

Iben I.Jr., Tutukov A.V., Yungelson L.R., 1997, ApJ 475, 291

Karl C., Napiwotzki R., Heber U., Dreizler S., Koester D., Reid I.N., 2004, A&A, submitted

Karl C., Napiwotzki R., Nelemans G., Christlieb N., Koester D., Heber U., Reimers D., 2003, A&A 410, 663

Kilkenny D., Heber U., Drilling J.S., 1988, SAAOC 12, 1

Kilkenny D., O'Donoghue D., Koen C., Stobie R.S., Chen A., 1997, MNRAS 287, 867

Koester D., Dreizler S., Weidemann V., Allard N.F., A&A 338, 612

Koester D., Napiwotzki R., Christlieb N., et al., 2001,A&A 379, 215

Kurucz R.L., 1992, *Proc. of the 149$^{\rm th}$ Symposium of the IAU*, eds.B. Barbuy, A. Renzini, Kluwer, Dordrecht, p. 225

Lamontagne R., Demers S., Wesemael F., Fontaine G. Irwin M.J., 2000, AJ, 119. 241

Landau L.D., Lifshitz E.M., 1951, *The Classical Theory of Fields*, Pergamon

Leibundgut B., 2001, ARA&A 39, 67

Li W., Filippenko A.V., Treffers R.R., Riess A.G., Hu J., Qiu Y., 2001, ApJ 546, 734

Lisker T., *Diploma Thesis*, Friedrich Alexander Universität Erlangen - Nürnberg

Lisker T., Heber U., Napiwotzki R., Christlieb N., Han Z., Homeier D., Reimers D., 2004, accepted

Livio M., 2000, in *Type Ia Supernovae: Theory and Cosmology*, Cambridge Univ. Press, p. 33

Lorenz L., Mayer P., Drechsel H., 1998, A&A 332, 909

Marsh T., 2000, NewAR 44, 119

Marsh T. R., Dhillon V. S., Duck S. R., 1995, MNRAS 275, 828

Maxted P.F.L., Marsh T.R., 1999, MNRAS 307, 122

Maxted P.F.L., Marsh T.R., Moran C.K.J., 2000a, MNRAS 319, 305

Maxted P.F.L., Marsh T.R., Moran C.K.J., Han Z., 2000b, MNRAS 314, 334

Maxted P.F.L., Marsh T.R., North R.C., 2000c, MNRAS 317, L41

Maxted P.F.L., Marsh T.R., Moran C.K.J., 2002a, MNRAS 332, 745

Maxted P.F.L., Marsh T.R., Heber U., et al., 2002c, MNRAS 333, 231

Maxted P.F.L., Burleigh M.R., Marsh T.R., Bannister N.P., 2002b, MNRAS, 334, 833

McCook G.P., Sion E.M., 1999, ApJ 121,1

Méndez R.H., Kudritzki R.P., Herrero A., Husfeld D., Groth H.G., 1988, A&A 190, 113

Moehler S., Richter T., de Boer K.S., Dettmar R.J., Heber U., 1990, A&AS 86, 53

Munari U., Renzini A., 1992, ApJ 397, L87

Napiwotzki R., 1999, A&A 350, 101

Napiwotzki R., Green P.,J., Saffer R.A., 1999, ApJ 517, 399

Napiwotzki R., Christlieb N., Drechsel H., et al., 2001a, AN 322, 201

Napiwotzki R., Edelmann H., Heber U., Karl C., Drechsel H., Pauli E.-M., Christlieb N., 2001b, A&A 378, L17

Napiwotzki R., Koester D., Nelemans G., et al., 2002, A&A 386, 957

Napiwotzki R., Christlieb N., Drechsel H., et al., 2003a, ESO Msngr 112, 25

Napiwotzki R., Christlieb N., Drechsel H., et al., 2003b, in *From Twilight to Highlight*, ed. W. Hillebrandt, B. Leibundgut, Springer Verlag Berlin, Heidelberg, p. 134

Nelemans G., Yungelson L.R., Portegies Zwart S.F., Verbunt F., 2001, A&A 365, 491

Pauli E.-M., Napiwotzki R., Altmann M., heber U., Odenkirchen M., Kerber F., 2003, A&A 400, 877

Phillips M.M., 1993, ApJL 413, L105

Rauch T., 2000, A&A 365, 665

Rauch T., Werner K., 2003, A&A 400, 271

Reimers D., Wisotzki L., 1997, ESO Msngr 88, 14

Riess A.G., Filippenko A.V., Challis P., Clocchiatti A., et al., 1998, AJ 116, 1009

Riess A.G., 2000, PASP 112, 1284

Saffer R.A., Bergeron P., Koester D., Liebert J., 1994, ApJ 432, 351

Saffer R.A., Livio M., Yungelson L.R., 1998, ApJ 502, 394

Simon K.P., Sturm E., 1994, A&A 281, 286

Stark M.A. Wade R.A., 2003, Aj 126, 1455

Stobie R.S., Kilkenny D., O'Donaghue D., et al. 1997, MNRAS 287, 848

Ströer A., 2004, *Diploma Thesis*, Friedrich Alexander Universität Erlangen - Nürnberg

Truran J.W., Livio M., 1986, ApJ 308, 721

van den Haeufel E.P.J., Bahttacharya D., Nomoto K. Rappaport S.A., 1992, A&A 262,97

Vennes S., Thorstensen J.R., Polomski E.F., 1999, ApJ 523, 386

Whelan J., Iben I.Jr., 1973, ApJ 186, 1007

Wiese W.L., Fuhr J.R., Deters T.M., 1996, *Atomic transition probabilities of carbon, nitrogen and oxygen: a critical data compilation*, eds. W.L. Wiese, J.R. Fuhr, T.M. Deters, American Chemical Scociety for the National Institute of Standards and Technology, Washington DC

Wisotzki L., Christlieb N., bade N. et al., 2000, A&A 358, 77

Wisotzki L., Koehler T., Groote D., Reimers D., 1996, A&AS 115,227

Wood M.A., 1995, in *White Dwarfs, Proceedings of the 9$^{\rm th}$ European Workshop on White Dwarfs*, Springer Verlag, Berlin, Heidelberg, New York, p. 51

Wright E.L., 2003 New Astronomy Review 47, 877

Acknowledgments

First of all I want to express my gratitude to my supervisors Ralf Napiwotzki and Uli Heber for setting the stage for this. They offered me the opportunity to do my PhD on a promising and inspiring field of astronomy by joining the SPY consortium. Without their continuous support and encouragement, their shared talent and knowledge and the vast amount of time spent on me (and even patience, I guess), the last years would be more stress and less pleasure.

I want to thank the SPY consortium as well. Especially Gijs Nelemans who generously shared radial velocity data for several stars, Norbert Christlieb for four wonderful weeks of collaboration in Hamburg, and Detlev Koester for doing all the spectral analysis.

Many thanks also to all my colleagues in the Dr. Remeis Sternwarte who made the institute more than a simple working place. I want to thank Irmela Bues for her steady interest in my work and for many useful comments made over the course of the years. I appreciate the support of Horst Drechsel who never refused me when I was confused by my computer or needed advice how to handle astronomical problems. Thank you, Rainer Sterzer, for the help with all the "little computer problems" and for the countless hours you spent on teaching me how simple life could be. My work also benefited from Norbert Przybilla's generous assistance, who was at hand whenever help was needed I am grateful to Siegfried Falter, Markus Ramspeck, and Heinz Edelmann for all the inspiring discussions about Astronomy and more. Furthermore I am thankful to Heinz' for all the useful tips and tricks about how to handle computers. I appreciate our native speaker Simon O'Toole who kindly agreed to read through my thesis and saved the reader from my crimes against his mother tongue. Thanks a lot to the rest of the "Remeis Team" Alex Ströer, Eva-Maria Pauli, Martin Altmann, Michael Bauer, Sabine Möhler, Stefan Nesslinger, Thorsten Lisker and Zorica Salomon for contributing to the nice atmosphere in our good, old institute. I also want to mention Edith Day for all the administration work she did during the last years.

I am grateful to all the astronomers I have met during the last years. By means of countless discussions on conferences, workshops, meetings and seminars I discovered how exceptional astronomers can be. Special thanks also to Klaus Werner for being a referee for this thesis, and to the staff of the Calar Alto Observatory, Spain and the la Silla Observatory, Chile, for the help, support and valuable assistance during my visits.

I made extensive use of NASAs Astrophysics Data System Abstract Service (ADS), the SIMBAD database, operated at CDS, Strasbourg, France, the Digital Sky Survey (DSS), and the LEO English/German Dictionary (`http://dict.leo.org`).

This work was supported by the Deutsche Forschungs Gemeinschaft (DFG) under grant Na 365/3-1. In addition, I gratefully acknowledge several travel grants to the Calar Alto observatory.

Thanks go also to all my friends who backed me over the years. Thank you for being friends.

And last but not least I want to thank my family who never lose faith on me. Thank you, Mum and Dad, Brother and Sister, and you too, little nephew, for being my "eye of the Hurricane" all the time. This work is dedicated to you.

Curriculum Vitae

Name:	Christian Anton Karl
Geburtsdatum:	28.07.1973
Geburtsort:	Bamberg
Staatsangehörigkeit:	Deutsch
Beruf:	Diplom Physiker Univ.
Familienstand:	Ledig
Konfession:	Römisch Katholisch
Anschrift:	Mainstrasse 61 96103 Hallstadt

Beruflicher Wertegang

1980 - 1984	Grundschule Dörfleins
1984 - 1993	Dientzenhofer-Gymnasium Bamberg
WS 1993/94 - WS 1999/2000	Studium der Physik an der Universität Bayreuth
SS 2000 - SS 2001	Studium der Physik an der Friedrich-Alexander-Universität Erlangen-Nürnberg
Sptember 2001	Diplomprüfung in Physik
Seit Oktober 2001	Beschäftigung als Wissenschaftlicher Mitarbeiter und Anfertigung der Dissertation an der Dr. Karl Remeis Sternwarte, Bamberg, dem Astronomischen Institut der Friedrich-Alexander-Universität Erlangen-Nürnberg